Cooperative Position and Orientation Estimation with Multi-Mode Antennas

Dissertation

zur Erlangung des akademischen Grades

Doktor der Ingenieurwissenschaften
(Dr.-Ing.)

der Technischen Fakultät
der Christian-Albrechts-Universität zu Kiel

vorgelegt von

Robert Pöhlmann

aus
Augsburg

Februar 2022

Tag der Einreichung: 01.02.2022
Tag der Disputation: 15.11.2022

Berichterstatter: Prof. Dr.-Ing. Peter Adam Höher
Prof. Dr.-Ing. Gerhard Bauch
Prof. Dr. Gonzalo Seco-Granados

Preface

This thesis is the outcome of my research at the Institute of Communications and Navigation of the German Aerospace Center (DLR).

First and foremost, I would like to thank my supervisor, Prof. Peter Adam Höher from the University of Kiel, for giving me the freedom to pursue this PhD topic in my own way, for his lasting support, valuable discussions and enjoyable visits to Kiel. Moreover, I would like to thank Prof. Uwe-Carsten Fiebig for his professional support of my PhD project in his department.

I am especially grateful to Dr. Armin Dammann, head of the mobile radio transmission group. Through his helpful, encouraging and open-minded manner, he was a real support throughout this journey. I would also like to thank all my current and former colleagues from DLR. A special thanks goes to Siwei, for countless scientific discussions, which often lasted until late in the evening. Another special thank you is in place for Emanuel, for his support with experiments and measurements. I would also like to thank Kazeem and Stefano for insightful discussions and for providing an antenna. Furthermore, I would like to thank my DLR colleagues Christian, Fabio, Markus U., Markus W., Michael W., Ronald, Rostislav, Thomas J., Wei and many more for interesting discussions, but also for a great time.

In addition, I would like to thank Niklas, Nils and Sami and the other colleagues from the University of Kiel for insightful discussions and for making my visits to Kiel truly joyful.

I owe deep gratitude to my parents Barbara and Wolfgang, who have always supported me, no matter what I have pursued. Sadly, my father could not witness this chapter of my life. Finally, I am deeply grateful to my fiancee Franziska for her patience and her unconditional support.

Munich, February 2022

Robert Pöhlmann

Abstract

Robotic multi-agent systems are envisioned for planetary exploration, but also for terrestrial applications like search and rescue and environmental monitoring. Autonomous operation of robots requires estimations of their positions and orientations, which are obtained from the direction-of-arrival (DoA) and the time-of-arrival (ToA) of radio signals. For cooperative radio localization, signals are exchanged among all agents. Within this thesis, we estimate the signal DoA and ToA using a multi-mode antenna (MMA). An MMA is a single antenna element, where multiple orthogonal current modes are excited by different antenna ports. So far, MMAs have been considered for multiple-input multiple-output (MIMO) communications. This thesis provides a first study on the use of MMAs for cooperative position and orientation estimation. We specifically explore the DoA estimation capabilities of MMAs. Assuming the agents of a cooperative network are equipped with MMAs, lower bounds on the achievable position and orientation accuracy are derived. We realize a gap between the theoretical lower bounds and real-world performance of a cooperative radio localization system. The reason are biased estimates due to deviations of antenna and transceiver calibration parameters. Consequentially, we theoretically analyze in-situ antenna calibration. We further introduce an algorithm for in-situ calibration of arbitrary multiport antennas, including MMAs, and show its effectiveness by simulation. To also improve calibration during operation, we propose cooperative simultaneous localization and calibration (SLAC), which leverages the large number of observations within a cooperative network. We show that cooperative SLAC is able to estimate antenna responses and ranging biases of the agents together with their positions and orientations, without external sensors. For that, a Bayesian filtering algorithm for cooperative SLAC is derived and simulations are performed, showing considerable improvements of position and orientation accuracy compared to mere localization. Finally, we validate the results from theory and simulation by experiments with four robotic rovers equipped with software-defined radios (SDRs). On one rover, a four-port MMA is installed. We experimentally demonstrate DoA estimation with a single MMA, in-situ calibration of an MMA and cooperative SLAC. In conclusion, we show that DoA estimation with an MMA is feasible, and accuracy can be improved by in-situ calibration and SLAC.

Zusammenfassung

Der Einsatz robotischer Multiagentensysteme für die planetare Exploration, aber auch für terrestrische Anwendungen wie Katastrophenschutz und Umweltüberwachung, gewinnt zunehmend an Bedeutung. Für den autonomen Betrieb von Robotern ist eine genaue Schätzung ihrer Position und Orientierung unerlässlich. Diese werden aus der Ankunftszeit (*time-of-arrival*) und der Einfallsrichtung (*direction-of-arrival*) von Funksignalen gewonnen. Für die kooperative Radiolokalisierung werden Signale zwischen allen Agenten ausgetauscht. Im Rahmen dieser Arbeit werden Einfallsrichtung und Ankunftszeit mit einer Multimoden-Antenne (MMA) geschätzt. Eine MMA ist ein einzelnes Antennenelement, auf dem mehrere orthogonale Moden des Oberflächenstroms durch verschiedene Antennentore angeregt werden. Bis dato wurden MMAs für die *multiple input multiple output* (MIMO) Kommunikation eingesetzt. Diese Arbeit untersucht erstmals die Verwendung von MMAs für die kooperative Positions- und Orientierungsschätzung, wobei ein besonderer Fokus auf der Richtungsschätzung liegt. Zunächst werden untere Schranken für die erreichbare Positions- und Orientierungsgenauigkeit in einem kooperativen Netzwerk hergeleitet, dessen Agenten mit MMAs ausgerüstet sind. Dabei wird eine Diskrepanz zwischen den theoretischen unteren Schranken und der im Experiment erzielten Genauigkeit von kooperativen Funklokalisierungssystemen deutlich. Die Hauptursachen sind Schätzungen mit Ablage aufgrund von Abweichungen der Antennencharakteristiken und Kalibrierungsparameter an Sender und Empfänger. Es wird daher die in-situ Antennenkalibrierung theoretisch analysiert. Außerdem wird ein Algorithmus zur in-situ Antennenkalibrierung beliebiger Mehrtor-Antennen einschließlich MMAs entwickelt und seine Wirksamkeit durch Simulationen gezeigt. Um die Kalibrierung auch während des Betriebs zu verbessern, wird die kooperative, simultane Lokalisierung und Kalibrierung (*simultaneous localization and calibration* - SLAC) vorgeschlagen. SLAC nutzt die große Anzahl zur Verfügung stehender Beobachtungen innerhalb eines kooperativen Netzwerks aus und ist damit in der Lage, die Antennencharakteristiken und Ablagen der Distanzschätzungen der Agenten zusammen mit deren Positionen und Orientierungen ohne externe Sensoren zu schätzen. Dazu wird ein Bayesscher Filter für das kooperative SLAC Verfahren hergeleitet. Simulationen zeigen eine erhebliche Verbesserung der Positions- und Orientierungsgenauigkeit

durch SLAC im Vergleich zur reinen Lokalisierung. Schließlich werden die Ergebnisse aus Theorie und Simulation durch Experimente mit vier robotischen Rovern validiert. Die Rover sind dazu mit *software-defined radios* (SDRs) ausgestattet und auf einem der Rover ist eine MMA mit vier Toren integriert. Es werden die Richtungsschätzung mit einer MMA, die in-situ Kalibrierung einer MMA, sowie das kooperative SLAC Verfahren experimentell demonstriert. Zusammenfassend wird gezeigt, dass MMAs zur genauen Richtungsschätzung geeignet sind. Die Schätzgenauigkeit kann durch in-situ Kalibration und SLAC verbessert werden.

Contents

1 Introduction **1**

1.1 Motivation 1

1.2 State-of-the-Art 3

1.3 Contributions and Structure 11

2 DoA and ToA Estimation with a Multi-Mode Antenna **15**

2.1 Multi-Mode Antennas 15

2.2 Signal Model 18

2.3 Wavefield Modeling and Manifold Separation 21

2.4 DoA Estimation with a Multi-Mode Antenna 25

2.4.1 Non-Coherent DoA Estimation 25

2.4.2 Coherent DoA Estimation 27

2.4.3 Joint DoA and Polarization Estimation 28

2.4.4 Simulation Results 31

2.5 Joint DoA and ToA Estimation with a Multi-Mode Antenna 37

2.5.1 Joint DoA and ToA Estimation 37

2.5.2 Simulation Results 39

3 Fundamental Limits for Cooperative Position and Orientation Estimation **41**

3.1 Definition of a Cooperative Network 41

3.2 Fisher Information in ToA and DoA Domain 43

3.3 Fisher Information in Position and Orientation Domain 46

3.4 Absolute Position and Orientation Error Bounds 47

3.5 Relative Position and Orientation Error Bounds 49

3.6 From Theory Towards Practice 51

4 In-Situ Antenna Calibration **55**

4.1 Concept 55

4.2 State Definition 56

4.3 Observation Model 57

4.4 In-Situ Antenna Calibration Algorithm 59
4.5 Information from Observations 60
4.6 Recursive Bayesian Cramér-Rao Bound 62
4.6.1 Known Propagation Channel 62
4.6.2 Unknown Propagation Channel 63
4.7 Qualitative Behavior of the BCRB 66
4.8 Simulation Results 69
4.8.1 Simulation Setup and Random Antenna Response 69
4.8.2 Single Impinging Signal 71
4.8.3 Multiple Impinging Signals 73

5 Cooperative Simultaneous Localization and Calibration 75
5.1 Concept 75
5.2 State Space 77
5.2.1 State Definition 77
5.2.2 State Transition 79
5.2.3 Observation Model 79
5.3 Cooperative SLAC Algorithm 81
5.3.1 Prediction 82
5.3.2 Update 83
5.3.3 Prior 85
5.4 Simulation Results 86
5.4.1 Simulation Setup 86
5.4.2 Position and Orientation Estimation 88
5.4.3 Antenna Calibration 89
5.4.4 Ranging Bias Calibration 90

6 Experimental Validation 93
6.1 Cooperative Localization Testbed 93
6.1.1 System Architecture 93
6.1.2 Software-Defined Radio Implementation 95
6.1.3 Hardware Integration 97
6.2 Measurement Results 98
6.2.1 DoA Estimation with a Multi-Mode Antenna 100
6.2.2 In-Situ Antenna Calibration 102
6.2.3 Cooperative Simultaneous Localization and Calibration 105

7 Conclusion and Outlook 113

7.1 Conclusion 113
7.2 Outlook 116

Bibliography **119**

Appendix A List of Acronyms and Abbreviations **139**

Appendix B List of Mathematical Notations **143**

Appendix C Definitions, Proofs and Derivations **151**

Appendix D List of Author's Publications **169**

Chapter 1

Introduction

1.1 Motivation

Robotic planetary exploration missions have a long history [1]. Past missions, e.g. National Aeronautics and Space Administration's (NASA's) Mars Science Laboratory mission with the robotic rover Curiosity [2], were single-robot missions. Curiosity is often driven manually by an operator on Earth with the aid of camera images. Considering that the one-way signal delay between Mars and Earth lies between 4 min and 24 min, the rover is driven cautiously at very low speed to not risk any damage. In more than nine years mission duration, the rover Curiosity has traveled roughly 26 km [3]. While the mission is impressive and considered a huge success, the figure appears small when compared to e.g. the dimensions of Valles Marineris: Valles Marineris is a canyon on Mars, which is 4000 km long, 200 km wide and 7 km deep and an area of high interest for planetary research [4, 5].

In order to increase the moving speed of robots and thus exploration speed, the goal of the German Aerospace Center (DLR) and international partners is to perform future missions with a higher level of autonomy [6, 7] and teams of robots, called robotic multi-agent systems [8, 9]. The recent NASA mission with the robotic rover Perseverance and the robotic helicopter Ingenuity is a first step in this direction [10]. Besides planetary exploration, robotic multi-agent systems are also considered for terrestrial applications like search and rescue [11] or environmental monitoring [12]. Compared to a single robot, multi-agent systems have several advantages: Multiple agents observe the environment simultaneously at different locations, thereby increasing exploration speed. When they cooperate by intelligent algorithms instead of acting independently of each other, exploration efficiency is increased [13]. Inherent redundancy is provided, as the failure of an individual agent does not automatically jeopardize the entire mission.

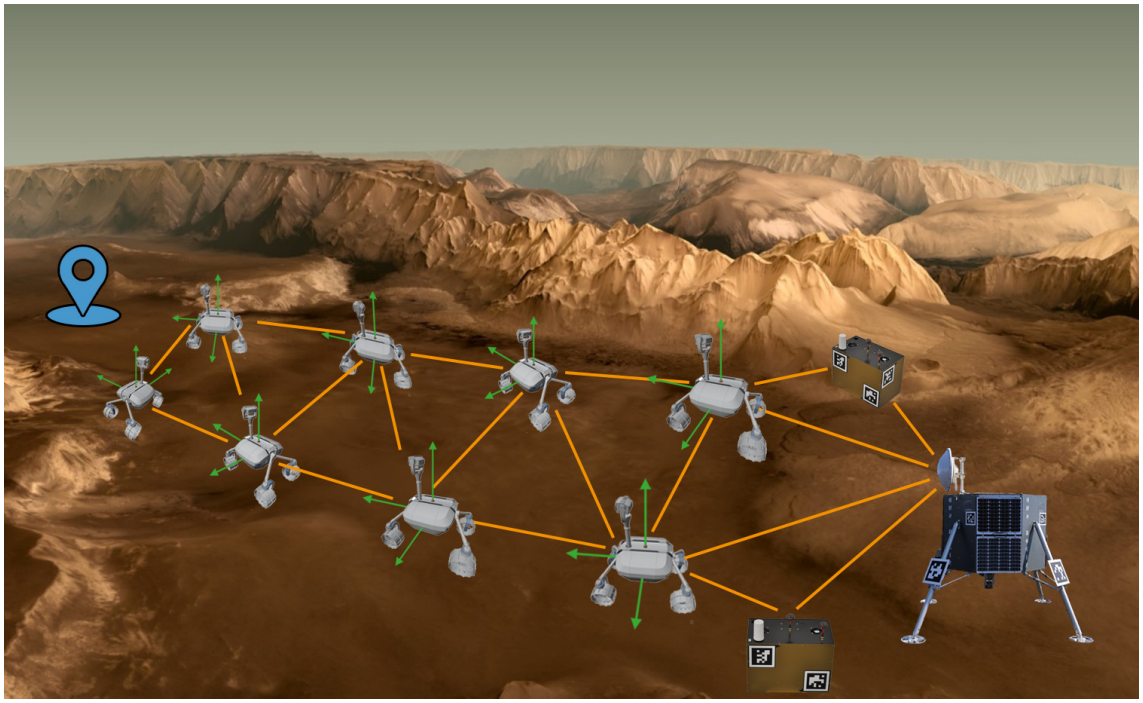

Figure 1.1. *Robotic multi-agent system exploring Valles Marineris on Mars. Valles Marineris image © ESA, DLR, G. Neukum.*

Furthermore, heterogeneous teams bring together the advantages of e.g. ground-based and airborne agents [9]. When the agents are properly synchronized, the formation can act as a distributed sensor aperture to sense spatio-temporal processes [14]. A closely related field is swarm robotics [15, 16, 17, 18], usually considering a large number of agents. Swarm robotics is inspired by nature e.g. fish schools or bird flocks. Characteristic for swarm robotics is a collective behavior of the robots based on simple rules. Collectively, the robots can solve tasks that would not be possible individually.

For autonomous operation of a robotic multi-agent system, where humans only interact with the system on a high level, reliable communication and localization is a crucial requirement. Fig. 1.1 shows a lander and multiple robotic agents on their way to a point of interest, exploring Valles Marineris on Mars. The figure highlights that autonomous operation of robotic agents requires means to estimate both, positions and orientations of the agents. The orientations are specifically needed for control, but also to know in which direction cameras and scientific instruments are pointing. As radio transceiver on the agents are needed for communication, radio localization, also called radio navigation, comes naturally. Furthermore, radio localization works also at night and e.g. during sandstorms.

Position and orientation estimation requires distance and direction information. By radio localization, distance and direction are obtained from the time-of-arrival (ToA)

and direction-of-arrival (DoA) of radio signals. With this thesis, we specifically study radio localization with multi-mode antennas (MMAs). An MMA is a single antenna element, where multiple orthogonal current modes are excited by different antenna ports. We start by showing how the signal DoA can be estimated by a single MMA. Multiple agents equipped with radio transceivers and MMAs form a cooperative network for radio localization. Estimation theory provides us the tools to determine lower bounds on the achievable position and orientation estimation error of the agents. However, experiments indicate that there is a considerable gap between the theoretical lower bounds and the performance achieved in practice. To bring real-world performance closer to the theoretical lower bounds, calibration and mitigating model mismatch is crucial. To this end, we theoretically investigate in-situ antenna calibration and present an algorithm suitable for an MMA. Furthermore, we take advantage of the cooperative network and propose simultaneous localization and calibration (SLAC), where antenna responses and ranging biases of the agents are estimated simultaneously with their positions and orientations. Bridging theory and practice, the proposed methods are validated by both, simulations and experiments. The main application of interest is a robotic multi-agent system for planetary exploration. However, the methods can also be applied to terrestrial radio localization, e.g. in global navigation satellite system (GNSS) denied environments. In the following, we discuss the state-of-the-art regarding the main topics of this thesis.

1.2 State-of-the-Art

Radio Localization Radio localization describes the process of finding the location of an entity using radio waves. This thesis focuses on radio localization in wireless networks, specifically robotic multi-agent systems, where all nodes transmit and receive radio signals. By localization we consider both, position and orientation, as both are mandatory to control the robots. We assume the network consists of mobile nodes called **agents** and static nodes with known position called **anchors**, see also Fig. 1.1. We further distinguish between non-cooperative and cooperative radio localization. For **non-cooperative** localization, only agents and anchors communicate, whereas for **cooperative** localization, agents also exchange radio signals among each other. Many theoretical investigations have shown that cooperative is in general superior to non-cooperative localization [19, 20, 21, 22], which has also been confirmed by measurements [19, 23]. Cooperative localization emerged in the context of wireless sensor networks [24] and was later also considered for cellular networks [25]. Radio signals exchanged in cooperative networks contain rich position and orientation in-

formation. This information can be classified as follows. Information regarding the **distance** between transmitter and receiver is contained in

1) the received signal strength (RSS). Assuming certain propagation conditions, e.g. free-space path loss (FSPL), the RSS can be used to estimate the distance. However, the assumed propagation conditions often do not match reality, which makes this approach prone to errors [24].

2) the carrier-phase of the received signal. The carrier phase wraps around after one wavelength, creating the need to also estimate the integer ambiguity. Having enough observations and good enough delay estimates of the baseband signal, this is in general feasible and widely used in geodetic GNSS receivers [26].

3) the delay of the baseband signal. The ToA of the radio signal observed at the receiver together with the transmit timestamp encoded into the signal can be used to calculate the time-of-flight (ToF). In a synchronized network, the distance can be obtained by multiplying the ToF with the speed of light. For unsynchronized networks, signals can be sent in both directions, e.g. using a two-way ranging (TWR) protocol. Having two observations, the clock offset is eliminated and the round-trip time (RTT) is calculated [27]. The distance is then half the RTT multiplied by the speed of light.

Relative **velocity** between transmitter and receiver leads to a carrier frequency offset of the received signal, called Doppler shift. The Doppler shift is additive to the carrier frequency offset caused by unsynchronized oscillators.

To obtain **direction** information, the radio signals observed at the receiver must depend on the signal direction. However, the radio signals are also influenced by the propagation channel, which is in general unknown. Thus, direction estimation must rely on relative signal observations. An example realization is a rotating singleport antenna with directional pattern, assuming the propagation channel to be constant during the observation time. For a static antenna, more than one antenna port is needed to estimate the signal direction despite the influence of the unknown propagation channel. Conventionally, an antenna array, consisting of multiple antenna elements, is considered. In this thesis, we investigate a single antenna element, where multiple characteristic modes are excited, which is called MMA. Using the known antenna response of a receiving multiport antenna, the signal DoA can be estimated [28, 29], which is also known as direction finding. Similarly, if the antenna response of a transmitting multiport antenna as well as the beamforming or precoding is known, the signal direction-of-departure (DoD) can be estimated [30, 31].

The major challenges for all radio based localization methods are the obstruction of the line-of-sight (LoS) propagation path, leading to non-line-of-sight (NLoS) condition, and multipath propagation in general. There are two different ways to tackle NLoS and multipath propagation. The first approach aims at detecting whether the condition is LoS or NLoS [32, 33] and separating the propagation paths [34, 35, 36]. When the LoS condition is correctly detected and the separation succeeds, the LoS path can be extracted, and the multipath influence is mitigated. By the second approach, the additional information contained in the multipath signals is exploited for localization [37, 38, 39, 33]. Such concepts called multipath-assisted localization can enable position and orientation estimation in cases which would otherwise be underdetermined.

DoA & ToA Estimation For low-complexity receivers, **non-coherent** or power-based **DoA** estimation can be performed based on RSS estimates. Non-coherent DoA estimation can be performed with multiple directional antennas pointing into different directions [40]. Alternatively, an actuator can be used to rotate a single antenna [41, 42]. Instead of rotating the antenna, the motion of the whole platform, e.g. a unmanned aerial vehicle (UAV), can be controlled [43]. To avoid physical motion or mechanical parts, antenna beams can also be switched [44] or electronically steered [45]. High-resolution algorithms for non-coherent DoA estimation can be found in [46, 47].

The default approach is **coherent DoA** estimation with antenna arrays, which requires multiple phase-coherent receiver channels. The array can span one dimension, e.g. a uniform linear array (ULA), two dimensions, e.g. a uniform rectangular array (URA) or a uniform circular array (UCA), or three dimensions, e.g. a conformal array. To reduce the amount of antennas and receiver channels, sparse arrays are considered [48, 49]. Often it is assumed that antenna arrays consist of omnidirectional or isotropic antenna elements and the phase response, also called steering vector, is purely defined by the geometry. We call an array following these assumptions an ideal antenna array, in order to distinguish from the antenna response of a real-world antenna array. In practice, there are gain-phase offsets and mutual coupling between the antenna elements, electromagnetic influences of the antenna surroundings etc. [50]. In contrast to the acoustic domain, where wideband algorithms are needed, most radio frequency (RF) DoA algorithms follow the narrowband assumption. Although the absolute signal bandwidth can be large, the relative bandwidth compared to the carrier frequency is usually small, which justifies the narrowband assumption. Furthermore, it has been shown that as long as signal spectrum and antenna response are symmetric with respect to (w.r.t.) the carrier frequency, the narrowband assumption is valid also for larger bandwidths [51, 52, 53]. DoA estimation algorithms can be categorized into beamform-

ing, subspace-based and parametric methods [54, 55]. For **beamforming** methods, a power spectrum versus the DoA is calculated, and the peak(s) are considered as DoA estimate(s). Conventional beamformer, Capon and minimum variance distortionless response (MVDR) fall into this category. They are computationally efficient, but often suffer from limited accuracy and resolution of multiple simultaneously impinging signals, especially if the impinging signals are correlated. **Subspace-based** methods exploit the eigenstructure of the spatial covariance matrix to calculate a pseudospectrum. The most prominent example is the multiple signal characterization (MUSIC) algorithm [56]. More recently, the partial relaxation approach was introduced [57]. Compared to beamforming methods, they provide better resolution of multiple impinging signals, but suffer from poor performance for correlated or coherent signals. Coherently impinging signals could occur e.g. in a static multipath scenario, as the different signals originate from the same transmitter. In such a case, the rank of the signal covariance matrix is lower than the actual number of impinging signals and the subspace decomposition fails. Correlation or coherency of the impinging signals is not to be confused with coherent DoA estimation mentioned earlier, which refers to the coherency of the receiver channels. For **parametric** methods, the impinging signals are assumed to be deterministic unknown or a stochastic random process. Parametric methods require an estimate of the model order, i.e. the number of impinging signals. The model order can be estimated based on e.g. the Akaike information criterion (AIC), the Bayesian information criterion (BIC), the generalized likelihood ratio test (GLRT) [58] or the information complexity criterion (ICOMP) [59, 60]. The deterministic or stochastic maximum likelihood (ML) estimators require a search process and provide better performance for correlated signals at the cost of higher computational complexity [61]. The process of a multidimensional search for all DoAs can be separated into multiple one dimensional searches as in the space-alternating generalized expectation maximization (SAGE) algorithm [62].

When the transmitted signal or at least its structure is known, the signal **ToA** can be estimated at the receiver. For a single impinging signal, the ML ToA estimator is essentially a peak search of the cross-correlation of the received and a replica of the transmitted signal. ToA estimation is usually done in frequency domain to achieve sub-sample resolution [63]. DoA and ToA can also be estimated jointly [64, 65]. The SAGE algorithm can also be applied to joint DoA and ToA estimation, in order to reduce complexity of the ML estimator [34, 62].

In contrast to antenna arrays, an MMA consists only of a single antenna element. Based on the theory of characteristic modes (TCM) [66, 67], multiple characteristic modes are excited independently [68, 69], resulting in a multiport antenna with a dis-

tinct antenna response for each port [70, 71, 68, 72, 73, 74, 69]. There is only one early work suggesting to exploit modes of a biconical horn antenna for DoA estimation [75]. Otherwise, prior to the works related to this thesis, MMAs have not been considered for DoA estimation or for localization in general. Recently, studies have shown how an MMA based on an airplane structure [76, 77, 78] and a cubic structure [79] can be used for DoA estimation.

Fundamental Limits for Cooperative Localization Estimation theory provides fundamental limits in terms of lower bounds on the estimation variance or the mean squared error (MSE). Fundamental limits are of interest in order to assess the feasibility of an estimation task and as a benchmark for algorithms. Very popular fundamental limits in the context of cooperative localization are the Cramér-Rao bound (CRB) for deterministic and the Bayesian Cramér-Rao bound (BCRB) for random parameters [80, 81]. Several other bounds exist [81], e.g. the Ziv-Zakai bound (ZZB) and the Weiss-Weinstein bound (WWB), but are less commonly used as they usually have to be evaluated numerically. The CRB can be calculated in closed-form and is an asymptotically tight bound, i.e. ZZB and WWB converge to the CRB for high signal-to-noise ratio (SNR) or large number of observations.

Most papers consider networks consisting of agents and anchors. The goal is to estimate the agent positions w.r.t. to the coordinate system defined by the anchors, which we call **absolute** localization. Interest in cooperative localization has arisen in the context of wireless sensor networks [24], where also fundamental limits have been investigated. In [82] a framework for calculating position and orientation error bounds based on the CRB is presented for non-cooperative networks. [20] extends the framework of [82] to cooperative localization, but does not consider orientation estimation. Position and orientation error bounds for cooperative networks with antenna arrays are derived in [83], where also different array geometries are compared. Both, [82] and [83] assume ideal antenna arrays with absolute phase synchronization between all nodes. [84] treats the more general case, where the absolute phase is unknown, but does not consider cooperation. The benefit of cooperation is proven by [21], which considers only the position domain. Position and orientation estimation with massive arrays is investigated by [85, 86, 87, 88], where the papers focus on a single link. The mentioned papers [82, 83, 84, 89, 86] are also limited to ideal antenna arrays.

Cooperation in the sense that agents exchange signals among each other is called spatial cooperation in [90, 91, 22, 92]. Spatial cooperation can be seen as cooperation on a per-snapshot basis. If prior knowledge on agent locations and agent dynamic models is assumed, information is also coupled over time. Additionally exploiting

the information coupling over time, e.g. by Bayesian filtering or recursive Bayesian estimation [93], is called spatio-temporal cooperation in [90, 91, 22, 92].

For certain scenarios in robotic navigation, only the formation or relative position and orientation of the agents w.r.t. each other is of interest, which is called **relative** or anchor-free localization. In [94, 95] CRBs for relative localization have been derived. Compared to absolute localization, the Fisher information matrix (FIM) for relative localization is singular. Furthermore, the choice of coordinate frame impacts relative localization performance. A CRB for an ideally chosen coordinate frame can be calculated with the Moore-Penrose pseudoinverse. In [96] the posterior CRB for relative tracking is derived.

The fundamental limits on cooperative localization found in the literature are limited to ideal antenna arrays, not considering nonidealities of real-world antennas like mutual coupling etc. [50]. Moreover, they cannot be applied to other types of multiport antennas like MMAs or co-located antennas [97, 98, 99].

In-Situ Antenna Calibration The algorithms presented in the paragraph on DoA estimation have in common that they rely on exact knowledge of the antenna response. Any mismatch between the assumed antenna response and the real one will impair DoA estimation performance [50]. In practice, antennas are thus calibrated by measuring their antenna response in a dedicated **measurement chamber** without multipath propagation, also called anechoic chamber. Using e.g. wavefield modeling and manifold separation [100, 101], a closed-form mathematical representation of the measured antenna response can be determined and used for DoA estimation. For cost and practicability reasons, often only the antenna alone is measured in a compact near-field measurement chamber. The far-field antenna response is then obtained from the near-field measurement data by a mathematical transformation [102]. Due to the size constraint of a near-field measurement chamber, only the antenna alone can be measured. However, the surrounding structure of an antenna influences its response. When the antenna is integrated in its final position, e.g. on a robotic rover, the installed antenna response is in general different compared to the antenna response of the antenna in free-space. Accurate calibration thus requires the whole device or robot to be measured in a large measurement chamber, e.g. a compact test range, which can become costly and impractical.

An attempt to solve the calibration issue are **auto-calibration** or self-calibration methods, which estimate the antenna parameters together with the DoA(s) [103]. However, all auto-calibration methods suffer from a severe limitation: In general, both DoA(s) and antenna parameters are not simultaneously identifiable from a collection

of received signal snapshots, unless strong assumptions are taken [104, 105]. When the antenna response of an ideal antenna array is assumed, it is possible to calibrate the gain and phase errors of individual antenna elements [106, 107]. Restricting the array geometry to ULA or UCA, it is possible to determine the mutual coupling matrix, which is a linear transformation of the antenna response [108, 109]. A maximum a posteriori (MAP) approach for auto-calibration, which integrates the aforementioned calibrations, is presented in [110]. Low complexity variants can be found in [110, 111]. The limiting assumption for [110, 111] is that the disturbances of the antenna response must be relatively small, i.e. not larger than the errors from observation noise. The assumption is relaxed by [112], which allows large errors of the assumed antenna element positions, but is still limited to ideal antenna arrays. For ideal linear antenna arrays, sparsity-based approaches exist, which outperform conventional approaches [113, 114].

In-situ calibration methods rely on transmitters in known directions to estimate the antenna parameters in unknown propagation conditions and without external synchronization. In [115], mutual coupling and antenna element positions of an array are calibrated. Additionally to mutual coupling and antenna element positions, also the power patterns of the antenna elements of an array are calibrated in [116]. In [117], mutual coupling and antenna element positions of multiple arrays are calibrated for a localization system.

To sum up, known auto-calibration and in-situ calibration methods are restricted to antenna arrays and cannot be applied to MMAs. Moreover, there is no guarantee that antenna response errors are restricted to gain-phase errors, mutual coupling or antenna element position errors. Due to manufacturing imperfections, the surrounding structure of the antenna etc. arbitrary nonlinear transformations of the antenna response of an ideal antenna array are possible [50].

Simultaneous Localization and Calibration As outlined in the paragraph on fundamental limits, rich literature exists on the cooperation aspect of localization. However, the calibration of a cooperative localization system is also of practical importance, but not well covered by literature. The challenge for cooperative localization is that an agent relies to a large extent on the observation of signals transmitted by its neighboring agents. Depending on the application, the agent hardware can be composed of low-cost commercial off-the-shelf (COTS) components.

For methods that rely on the propagation time of the signal like ToA or RTT, internal **group delays** in the transceivers need to be calibrated. Transceiver group delays can be calibrated by connecting the node transceivers to a calibrated reference or signal splitter. Such a calibration can only be performed before operation. However,

group delays of the transceiver transmit and receive chains can vary over time, e.g. caused by temperature variations. Especially low-cost COTS hardware is susceptible to group delay variations, which cause ranging biases [118, 119].

As highlighted in the previous paragraph, DoA estimation relies on accurate knowledge of the antenna response, causing the need for **antenna calibration**. When the surroundings of the antenna are changing, calibrating the antenna only once before operation is conceptually problematic. An example for changing surroundings is a manipulator arm on a robotic rover [120]. Furthermore, devices sent on planetary exploration missions suffer from dust, radiation, large temperature differences etc. Proper condition of the system must thus be monitored. If anomalies are detected, a re-calibration can only be performed during the mission.

Calibration during operation is often an integral part of simultaneous localization and mapping (SLAM) [121, 122]. In [123] a microphone array is calibrated for sound source localization using a SLAM approach. [124] presents SLAM with robot odometry calibration. Other examples include electromagnetic localization of instruments in a patient's body during surgery and simultaneous calibration of electromagnetic distortions [125]. With millimeter wave (mmWave) communications becoming popular, SLAM has recently gained attention for radio localization in 5G and 6G cellular networks. The high temporal and spatial resolution of mmWave systems allows to estimate the parameters of each propagation path, which makes it possible to use NLoS paths for localization [85]. By SLAM, a map of the radio environment is created simultaneously to localization [126, 127, 128], allowing position and orientation estimation in NLoS scenarios. A SLAM approach to calibrate the ULA of an automotive radar is proposed in [129]. The approach uses targets of opportunity, but is limited to gain-phase calibration of the individual antenna elements. When the focus is on calibration, the term simultaneous localization and calibration (SLAC) is used. Examples can be found in [130], where radio-frequency identification (RFID) tags are localized, while calibrating RFID tag positions and in [131], where indoor localization with fingerprinting is performed, while a sensor and a walking model are calibrated. In the context of non-cooperative localization in a sensor network, ranging bias calibration is proposed in [132].

How to calibrate the antenna response of an arbitrary antenna, e.g. an MMA, simultaneously with cooperative localization, is not part of the state-of-the-art.

Experimental Validation Antenna arrays are widely used for DoA estimation in practical applications, see e.g. [133]. Regarding cooperative localization, the importance of experimental validation is highlighted in [23], which also provides indoor

ultra-wideband (UWB) measurements. Further measurements with UWB ToA or RTT ranging in indoor environments can be found in [134, 19, 32, 135, 136]. In [118], RTT ranging and localization experiments with COTS hardware are performed.

In contrast to DoA estimation with an antenna array, DoA estimation with a single MMA has not been validated experimentally. Furthermore, cooperative radio localization for a robotic multi-agent system for planetary exploration has received less attention compared to wireless sensor networks and indoor localization. Specifically, experimental validation of in-situ calibration with an MMA and experimental validation of cooperative SLAC with robotic rovers is not covered.

1.3 Contributions and Structure

The main contributions of this thesis can be divided into five areas, which are linked to Chapters 2 to 6.

DoA & ToA Estimation In Chapter 2, we introduce DoA estimation with a single MMA. To this end, we define an appropriate signal model and show how the antenna response of an MMA can be expressed in closed-form using wavefield modeling and manifold separation. We then introduce a non-coherent, i.e. RSS-based, ML DoA estimator and a reduced-complexity version. We further show how coherent DoA estimation, using the phase response of the MMA, is performed. In case the polarization of impinging signals is unknown, we present joint DoA and polarization estimation by an MMA. Finally, we provide a performance analysis based on extensive simulations of 2D and 3D non-coherent and coherent DoA estimation, joint DoA and polarization estimation, as well as joint DoA and ToA estimation with a single MMA. Parts of Chapter 2 have been published in [J1] and [C1, C2].

Fundamental Limits for Cooperative Localization In Chapter 3, we derive fundamental limits based on Fisher information and the CRB for cooperative position and orientation estimation. Using wavefield modeling and manifold separation, we obtain a closed-form expression of the FIM, which is valid for arbitrary multiport antennas, including MMAs, real-world arrays, and co-located antennas. The derived FIM allows an intuitive interpretation regarding the impact of unknown absolute amplitude and phase of the received signal depending on the antenna type. Position and orientation error bounds are defined for both, absolute and relative localization. Based on an exemplary scenario, the differences between absolute and relative localization with MMAs are examined. We further show how the derived fundamental limits can be

utilized to optimize a certain formation by moving one agent. Parts of Chapter 3 have been published in [C3, C4].

In-Situ Antenna Calibration In Chapter 4, we show how an arbitrary multiport antenna, e.g. an MMA, is calibrated in-situ without knowledge about the propagation channel and without external synchronization. First, we derive the recursive BCRB for in-situ calibration with noisy direction observations for one of the impinging signals, which are provided by an external sensor. We distinguish the cases of known and unknown propagation channel. The derivation of the BCRB for the unknown propagation channel is more complicated, as the Bayesian information matrix (BIM) without prior is singular. We perform a theoretical observability analysis based on the derived BCRB and discuss the qualitative behavior of the BCRB. Furthermore, we introduce an in-situ antenna calibration algorithm based on MAP estimation. The algorithm can estimate arbitrary antenna responses and thus capture real-world antenna nonidealities including gain-phase offsets, mutual coupling, etc. We evaluate the proposed in-situ calibration algorithm by simulation and show that it operates close to the derived BCRB. Chapter 4 is based on the publications [J3] and [C8].

Simultaneous Localization and Calibration In Chapter 5 we introduce cooperative SLAC for radio navigation, where antenna responses and ranging biases are calibrated during operation without external sensors. We show how cooperative SLAC is implemented as a Bayesian filtering algorithm, which is challenging due to high state dimensionality and high nonlinearity of the observations. The algorithm uses suitable motion and observation models and considers prior knowledge of the calibration states. To show the feasibility of antenna response and ranging bias calibration by cooperative SLAC, we perform simulations with random agent trajectories and random antenna responses. Assuming realistic ranging biases and antenna response deviations, we show that cooperative SLAC outperforms cooperative localization and exhibits considerably lower position and orientation errors. Chapter 5 is based on the publications [J2] and [C9].

Experimental Validation In Chapter 6, we introduce the architecture of a cooperative localization testbed based on software-defined radio (SDR). To proof the feasibility of radio localization with a single MMA, a coherent multichannel SDR transceiver and an MMA are integrated into a robotic rover. We then present the results of outdoor experiments with four robotic rovers and three anchor nodes. The measurements are utilized to validate the simulation results presented in this thesis. Firstly, we show that DoA estimation with a single MMA is feasible in practice. Secondly, we evaluate

the introduced in-situ calibration algorithm with measurement data. We show that by in-situ calibration, the DoA estimation performance is improved, compared to calibrating the MMA in a near-field measurement chamber. Thirdly, we show how the proposed cooperative SLAC algorithm improves position and orientation estimation accuracy compared to mere localization. Parts of Chapter 6 have been published in [J2, J3] and [C5, C8, C9].

Chapter 2

DoA and ToA Estimation with a Multi-Mode Antenna

In this chapter, we review the concept of an MMA and introduce two specific MMAs investigated in this thesis. We define a signal model and show how the MMA antenna response is represented by the sampling matrix $\boldsymbol{G}$ with wavefield modeling and manifold separation. Then, we introduce different variants of DoA estimation with a single MMA, as well as joint DoA and ToA estimation. Finally, we analyze the different variants of DoA and ToA estimation with an MMA by simulation.

2.1 Multi-Mode Antennas

The theoretical foundation for multi-mode antennas (MMAs) is given by the theory of characteristic modes (TCM). The TCM was published already in the 1970s [66, 67, 137], but has not received much attention for three decades [138]. Its popularity started to grow in the 2000s, when antennas for compact handheld devices needed to be developed. At that time it has been realized that for efficient radiation, the dominating characteristic mode of the device chassis should be excited [139]. Since then, the TCM has received an increasing amount of attention within the antenna community [138], as it provides insight into the physics governing the antenna [140, 141]. The characteristic modes depend only on the shape of a radiator and are independent of the excitation. Furthermore, they are orthogonal by definition.

In order to gain an intuitive understanding of the TCM, we investigate a simple example. Fig. 2.1 shows the surface current density distributions and corresponding electric far-field patterns of three characteristic modes on a rectangular conducting plate. The maxima of the three current distributions are located at distinct points on

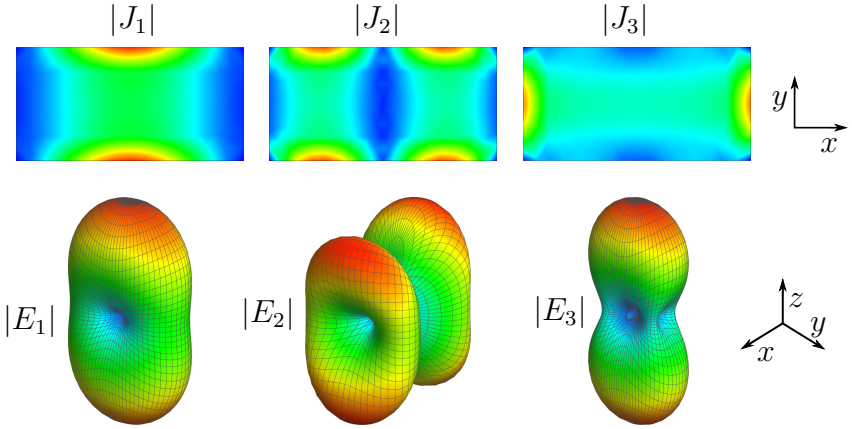

Figure 2.1. *Absolute values of the surface current density distributions J_1, J_2, J_3 and electric far-field patterns E_1, E_2, E_3 of three characteristic modes of a rectangular plate.*

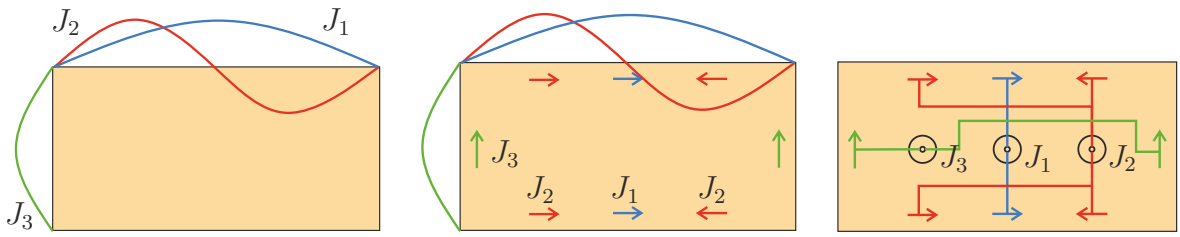

(a) *Surface current density distributions abstracted as harmonic modes.*

(b) *Excitation points at the surface current density distribution maxima.*

(c) *Connections of the respective excitation points and antenna ports.*

Figure 2.2. *Simplified illustration of an MMA based on the characteristic modes on a rectangular conducting plate.*

the plate. According to the TCM, the three surface current density distributions are orthogonal, and the three corresponding electric far-fields are also orthogonal. The orthogonality is not necessarily obvious from the absolute value of the total field strength shown in Fig. 2.1, as also phase and polarization need to be considered.

When multiple-input multiple-output (MIMO) communication systems became popular, the TCM was applied to excite multiple characteristic modes independently, leveraging their orthogonality property [142, 143, 144, 145]. We define a multi-mode antenna (MMA) as a multiport antenna, where each antenna port independently excites a different characteristic mode or a combination of characteristic modes. Examples of MMAs can be found in [70, 71, 68, 72, 73, 74, 69]. The principle of an MMA in terms of surface current density distributions, excitation points and antenna ports is illustrated in Fig. 2.2. To highlight that the current modes can be understood as a resonance phenomenon, they are abstracted as fundamental and higher harmonic modes. Excitation is performed at the respective maxima of the surface current density distributions by inductive coupling [146]. Appropriately connecting the

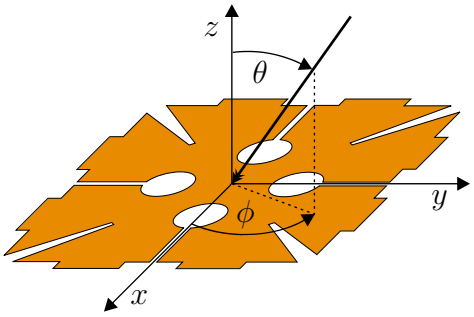

Figure 2.3. *Drawing of MMA-1 in x-y-plane with coordinate system and incoming signal © 2019 IEEE [147].*

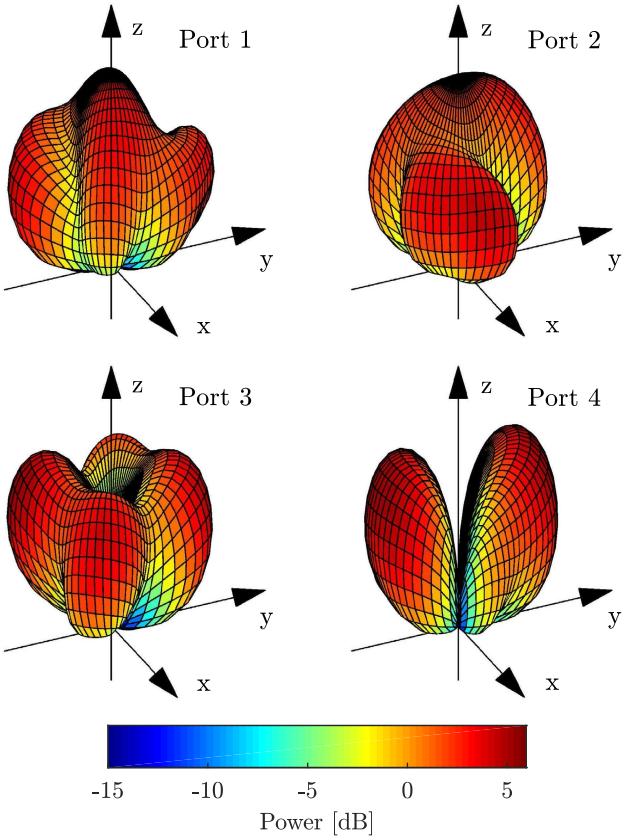

Figure 2.4. *3D power patterns for right-hand circular polarization (RHCP) of MMA-1.*

excitation points to ports yields a three-port MMA, where each ports excites a specific characteristic mode.

The first MMA investigated in this thesis, referred to as *MMA-1*, is based on a modified square conducting plate shown in Fig. 2.3. The antenna has four ports. The respective power patterns for right-hand circular polarization (RHCP) are shown in Fig. 2.4. Details about the antenna can be found in [70]. The simulation results from Chapter 2 are based on electromagnetic (EM) simulation data of this antenna.

The second investigated MMA, *MMA-2*, is a dielectric resonator antenna in the

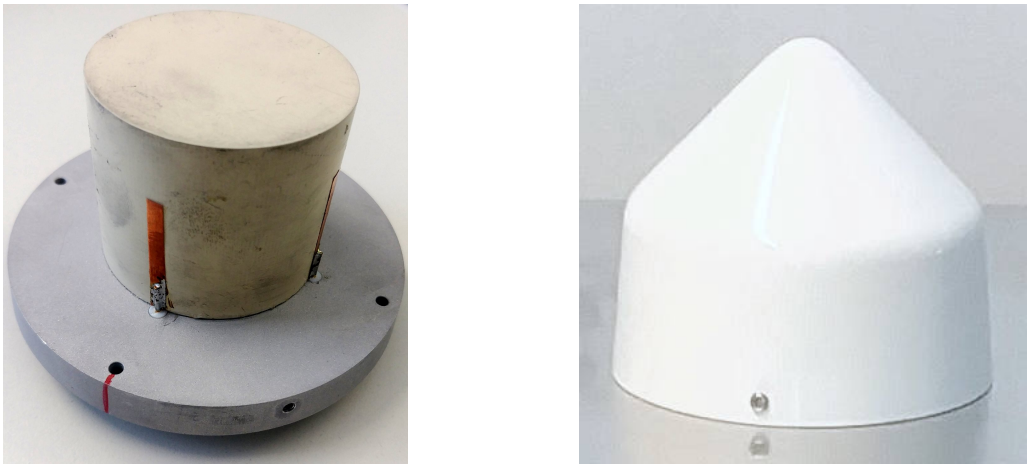

(a) *MMA-2 with four ports on the bottom.* **(b)** *MMA-2 with radome.*

Figure 2.5. *Pictures of MMA-2.*

form of a ceramic cylinder on a ground plane, see Fig. 2.5a. Four metallic feeding strips are attached to the cylinder, leading to four ports on the bottom of the ground plane, see [148]. For the experimental validation in Chapter 6, measurement data with *MMA-2* installed on a robotic rover has been obtained, see Section 6.1.3. For that purpose, the antenna was protected with the radome shown in Fig. 2.5b.

2.2 Signal Model

Wideband Signal Model

The far-field antenna response for a specific polarization is defined by gain $g(\omega, \theta, \phi)$ and phase response $\Phi(\omega, \theta, \phi)$, which depend on the angular frequency ω and the direction defined by inclination θ and azimuth ϕ, see Fig. 2.3 and [149, 150]. Assuming the antenna is illuminated by an isotropic point source at distance d emitting a continuous wave (CW) signal with angular frequency ω, the noiseless signal at the antenna port takes the form

$$y(t) = \sqrt{g(\omega, \theta, \phi)} e^{\mathrm{j}\Phi(\omega,\theta,\phi)} e^{\mathrm{j}\omega(t-d/c)} \alpha, \tag{2.1}$$

with time t, speed of light c and real-valued amplitude α [151, 152]. We now extend the scope to a multiport antenna with M ports, e.g. an MMA. The antenna gain $g_m(\omega, \theta, \phi)$ and phase response $\Phi_m(\omega, \theta, \phi)$ are then defined for all antenna ports $m \in \{1, ..., M\}$ individually. Furthermore, we assume an orthogonal frequency-division multiplexing (OFDM) signal, which is commonly used in modern wireless communication systems such as Institute of Electrical and Electronics Engineers (IEEE) 802.11 Wi-Fi and 4G/5G mobile cellular networks. Nonetheless, the methods presented in this thesis

can be generalized to other waveforms. The OFDM signal in baseband is

$$x(t) = \frac{1}{\sqrt{N}} \sum_{n \in \mathbb{N}_{\mathrm{sc}}} s(n)\, e^{\mathrm{j}2\pi n f_{\mathrm{sc}} t}, \tag{2.2}$$

with subcarrier index n, number of occupied subcarriers $N = |\mathbb{N}_{\mathrm{sc}}|$, complex symbol $s(n)$, sampling rate B_{s} and subcarrier spacing $f_{\mathrm{sc}} = \frac{B_{\mathrm{s}}}{N_{\mathrm{fft}}}$ with fast Fourier transform (FFT) length N_{fft}. If all subcarriers are occupied, $\mathbb{N}_{\mathrm{sc}} = \left\{ \lfloor -\frac{N_{\mathrm{fft}}-1}{2} \rfloor, ..., \lfloor \frac{N_{\mathrm{fft}}-1}{2} \rfloor \right\}$. As in general not all subcarriers are occupied, $N \leq N_{\mathrm{fft}}$, the occupied bandwidth $B = f_{\mathrm{sc}} \left(|\min(\mathbb{N}_{\mathrm{sc}})| + |\max(\mathbb{N}_{\mathrm{sc}})| \right) \leq B_{\mathrm{s}}$. The signal $x(t)$ is modulated onto a carrier with angular frequency $\omega_{\mathrm{c}} = 2\pi f_{\mathrm{c}}$. The transmission starts at $t = t_{\mathrm{Tx}}$. The receiving multiport antenna is connected to a coherent multichannel receiver. At the receiver, the signals are downconverted to in-phase and quadrature baseband components, low-pass filtered and sampled at $t = t_{\mathrm{Rx}} + \frac{k}{B_{\mathrm{s}}}$ with $k = 0, ..., N_{\mathrm{fft}} - 1$. The relevant part of the time-discrete complex signal is cut out and transformed to discrete frequency domain, where the carrier frequency offset (CFO) is compensated. The signal received at antenna port m in discrete frequency domain after CFO compensation can then be described by the signal model

$$r_m(n) = \underbrace{\sqrt{g_m(\omega_n, \theta, \phi)} e^{\mathrm{j}\Phi_m(\omega_n, \theta, \phi)}}_{= a_m(\omega_n, \theta, \phi)} s\left(n, d/c + \tau_m(\theta, \phi) + t_{\mathrm{Rx}} - t_{\mathrm{Tx}}\right) \alpha\, e^{\mathrm{j}\varphi} + w_m(n), \tag{2.3}$$

where $a_m(\omega_n, \theta, \phi)$ is the complex-valued antenna response composed of amplitude $\sqrt{g_m(\omega_n, \theta, \phi)}$ and phase $\Phi_m(\omega_n, \theta, \phi)$, $\omega_n = \omega_{\mathrm{c}} + 2\pi n f_{\mathrm{sc}}$ is the angular frequency of the n-th subcarrier,

$$s(n, \tau) = s(n)\, e^{-\mathrm{j}2\pi n f_{\mathrm{sc}} \tau} \tag{2.4}$$

is a delayed version of the OFDM symbol $s(n)$ in discrete frequency domain, d/c is the propagation delay, $\tau_m(\theta, \phi) = \frac{-\partial \Phi_m(\omega_n, \theta, \phi)}{\partial \omega_n}|_{\omega_n = \omega_{\mathrm{c}}}$ is the group delay for the respective antenna port, t_{Tx} and t_{Rx} are transmitter and receiver clock offsets, and $w_m(n) \sim \mathcal{CN}(0, \sigma_r^2)$ is independent and identically distributed (i.i.d.) circular symmetric Gaussian noise. We call α and φ absolute amplitude and phase, since they are common to all ports and to distinguish them from relative amplitude and phase differences between antenna ports. The attenuation due to free-space path loss is included in α and the carrier phase propagation delay in φ. Both are considered to be unknown.

Narrowband Signal Model

A very common assumption in array processing is that $\frac{B}{f_{\mathrm{c}}} \ll 1$, i.e. the signal bandwidth is small compared to the carrier frequency. Given that the signal spectrum

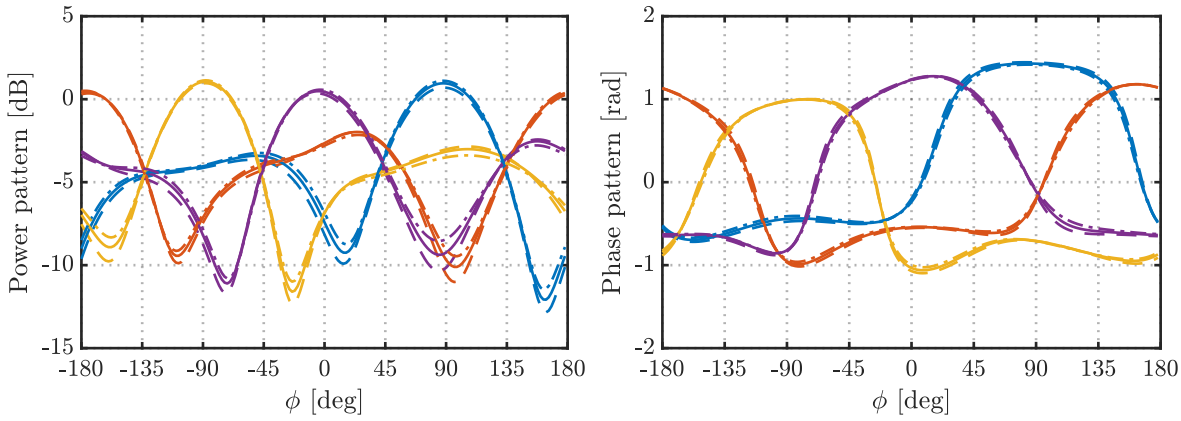

(a) *Power pattern.* **(b)** *Phase pattern.*

Figure 2.6. *Antenna response of MMA-2 in x-y-plane for linear vertical polarization measured in near-field measurement chamber. Solid lines represent frequency f_c, dashed and dashed-dotted lines $f_\mathrm{c} - B/2$ and $f_\mathrm{c} + B/2$, respectively.*

is symmetric, DoA estimation algorithms considering only the antenna response at the carrier frequency are known to be robust w.r.t. nonzero bandwidth [51, 52, 53]. Thus the term narrowband DoA estimation evolved. Within this thesis, we assume an OFDM signal with an odd number of occupied subcarriers N, which has a symmetric spectrum. Fig. 2.6 shows the measured power and phase patterns of *MMA-2* in x-y-plane for linear vertical polarization. The patterns are shown for $f_\mathrm{c} = 1.68\,\mathrm{GHz}$ and $f_\mathrm{c} \pm B/2$ with $B = 28.2\,\mathrm{MHz}$, which corresponds to the experimental setup in Chapter 6. Minor deviations of the power patterns are visible at the spectrum edges, compared to the patterns at the carrier frequency. However, the deviations are small and occur mostly where the gain of the respective mode is low, so their influence is very limited. The phase patterns at the spectrum edges are almost identical to the phase pattern at the carrier frequency. Overall, the antenna response is approximately constant w.r.t. frequency over the occupied bandwidth, which further justifies the narrowband assumption. Thus, with the assumption

$$a_m(\omega_n, \theta, \phi) \approx a_m(\theta, \phi)\, \forall\, n \in \mathbb{N}_\mathrm{sc}, \tag{2.5}$$

it is sufficient to consider antenna gain, phase and group delay only at the carrier angular frequency ω_c. The model (2.3) then simplifies to

$$r_m(n) = \underbrace{\sqrt{g_m(\theta,\phi)}e^{\mathrm{j}\Phi_m(\theta,\phi)}}_{=a_m(\theta,\phi)} s\left(n, d/c + \tau_m(\theta,\phi) + t_\mathrm{Rx} - t_\mathrm{Tx}\right) \alpha\, e^{\mathrm{j}\varphi} + w_m(n). \tag{2.6}$$

Using a TWR protocol [134, 153], the transmitter and receiver clock offsets can be eliminated. We assume that the processing time between forward and backward transmission is compensated and very short, such that the impact of the relative frequency offset of the two oscillators can be neglected. Otherwise, the oscillator behavior must be taken into account with an appropriate clock model [154]. Assuming the antenna group delays are also compensated, we arrive at

$$r_m(n) = \underbrace{\sqrt{g_m(\theta,\phi)}e^{\mathrm{j}\Phi_m(\theta,\phi)}}_{=a_m(\theta,\phi)} s\left(n,\tau\right)\alpha\, e^{\mathrm{j}\varphi} + w_m(n) \tag{2.7}$$

with the ToA $\tau = d/c$.

We now take multipath propagation into account by assuming that P superposed signals with index $p \in \{1, ..., P\}$, DoAs with inclination $\boldsymbol{\theta} = [\theta_1, ..., \theta_P]^T$ and azimuth $\boldsymbol{\phi} = [\phi_1, ..., \phi_P]^T$ and ToAs $\boldsymbol{\tau} = [\tau_1, ..., \tau_P]^T$ arrive at the multiport antenna. They originate from the same source, but have different DoAs, ToAs, absolute amplitudes $\boldsymbol{\alpha} = [\alpha_1, ..., \alpha_P]^T$ and absolute phases $\boldsymbol{\varphi} = [\varphi_1, ..., \varphi_P]^T$. Using vector notation, the received signal in discrete frequency domain signal $\boldsymbol{r}(n) = [r_1(n), ..., r_M(n)]^T$ is defined as

$$\boldsymbol{r}(n) = \sum_{p=1}^{P} \boldsymbol{a}(\theta_p, \phi_p) s(n, \tau_p)\alpha_p\, e^{\mathrm{j}\varphi_p} + \boldsymbol{w}(n), \tag{2.8}$$

with the antenna response vector

$$\boldsymbol{a}(\theta,\phi) = \begin{bmatrix} a_1(\theta,\phi) & \dots & a_M(\theta,\phi) \end{bmatrix}^T \tag{2.9}$$

and i.i.d. circular symmetric Gaussian noise $\boldsymbol{w}(n) \sim \mathcal{CN}(0, \sigma_{\boldsymbol{r}}^2 \mathbb{I}_M)$. The signal model (2.8) is used throughout the thesis and extended or simplified where necessary. The average transmit power is

$$P_{\mathrm{Tx}} = \frac{1}{N} \sum_{n \in \mathbb{N}_{\mathrm{sc}}} |s(n)|^2 \tag{2.10}$$

and the SNR is always defined for the first propagation path $p = 1$ and with respect to an isotropic antenna with unit gain, i.e.

$$\mathrm{SNR} = \frac{\alpha_1^2 P_{\mathrm{Tx}}}{\sigma_{\boldsymbol{r}}^2}. \tag{2.11}$$

2.3 Wavefield Modeling and Manifold Separation

In order to perform DoA estimation, a continuous and closed-form expression of the antenna response (2.9) is required. For ideal antenna arrays, (2.9) is called steering

vector and can be defined based on the underlying physics. For an MMA, however, it is not straightforward to find an analytical expression. We thus apply wavefield modeling and manifold separation [100, 101], which allows to decompose the antenna response

$$\boldsymbol{a}(\theta,\phi) = \boldsymbol{G}\,\boldsymbol{b}(\theta,\phi) \tag{2.12}$$

into a product of the sampling matrix $\boldsymbol{G} \in \mathbb{C}^{M\times U}$, which describes the antenna, and a pre-defined basis vector $\boldsymbol{b}(\theta,\phi) \in \mathbb{C}^{U\times 1}$, which is a function of the DoA [100]. The U basis functions must be orthonormal on the antenna manifold $\theta \in [0,\pi]$, $\phi \in [0,2\pi)$ for inclination and azimuth estimation and $\theta \in [-\pi,\pi)$ or $\phi \in [-\pi,\pi)$ for single angle estimation in a plane. Additionally, the antenna response vector $\boldsymbol{a}(\theta,\phi)$ has to be square integrable on the manifold. A suitable basis for 2D DoA estimation of the inclination is given by the Fourier functions

$$\boldsymbol{b}(\theta) = \frac{1}{\sqrt{2\pi}} e^{\mathrm{j}\theta u_\theta},\ u_\theta = \left\lfloor -\frac{U-1}{2} \right\rfloor, ..., 0, ..., \left\lfloor \frac{U-1}{2} \right\rfloor, \tag{2.13}$$

where the components of the vector $\boldsymbol{b}(\theta)$ are given by complex exponentials. For 2D DoA estimation of the azimuth, $\boldsymbol{b}(\phi)$ is defined analogously. For 3D, i.e. inclination and azimuth estimation, the spherical harmonic functions

$$Y_l^m(\theta,\phi) = \sqrt{\frac{2l+1}{4\pi}\frac{(l-m)!}{(l+m)!}} P_l^m(\cos(\theta)) e^{\mathrm{j}m\phi}, \tag{2.14}$$

with degree $l \in \{0, ..., L\}$ for maximum degree L and order $m \in \{-l, ..., l\}$ fulfill the orthonormality condition [155]. To be consistent with the literature, l and m are used to denote degree and order, where m is not to be confused with the antenna port. $P_l^m(\cdot)$ is the associated Legendre polynomial, see Appendix C.1. Defining $Y_u(\theta,\phi) := Y_l^m(\theta,\phi)$ with the enumeration $u = (l+1)l + m + 1$ for $u \in \{1, ..., U\}$, the basis

$$\boldsymbol{b}(\theta,\phi) = \begin{bmatrix} Y_1(\theta,\phi) & ... & Y_U(\theta,\phi) \end{bmatrix}^T \tag{2.15}$$

is formed. Alternatively, the 2D Fourier functions

$$\boldsymbol{b}(\theta) = \frac{1}{\sqrt{2\pi}} e^{\mathrm{j}\theta u_\theta},\ u_\theta = \left\lfloor -\frac{\sqrt{U}-1}{2} \right\rfloor, ..., 0, ..., \left\lfloor \frac{\sqrt{U}-1}{2} \right\rfloor, \tag{2.16a}$$

$$\boldsymbol{b}(\phi) = \frac{1}{\sqrt{2\pi}} e^{\mathrm{j}\phi u_\phi},\ u_\phi = \left\lfloor -\frac{\sqrt{U}-1}{2} \right\rfloor, ..., 0, ..., \left\lfloor \frac{\sqrt{U}-1}{2} \right\rfloor \tag{2.16b}$$

can be used to form the basis vector

$$\boldsymbol{b}(\theta, \phi) = \boldsymbol{b}_\theta(\theta) \otimes \boldsymbol{b}_\phi(\phi), \tag{2.17}$$

which is called effective aperture distribution function (EADF) in the literature [156]. With this definition, U is limited to square numbers in order to unify the definition of U for (2.13), (2.15) and (2.17). In practice, U can be chosen arbitrarily, and may also be different for θ and ϕ domain. However, 2D Fourier functions are orthonormal on the torus, not on the sphere, which means the data must be expanded to be periodic in both azimuth and inclination [101].

In [100] it is shown that when the number of coefficients U is increased, the magnitude of the elements of G decays superexponentially for $|u_\theta| > \kappa_\mathrm{c} R$, $|u_\phi| > \kappa_\mathrm{c} R$ and $l > \kappa_\mathrm{c} R$, where $\kappa_\mathrm{c} = \frac{2\pi}{\lambda_\mathrm{c}}$ is the carrier wavenumber and R is the radius of the smallest sphere enclosing the antenna. As a rule of thumb, the expansion can thus be truncated at $2\kappa_\mathrm{c} R$ [100]. This leads to $U \approx 4\kappa_\mathrm{c} R + 1$ coefficients for the Fourier series, $U \approx 8\kappa_\mathrm{c}^2 R^2 + 4\kappa_\mathrm{c} R + 1$ for spherical harmonics and $U \approx (4\kappa_\mathrm{c} R + 1)^2$ for the 2D Fourier series. Alternatively, U can also be chosen such that the sampling only contains elements with an absolute value at least one order of magnitude above the noise floor of the calibration measurements [156].

In contrast to simulations, the true sampling matrix $\boldsymbol{G}$ is not known in practice. Nevertheless, an estimated sampling matrix $\hat{\boldsymbol{G}}$ can be obtained in different ways. In Chapter 4, it is shown how $\hat{\boldsymbol{G}}$ can be estimated by in-situ calibration and in Chapter 5 it is shown how $\hat{\boldsymbol{G}}$ can be estimated by SLAC. In both cases, the propagation channel parameters, namely absolute amplitudes $\boldsymbol{\alpha}$ and absolute phases $\boldsymbol{\varphi}$ from (2.8), are unknown. In contrast to that, by EM simulation or in a calibrated measurement chamber, the antenna response can be observed directly at discrete DoAs. Assume the spatial samples

$$\boldsymbol{e}_q = \begin{bmatrix} e_{q,1} & \dots & e_{q,M} \end{bmatrix}^T \tag{2.18}$$

of the antenna response for DoAs $\{\theta_q, \phi_q\}$ are available for all M ports. Writing the spatial samples in matrix form for a total of Q DoAs, covering the entire manifold, yields

$$\boldsymbol{E} = \begin{bmatrix} \boldsymbol{e}_1 & \dots & \boldsymbol{e}_Q \end{bmatrix}. \tag{2.19}$$

Now, the sampling matrix $\boldsymbol{G}$ for a given basis $\boldsymbol{B} = [\boldsymbol{b}(\theta_1, \phi_1), ..., \boldsymbol{b}(\theta_Q, \phi_Q)]$ can be determined by least squares,

$$\hat{\boldsymbol{G}}^0 = \boldsymbol{E}\boldsymbol{B}^H \left(\boldsymbol{B}\boldsymbol{B}^H\right)^{-1}, \tag{2.20}$$

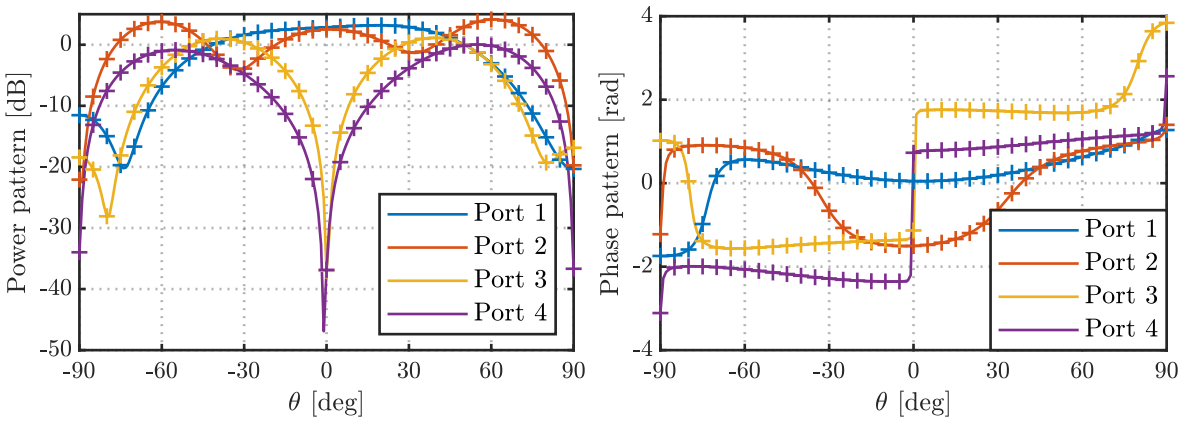

(a) *Power pattern.* **(b)** *Phase pattern.*

Figure 2.7. *Samples from EM simulation and continuous representation by wavefield modeling and manifold separation of the x-z-plane power and phase patterns of MMA-1 for right-hand circular polarization (RHCP).*

which we call $\hat{\boldsymbol{G}}^0$ to distinguish it from the estimates by in-situ calibration in Chapter 4 and SLAC in Chapter 5. For this equation to be solvable, in general it is required that $M \leq U \leq Q$. Antenna measurements are often performed on a regular grid, which is nonuniform on the sphere. In that case it should be ensured that $Q \gg U$ [102].

As an alternative to wavefield modeling and manifold separation, the array interpolation technique (AIT) can be used to represent the MMA antenna response [157, 147]. The AIT aims at representing the MMA antenna response by a linear transformation of the response of an ideal antenna array, e.g. a ULA. Without excessive errors, this is only possible for a small angular sector. With AIT, low complexity DoA estimation algorithms for ideal arrays can be applied. However, due to sectorization, the AIT can suffer from out-of-sector errors in the case of multiple impinging signals. AIT can also cause discontinuities at the sector borders, which prevents the calculation of the CRB for theoretical analysis. Within this thesis, we exclusively use wavefield modeling and manifold separation the represent the MMA antenna response.

We now illustrate wavefield modeling and manifold separation for an x-z-plane cut of *MMA-1* using Fourier functions (2.13) with $U = 15 \approx 4\kappa_c R + 1$ coefficients per port. The spatials samples $\boldsymbol{E}$ have been obtained by an EM simulation. Fig. 2.7a shows the power pattern and Fig. 2.7b the phase pattern for RHCP. Plotted are both the discrete spatial samples and the continuous antenna response obtained by wavefield modeling. Continuous and discrete representation match in both, power and phase. From the plots it is also apparent that the different ports of the MMA have distinct characteristics, as discussed in Section 2.1. In the next section, it is shown how these characteristics can be exploited to estimate the DoA of incoming signals.

2.4 DoA Estimation with a Multi-Mode Antenna

2.4.1 Non-Coherent DoA Estimation

A first approach to DoA estimation with an MMA is based on the received signal power at the different ports, called RSS. The approach does not need a coherent multichannel receiver, and is thus suitable for low-cost and low-complexity devices. This estimator is referred to as non-coherent and limited to a single impinging signal. Based on (2.8), the estimated RSS of port m, averaged over N subcarriers, is calculated by

$$\check{r}_m = \frac{1}{N} \sum_{n \in \mathbb{N}_{\text{sc}}} |r_m(n)|^2. \tag{2.21}$$

Due to the noise in $r_m(n)$, the estimated RSS $\check{r}_m$ follows a noncentral χ^2 distribution. In Appendix C.3 it is shown, when the number of occupied subcarriers $N > 25$, the RSS observations $\check{\boldsymbol{r}} = [\check{r}_1, ..., \check{r}_M]^T$ can be approximated by a Gaussian distribution $\check{\boldsymbol{r}} \sim \mathcal{N}(\check{\boldsymbol{\mu}}, \check{\boldsymbol{\Sigma}})$ with mean

$$\check{\boldsymbol{\mu}} = \mathrm{E}\{\check{\boldsymbol{r}}\} = \boldsymbol{g}(\theta, \phi)\check{s} + \mathbf{1}_M \sigma_{\boldsymbol{r}}^2 \tag{2.22}$$

and diagonal covariance matrix

$$\check{\boldsymbol{\Sigma}} = \mathrm{diag}\left\{ \begin{bmatrix} \check{\sigma}_1^2 & ... & \check{\sigma}_m^2 & ... & \check{\sigma}_M^2 \end{bmatrix} \right\} \tag{2.23}$$

with elements

$$\check{\sigma}_m^2 = N^{-1}(\sigma_{\boldsymbol{r}}^4 + 2g_m(\theta, \phi)\check{s}\sigma_{\boldsymbol{r}}^2), \tag{2.24}$$

where $\boldsymbol{g}(\theta, \phi) = [g_1(\theta, \phi), ..., g_M(\theta, \phi)]^T$ is the antenna gain vector, $\check{s} = \frac{\alpha^2}{N} \sum_{n \in \mathbb{N}_{\text{sc}}} |s(n)|^2$ is the average signal power and $\sigma_{\boldsymbol{r}}^2 = \frac{1}{N} \sum_{n \in \mathbb{N}_{\text{sc}}} \mathrm{E}\{|w_m(n)|^2\}$ the noise power. The equations (2.22) and (2.24) contain only the real-valued antenna gain, not the complex-valued antenna response. The expansion can thus be performed on the real-valued antenna gain vector

$$\boldsymbol{g}(\theta, \phi) = \boldsymbol{G}\, \boldsymbol{b}(\theta, \phi), \tag{2.25}$$

instead of the complex-valued antenna response vector as in (2.12). The basis vector $\boldsymbol{b}(\theta, \phi)$ is defined by (2.13) or (2.17), but to obtain real values, the elements of the sampling matrix $\boldsymbol{G}$ related to negative u_θ or u_ϕ values are fixed to the complex conjugate of the corresponding positive u_θ or u_ϕ values. The real-valued form of the spherical harmonics for defining the basis $\boldsymbol{b}(\theta, \phi)$ and its derivatives are summarized in Appendix C.2. First, the general case is considered, where both signal power $\check{s}$ and

noise power $\sigma_{\boldsymbol{r}}^2$ are unknown. The parameters to be estimated are defined by

$$\boldsymbol{\zeta} = \begin{bmatrix} \theta & \phi & \check{s} & \sigma_{\boldsymbol{r}}^2 \end{bmatrix}^T, \tag{2.26}$$

and the log-likelihood function is given by

$$\begin{aligned} L_{\check{\boldsymbol{r}}}(\boldsymbol{\zeta}) = \ln p(\check{\boldsymbol{r}}|\boldsymbol{\zeta}) &= -\frac{M}{2}\ln(2\pi) - \frac{1}{2}\ln\left(\det\{\check{\boldsymbol{\Sigma}}\}\right) - \frac{1}{2}(\check{\boldsymbol{r}} - \check{\boldsymbol{\mu}})^T\check{\boldsymbol{\Sigma}}^{-1}(\check{\boldsymbol{r}} - \check{\boldsymbol{\mu}}) \\ &= -\sum_{m=1}^{M}\left(\frac{1}{2}\ln(2\pi\check{\sigma}_m^2) + \frac{1}{2\check{\sigma}_m^2}\left(\check{r}_m - (g_m(\theta,\phi)\check{s} + \sigma_{\boldsymbol{r}}^2)\right)^2\right). \end{aligned} \tag{2.27}$$

Based on (2.27), the non-coherent ML estimator *NC-ML*,

$$\begin{aligned} \hat{\boldsymbol{\zeta}} &= \arg\max_{\boldsymbol{\zeta}} \; L_{\check{\boldsymbol{r}}}(\boldsymbol{\zeta}) \\ &= \arg\min_{\boldsymbol{\zeta}} \sum_{m=1}^{M}\left(\ln\left(2\pi N^{-1}(\sigma_{\boldsymbol{r}}^4 + 2g_m(\theta,\phi)\check{s}\sigma_{\boldsymbol{r}}^2)\right) + \frac{N(\check{r}_m - g_m(\theta,\phi)\check{s} - \sigma_{\boldsymbol{r}}^2)^2}{\sigma_{\boldsymbol{r}}^4 + 2g_m(\theta,\phi)\check{s}\sigma_{\boldsymbol{r}}^2}\right), \end{aligned} \tag{2.28}$$

is obtained. As a benchmark for the estimator, we derive the CRB. The CRB is a lower bound on the achievable estimation variance of any unbiased estimator [80], and is frequently used throughout this thesis. The CRB for the non-coherent case, *NC-CRB*, is given by

$$\mathrm{var}\{\hat{\theta}\} \geq \mathrm{CRB}(\theta) = [\boldsymbol{I}_{\boldsymbol{\zeta}}^{-1}]_{1,1}, \tag{2.29a}$$

$$\mathrm{var}\{\hat{\phi}\} \geq \mathrm{CRB}(\phi) = [\boldsymbol{I}_{\boldsymbol{\zeta}}^{-1}]_{2,2}, \tag{2.29b}$$

where $\boldsymbol{I}_{\boldsymbol{\zeta}} \in \mathbb{R}^{4\times 4}$ is the FIM defined by

$$[\boldsymbol{I}_{\boldsymbol{\zeta}}]_{v,w} = -\mathrm{E}\left\{\frac{\partial^2 \ln p(\check{\boldsymbol{r}}|\boldsymbol{\zeta})}{\partial[\boldsymbol{\zeta}]_v \partial[\boldsymbol{\zeta}]_w}\right\} = \mathrm{E}\left\{\frac{\partial \ln p(\check{\boldsymbol{r}}|\boldsymbol{\zeta})}{\partial[\boldsymbol{\zeta}]_v}\frac{\partial \ln p(\check{\boldsymbol{r}}|\boldsymbol{\zeta})}{\partial[\boldsymbol{\zeta}]_w}\right\}. \tag{2.30}$$

Since the observations follow a Gaussian distribution, the FIM elements are calculated according to [80] as

$$\begin{aligned} [\boldsymbol{I}_{\boldsymbol{\zeta}}]_{v,w} &= \frac{\partial \check{\boldsymbol{\mu}}^T}{\partial[\boldsymbol{\zeta}]_v}\check{\boldsymbol{\Sigma}}^{-1}\frac{\partial \check{\boldsymbol{\mu}}}{\partial[\boldsymbol{\zeta}]_w} + \frac{1}{2}\mathrm{tr}\left\{\check{\boldsymbol{\Sigma}}^{-1}\frac{\partial \check{\boldsymbol{\Sigma}}}{\partial[\boldsymbol{\zeta}]_v}\check{\boldsymbol{\Sigma}}^{-1}\frac{\partial \check{\boldsymbol{\Sigma}}}{\partial[\boldsymbol{\zeta}]_w}\right\} \\ &= \sum_{m=1}^{M}\left(\frac{1}{\check{\sigma}_m^2}\frac{\partial[\check{\boldsymbol{\mu}}]_m}{\partial[\boldsymbol{\zeta}]_v}\frac{\partial[\check{\boldsymbol{\mu}}]_m}{\partial[\boldsymbol{\zeta}]_w} + \frac{1}{2\check{\sigma}_m^4}\frac{\partial\check{\sigma}_m^2}{\partial[\boldsymbol{\zeta}]_v}\frac{\partial\check{\sigma}_m^2}{\partial[\boldsymbol{\zeta}]_w}\right). \end{aligned} \tag{2.31}$$

The non-linear optimization problem (2.28) has four unknowns. Solving that could be unfavorable for a low-cost and low-complexity receiver. For that reason, a reduced

complexity (RC) alternative to the ML estimator (2.28) is derived. It uses the fact that often an estimate of the noise power $\hat{\sigma}_{\boldsymbol{r}}^2$ can be obtained separately, e.g. from unoccupied time-division multiple access (TDMA) slots. The unknowns then reduce to

$$\boldsymbol{\zeta}' = \begin{bmatrix} \theta & \phi & \check{s} \end{bmatrix}^T . \tag{2.32}$$

Neglecting the constant and the log-term in (2.27) and maximizing the remaining term yields

$$\hat{\boldsymbol{\zeta}}' = \arg\min_{\boldsymbol{\zeta}'} ||\check{\boldsymbol{r}}' - \boldsymbol{g}(\theta,\phi)\check{s}||^2, \tag{2.33}$$

with $\check{\boldsymbol{r}}' = \check{\boldsymbol{r}} - \hat{\sigma}_{\boldsymbol{r}}^2$. To further reduce the number of unknowns, we follow the principle from [158] and plug the minimum of (2.33) w.r.t. the signal power, $\hat{\check{s}} = \boldsymbol{g}(\theta,\phi)^\dagger \check{\boldsymbol{r}}'$, back into (2.33) to obtain the *NC-RC* estimator

$$\begin{aligned} \begin{bmatrix} \hat{\theta} & \hat{\phi} \end{bmatrix}^T &= \arg\min_{\{\theta,\phi\}} ||\left(\mathbb{I}_M - \boldsymbol{g}(\theta,\phi)\boldsymbol{g}(\theta,\phi)^\dagger\right)\check{\boldsymbol{r}}'||^2 \\ &= \arg\min_{\{\theta,\phi\}} \operatorname{tr}\left\{\left(\mathbb{I}_M - \boldsymbol{g}(\theta,\phi)\boldsymbol{g}(\theta,\phi)^\dagger\right)\check{\boldsymbol{r}}'\check{\boldsymbol{r}}'^T\right\}. \end{aligned} \tag{2.34}$$

The number of unknowns has been reduced from four to two. In practice, to further reduce the complexity, $\left(\mathbb{I}_M - \boldsymbol{g}(\theta,\phi)\boldsymbol{g}(\theta,\phi)^\dagger\right)$ can be precomputed for a θ-ϕ grid with required accuracy. The CRB for the non-coherent RC estimator, *NC-RC-CRB*, is calculated analogous to (2.29), where the unknown vector $\boldsymbol{\zeta}$ is replaced by the reduced unknown vector $\boldsymbol{\zeta}'$.

2.4.2 Coherent DoA Estimation

Defining the antenna response matrix

$$\boldsymbol{A}(\boldsymbol{\theta},\boldsymbol{\phi}) = \begin{bmatrix} \boldsymbol{a}(\theta_1,\phi_1) & \dots & \boldsymbol{a}(\theta_P,\phi_P) \end{bmatrix} \tag{2.35}$$

for P impinging signals and gathering the other deterministic components of (2.8) into arbitrary, deterministic signals $\tilde{\boldsymbol{s}}(n) \in \mathbb{C}^{P\times 1}$, the standard array processing model

$$\boldsymbol{r}(n) = \boldsymbol{A}(\boldsymbol{\theta},\boldsymbol{\phi})\tilde{\boldsymbol{s}}(n) + \boldsymbol{w}(n) \tag{2.36}$$

is obtained [55, 159, 28]. For geometric array models like ULA or URA, (2.35) is often called steering matrix and describes phase relationships between the antennas, while in our case $\boldsymbol{A}(\boldsymbol{\theta},\boldsymbol{\phi})$ is the antenna response matrix containing both gain and phase information. The equation for the log-likelihood function however remains the same

and is given by

$$L_{\boldsymbol{r}}(\boldsymbol{\theta}, \boldsymbol{\phi}, \tilde{\boldsymbol{s}}(1), ..., \tilde{\boldsymbol{s}}(N), \sigma_{\boldsymbol{r}}^2) = -NM \ln(\pi\sigma_{\boldsymbol{r}}^2) - \frac{1}{\sigma_{\boldsymbol{r}}^2} \sum_{n \in \mathbb{N}_{\text{sc}}} ||\boldsymbol{r}(n) - \boldsymbol{A}(\boldsymbol{\theta}, \boldsymbol{\phi})\tilde{\boldsymbol{s}}(n)||^2. \quad (2.37)$$

Based on N occupied subcarriers, we can calculate the sample covariance matrix

$$\hat{\boldsymbol{R}}_{\boldsymbol{r}} = \frac{1}{N} \sum_{n \in \mathbb{N}_{\text{sc}}} \boldsymbol{r}(n)\boldsymbol{r}^H(n) \quad (2.38)$$

and obtain the coherent ML estimator *C-ML*

$$\begin{bmatrix} \hat{\boldsymbol{\theta}}^T & \hat{\boldsymbol{\phi}}^T \end{bmatrix}^T = \arg \min_{\{\boldsymbol{\theta}, \boldsymbol{\phi}\}} \text{Re}\{\text{tr}\{\boldsymbol{\Pi}_{\boldsymbol{A}}^{\perp} \hat{\boldsymbol{R}}_{\boldsymbol{r}}\}\}, \quad (2.39)$$

with the projector onto the noise subspace

$$\boldsymbol{\Pi}_{\boldsymbol{A}}^{\perp} = \mathbb{I}_M - \boldsymbol{\Pi}_{\boldsymbol{A}} \quad (2.40)$$

and the projector onto the signal subspace

$$\boldsymbol{\Pi}_{\boldsymbol{A}} = \boldsymbol{A}(\boldsymbol{\theta}, \boldsymbol{\phi}) \left(\boldsymbol{A}^H(\boldsymbol{\theta}, \boldsymbol{\phi})\boldsymbol{A}(\boldsymbol{\theta}, \boldsymbol{\phi})\right)^{-1} \boldsymbol{A}^H(\boldsymbol{\theta}, \boldsymbol{\phi}), \quad (2.41)$$

see e.g. [28, 55]. In [160] it is shown that the CRB matrix for the coherent case, *C-CRB*, can be calculated as

$$\text{CRB}\left(\begin{bmatrix} \hat{\boldsymbol{\theta}}^T & \hat{\boldsymbol{\phi}}^T \end{bmatrix}^T\right) = \frac{\sigma_{\boldsymbol{r}}^2}{2N} \text{Re}\{\boldsymbol{D}^H \boldsymbol{\Pi}_{\boldsymbol{A}}^{\perp} \boldsymbol{D} \odot \boldsymbol{Z}^T \boldsymbol{R}_{\tilde{\boldsymbol{s}}} \boldsymbol{Z}\}^{-1}, \quad (2.42)$$

with

$$\boldsymbol{D} = \begin{bmatrix} \frac{\partial \boldsymbol{a}(\theta_1,\phi_1)}{\partial \theta_1} & ... & \frac{\partial \boldsymbol{a}(\theta_P,\phi_P)}{\partial \theta_P} & \frac{\partial \boldsymbol{a}(\theta_1,\phi_1)}{\partial \phi_1} & ... & \frac{\partial \boldsymbol{a}(\theta_P,\phi_P)}{\partial \phi_P} \end{bmatrix}, \quad (2.43)$$

the selection matrix $\boldsymbol{Z} = \begin{bmatrix} \mathbb{I}_P & \mathbb{I}_P \end{bmatrix}$ and the signal covariance matrix $\boldsymbol{R}_{\tilde{\boldsymbol{s}}} = \frac{1}{N} \sum_{n \in \mathbb{N}_{\text{sc}}} \tilde{\boldsymbol{s}}(n)\tilde{\boldsymbol{s}}^H(n)$. This requires the partial derivatives of the basis function $\boldsymbol{b}(\theta, \phi)$ from (2.12) w.r.t. θ and ϕ. For the Fourier functions (2.13) and 2D Fourier functions (2.17), the partial derivatives are trivial to obtain. For spherical harmonics (2.14), the derivatives are provided in Appendices C.1 and C.2.

2.4.3 Joint DoA and Polarization Estimation

The models (2.8) and (2.36) are valid for a single polarization component of the electric field and can be applied when the polarization of the incoming wave is known. If the polarization is unknown, it needs to be estimated together with the DoA(s). For

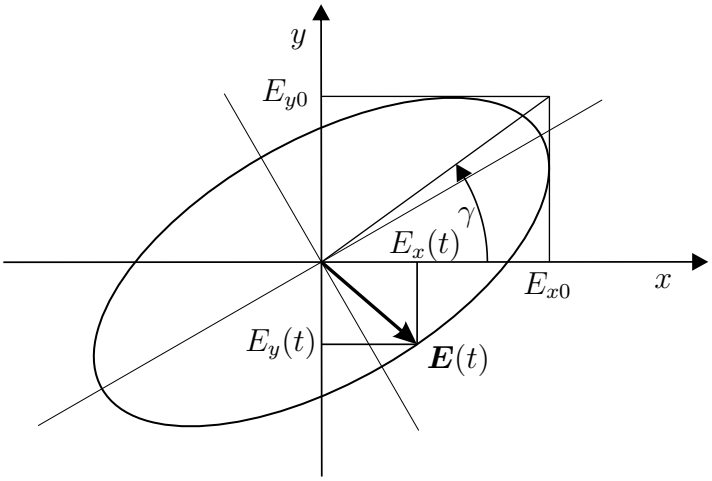

Figure 2.8. *Polarization ellipse for EM wave travelling in positive z-direction out of the page, observed at $z = 0$.*

that, (2.36) is extended to account for polarization. Assuming free-space propagation and far-field conditions, the EM wave radiated by an antenna can be approximated by a plane wave. A plane wave traveling in positive z-direction, i.e. $d = z$, can be decomposed into x- and y-components

$$\boldsymbol{E}(t, z) = E_x(t, z)\boldsymbol{u}_x + E_y(t, z)\boldsymbol{u}_y. \tag{2.44}$$

Fixing the location to $z = 0$ to observe the time behavior, we get

$$\boldsymbol{E}(t) = E_{x0}\cos(\omega t)\boldsymbol{u}_x + E_{y0}\cos(\omega t + \beta)\boldsymbol{u}_y, \tag{2.45}$$

with the polarization phase β [161]. The polarization ellipse is visualized in Fig. 2.8 with the auxiliary angle

$$\gamma = \arctan\left(\frac{E_{y0}}{E_{x0}}\right). \tag{2.46}$$

Together, the auxiliary angle $0 \leq \gamma \leq \frac{\pi}{2}$ and the polarization phase $-\pi \leq \beta < \pi$ parameterize the polarization state of the EM wave. For instance, for circularly polarized waves $\gamma = \frac{\pi}{4}$ and $\beta = \pm\frac{\pi}{2}$ for left/right hand circular polarization.

Using β and γ, the signal model (2.36) can be extended to perform joint DoA and polarization estimation [162, 163, 164]. First, we define the partial antenna response vectors for a single impinging signal and antenna port m,

$$a_{\mathrm{co},m}(\theta, \phi) = \sqrt{g_{\mathrm{co},m}(\theta, \phi)}e^{\mathrm{j}\Phi_{\mathrm{co},m}(\theta,\phi)}, \tag{2.47a}$$

$$a_{\mathrm{cross},m}(\theta, \phi) = \sqrt{g_{\mathrm{cross},m}(\theta, \phi)}e^{\mathrm{j}\Phi_{\mathrm{cross},m}(\theta,\phi)}. \tag{2.47b}$$

Here, $a_{\mathrm{co},m}(\theta,\phi)$ is the antenna response when being illuminated by a wave with the reference polarization, arriving from DoA $\{\theta,\phi\}$, and $a_{\mathrm{cross},m}(\theta,\phi)$ results from a wave with orthogonal polarization. Correspondingly, $g_{\mathrm{co},m}(\theta,\phi)$ and $g_{\mathrm{cross},m}(\theta,\phi)$ are the partial gains and $\Phi_{\mathrm{co},m}(\theta,\phi)$ and $\Phi_{\mathrm{cross},m}(\theta,\phi)$ the partial phase responses. Defining the partial antenna response vectors

$$\boldsymbol{a}_{\mathrm{co}}(\theta,\phi) = \begin{bmatrix} a_{\mathrm{co},1}(\theta,\phi) & ... & a_{\mathrm{co},M}(\theta,\phi) \end{bmatrix}^T, \tag{2.48a}$$

$$\boldsymbol{a}_{\mathrm{cross}}(\theta,\phi) = \begin{bmatrix} a_{\mathrm{cross},1}(\theta,\phi) & ... & a_{\mathrm{cross},M}(\theta,\phi) \end{bmatrix}^T, \tag{2.48b}$$

the polarimetric antenna response vector is given by

$$\boldsymbol{a}(\theta,\phi,\gamma,\beta) = \sin(\gamma)e^{\mathrm{j}\beta}\boldsymbol{a}_{\mathrm{co}}(\theta,\phi) + \cos(\gamma)\boldsymbol{a}_{\mathrm{cross}}(\theta,\phi). \tag{2.49}$$

Defining $\boldsymbol{\gamma} = [\gamma_1, ..., \gamma_P]^T$ and $\boldsymbol{\beta} = [\beta_1, ..., \beta_P]^T$ for P impinging signals, the polarimetric antenna response matrix

$$\boldsymbol{A}(\boldsymbol{\theta},\boldsymbol{\phi},\boldsymbol{\gamma},\boldsymbol{\beta}) = \begin{bmatrix} \boldsymbol{a}(\theta_1,\phi_1,\gamma_1,\beta_1) & ... & \boldsymbol{a}(\theta_P,\phi_P,\gamma_P,\beta_P) \end{bmatrix} \tag{2.50}$$

is constructed, and the signal model (2.36) is extended to

$$\boldsymbol{r}(n) = \boldsymbol{A}(\boldsymbol{\theta},\boldsymbol{\phi},\boldsymbol{\gamma},\boldsymbol{\beta})\tilde{\boldsymbol{s}}(n) + \boldsymbol{w}(n). \tag{2.51}$$

The polarimetric ML estimator, *P-ML*, is given by

$$\begin{bmatrix} \hat{\boldsymbol{\theta}}^T & \hat{\boldsymbol{\phi}}^T & \hat{\boldsymbol{\gamma}}^T & \hat{\boldsymbol{\beta}}^T \end{bmatrix}^T = \arg \min_{[\boldsymbol{\theta},\boldsymbol{\phi},\boldsymbol{\gamma},\boldsymbol{\beta}]} \mathrm{Re}\{\mathrm{tr}\{\boldsymbol{\Pi}_{\boldsymbol{A}}^{\perp}\hat{\boldsymbol{R}}_{\boldsymbol{r}}\}\}, \tag{2.52}$$

where it is assumed that the polarization parameters are constant during the observation time. The CRB matrix (2.42) is extended for the polarimetric *P-CRB* as

$$\mathrm{CRB}\left(\begin{bmatrix} \hat{\boldsymbol{\theta}}^T & \hat{\boldsymbol{\phi}}^T & \hat{\boldsymbol{\gamma}}^T & \hat{\boldsymbol{\beta}}^T \end{bmatrix}^T\right) = \frac{\sigma_{\boldsymbol{r}}^2}{2N}\mathrm{Re}\left\{\boldsymbol{D}^H\boldsymbol{\Pi}_{\boldsymbol{A}}^{\perp}\boldsymbol{D} \odot \boldsymbol{Z}^T\boldsymbol{R}_{\tilde{\boldsymbol{s}}}\boldsymbol{Z}\right\}^{-1}. \tag{2.53}$$

Setting $\boldsymbol{a}_p = \boldsymbol{a}(\theta_p,\phi_p,\gamma_p,\beta_p)$,

$$\boldsymbol{D} = \begin{bmatrix} ... & \frac{\partial \boldsymbol{a}_p}{\partial \theta_p} & ... & \frac{\partial \boldsymbol{a}_p}{\partial \phi_p} & ... & \frac{\partial \boldsymbol{a}_p}{\partial \gamma_p} & ... & \frac{\partial \boldsymbol{a}_p}{\partial \beta_p} & ... \end{bmatrix} \tag{2.54}$$

is defined analogously to (2.43) for $p \in \{1, ..., P\}$ and $\boldsymbol{Z} = \begin{bmatrix} \mathbb{I}_P & \mathbb{I}_P & \mathbb{I}_P & \mathbb{I}_P \end{bmatrix}$. The DoA estimators introduced in this section, as well as their corresponding estimation variance bounds given by the CRB, are summarized in Table 2.1.

Table 2.1. *DoA estimators and corresponding Cramér-Rao bounds.*

Signal model	Estimator	CRB
Non-coherent	*NC-ML* (2.28) *NC-RC* (2.34)	*NC-CRB* (2.26) and (2.29) *NC-RC-CRB* (2.29) and (2.32)
Coherent	*C-ML* (2.39)	*C-CRB* (2.42)
Polarimetric	*P-ML* (2.52)	*P-CRB* (2.53)

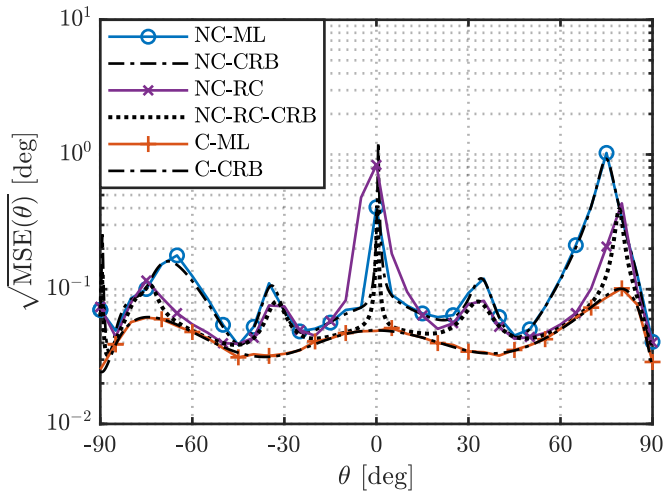

Figure 2.9. *Simulated RMSE for θ estimation with non-coherent ML estimator* (2.28)*, non-coherent RC estimator* (2.34)*, coherent ML estimator* (2.39) *and their respective CRBs versus θ for SNR* $= 20\,\mathrm{dB}$ *© 2019 IEEE [147].*

2.4.4 Simulation Results

2D DoA Estimation

Extensive simulations are performed to assess the DoA estimation performance of *MMA-1*, see Section 2.1, using the different estimators introduced in Sections 2.4.1 to 2.4.3 based on wavefield modeling and manifold separation introduced in Section 2.3. For the simulations, the received signals are generated based on the signal models (2.8) and (2.36) and the true antenna response is given by the original EM simulation data with a 5° sampling grid. In this section, the focus is on estimating θ for a transmitter located in the x-z-plane of the antenna, i.e. $\phi = 0°$. The number of occupied subcarriers is $N = 1000$ and 1000 Monte Carlo runs are performed to evaluate the DoA estimation root-mean-square error (RMSE). For the non-coherent estimators, the relation between signal power $\check{s}$ and noise variance $\sigma_{\boldsymbol{r}}^2$ is nonlinear. For the simulations, we assume $\sigma_{\boldsymbol{r}}^2 = k_\mathrm{B} T_\mathrm{n} B$ with Boltzmann constant k_B, noise temperature $T_\mathrm{n} = 290\,\mathrm{K}$ and bandwidth $B = 1\,\mathrm{MHz}$. For the non-coherent reduced-complexity (NC-RC) estimator, $\hat{\sigma}_{\boldsymbol{r}}^2$ is estimated from $N = 1000$ noise samples, where no signal is present.

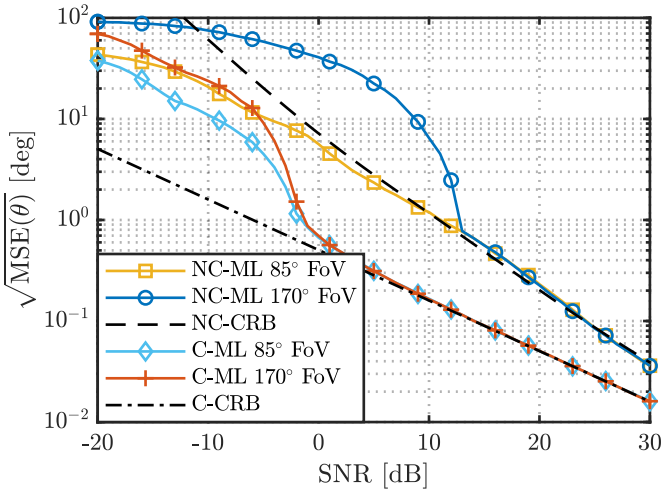

Figure 2.10. *Simulated RMSE for θ estimation with non-coherent ML estimator* (2.28)*, coherent ML estimator* (2.39) *and their respective CRBs versus SNR © 2019 IEEE [147].*

Fig. 2.9 shows the RMSE for the estimation of the inclination θ with the non-coherent, i.e. RSS based, and coherent estimators for SNR $= 20\,\mathrm{dB}$. The non-coherent ML estimator performs close to the corresponding CRB. However, the performance of non-coherent DoA estimation strongly depends on θ. The RMSE of the RC estimator is mostly close to the corresponding CRB, except around $\theta = 0°$. There, errors are likely caused by large gain differences between the ports together with the approximation in (2.33). The coherent ML estimator operates close to its CRB for all θ values. Moreover, the performance is relatively constant over θ compared to the non-coherent ML estimator.

For Fig. 2.10, the RMSE is calculated over $\theta \in [-85°, 85°]$ for 170° field of view (FoV), and over $\theta \in [-85°, 0°]$ and $\theta \in [0°, 85°]$ for 85° FoV, corresponding to the beam of the antenna. The plot reveals that the non-coherent estimator for 170° FoV exhibits much higher errors in the low SNR regime compared to 85° FoV. This can be explained by the relatively symmetric power pattern, see Fig. 2.7a, which makes it difficult for the estimator to distinguish positive and negative θ values. For SNR $\geq 13\,\mathrm{dB}$, both curves asymptotically approach the CRB. The coherent estimator asymptotically approaches the corresponding CRB for SNR $> 7\,\mathrm{dB}$. For lower SNR values, the difference between 170° FoV and 85° FoV is much smaller compared to the non-coherent case. The phase response of the MMA, see Fig. 2.7b, provides valuable information to distinguish between positive and negative θ, which explains the better performance of the coherent estimator.

Fig. 2.11 shows the RMSE over $\theta \in [-85°, 85°]$ versus SNR for both non-coherent ML and RC estimator. For the RC estimator, $\hat{\sigma}_{\boldsymbol{r}}^2$ is again estimated from $N = 1000$ noise samples. Thus $\sigma_{\boldsymbol{r}}^2$ is omitted from the unknowns of the non-coherent RC estima-

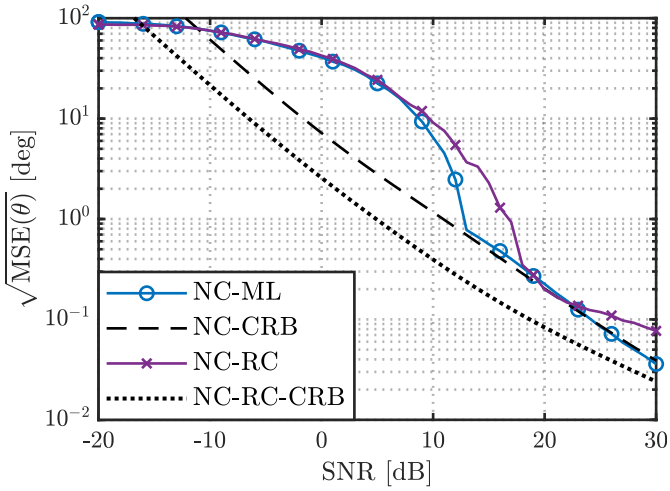

Figure 2.11. *Simulated RMSE for θ estimation with non-coherent ML estimator* (2.28)*, non-coherent RC estimator* (2.34) *and their respective CRBs versus SNR © 2019 IEEE [147].*

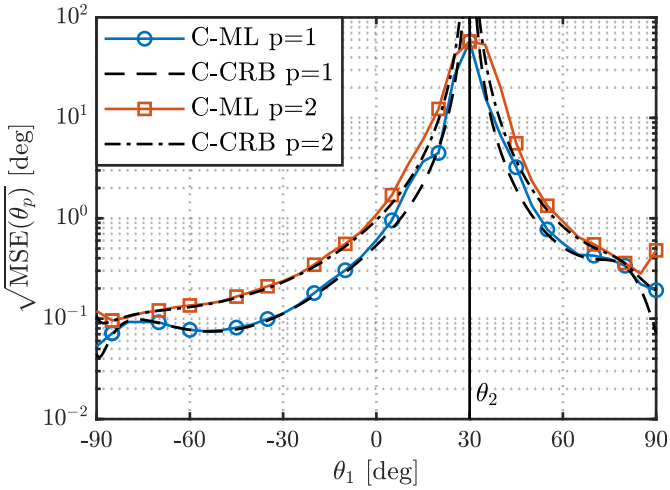

Figure 2.12. *Simulated RMSE for the coherent ML estimator and CRB for two impinging signals from directions $\theta_1 \in [-90°, 90°]$ and $\theta_2 = 30°$. The second signal has 6 dB less power © 2019 IEEE [147].*

tor, see (2.32), and the corresponding CRB with fewer unknowns is lower. The ML and RC estimators perform similar. However, in contrast to the RC estimator, the ML estimator asymptotically approaches the corresponding CRB. We conclude that the RC estimator is a suitable alternative for low-complexity non-coherent DoA estimation.

In Fig. 2.12, coherent DoA estimation for $P = 2$ incoming signals is investigated. The first signal arrives from a variable angle $\theta_1 \in [-90°, 90°]$. The second signal arrives from $\theta_2 = 30°$ with 6 dB less power. The results reveal that the estimator is able to separate the two signals and the RMSEs are close to the respective CRBs, unless the two signals are very closely spaced. When approaching each other, separation becomes

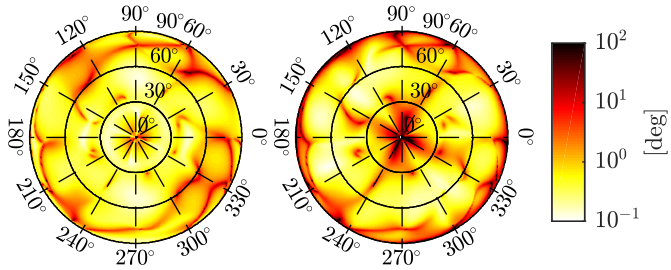

(a) $\sqrt{\mathrm{CRB}(\theta)}$ *(left) and* $\sqrt{\mathrm{CRB}(\phi)}$ *(right)*

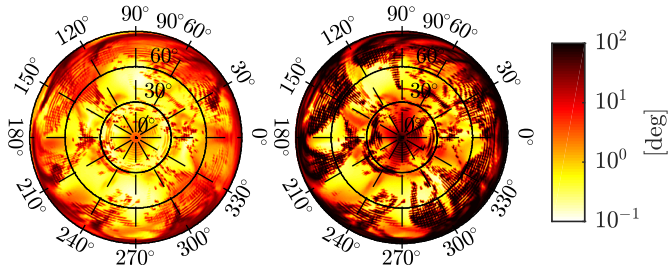

(b) $\sqrt{\mathrm{MSE}(\theta)}$ *(left) and* $\sqrt{\mathrm{MSE}(\phi)}$ *(right)*

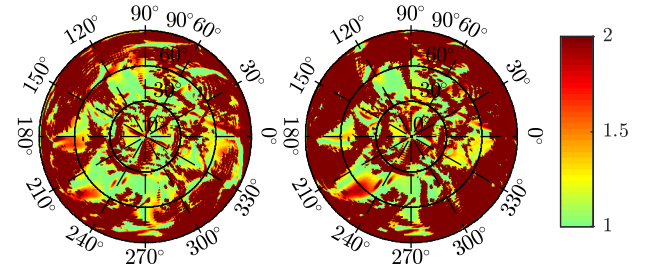

(c) $\sqrt{\mathrm{MSE}(\theta)}/\sqrt{\mathrm{CRB}(\theta)}$ *(left) and* $\sqrt{\mathrm{MSE}(\phi)}/\sqrt{\mathrm{CRB}(\phi)}$ *(right)*

Figure 2.13. *Simulated RMSE for θ and ϕ estimation with the non-coherent ML estimator* (2.28) *and corresponding CRB* (2.26) *and* (2.29) *with SNR* $= 10\,\mathrm{dB}$. *Radius of the polar plots represents $\theta \in [0°, 90°]$, angle represents $\phi \in [0°, 360°)$ © 2019 IEEE [147].*

more challenging, leading to increasing RMSE and CRB. In the limit, for very closely spaced signals, separation is not possible any more.

3D DoA Estimation

In order to evaluate DoA estimation performance on a finer θ and ϕ grid of 1° compared to the original EM simulation data with 5° resolution, we interpolate the EM simulation data. To ensure accurate interpolation, we use wavefield modeling with spherical harmonic functions (2.15) as basis and $U = 144$ coefficients. The estimator for 3D DoA estimation of inclination θ and azimuth ϕ uses spherical harmonic functions with $U = 64 \approx 8\kappa_c^2 R^2 + 4\kappa_c R + 1$ coefficients.

Fig. 2.13 shows the simulated RMSE and CRB for 3D non-coherent DoA estimation

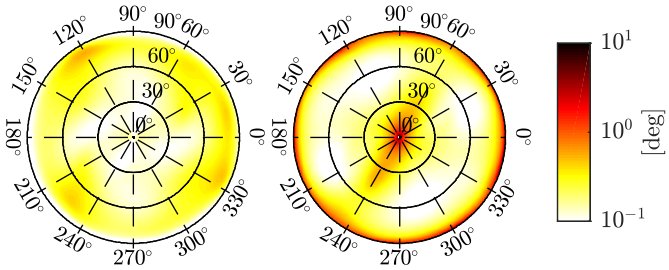

(a) $\sqrt{\mathrm{CRB}(\theta)}$ *(left) and* $\sqrt{\mathrm{CRB}(\phi)}$ *(right)*

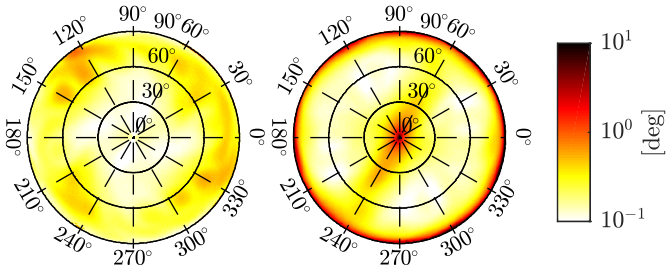

(b) $\sqrt{\mathrm{MSE}(\theta)}$ *(left) and* $\sqrt{\mathrm{MSE}(\phi)}$ *(right)*

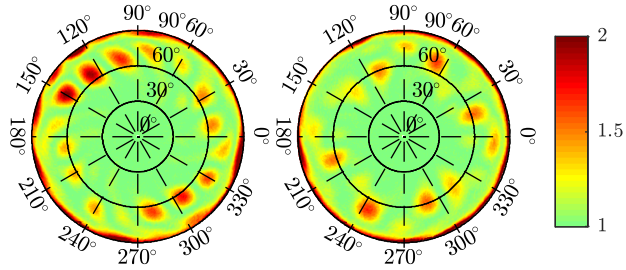

(c) $\sqrt{\mathrm{MSE}(\theta)}/\sqrt{\mathrm{CRB}(\theta)}$ *(left) and* $\sqrt{\mathrm{MSE}(\phi)}/\sqrt{\mathrm{CRB}(\phi)}$ *(right)*

Figure 2.14. *Simulated RMSE for θ and ϕ estimation with the coherent ML estimator* (2.39) *and corresponding CRB* (2.42) *with SNR* $= 10\,\mathrm{dB}$. *Radius of the polar plots represents $\theta \in [0°, 90°]$, angle represents $\phi \in [0°, 360°)$ © 2019 IEEE [147].*

of θ and ϕ. The CRB for non-coherent DoA estimation strongly depends on θ and ϕ. The ratio between the RMSE of the non-coherent ML estimator and the CRB is shown in Fig. 2.13c. When the ratio is close to one, the estimator approaches the CRB. For the non-coherent estimator, this is only the case for certain angles with inclination $\theta < 60°$. For $\theta \geq 60°$, excessive estimation errors occur and the RMSE is far from the CRB. This behavior can be explained by the antenna power pattern, see Figs. 2.4 and 2.7a. When θ approaches 90°, antenna gain and thus SNR values are very low. Another explanation is that the non-coherent estimator suffers from estimation ambiguities, which we also discuss in connection with Figs. 2.10 and 2.15.

The simulated RMSE and CRB for 3D coherent DoA estimation are visualized in Fig. 2.14. Compared to the non-coherent case from Fig. 2.13, both RMSE and CRB

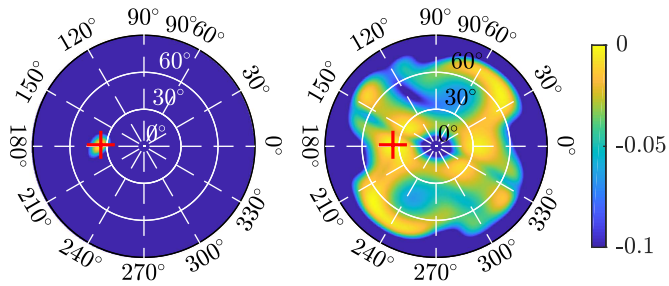

Figure 2.15. *Log-likelihood functions for the C-ML* (2.37)*, left, and NC-ML estimator* (2.27)*, right, normalized to* $[-1, 0]$*, for a signal coming from* $\theta = 35°$*,* $\phi = 178°$ *(red cross) with SNR* $= 15\,\text{dB}$*. Radius of the polar plot represents* $\theta \in [0°, 90°]$*, angle represents* $\phi \in [0°, 360°)$ *© 2019 IEEE [147].*

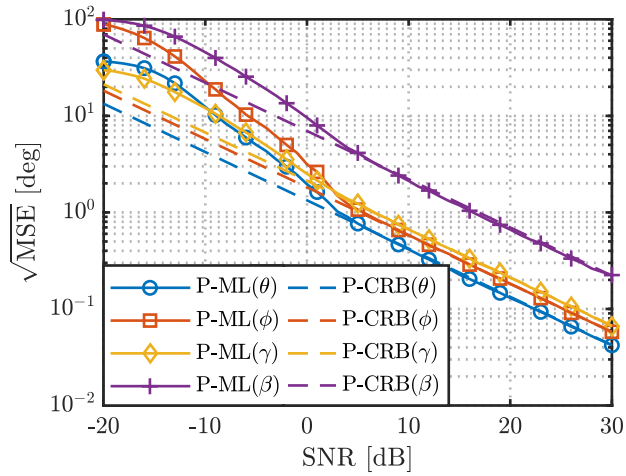

Figure 2.16. *Simulated RMSE for joint estimation of* θ*,* ϕ*,* γ*,* β *with the polarimetric ML estimator* (2.52) *and corresponding CRBs © 2019 IEEE [147].*

are lower and more uniform. The ratio between RMSE and CRB shown in Fig. 2.14c shows that the RMSE of the coherent estimator is close to the CRB for $\theta < 45°$. For $\theta \geq 45°$, the RMSE deviates from the bound for certain angles. However, compared to the non-coherent estimator, the deviation of the coherent estimator from the CRB is small. The non-coherent estimator is clearly outperformed in the 3D case.

To further investigate the performance difference between coherent and non-coherent estimator, the corresponding log-likelihood functions for a signal arriving from a fixed DoA are shown in Fig. 2.15. It is apparent that the coherent log-likelihood function has only one sharp peak at the true DoA. In contrast to that, the non-coherent log-likelihood function has multiple peaks. In the presence of noise, the estimator may choose the wrong peak, leading to a larger RMSE and thus a deviation of the non-coherent estimator from the CRB, see Fig. 2.13.

Fig. 2.16 shows the simulated RMSE for joint estimation of θ, ϕ, γ, β with the

polarimetric ML estimator (2.52). The RMSE is calculated for the estimated DoA parameters $\theta \in [0°, 80°)$, $\phi \in [0°, 360°)$ and the polarization parameters $\gamma \in [10°, 80°]$ and $\beta \in [-180°, 180°)$. For SNR $\geq$ 2 dB, the estimation RMSE of all parameters asymptotically approaches the respective CRB. *MMA-1* can thus be used to determine the signal polarization.

2.5 Joint DoA and ToA Estimation with a Multi-Mode Antenna

2.5.1 Joint DoA and ToA Estimation

For localization, valuable information is contained not only in the DoA of the received signal, but also the ToA, see Section 1.2. A successive approach to DoA and ToA estimation with an MMA is to first estimate the DoA(s) $\{\hat{\boldsymbol{\theta}}, \hat{\boldsymbol{\phi}}\}$ by (2.39) and then coherently combine the signals from the different antenna ports by beamforming, followed by ToA estimation. The weight vector for the conventional beamformer [55, 28] for the respective DoA $\{\theta_p, \phi_p\}$ is

$$\boldsymbol{w}_{\mathrm{BF},p} = \frac{\boldsymbol{a}\left(\hat{\theta}_p, \hat{\phi}_p\right)}{\left\|\boldsymbol{a}\left(\hat{\theta}_p, \hat{\phi}_p\right)\right\|}, \tag{2.55}$$

which is applied to linearly combine the received signals

$$r_{\mathrm{BF},p}(n) = \boldsymbol{w}_{\mathrm{BF},p}^H \boldsymbol{r}(n). \tag{2.56}$$

The log-likelihood function for successive ToA estimation is then

$$L_{\boldsymbol{r}_{\mathrm{BF},p}}(\tau_p, \alpha_p, \varphi_p, \sigma_{\boldsymbol{r}}^2) = -N \ln(\pi\sigma_{\boldsymbol{r}}^2) - \frac{1}{\sigma_{\boldsymbol{r}}^2} \sum_{n \in \mathbb{N}_{\mathrm{sc}}} \left| r_{\mathrm{BF},p}(n) - s(n, \tau_p)\alpha_p e^{\mathrm{j}\varphi_p} \right|^2, \tag{2.57}$$

with

$$\boldsymbol{r}_{\mathrm{BF},p} = \begin{bmatrix} \dots & r_{\mathrm{BF},p}(n) & \dots \end{bmatrix}^T, \; n \in \mathbb{N}_{\mathrm{sc}}. \tag{2.58}$$

Plugging the maximum of (2.57) w.r.t. α_p and φ_p back into (2.57), defining

$$\boldsymbol{s}(\tau_p) = \begin{bmatrix} \dots & s(n, \tau_p) & \dots \end{bmatrix}^T, \; n \in \mathbb{N}_{\mathrm{sc}} \tag{2.59}$$

and neglecting the constant term, we obtain the concentrated log-likelihood function

$$\tilde{L}_{\boldsymbol{r}_{\mathrm{BF},p}}(\tau_p) = \frac{1}{\sigma_{\boldsymbol{r}}^2} \frac{|\boldsymbol{s}^H(\tau_p)\boldsymbol{r}_{\mathrm{BF},p}|^2}{\|\boldsymbol{s}(\tau_p)\|}, \tag{2.60}$$

and the *T-ML* estimator

$$\hat{\tau}_p = \arg\max_{\tau_p} \tilde{L}_{\boldsymbol{r}_{\mathrm{BF},p}}(\tau_p). \tag{2.61}$$

However, this successive approach has two drawbacks. First, the impinging signals must be separable in DoA domain. Second, as shown in Section 2.5.2, performance for low SNR values is worse compared to a joint approach.

Instead, one can also estimate DoA and ToA jointly based on the joint log-likelihood function

$$L_{\boldsymbol{r}}(\boldsymbol{\theta}, \boldsymbol{\phi}, \boldsymbol{\tau}, \boldsymbol{\alpha}, \boldsymbol{\varphi}, \sigma_{\boldsymbol{r}}^2) = -N \ln(\pi\sigma_{\boldsymbol{r}}^2) - \frac{1}{\sigma_{\boldsymbol{r}}^2} \sum_{n\in\mathbb{N}_{\mathrm{sc}}} \left\| \boldsymbol{r}(n) - \sum_{p=1}^{P} \boldsymbol{a}(\theta_p, \phi_p) s(n, \tau_p) \alpha_p e^{\mathrm{j}\varphi_p} \right\|^2, \tag{2.62}$$

with

$$\boldsymbol{r} = \begin{bmatrix} \dots & \boldsymbol{r}^T(n) & \dots \end{bmatrix}^T, n \in \mathbb{N}_{\mathrm{sc}}. \tag{2.63}$$

Plugging the maximum of (2.62) w.r.t. $\boldsymbol{\alpha}$ and $\boldsymbol{\varphi}$ back into (2.62), see [65, 158], and neglecting the constant term, we obtain the concentrated log-likelihood function

$$\tilde{L}_{\boldsymbol{r}}(\boldsymbol{\theta}, \boldsymbol{\phi}, \boldsymbol{\tau}) = \frac{1}{\sigma_{\boldsymbol{r}}^2} \left\| \boldsymbol{V}^{\perp} \boldsymbol{r} \right\|^2 \tag{2.64}$$

with

$$\boldsymbol{V}^{\perp} = \boldsymbol{V}(\boldsymbol{V}^H\boldsymbol{V})^{-1}\boldsymbol{V}^H, \tag{2.65}$$

where $\boldsymbol{V} \in \mathbb{C}^{MN\times P}$ is defined column-wise by

$$[\boldsymbol{V}]_{:,p} = \mathrm{vec}\left\{ \boldsymbol{a}(\theta_p, \phi_p) \boldsymbol{s}^T(\tau_p) \right\}. \tag{2.66}$$

The joint DoA-ToA ML estimator, *J-ML*, is then given by

$$\{\hat{\boldsymbol{\theta}}, \hat{\boldsymbol{\phi}}, \hat{\boldsymbol{\tau}}\} = \arg\max_{\boldsymbol{\theta},\boldsymbol{\phi},\boldsymbol{\tau}} \tilde{L}_{\boldsymbol{r}}(\boldsymbol{\theta}, \boldsymbol{\phi}, \boldsymbol{\tau}). \tag{2.67}$$

In Section 3.2 and Appendix C.4, the CRB for joint DoA and ToA estimation (3.13) is derived. As the off-diagonal elements of (3.13) are zero, the CRBs for joint estimation are equal to the individual DoA and ToA estimation CRBs. The independence of DoA and ToA estimation in terms of the CRB is a consequence of the narrowband assumption and the symmetric signal spectrum, see Section 3.2 and Appendix C.4.

Table 2.2. *DoA-ToA estimators and corresponding Cramér-Rao bounds.*

Approach	**Estimators**	**CRB**
Successive	*C-ML* (2.39), *T-ML* (2.61)	*C-CRB* (2.42), *T-CRB* (2.68)
Joint	*J-ML* (2.67)	*C-CRB* (2.42), *T-CRB* (2.68)

However, the CRB is a tight bound only for high SNR values. As we show in Section 2.5.2, joint estimation of DoA and ToA estimation is nevertheless beneficial in the low SNR regime. The DoA estimation CRB is thus given by (2.42). From (3.13) and [63], the ToA estimation CRB for an OFDM signal, abbreviated as *T-CRB*, is given by

$$\mathrm{CRB}(\tau_p) = \frac{\sigma_r^2}{2\alpha_p^2 N \|\boldsymbol{a}(\theta_p, \phi_p)\|^2 \bar{\beta}^2}, \tag{2.68}$$

with the mean square bandwidth $\bar{\beta}^2$ defined by (3.14). The ToA CRB (2.68) is valid for a single propagation path ($P = 1$). However, given that the different propagation paths are resolvable in ToA domain, i.e. $|\tau_p - \tau_q| \gg \frac{1}{B} \, \forall \, p \neq q; \, p, q \in \{1, ..., P\}$ [165], the CRB (2.68) also applies in the multipath case [166]. The estimators introduced in this section together with their CRBs are summarized in Table 2.2.

2.5.2 Simulation Results

Simulations are performed to compare the successive approach of DoA estimation with *C-ML* (2.39), coherent combining (2.56) and subsequent ToA estimation with *T-ML* (2.61) to the joint DoA-ToA ML estimator (2.67). For this simulation, we assume the antenna response of *MMA-2*, see Section 2.1. We are interested in estimating the azimuth ϕ, focusing on the x-y-plane of the antenna. The transmitted signal is a Zadoff-Chu sequence [167] of length $N = 463$, which is mapped onto 925 subcarriers out of $N_{\mathrm{fft}} = 1024$ by occupying every second subcarrier, see also Section 6.1.1. The SNR is defined by (2.11). 1000 Monte Carlo runs are performed to calculate the estimation RMSEs, where the mean is also taken over the manifold $\phi \in [-180°, 180°[$. Theoretical lower bounds are given in terms of the CRBs (2.42) and (2.68) for DoA and ToA, respectively.

First, we have a look at the DoA estimation RMSE shown in Fig. 2.17. Both *C-ML* and *J-ML* asymptotically approach the CRB for high SNR values. However, *J-ML* enters the threshold region at approximately 7 dB lower SNR. Furthermore, *J-ML* operates close to the CRB already in the beginning of the asymptotic region, whereas *C-ML* slowly approaches it. Despite performance being very similar in the mid to high SNR region, joint estimation is clearly superior in the low SNR regime.

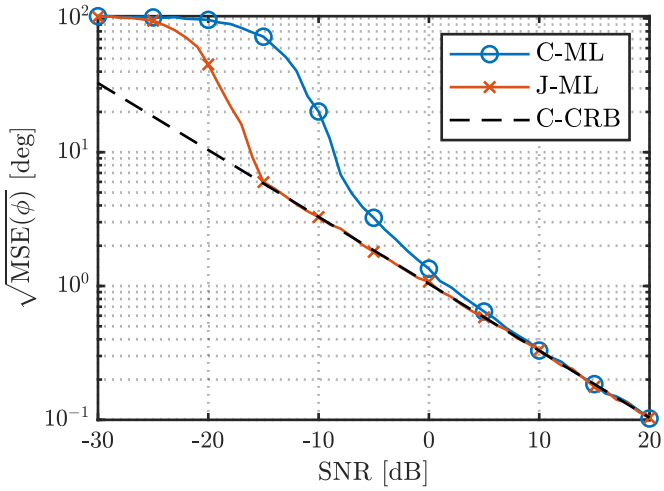

Figure 2.17. *Simulated RMSE of DoA estimation with DoA ML estimator* (2.39) *and joint DoA-ToA ML estimator* (2.67).

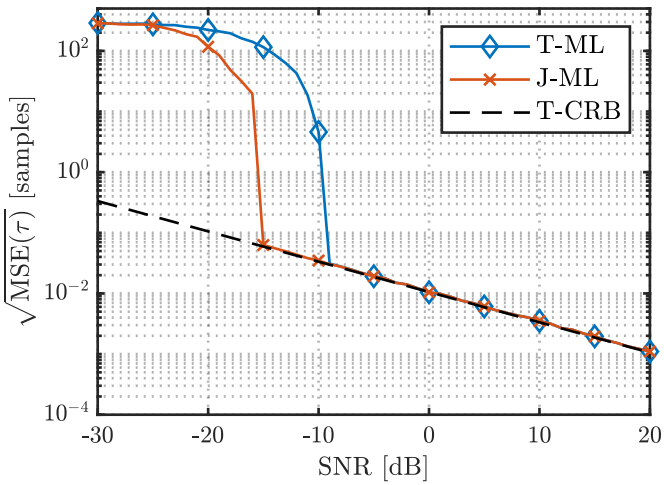

Figure 2.18. *Simulated RMSE of ToA estimation with coherent combining after DoA estimation in conjunction with the ToA ML estimator* (2.61)*, and with the joint DoA-ToA ML estimator* (2.67).

Next, we investigate the ToA estimation RMSE plotted in Fig. 2.18. Both, *T-ML* and *J-ML* asymptotically approach the CRB. However, *T-ML* is close to the CRB for SNR $> -9\,\mathrm{dB}$ on, whereas *J-ML* is close to the CRB for SNR $> -16\,\mathrm{dB}$. Thus also for ToA, joint estimation outperforms the successive approach in the low SNR region.

Chapter 3

Fundamental Limits for Cooperative Position and Orientation Estimation

In this chapter, we define a cooperative network. Using the antenna response representation from Chapter 2, we derive the Fisher information for nodes equipped with MMAs in ToA and DoA domain and perform the transformation to position and orientation domain. We then derive position and orientation error bounds based on the CRB for absolute and relative localization and investigate exemplary formations. Finally, we discuss how theoretical error bounds relate to errors observed in experiments.

3.1 Definition of a Cooperative Network

The network consists of agents (for example robotic rovers) denoted by the agent set $\mathbb{R}$, and anchors denoted by the anchor set $\mathbb{A}$. Together, they form the node set $\mathbb{N} = \mathbb{R} \cup \mathbb{A}$. Agents are mobile radio nodes with unknown position and orientation, whereas anchors are static radio nodes with known position and orientation. The focus in this chapter is on the static case. In Chapter 5, the definition of a cooperative network is extended to moving agents. The basic geometric relationships are shown in Fig. 3.1 for two exemplary agents i and j. The figure contains three coordinate frames. A common frame for the entire network, span by the x and y axes, and two body frames of agents i and j, which are fixed to the respective agent center and rotate with the agent. The position of agent i, $\boldsymbol{p}_i = \begin{bmatrix} x_i & y_i \end{bmatrix}^T$, is defined in the common frame. The orientation ψ_i describes the rotation of the body frame of agent i w.r.t. the common frame. Furthermore, the distance $d_{i,j}$ between the two agents and the DoAs $\phi_{i,j}$ and $\phi_{j,i}$, defined in the respective body frames of the agents are shown. The entities of other agents are defined analogously. For the derivation of the fundamental limits, we follow

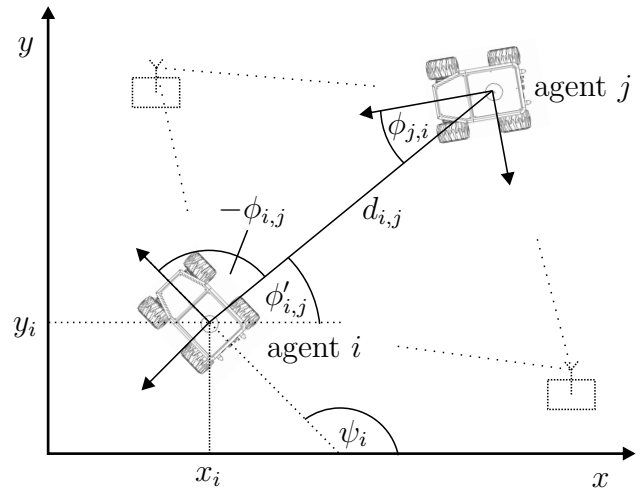

Figure 3.1. *Two agents i and j, the distance $d_{i,j}$ between the agents, the DoAs $\phi_{i,j}$ and $\phi_{j,i}$ and the position $\boldsymbol{p}_i = [x_i \; y_i]^T$ and orientation ψ_i of agent i, as well as two optional anchors.*

the commonly used synchronization assumption [20, 39]. In [82] it is shown, that the lower bounds for an asynchronous network are larger or equal to the lower bounds of a synchronous network. Lower bounds derived with the synchronization assumption are thus also lower bounds for asynchronous networks. Furthermore, employing a TWR protocol, the clock biases can be eliminated [134, 153]. Assuming that the processing time between forward and backward transmissions is compensated and very short, the impact of the relative frequency offset of the two clocks can be neglected [166]. Under the stated assumption, the ToA of a signal received by agent i, sent by agent j, is then given by

$$\tau_{i,j} = \frac{d_{i,j}}{c} = \frac{\|\boldsymbol{p}_j - \boldsymbol{p}_i\|}{c}. \tag{3.1}$$

The signal DoA measured in the body frame of agent i is defined as

$$\phi_{i,j} = \phi'_{i,j} - \psi_i = \operatorname{arctan2}\left(y_j - y_i,\, x_j - x_i\right) - \psi_i. \tag{3.2}$$

The position and orientation states of agent i are thus given by

$$\boldsymbol{x}_i = \begin{bmatrix} (\boldsymbol{p}_i)^T & \psi_i \end{bmatrix}^T. \tag{3.3}$$

The state vector for the entire network is formed by stacking the agent states,

$$\boldsymbol{x} = \begin{bmatrix} (\boldsymbol{x}_1)^T & \dots & (\boldsymbol{x}_i)^T & \dots & (\boldsymbol{x}_{|\mathbb{R}|})^T \end{bmatrix}^T. \tag{3.4}$$

In order to obtain a true fundamental limit, we take the received signals as observations, instead of extracted signal metrics such as ToA or DoA. The signal model is based on (2.8), where we add indices for the transmitting and receiving agent. To focus on the cooperative aspect and since the propagation environment is unknown in practice, we assume $P = 1$. A signal transmitted by node j and received by node i is then written in discrete frequency domain as

$$\boldsymbol{r}_{i,j}(n) = \boldsymbol{a}_i(\phi_{i,j}) s(n, \tau_{i,j}) \alpha_{i,j} e^{\mathrm{j}\varphi_{i,j}} + \boldsymbol{w}_{i,j}(n), \tag{3.5}$$

where $\boldsymbol{a}_i(\phi_{i,j})$ is the antenna response of the receiving antenna. Each node i receives signals from its neighboring nodes in the set $\mathbb{L}_i \subseteq \mathbb{N} \setminus \{i\}$. If e.g. the link between node i and a certain neighboring node is blocked, the neighboring node is not a member of the set $\mathbb{L}_i$.

3.2 Fisher Information in ToA and DoA Domain

We start by deriving the Fisher information in ToA and DoA domain. Defining $l(i, j)$ as a function returning the index of the link between transmitting node j and receiving node i, we can form a vector containing the ToA $\tau_{i,j}$ and DoA $\phi_{i,j}$ for the respective link,

$$\boldsymbol{l}_{l(i,j)} = \begin{bmatrix} \tau_{i,j} & \phi_{i,j} \end{bmatrix}^T, \tag{3.6}$$

and the vector

$$\boldsymbol{l} = \begin{bmatrix} \dots & \boldsymbol{l}_{l(i,j)}^T & \dots \end{bmatrix}^T \tag{3.7}$$

containing ToAs and DoAs of all links. Although not of direct interest, we must also estimate the unwanted parameters absolute amplitude $\alpha_{i,j}$ and absolute phase $\varphi_{i,j}$. We collect both parameters in a vector for the respective link,

$$\boldsymbol{n}_{l(i,j)} = \begin{bmatrix} \alpha_{i,j} & \varphi_{i,j} \end{bmatrix}^T, \tag{3.8}$$

and for all links in the network

$$\boldsymbol{n} = \begin{bmatrix} \dots & \boldsymbol{n}_{l(i,j)}^T & \dots \end{bmatrix}^T. \tag{3.9}$$

The elements of the FIM $\boldsymbol{I} \in \mathbb{R}^{4L \times 4L}$ for Gaussian noise $\boldsymbol{w}_{i,j}(n)$ are then given by

$$[\boldsymbol{I}]_{p,q} = \frac{2}{\sigma_{\boldsymbol{r}}^2} \operatorname{Re} \left\{ \sum_{i \in \mathbb{N}} \sum_{j \in \mathbb{L}_i} \sum_{n \in \mathbb{N}_{\mathrm{sc}}} \frac{\partial \operatorname{E}\{\boldsymbol{r}_{i,j}(n)\}^H}{\partial [\boldsymbol{l}^T \, \boldsymbol{n}^T]_p} \frac{\partial \operatorname{E}\{\boldsymbol{r}_{i,j}(n)\}}{\partial [\boldsymbol{l}^T \, \boldsymbol{n}^T]_q} \right\}, \tag{3.10}$$

see [80]. We partition the FIM into sub-matrices,

$$\boldsymbol{I} = \begin{bmatrix} \boldsymbol{I_l} & \boldsymbol{I_{ln}} \\ \boldsymbol{I_{ln}^T} & \boldsymbol{I_n} \end{bmatrix}, \tag{3.11}$$

in order to separate the parameters of interest from the unwanted parameters. The ToA-DoA equivalent Fisher information matrix (EFIM) [82] is then

$$\boldsymbol{I_l^{\mathrm{e}}} = \boldsymbol{I_l} - \boldsymbol{I_{ln}}\boldsymbol{I_n^{-1}}\boldsymbol{I_{ln}^T} \in \mathbb{R}^{2L\times 2L}. \tag{3.12}$$

The EFIM contains the Fisher information for the ToAs and DoAs, while considering the impact of the unknown absolute amplitudes and phases. It is calculated with the Schur complement [168]. In Appendix C.4, we derive the following compact form of the ToA-DoA EFIM (3.12):

$$[\boldsymbol{I_l^{\mathrm{e}}}]_{l(i,j),l(i,j)} = \frac{2\alpha_{i,j}^2 N P_{\mathrm{Tx}} \|\boldsymbol{a}(\phi_{i,j})\|^2}{\sigma_{\boldsymbol{r}}^2} \begin{bmatrix} \bar{\beta}^2 & 0 \\ 0 & \bar{\gamma}^2(\phi_{i,j}) - \bar{\alpha}^2(\phi_{i,j}) - \bar{\varphi}^2(\phi_{i,j}) \end{bmatrix}. \tag{3.13}$$

We assume that the number of occupied subcarriers N is odd and the signal spectrum is symmetric, $|s(-n)| = |s(n)|\,\forall\, n \in \mathbb{N}_{\mathrm{sc}}$. The average transmit power P_{Tx} is defined by (2.10). The different entities of the ToA-DoA EFIM (3.13) are defined by (3.14) and (3.16) to (3.18). The mean square bandwidth of an OFDM signal is given by

$$\bar{\beta}^2 := \frac{\sum_{n\in\mathbb{N}_{\mathrm{sc}}} \left|\frac{\partial s(n,\tau_{i,j})}{\partial \tau_{i,j}}\right|^2}{\sum_{n\in\mathbb{N}_{\mathrm{sc}}} |s(n,\tau_{i,j})|^2} = \frac{4\pi^2 f_{\mathrm{sc}}^2}{N P_{\mathrm{Tx}}} \sum_{n\in\mathbb{N}_{\mathrm{sc}}} n^2 |s(n)|^2, \tag{3.14}$$

see [63]. The mean square bandwidth [80], also called squared effective bandwidth [166], is an indicator how well a certain signal is suited for ToA estimation. However, being a measure of the curvature of the autocorrelation function mainlobe at zero, it does not consider sidelobes [169]. For phase-shift keying (PSK) with uniformly distributed energy and fully occupied subcarriers, $N = N_{\mathrm{fft}}$, the mean square bandwidth is given by

$$\bar{\beta}^2 = \frac{1}{3}\pi^2 f_{\mathrm{sc}}^2 (N^2 - 1). \tag{3.15}$$

Similarly,

$$\bar{\gamma}^2(\phi_{i,j}) := \frac{\left\|\frac{\partial \boldsymbol{a}(\phi_{i,j})}{\partial \phi_{i,j}}\right\|^2}{\|\boldsymbol{a}(\phi_{i,j})\|^2} \tag{3.16}$$

indicates how well the antenna response is suited for DoA estimation. The impact of the unknown absolute amplitude $\alpha_{i,j}$ on DoA estimation is represented by

$$\bar{\alpha}^2(\phi_{i,j}) := \frac{\mathrm{Re}\left\{\frac{\partial \boldsymbol{a}^H(\phi_{i,j})}{\partial \phi_{i,j}} \boldsymbol{a}(\phi_{i,j})\right\}^2}{\|\boldsymbol{a}(\phi_{i,j})\|^4}, \tag{3.17}$$

and the impact of unknown absolute phase $\varphi_{i,j}$ on DoA estimation by

$$\bar{\varphi}^2(\phi_{i,j}) := \frac{\mathrm{Im}\left\{\frac{\partial \boldsymbol{a}^H(\phi_{i,j})}{\partial \phi_{i,j}} \boldsymbol{a}(\phi_{i,j})\right\}^2}{\|\boldsymbol{a}(\phi_{i,j})\|^4}. \tag{3.18}$$

The ToA-DoA EFIM (3.13) allows insights: It is evident that $\bar{\beta}^2$ and $\bar{\gamma}^2$ show up with a positive sign, corresponding to an information gain, whereas $\bar{\alpha}^2(\phi_{i,j})$ and $\bar{\varphi}^2(\phi_{i,j})$ have a negative sign, corresponding to information loss. Furthermore, the off-diagonal elements of (3.13), called baseband-carrier correlation in [84], are zero. The inverse of the ToA-related element of (3.13) is equivalent to the ToA estimation CRB (2.68), which is also found in the literature [63]. In Appendix C.7 it is shown that the inverse of the DoA-related element of (3.13) is equivalent to the coherent DoA estimation CRB *C-CRB* (2.42), which can also be found in [160]. Thus, the CRBs for joint estimation are equal to the individual DoA and ToA estimation CRBs. The independence of DoA and ToA estimation in terms of the CRB is a consequence of the narrowband assumption and the assumed symmetric spectrum of the signal, see Appendix C.4. Intuitively, ToA is estimated from the observation of a delayed baseband signal, while DoA is estimated from relative amplitudes and phases between the ports, see also [14]. However, the CRB is a tight bound only for high SNR values. As we show in Section 2.5.2, joint estimation of DoA and ToA estimation is nevertheless beneficial in the low SNR regime. Compared to (2.42) and [160], the representation of the DoA estimation CRB in (3.13) allows further interpretation. Two special cases are of interest. For ideal antenna arrays, $\bar{\alpha}^2(\phi_{i,j}) = 0$, see the proof in Appendix C.5. For an ideal antenna array, the unknown absolute amplitude $\alpha_{i,j}$ does not impact DoA estimation performance. For an ideal UCA, also $\bar{\varphi}^2(\phi_{i,j}) = 0$, see the proof in Appendix C.6. For an ideal UCA, the unknown absolute phase $\varphi_{i,j}$ also does not impact DoA estimation.

3.3 Fisher Information in Position and Orientation Domain

For cooperative localization, the domains of interest are position and orientation. Thus, we perform a transformation [80] of the FIM (3.11),

$$\boldsymbol{I}' = \boldsymbol{T}^T \boldsymbol{I}\, \boldsymbol{T}, \tag{3.19}$$

with the Jacobian matrix

$$\boldsymbol{T} = \frac{\partial [\boldsymbol{l}^T\, \boldsymbol{n}^T]^T}{\partial [\boldsymbol{x}^T\, \boldsymbol{n}^T]^T} = \begin{bmatrix} \frac{\partial \boldsymbol{l}}{\partial \boldsymbol{x}} & \mathbb{0}_{2L} \\ \mathbb{0}_{2L\times 3|\mathbb{R}|} & \mathbb{I}_{2L} \end{bmatrix}. \tag{3.20}$$

The elements of $\frac{\partial \boldsymbol{l}}{\partial \boldsymbol{x}} \in \mathbb{R}^{2L\times 3|\mathbb{R}|}$ are given by

$$\left[\frac{\partial \boldsymbol{l}}{\partial \boldsymbol{x}}\right]_{l(i,j),i} = \begin{bmatrix} \frac{\partial \tau_{i,j}}{\partial \boldsymbol{p}_i} & \frac{\partial \tau_{i,j}}{\partial \psi_i} \\ \frac{\partial \phi_{i,j}}{\partial \boldsymbol{p}_i} & \frac{\partial \phi_{i,j}}{\partial \psi_i} \end{bmatrix}, \tag{3.21}$$

$$\left[\frac{\partial \boldsymbol{l}}{\partial \boldsymbol{x}}\right]_{l(i,j),j} = \begin{bmatrix} \frac{\partial \tau_{i,j}}{\partial \boldsymbol{p}_j} & \frac{\partial \tau_{i,j}}{\partial \psi_j} \\ \frac{\partial \phi_{i,j}}{\partial \boldsymbol{p}_j} & \frac{\partial \phi_{i,j}}{\partial \psi_j} \end{bmatrix}, \tag{3.22}$$

and correspondingly for $l(j,i)$. The Jacobian matrix $\frac{\partial \boldsymbol{l}}{\partial \boldsymbol{x}}$ represents the formation of the agents and its elements are given by (3.23) to (3.26). The partial derivative of ToA $\tau_{i,j}$, see (3.1), w.r.t. position evaluates to

$$\frac{\partial \tau_{i,j}}{\partial \boldsymbol{p}_i} = \frac{-(\boldsymbol{p}_j - \boldsymbol{p}_i)}{c||\boldsymbol{p}_j - \boldsymbol{p}_i||} = -\frac{\partial \tau_{j,i}}{\partial \boldsymbol{p}_i} = -\frac{\partial \tau_{i,j}}{\partial \boldsymbol{p}_j}. \tag{3.23}$$

Since ToA does not provide orientation information, we have

$$\frac{\partial \tau_{i,j}}{\partial \psi_i} = 0. \tag{3.24}$$

The partial derivative of DoA $\phi_{i,j}$, see (3.2), w.r.t. position is given by

$$\frac{\partial \phi_{i,j}}{\partial \boldsymbol{p}_i} = \frac{-(\boldsymbol{p}_j - \boldsymbol{p}_i)}{||\boldsymbol{p}_j - \boldsymbol{p}_i||^2} \begin{bmatrix} 0 & 1 \\ -1 & 0 \end{bmatrix} = -\frac{\partial \phi_{i,j}}{\partial \boldsymbol{p}_j}, \tag{3.25}$$

and w.r.t. orientation by

$$\frac{\partial \phi_{i,j}}{\partial \psi_i} = -1. \tag{3.26}$$

Inserting (3.11) and (3.20) into (3.19), we obtain

$$\boldsymbol{I}' = \begin{bmatrix} \left(\frac{\partial \boldsymbol{l}}{\partial \boldsymbol{x}}\right)^T \boldsymbol{I}_{\boldsymbol{l}} \left(\frac{\partial \boldsymbol{l}}{\partial \boldsymbol{x}}\right) & \left(\frac{\partial \boldsymbol{l}}{\partial \boldsymbol{x}}\right)^T \boldsymbol{I}_{\boldsymbol{ln}} \\ \boldsymbol{I}_{\boldsymbol{ln}}^T \left(\frac{\partial \boldsymbol{l}}{\partial \boldsymbol{x}}\right) & \boldsymbol{I}_{\boldsymbol{n}} \end{bmatrix}. \tag{3.27}$$

Applying the Schur complement [168], we obtain the position and orientation EFIM

$$\begin{aligned} \boldsymbol{I}_{\boldsymbol{x}}^{\mathrm{e}} &= \left(\frac{\partial \boldsymbol{l}}{\partial \boldsymbol{x}}\right)^T \boldsymbol{I}_{\boldsymbol{l}} \left(\frac{\partial \boldsymbol{l}}{\partial \boldsymbol{x}}\right) - \left(\frac{\partial \boldsymbol{l}}{\partial \boldsymbol{x}}\right)^T \boldsymbol{I}_{\boldsymbol{ln}} \boldsymbol{I}_{\boldsymbol{n}}^{-1} \boldsymbol{I}_{\boldsymbol{ln}}^T \left(\frac{\partial \boldsymbol{l}}{\partial \boldsymbol{x}}\right) \\ &= \left(\frac{\partial \boldsymbol{l}}{\partial \boldsymbol{x}}\right)^T \boldsymbol{I}_{\boldsymbol{l}}^{\mathrm{e}} \left(\frac{\partial \boldsymbol{l}}{\partial \boldsymbol{x}}\right). \end{aligned} \tag{3.28}$$

The structure of (3.28) allows insight into the determining factors of the available position and orientation information: First, position and orientation information is determined by the ToA and DoA information $\boldsymbol{I}_{\boldsymbol{l}}^{\mathrm{e}}$ defined in (3.13). Second, position and orientation information is influenced by the formation geometry represented by the Jacobian matrix $\frac{\partial \boldsymbol{l}}{\partial \boldsymbol{x}}$.

3.4 Absolute Position and Orientation Error Bounds

When the anchors uniquely define a 2D Cartesian coordinate system, the position and orientation EFIM is full rank $\operatorname{rank}\{\boldsymbol{I}_{\boldsymbol{x}}^{\mathrm{e}}\} = 3\,|\mathbb{R}|$. This is the case, when at least three parameters are known, e.g. the x and y coordinates of one anchor and either x or y of a second anchor. Thus in practice, at least two anchors with singleport antenna are required. Alternatively, one anchor whose orientation is known and which is equipped with multiport antenna capable of DoA estimation is also sufficient. When the EFIM is full rank, the corresponding CRB

$$\mathrm{CRB}(\boldsymbol{x}) = \left(\boldsymbol{I}_{\boldsymbol{x}}^{\mathrm{e}}\right)^{-1} \tag{3.29}$$

can be obtained by taking the inverse. The lower bound on the covariance of the position estimate for agent i is obtained by extracting the corresponding 2×2 submatrix,

$$\operatorname{cov}\{\hat{\boldsymbol{p}}_i\} \succcurlyeq \mathrm{CRB}(\boldsymbol{p}_i) := \begin{bmatrix} [\mathrm{CRB}(\boldsymbol{x})]_{3i-2,3i-2} & [\mathrm{CRB}(\boldsymbol{x})]_{3i-2,3i-1} \\ [\mathrm{CRB}(\boldsymbol{x})]_{3i-1,3i-2} & [\mathrm{CRB}(\boldsymbol{x})]_{3i-1,3i-1} \end{bmatrix}. \tag{3.30}$$

By an eigendecomposition,

$$\mathrm{CRB}(\boldsymbol{p}_i) = \boldsymbol{Q} \begin{bmatrix} \lambda_1 & 0 \\ 0 & \lambda_2 \end{bmatrix} \boldsymbol{Q}^T, \tag{3.31}$$

the square root of the position CRB can be interpreted as an ellipse with major axis $\sqrt{\lambda_1}$ and minor axis $\sqrt{\lambda_2}$ rotated by the rotation matrix Q. The variance of the orientation estimate of agent i is lower bounded by

$$\mathrm{var}\left\{\hat{\psi}_i\right\} \geq \mathrm{CRB}(\psi_i) := [\mathrm{CRB}(\boldsymbol{x})]_{3i,3i}. \tag{3.32}$$

We now investigate an exemplary formation of six agents and three anchors. The system parameters comply with the validation in Chapter 6, i.e. the transmitted signal is a Zadoff-Chu sequence [167] of length $N = 463$, which is mapped onto 925 subcarriers out of $N_{\mathrm{fft}} = 1024$ by occupying every second subcarrier, see also Section 6.1.1. For the sampling rate $B_{\mathrm{s}} = 31.25\,\mathrm{MHz}$, the occupied bandwidth is thus $B \approx 28.2\,\mathrm{MHz}$. To setup a noise level for internal receiver noise [133], we assume $P_{\mathrm{Tx}} = -15\,\mathrm{dBm}$ transmit power, $T_{\mathrm{n}} = 290\,\mathrm{K}$ receiver noise temperature, a noise figure of 8 dB and free-space path loss for $f_{\mathrm{c}} = 1.68\,\mathrm{GHz}$. Fig. 3.2a shows the position error bounds for agents equipped with dipole antennas, thus not capable of DoA estimation. Fig. 3.2b shows the position and orientation error bounds for agents equipped with MMAs, which can estimate DoAs. The position error bounds are drawn as ellipses according to (3.31) and the orientation error bounds are drawn as sectors. As the position error bounds are in the order of centimeters, and the orientation error bounds in the sub-degree range, 300σ position and orientation error bounds are plotted to make them visible. With dipole antennas, no orientation information of the agents can be obtained. When the agents are equipped with MMAs, in addition to the gained orientation information, the position error bounds of the agents are smaller. The position and orientation error bounds of agents #1, #2 and #4, which are closest to anchors, are smallest. Agent #5, which has the largest distance to the anchors, has the largest position and orientation error bounds. Thus, for fixed system parameters and antenna types, the position and orientation error bounds depend on the SNR, i.e. the distance, and the geometry of the formation.

The derived bounds can be used to asses the quality of a certain swarm formation for position and orientation estimation, or to optimize formations. As an example, we answer the question where agent #6 of the formation shown in Fig. 3.2 should move to obtain the lowest position and orientation error bounds. For that we calculate the average position error bound $\sqrt{\frac{1}{|\mathbb{R}|}\sum_{i=1}^{|\mathbb{R}|} \mathrm{tr}\left\{\mathrm{CRB}(\boldsymbol{p}_i)\right\}}$ and the average orientation er-

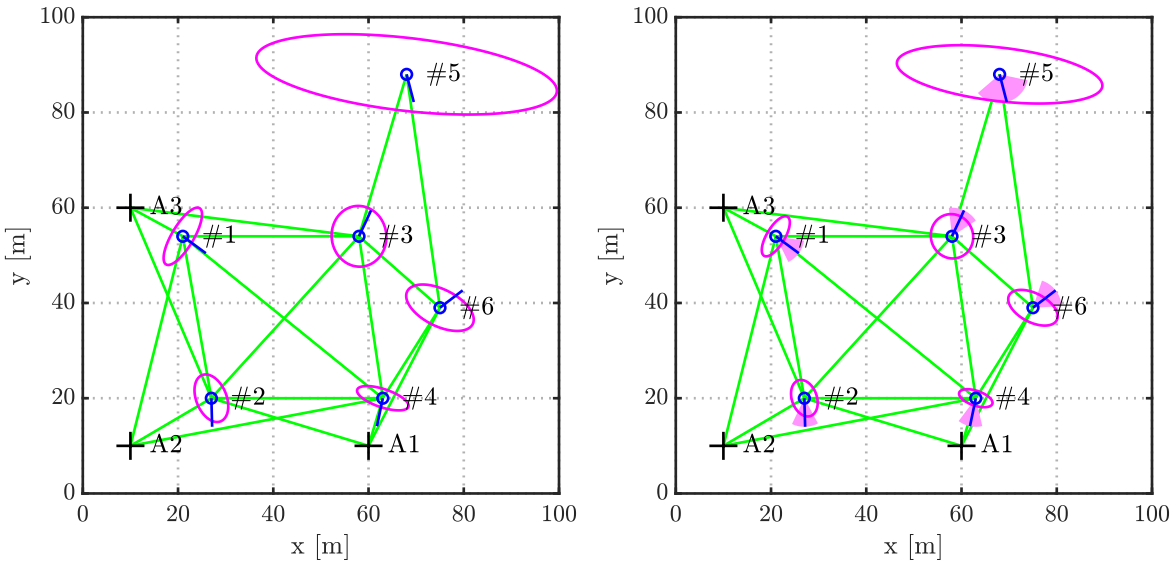

(a) *Agents with dipole antennas.* **(b)** *Agents with MMAs.*

Figure 3.2. 300σ *position and orientation error bounds for exemplary formation of six agents and three anchors.*

ror bound $\sqrt{\frac{1}{|\mathbb{R}|}\sum_{i=1}^{|\mathbb{R}|}\mathrm{CRB}(\psi_i)}$ over all agents. Fig. 3.3a shows the average position error bound and Fig. 3.3b shows the average orientation error bound, depending on the position of agent #6. The assumed maximum communication range is 50 m. The dark blue areas are favorable positions for agent #6. These areas of favorable positions are similar for position and orientation estimation. For the given formation, the interpretation is that agent #6 should move to a position where it can better aid the localization of agent #5, which has the largest position and orientation error bounds, see Fig. 3.2b. Agent #6 is plotted in red at the position where the lowest position and orientation error bound is obtained, respectively. The positions are different for position and orientation, however it should be noted that the entire dark blue area is favorable, with little performance difference within the area.

3.5 Relative Position and Orientation Error Bounds

Without anchors, although it is not possible to estimate positions and orientations w.r.t. a global coordinate system, it is still possible to estimate the relative positions and orientations of the agents. For the anchor-free case, $\mathrm{rank}\,\{\boldsymbol{I}_{\boldsymbol{x}}^{\mathrm{e}}\} = 3|\mathbb{R}| - 3$, i.e. the position and orientation EFIM is rank deficient by three. The rank deficiency corresponds to one rotational and two translational degrees of freedom [95]. Hence

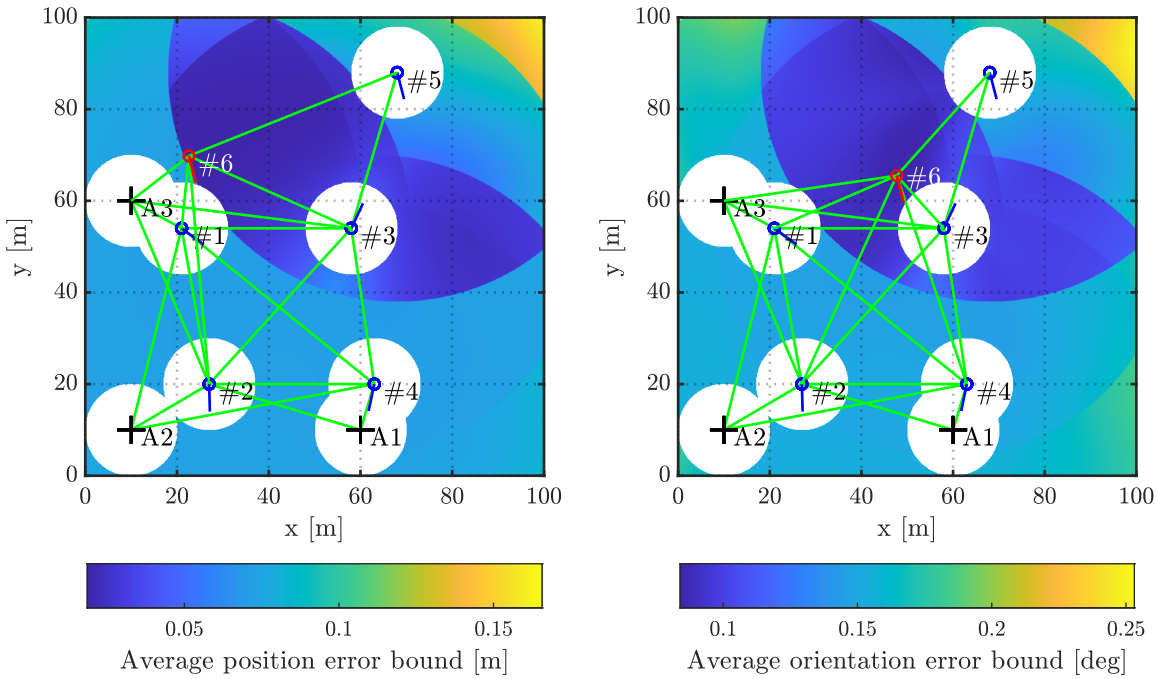

(a) *Average position error bound.* **(b)** *Average orientation error bound.*

Figure 3.3. *Average position and orientation error bounds depending on the position of agent #6 according to position error bound.*

the regular EFIM inverse does not exist. However, one can define three parametric constraints [95, 170] to obtain a constrained CRB [171]. In [95] it is shown that the constrained CRB can also be expressed with the Moore-Penrose pseudoinverse of the EFIM,

$$\mathrm{CRB}(\boldsymbol{x}) = (\boldsymbol{I}_{\boldsymbol{x}}^{\mathrm{e}})^{\dagger} \,. \tag{3.33}$$

The relative position and orientation errors bounds for the respective agents can be extracted from (3.33) by (3.30) and (3.32). The CRB (3.33) inherently assumes that an optimal coordinate system is chosen for relative position and orientation estimation [95]. Other sub-optimal choices would lead to an increase of the CRB.

Fig. 3.4 shows the relative position and orientation error bounds for relative localization without anchors. The formation is the same as in the absolute localization case shown in Fig. 3.2. For Fig. 3.4a the agents are equipped with dipole antennas, which means they cannot estimate the DoA. For Fig. 3.4b the agents are equipped with MMAs and are thus capable of DoA estimation. Similar to the absolute case, orientations can only be determined with MMAs, not with dipoles. Moreover, the position error bounds are smaller when MMAs are employed, compared to dipoles. Compared to the absolute position and orientation error bounds from Fig. 3.2, which differ largely depending on the distance to the anchors, the relative position and orientation error

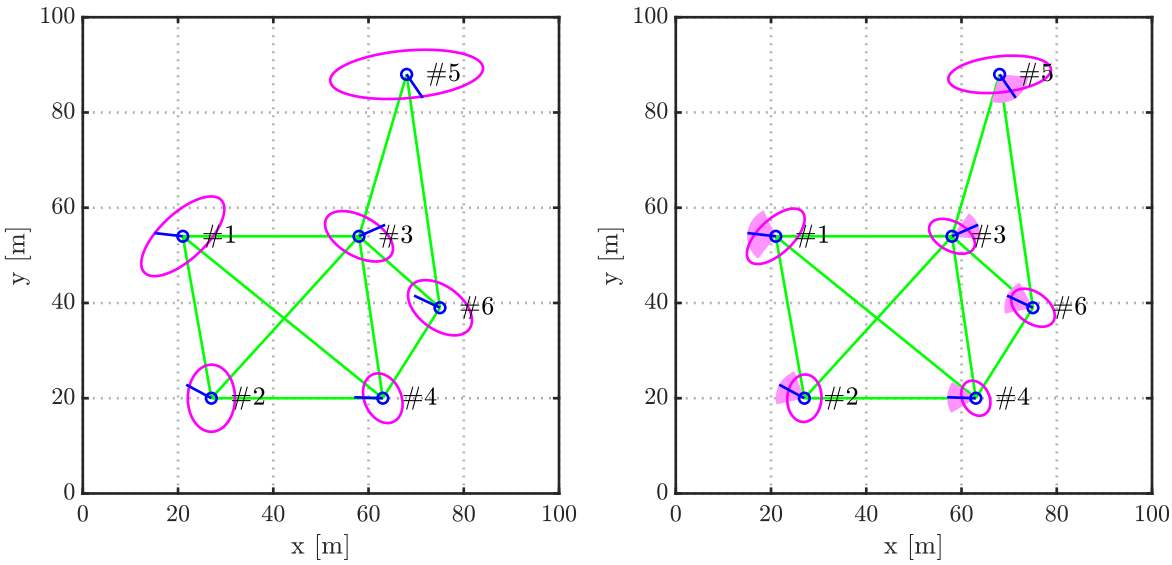

(a) *Agents with dipole antennas.* **(b)** *Agents with MMAs.*

Figure 3.4. *Relative position and orientation error bounds for exemplary formation of six agents.*

bounds in Fig. 3.4 are more uniform. However, agent #5 still has the largest error bounds due to unfavorable geometry.

With the same assumptions as in the last section, but this time without anchors, we optimize the formation of Fig. 3.4. Depending on the position of agent #6, the average position error bound is shown in Fig. 3.5a and the average orientation error bound in Fig. 3.5b. It is striking that the dark blue areas, corresponding to favorable positions of agent #6, appear to be similar as in the absolute case in Fig. 3.3. Also, the favorable areas are again similar for position and orientation estimation. As agent #5 has the largest error bounds also for relative localization, see Fig. 3.4b, it is intuitive that again agent #6 should move to a position, where it can help to improve the localization accuracy of #5. The optimum positions of agent #6 plotted in red in Fig. 3.5 are different compared to Fig. 3.3, however, performance differences within the dark blue areas are negligible. The exact position of the minimum within theses areas is thus of subordinate importance. As a further step, they could also be used to control the swarm formation to ensure accurate position and orientation estimation [14], which however is beyond the scope of this thesis.

3.6 From Theory Towards Practice

The derived position and orientation CRBs are a versatile tool to determine how favorable a certain formation is for localization, to obtain a benchmark for algorithms

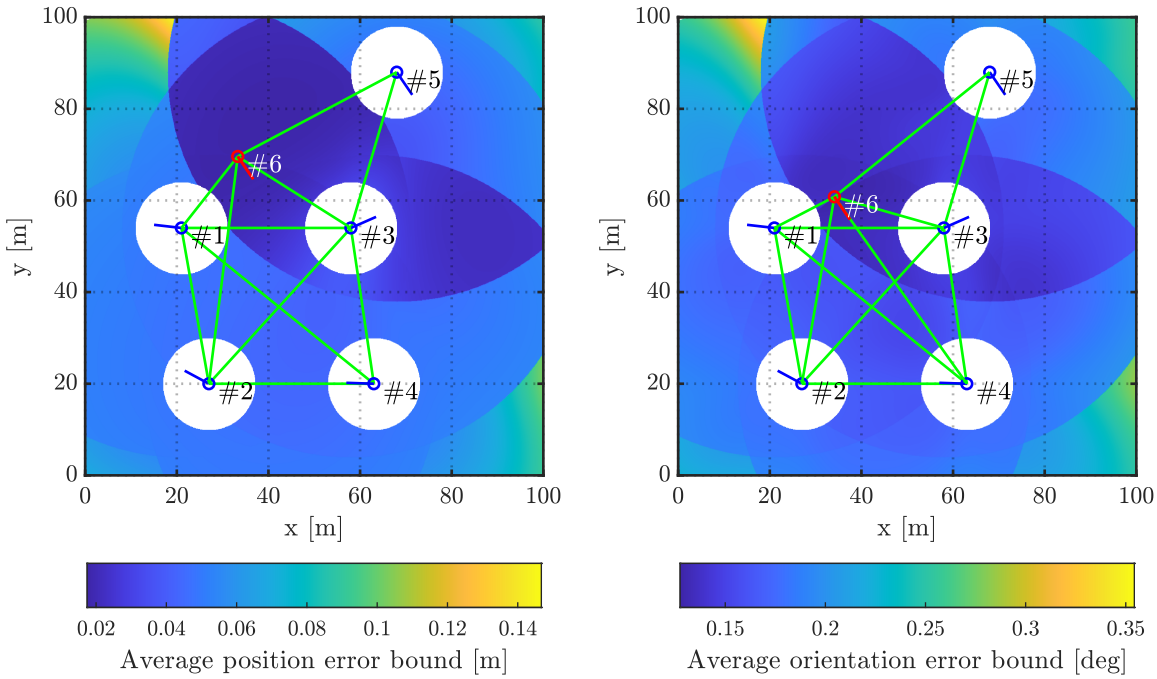

(a) *Average position error bound.* **(b)** *Average orientation error bound.*

Figure 3.5. *Average relative position and orientation error bounds depending on the position of agent #6 according to position error bound.*

and to take localization uncertainty into account for control algorithms [14]. It is important to keep in mind that the CRB is only a bound on the estimation variance [80]. However, the MSE is composed of variance and bias, and in practice often bias is the dominating factor.

For RTT ranging it has been shown that in practically relevant settings, the ranging bias is often much larger than the ranging variance due to observation noise [23, 119]. RTT ranging is sensitive to group delay variations in the transmit and receive chains, from the antenna to the digital domain. For instance due to temperature variations, transceiver internal group delay can change over time, leading to a ranging bias. Low-cost COTS hardware is especially vulnerable to group delay variations.

Similarly, the limiting factor for DoA estimation performance is usually the accuracy of the assumed antenna response, not the observation noise [50, 103, 111]. The antenna response is e.g. influenced by the surrounding structure of the antenna. When only the antenna alone is measured in a near-field measurement chamber before it is integrated into a vehicle or robot, the true antenna response can deviate from the measurement. Furthermore, the surroundings of the antenna could be changing, consider e.g. a robot with a manipulator arm to grab and carry boxes [120].

The statements from the literature are very much in line with the experiences from our own measurements, see Chapter 6, where we have also found that bias and

model mismatch are limiting the performance. Consequently, the next two chapters of this thesis are dedicated to mitigate bias and model mismatch and bring the practical performance closer to the theoretical fundamental limits. In the next Chapter 4, we investigate how the assumed antenna response can be improved by in-situ calibration. Chapter 5 is dedicated to calibrating ranging biases and antenna responses and simultaneously estimating positions and orientations by SLAC.

Chapter 4

In-Situ Antenna Calibration

In Chapters 2 and 3, we have assumed that the true sampling matrix $\boldsymbol{G}$ describing the antenna response is known, which is not realistic in practice. Instead, only an estimated sampling matrix $\hat{\boldsymbol{G}}^0$ according to (2.20) is available, which could be based on EM simulation data or antenna measurements in a measurement chamber. However, EM simulation cannot take manufacturing imperfections into account. Often, only the antenna alone is measured in a near-field measurement chamber. When the antenna is later mounted onto e.g. a robot, the antenna response changes due to the influence of the surrounding structure. Thus, in general $\hat{\boldsymbol{G}}^0$ will deviate from the true $\boldsymbol{G}$.

This chapter is dedicated to obtaining a better estimate of the sampling matrix $\hat{\boldsymbol{G}}$ by in-situ antenna calibration of an arbitrary multiport antenna, e.g. an MMA, and thus to improving the DoA estimation performance. Therefore, we define the state space and observation model and introduce a Bayesian in-situ antenna calibration algorithm. To analyze in-situ antenna calibration theoretically by Bayesian information, we derive the recursive BCRB. We discuss the qualitative behavior of the BCRB and analyze the observability. The observability analysis of in-situ antenna calibration, focusing on a single transmitter and receiver, also paves the way for SLAC in Chapter 5. Finally, we evaluate the in-situ calibration algorithm by simulation, where we consider the BCRB as benchmark.

4.1 Concept

An exemplary in-situ antenna calibration setup is shown in Fig. 4.1. A robotic rover with installed MMA is rotating on the spot, while receiving signals with snapshot index $s \in \{1, ..., S\}$ from a fixed transmitter. As the duration of the individual signal snapshots is very short and the rotation is slow, the DoAs of the impinging signals are approximately constant for one snapshot. An external sensor on the robotic rover is

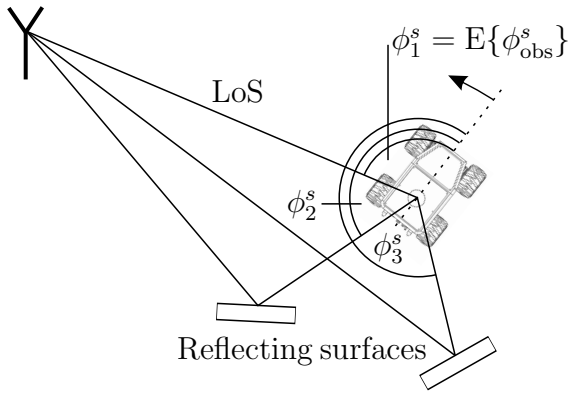

Figure 4.1. *Example in-situ antenna calibration scenario, where the LoS and two multipath signals, i.e. $P = 3$ impinging signals, arrive at the antenna to be calibrated. The robotic rover is turning on the spot.*

also part of the setup, which measures the DoA ϕ_1^s of the LoS signal from the transmitter. The general procedure is analogous to antenna calibration in a measurement chamber. The calibration is done by received signals from discrete DoAs, which span the entire manifold. However, there are three important differences to calibration in a measurement chamber. First, there is no external synchronization between transmitter and receiver by cable. Second, the environment is not an anechoic chamber. Due to multipath propagation, multiple superposed signals arrive at the MMA from different DoAs ϕ_p^s. Third, in contrast to an antenna positioner in a measurement chamber, the external sensor measuring the LoS DoA ϕ_1^s is not close to perfect. Such an external sensor could be e.g. a multi-antenna GNSS real-time kinematic (RTK), providing the orientation of the robotic rover. Together with the transmitter and rover positions, the LoS DoA ϕ_1^s can be calculated. Thus, instead of the true LoS DoA ϕ_1^s, only the noisy observable DoA ϕ_{obs}^s is available.

4.2 State Definition

In Chapters 4 and 5 of this thesis, we interpret the sampling matrix $\boldsymbol{G}$ as a random variable in a Bayesian framework, which allows to consider the sampling matrix from EM simulation or near-field measurement $\hat{\boldsymbol{G}}^0$, see (2.20), as prior sampling matrix. The goal of in-situ calibration is to obtain a better estimate $\hat{\boldsymbol{G}}$, thus a better estimate of the antenna response

$$\hat{\boldsymbol{a}}(\phi) = \hat{\boldsymbol{G}}\boldsymbol{b}(\phi). \tag{4.1}$$

For notational convenience, we vectorize the sampling matrix

$$\boldsymbol{g} = \mathrm{vec}\,\{\boldsymbol{G}\} \tag{4.2}$$

and split it into real and imaginary parts,

$$\boldsymbol{g}_{\mathrm{RI}} = \begin{bmatrix} \boldsymbol{g}_{\mathrm{R}} \\ \boldsymbol{g}_{\mathrm{I}} \end{bmatrix} = \begin{bmatrix} \mathrm{Re}\left\{\boldsymbol{g}\right\} \\ \mathrm{Im}\left\{\boldsymbol{g}\right\} \end{bmatrix}. \tag{4.3}$$

In the following, we use $\boldsymbol{G}$, $\boldsymbol{g}$ or $\boldsymbol{g}_{\mathrm{RI}}$ depending on the context. The vectorized versions of the estimated sampling matrix $\hat{\boldsymbol{G}}$ and the prior sampling matrix $\hat{\boldsymbol{G}}^0$ are defined analogously. The prior probability density function (pdf) in logarithm domain is then defined as

$$\ln p(\boldsymbol{g}^0) = -MU \ln(\pi \sigma_{\boldsymbol{g}^0}^2) - \frac{1}{\sigma_{\boldsymbol{g}^0}^2} \left\| \boldsymbol{g}^0 - \hat{\boldsymbol{g}}^0 \right\|^2, \tag{4.4}$$

which is a circular symmetric Gaussian distribution with mean $\hat{\boldsymbol{g}}^0 = \mathrm{E}\left\{\boldsymbol{g}^0\right\}$ and variance $\sigma_{\boldsymbol{g}^0}^2 = \frac{1}{MU} \operatorname{tr}\left\{\mathrm{E}\left\{(\boldsymbol{g}^0 - \hat{\boldsymbol{g}}^0)(\boldsymbol{g}^0 - \hat{\boldsymbol{g}}^0)^H\right\}\right\}$. Empirically, we have found that (4.4) is a feasible model to describe antenna response deviations, see also Section 4.8.1. Including the DoAs of the P impinging signals

$$\boldsymbol{\phi}^s = \begin{bmatrix} \phi_1^s & \dots & \phi_P^s \end{bmatrix}^T, \tag{4.5}$$

the state vector for snapshot s, which contains the parameters to be estimated, is defined as

$$\boldsymbol{x}^s = \begin{bmatrix} \boldsymbol{g}_{\mathrm{RI}} \\ \boldsymbol{\phi}^s \end{bmatrix} \in \mathbb{R}^{(MU+P)\times 1}, \tag{4.6}$$

and the state vector for all snapshots $s \in \{1, ..., S\}$ is

$$\boldsymbol{x}^{1:S} = \begin{bmatrix} \boldsymbol{g}_{\mathrm{RI}} \\ \boldsymbol{\phi}^{1:S} \end{bmatrix} \in \mathbb{R}^{(MU+PS)\times 1} \tag{4.7}$$

with

$$\boldsymbol{\phi}^{1:S} = \begin{bmatrix} (\boldsymbol{\phi}^1)^T & \dots & (\boldsymbol{\phi}^S)^T \end{bmatrix}^T. \tag{4.8}$$

4.3 Observation Model

At time instances $t = sT$, the transmitter sends out signal bursts, which are referred to as snapshots with index $s \in \{1, ..., S\}$ and interval T. Based on the signal model (2.8), the received signals are described in discrete frequency domain by

$$\boldsymbol{r}^s(n) = \sum_{p=1}^{P} \boldsymbol{a}(\phi_p^s) s(n, \tau_p^s) \alpha_p^s e^{\mathrm{j}\varphi_p^s} + \boldsymbol{w}^s(n), \tag{4.9}$$

where n is the subcarrier index and $N = |\mathbb{N}_{\text{sc}}|$ is number of occupied subcarriers. For convenience, we define the vector

$$\boldsymbol{r}^s = \begin{bmatrix} ... & (\boldsymbol{r}^s(n))^T & ... \end{bmatrix}^T, n \in \mathbb{N}_{\text{sc}}. \tag{4.10}$$

The log-likelihood function for the received signals,

$$L_{\boldsymbol{r}^s}(\boldsymbol{\phi}^s, \boldsymbol{\tau}^s, \boldsymbol{\alpha}^s, \boldsymbol{\varphi}^s, \sigma^2_{\boldsymbol{r}}, \boldsymbol{g}) = -N \ln(\pi\sigma^2_{\boldsymbol{r}}) - \frac{1}{\sigma^2_{\boldsymbol{r}}} \sum_{n \in \mathbb{N}_{\text{sc}}} \left\| \boldsymbol{r}^s(n) - \sum_{p=1}^{P} \boldsymbol{a}(\phi^s_p) s(n, \tau^s_p) \alpha^s_p e^{\mathrm{j}\varphi^s_p} \right\|^2, \tag{4.11}$$

is then defined according to (2.62). The concentrated log-likelihood function of the DoAs $\boldsymbol{\phi}$ and the sampling matrix elements $\boldsymbol{g}$ is

$$\tilde{L}_{\boldsymbol{r}^s}(\boldsymbol{\phi}^s, \boldsymbol{g}) = \frac{1}{\sigma^2_{\boldsymbol{r}}} \left\| \boldsymbol{V}^{\perp} \boldsymbol{r}^s \right\|^2 \tag{4.12}$$

according to (2.64), with $\boldsymbol{V}^{\perp}$ defined by (2.65) and (2.66). In order to focus on the antenna calibration aspect, in this chapter we assume that the ToAs $\boldsymbol{\tau}^s = [\tau^s_1, ..., \tau^s_P]^T$ are known or estimated separately. For medium to high SNR values, ToA and DoA can be estimated independently, see Sections 2.5.2 and 3.2, which justifies the assumption. For the scope of this thesis, we also assume that the model order P is known. In practice, it can be estimated [58, 59, 60].

As explained in Section 4.1, we assume that the DoA of the first impinging signal ($p = 1$) can be observed by an external sensor. The noisy observable DoA is given by

$$\phi^s_{\text{obs}} = \phi^s_1 + w^s_{\phi_{\text{obs}}}, \tag{4.13}$$

which is the true DoA ϕ^s_1 with additive errors following a von Mises distribution $w^s_{\phi_{\text{obs}}} \sim \mathcal{M}(0, \kappa_{\phi_{\text{obs}}})$ with concentration $\kappa_{\phi_{\text{obs}}}$ [172]. The concentration $\kappa_{\phi_{\text{obs}}}$ is expected to be high, so the von Mises distribution can be approximated by a Gaussian distribution $w^s_{\phi_{\text{obs}}} \sim \mathcal{N}(0, \sigma^2_{\phi_{\text{obs}}} = 1/\kappa_{\text{obs}})$, see [172]. The log-likelihood function of the observed DoA is then defined as

$$L_{\phi^s_{\text{obs}}}(\phi^s_1) = \ln p(\phi^s_{\text{obs}} | \phi^s_1) = -\frac{1}{2} \ln(2\pi\sigma^2_{\phi_{\text{obs}}}) - \frac{1}{2\sigma^2_{\phi_{\text{obs}}}} (\phi^s_{\text{obs}} - \phi^s_1)^2. \tag{4.14}$$

Putting together (4.10) and (4.13), the observation vector for snapshot s is

$$\boldsymbol{z}^s = \begin{bmatrix} \boldsymbol{r}^s \\ \phi^s_{\text{obs}} \end{bmatrix} \in \mathbb{C}^{(MN+1)\times 1}. \tag{4.15}$$

Algorithm 1 In-Situ Antenna Calibration

1: Given $\hat{\boldsymbol{g}}_{\mathrm{RI}}^{0}$, $\boldsymbol{r}^{s}$ and $\phi_{\mathrm{obs}}^{s}\ \forall\, s \in \{1, ..., S\}$
2: Initialize with prior $\hat{\boldsymbol{g}}_{\mathrm{RI}}^{1} = \hat{\boldsymbol{g}}_{\mathrm{RI}}^{0}$
3: Initialize DoAs $\hat{\boldsymbol{\phi}}^{1}$ with ML estimator (2.39)
4: **for** $s = 2$ to S **do**
5: Solve (4.19) for $\hat{\boldsymbol{x}}_{\mathrm{MAP}}^{1:s}$ by BFGS initialized with

$$\boldsymbol{x}_{\mathrm{init}}^{0:s} = \begin{bmatrix} \hat{\boldsymbol{g}}_{\mathrm{RI}}^{(s-1)} \\ \hat{\boldsymbol{\phi}}^{1:(s-1)} \\ \hat{\boldsymbol{\phi}}^{(s-1)} + \mathbf{1}_{P}\left(\phi_{\mathrm{obs}}^{s} - \phi_{\mathrm{obs}}^{(s-1)}\right) \end{bmatrix}$$

using gradient (4.20)
6: **end for**

4.4 In-Situ Antenna Calibration Algorithm

The posterior pdf is given by

$$\begin{aligned} p(\boldsymbol{x}^{0:S}|\boldsymbol{z}^{1:S}) &= \frac{p(\boldsymbol{z}^{1:S}|\boldsymbol{x}^{0:S})p(\boldsymbol{x}^{0:S})}{p(\boldsymbol{z}^{1:S})} \\ &\propto p(\boldsymbol{x}^{0}) \prod_{s=1}^{S} p(\boldsymbol{z}^{s}|\boldsymbol{x}^{s})\, p(\boldsymbol{x}^{s}|\boldsymbol{x}^{(s-1)}), \end{aligned} \tag{4.16}$$

where we have used Bayes theorem and the first order Markov assumption. We assume a stationary sampling matrix, non-informative transition and prior pdfs for $\boldsymbol{\phi}^{s}$, and independent noise for the received signal (4.9) and the observable DoA (4.13). Inserting (4.6) and (4.15) into (4.16) yields

$$\begin{aligned} p(\boldsymbol{x}^{0:S}|\boldsymbol{z}^{1:S}) &\propto p(\boldsymbol{g}^{0}) \prod_{s=1}^{S} p(\boldsymbol{r}^{s}, \phi_{\mathrm{obs}}^{s}|\boldsymbol{\phi}^{s}, \boldsymbol{g}) \\ &= p(\boldsymbol{g}^{0}) \prod_{s=1}^{S} p(\boldsymbol{r}^{s}|\boldsymbol{\phi}^{s}, \boldsymbol{g})\, p(\phi_{\mathrm{obs}}^{s}|\phi_{1}^{s}). \end{aligned} \tag{4.17}$$

Defining

$$q(\boldsymbol{x}^{0:S}) := -\ln p(\boldsymbol{g}^{0}) - \sum_{s=1}^{S} \tilde{L}_{\boldsymbol{r}^{s}}(\boldsymbol{\phi}^{s}, \boldsymbol{g}) - \sum_{s=1}^{S} L_{\phi_{\mathrm{obs}}^{s}}(\phi_{1}^{s}), \tag{4.18}$$

which is proportional to the negative posterior pdf in logarithm domain, the maximum a posteriori (MAP) estimator is given by

$$\hat{\boldsymbol{x}}_{\mathrm{MAP}}^{1:S} = \arg\max_{\boldsymbol{x}^{0:S}} p(\boldsymbol{x}^{0:S}|\boldsymbol{z}^{1:S}) = \arg\min_{\boldsymbol{x}^{0:S}} q(\boldsymbol{x}^{0:S}). \tag{4.19}$$

Solving (4.19) is a challenging nonlinear optimization problem with $2MU + PS$ un-

knowns. For example, with the assumed parameters from the simulation results in Section 4.8, this would be 1052 unknowns for $P = 1$ impinging signal and 3052 unknowns for $P = 3$ impinging signals. We use the Broyden–Fletcher–Goldfarb–Shanno (BFGS) algorithm, which is a quasi-Newton method to solve unconstrained nonlinear optimization problems [173]. BFGS requires an analytical expression of the gradient. In our case, the gradient of (4.18) has the structure

$$\nabla q(\boldsymbol{x}^{0:S}) = \begin{bmatrix} \frac{\partial q(\boldsymbol{x}^{0:S})}{\partial \boldsymbol{g}_{\mathrm{R}}} \\ \frac{\partial q(\boldsymbol{x}^{0:S})}{\partial \boldsymbol{g}_{\mathrm{I}}} \\ \frac{\partial q(\boldsymbol{x}^{0:S})}{\partial \boldsymbol{\phi}^{1}} \\ \vdots \\ \frac{\partial q(\boldsymbol{x}^{0:S})}{\partial \boldsymbol{\phi}^{S}} \end{bmatrix} . \tag{4.20}$$

The partial derivatives contained in (4.20) are derived in Appendix C.9. Global convergence of BFGS has been proven for convex functions [173]. Problem (4.19) is nonconvex, hence we must ensure an initialization close to the global solution, so that local convergence is sufficient. To ensure sufficiently close initialization, we propose Algorithm 1. For each snapshot $s \in \{1, ..., S\}$, we apply the BFGS algorithm to obtain

$$\hat{\boldsymbol{x}}_{\mathrm{MAP}}^{1:s} = \begin{bmatrix} \hat{\boldsymbol{g}}^{s} \\ \hat{\boldsymbol{\phi}}^{1:s} \end{bmatrix} . \tag{4.21}$$

Hereby, the result of the previous step is used to initialize the current step, see Algorithm 1. By gradually adding more snapshots, the convergence is improved. The simulation results shown in Section 4.8 demonstrate the convergence of Algorithm 1. As a benchmark for the proposed algorithm, in the next two sections we derive the BCRB as a lower bound on the achievable estimation MSE.

4.5 Information from Observations

The parameters of interest are defined by the state vector (4.6). We also need to consider the nuisance parameters absolute amplitude $\boldsymbol{\alpha}^s = [\alpha_1^s, ..., \alpha_P^s]^T$ and absolute phase $\boldsymbol{\varphi}^s = [\varphi_1^s, ..., \varphi_P^s]^T$ for P impinging signals, see (4.9). Thus, we augment the state vector (4.6) to

$$\tilde{\boldsymbol{x}}^s = \begin{bmatrix} \boldsymbol{x}^s \\ \boldsymbol{\alpha}^s \\ \boldsymbol{\varphi}^s \end{bmatrix} . \tag{4.22}$$

For the calculation of the recursive BCRB in Section 4.6 according to [81], we need the information that is contained in the single-snapshot observation vector $\boldsymbol{z}^s$,

$$\begin{aligned}\left[\tilde{\boldsymbol{I}}^s\right]_{v,w} &:= \mathrm{E}_{\tilde{\boldsymbol{x}}^s}\left\{\mathrm{E}_{\boldsymbol{z}^s|\tilde{\boldsymbol{x}}^s}\left\{\frac{\partial \ln p(\boldsymbol{z}^s|\tilde{\boldsymbol{x}}^s)}{\partial[\tilde{\boldsymbol{x}}^s]_v}\frac{\partial \ln p(\boldsymbol{z}^s|\tilde{\boldsymbol{x}}^s)}{\partial[\tilde{\boldsymbol{x}}^s]_w}\right\}\right\} \\ &= \mathrm{E}_{\tilde{\boldsymbol{x}}^s}\left\{[\boldsymbol{I}^s]_{v,w}\right\},\end{aligned} \tag{4.23}$$

which is the expectation of the snapshot FIM $\boldsymbol{I}^s$ w.r.t. the augmented state vector $\tilde{\boldsymbol{x}}^s$. According to [80], the snapshot FIM is given by

$$[\boldsymbol{I}^s]_{v,w} = 2\,\mathrm{Re}\left\{\frac{\partial\,\mathrm{E}_{\boldsymbol{z}^s|\tilde{\boldsymbol{x}}^s}\{\boldsymbol{z}^s\}^H}{\partial[\tilde{\boldsymbol{x}}^s]_v}\boldsymbol{\Sigma}_{\boldsymbol{z}}^{-1}\frac{\partial\,\mathrm{E}_{\boldsymbol{z}^s|\tilde{\boldsymbol{x}}^s}\{\boldsymbol{z}^s\}}{\partial[\tilde{\boldsymbol{x}}^s]_w}\right\} \tag{4.24}$$

with the covariance matrix

$$\boldsymbol{\Sigma}_{\boldsymbol{z}} = \mathrm{diag}\left\{\left[\sigma_{\boldsymbol{r}}^2\mathbf{1}_{MN}^T,\, 2\sigma_{\phi_{\mathrm{obs}}}^2\right]^T\right\}. \tag{4.25}$$

Inserting (4.15), we obtain

$$\begin{aligned}[\boldsymbol{I}^s]_{v,w} =& \frac{2}{\sigma_{\boldsymbol{r}}^2}\,\mathrm{Re}\left\{\sum_{n\in\mathbb{N}_{\mathrm{sc}}}\frac{\partial\,\mathrm{E}_{\boldsymbol{r}^s(n)|\tilde{\boldsymbol{x}}^s}\{\boldsymbol{r}^s(n)\}^H}{\partial[\tilde{\boldsymbol{x}}^s]_v}\frac{\partial\,\mathrm{E}_{\boldsymbol{r}^s(n)|\tilde{\boldsymbol{x}}^s}\{\boldsymbol{r}^s(n)\}}{\partial[\tilde{\boldsymbol{x}}^s]_w}\right\} \\ &+ \frac{1}{\sigma_{\phi_{\mathrm{obs}}}^2}\,\mathrm{Re}\left\{\frac{\partial\,\mathrm{E}_{\phi_{\mathrm{obs}}^s|\tilde{\boldsymbol{x}}^s}\{\phi_{\mathrm{obs}}^s\}^H}{\partial[\tilde{\boldsymbol{x}}^s]_v}\frac{\partial\,\mathrm{E}_{\phi_{\mathrm{obs}}^s|\tilde{\boldsymbol{x}}^s}\{\phi_{\mathrm{obs}}^s\}}{\partial[\tilde{\boldsymbol{x}}^s]_w}\right\}.\end{aligned} \tag{4.26}$$

We partition $\tilde{\boldsymbol{I}}^s$ from (4.23) into

$$\tilde{\boldsymbol{I}}^s = \begin{bmatrix}\tilde{\boldsymbol{I}}_{\boldsymbol{g}}^s & \tilde{\boldsymbol{I}}_{\boldsymbol{g}\boldsymbol{\phi}}^s & \tilde{\boldsymbol{I}}_{\boldsymbol{g}\mathrm{n}}^s \\ (\tilde{\boldsymbol{I}}_{\boldsymbol{g}\boldsymbol{\phi}}^s)^T & \tilde{\boldsymbol{I}}_{\boldsymbol{\phi}}^s & \tilde{\boldsymbol{I}}_{\boldsymbol{\phi}\mathrm{n}}^s \\ (\tilde{\boldsymbol{I}}_{\boldsymbol{g}\mathrm{n}}^s)^T & (\tilde{\boldsymbol{I}}_{\boldsymbol{\phi}\mathrm{n}}^s)^T & \tilde{\boldsymbol{I}}_{\mathrm{n}}^s\end{bmatrix} = \mathrm{E}_{\tilde{\boldsymbol{x}}}\left\{\begin{bmatrix}\boldsymbol{I}_{\boldsymbol{g}}^s & \boldsymbol{I}_{\boldsymbol{g}\boldsymbol{\phi}}^s & \boldsymbol{I}_{\boldsymbol{g}\mathrm{n}}^s \\ (\boldsymbol{I}_{\boldsymbol{g}\boldsymbol{\phi}}^s)^T & \boldsymbol{I}_{\boldsymbol{\phi}}^s & \boldsymbol{I}_{\boldsymbol{\phi}\mathrm{n}}^s \\ (\boldsymbol{I}_{\boldsymbol{g}\mathrm{n}}^s)^T & (\boldsymbol{I}_{\boldsymbol{\phi}\mathrm{n}}^s)^T & \boldsymbol{I}_{\mathrm{n}}^s\end{bmatrix}\right\}. \tag{4.27}$$

The first main diagonal matrix block corresponds to the sampling matrix elements

$$\boldsymbol{I}_{\boldsymbol{g}}^s = \begin{bmatrix}\boldsymbol{I}_{\boldsymbol{g}_{\mathrm{R}}}^s & \boldsymbol{I}_{\boldsymbol{g}_{\mathrm{R}}\boldsymbol{g}_{\mathrm{I}}}^s \\ (\boldsymbol{I}_{\boldsymbol{g}_{\mathrm{R}}\boldsymbol{g}_{\mathrm{I}}}^s)^T & \boldsymbol{I}_{\boldsymbol{g}_{\mathrm{I}}}^s\end{bmatrix}, \tag{4.28}$$

which are split into real part $\boldsymbol{I}_{\boldsymbol{g}_{\mathrm{R}}}^s$ and imaginary part $\boldsymbol{I}_{\boldsymbol{g}_{\mathrm{I}}}^s$. The second main diagonal matrix block $\boldsymbol{I}_{\boldsymbol{\phi}}^s$ refers to the DoAs. The third main diagonal matrix block

$$\boldsymbol{I}_{\mathrm{n}}^s = \begin{bmatrix}\boldsymbol{I}_{\boldsymbol{\alpha}}^s & \boldsymbol{I}_{\boldsymbol{\alpha}\boldsymbol{\varphi}}^s \\ (\boldsymbol{I}_{\boldsymbol{\alpha}\boldsymbol{\varphi}}^s)^T & \boldsymbol{I}_{\boldsymbol{\varphi}}^s\end{bmatrix} \tag{4.29}$$

corresponds to the nuisance parameters, which are split into real-valued absolute amplitudes $\boldsymbol{I}^s_{\boldsymbol{\alpha}}$ and phases $\boldsymbol{I}^s_{\boldsymbol{\varphi}}$. The off-diagonal matrix blocks

$$\boldsymbol{I}^s_{\boldsymbol{g}\boldsymbol{\phi}} = \begin{bmatrix} \boldsymbol{I}^s_{\boldsymbol{g}_{\mathrm{R}}\boldsymbol{\phi}} \\ \boldsymbol{I}^s_{\boldsymbol{g}_{\mathrm{I}}\boldsymbol{\phi}} \end{bmatrix}, \tag{4.30}$$

$$\boldsymbol{I}^s_{\boldsymbol{g}\mathrm{n}} = \begin{bmatrix} \boldsymbol{I}^s_{\boldsymbol{g}_{\mathrm{R}}\boldsymbol{\alpha}} & \boldsymbol{I}^s_{\boldsymbol{g}_{\mathrm{R}}\boldsymbol{\varphi}} \\ \boldsymbol{I}^s_{\boldsymbol{g}_{\mathrm{I}}\boldsymbol{\alpha}} & \boldsymbol{I}^s_{\boldsymbol{g}_{\mathrm{I}}\boldsymbol{\varphi}} \end{bmatrix}, \tag{4.31}$$

$$\boldsymbol{I}^s_{\boldsymbol{\phi}\mathrm{n}} = \begin{bmatrix} \boldsymbol{I}^s_{\boldsymbol{\phi}\boldsymbol{\alpha}} & \boldsymbol{I}^s_{\boldsymbol{\phi}\boldsymbol{\varphi}} \end{bmatrix}, \tag{4.32}$$

refer to the relationship between sampling matrix and DoAs $\boldsymbol{I}^s_{\boldsymbol{g}\boldsymbol{\phi}}$, the relationship between sampling matrix and nuisance parameters $\boldsymbol{I}^s_{\boldsymbol{g}\mathrm{n}}$ and the relationship between sampling DoAs and nuisance parameters $\boldsymbol{I}^s_{\boldsymbol{\phi}\mathrm{n}}$, respectively. The elements of (4.28) to (4.32) are derived in Appendix C.10.

4.6 Recursive Bayesian Cramér-Rao Bound

For the derivation of the recursive BCRB, we distinguish the two cases where the propagation channel described by the absolute amplitudes $\boldsymbol{\alpha}^s$ and absolute phases $\boldsymbol{\varphi}^s$ of all impinging signals is known and unknown. The conceptually simpler case where $\boldsymbol{\alpha}^s$ and $\boldsymbol{\varphi}^s$ are known is treated in Section 4.6.1 and the case where $\boldsymbol{\alpha}^s$ and $\boldsymbol{\varphi}^s$ are unknown in Section 4.6.2.

4.6.1 Known Propagation Channel

Applying the Schur complement [81] to the snapshot information matrix $\tilde{\boldsymbol{I}}^s$ defined by (4.24), we derive the equivalent Bayesian information matrix (EBIM) for the sampling matrix elements

$$\boldsymbol{J}^s_{\boldsymbol{g},\mathrm{sync}} = \boldsymbol{J}^{(s-1)}_{\boldsymbol{g},\mathrm{sync}} + \tilde{\boldsymbol{I}}^s_{\boldsymbol{g}} - \tilde{\boldsymbol{I}}^s_{\boldsymbol{g}\boldsymbol{\phi}} \left(\tilde{\boldsymbol{I}}^s_{\boldsymbol{\phi}}\right)^{-1} (\tilde{\boldsymbol{I}}^s_{\boldsymbol{g}\boldsymbol{\phi}})^T \tag{4.33}$$

with subscript $_{\mathrm{sync}}$ to indicate perfect propagation channel knowledge. The sampling matrix EBIM quantifies the Bayesian information for the sampling matrix elements, while considering the impact the unknown DoAs. Equation (4.33) is calculated recursively, by adding up the information contained in individual snapshots, starting with $\boldsymbol{J}^0_{\boldsymbol{g},\mathrm{sync}}$. With prior, $\boldsymbol{J}^0_{\boldsymbol{g},\mathrm{sync}} = \frac{2}{\sigma^2_{\boldsymbol{g}^0}}\mathbb{I}_{2MU}$ is a diagonal matrix according to the prior pdf (4.4). Without prior, $\boldsymbol{J}^0_{\boldsymbol{g},\mathrm{sync}} = \mathbb{0}_{2MU}$ is a zero matrix. Defining the MSE of the sampling matrix elements as the trace of the MSE matrix divided by the number of

complex coefficients MU,

$$\mathrm{MSE}\left\{\hat{\boldsymbol{g}}^s\right\} = \frac{1}{MU}\,\mathrm{tr}\left\{\mathrm{E}_{\boldsymbol{z},\tilde{\boldsymbol{x}}}\left\{(\hat{\boldsymbol{g}}^s - \boldsymbol{g})(\hat{\boldsymbol{g}}^s - \boldsymbol{g})^H\right\}\right\}, \tag{4.34}$$

we can now state the BCRB as a lower bound on the estimation MSE of the sampling matrix elements for the known propagation channel case,

$$\mathrm{MSE}\left\{\hat{\boldsymbol{g}}^s\right\} \geq \mathrm{BCRB}_{\mathrm{sync}}(\boldsymbol{g}) \coloneqq \frac{1}{MU}\,\mathrm{tr}\left\{\left(\boldsymbol{J}^s_{\boldsymbol{g},\mathrm{sync}}\right)^{-1}\right\}. \tag{4.35}$$

Again applying the Schur complement, we obtain the EBIM for the DoAs

$$\boldsymbol{J}^s_{\boldsymbol{\phi},\mathrm{sync}} = \tilde{\boldsymbol{I}}^s_{\boldsymbol{\phi}} - (\tilde{\boldsymbol{I}}^s_{\boldsymbol{g}\boldsymbol{\phi}})^T \left(\boldsymbol{J}^{(s-1)}_{\boldsymbol{g},\mathrm{sync}} + \tilde{\boldsymbol{I}}^s_{\boldsymbol{g}}\right)^{-1} \tilde{\boldsymbol{I}}^s_{\boldsymbol{g}\boldsymbol{\phi}} \tag{4.36}$$

and the BCRB as a lower bound on the estimation MSE of the p-th DoA for the known propagation channel case,

$$\mathrm{MSE}\left\{\hat{\phi}^s_p\right\} \geq \mathrm{BCRB}_{\mathrm{sync}}(\phi^s_p) \coloneqq \left[(\boldsymbol{J}^s_{\boldsymbol{\phi},\mathrm{sync}})^{-1}\right]_{p,p}. \tag{4.37}$$

4.6.2 Unknown Propagation Channel

Now, we derive the recursive BCRB for the case where absolute amplitudes $\boldsymbol{\alpha}^s$ and phases $\boldsymbol{\varphi}^s$ of the impinging signals are unknown. Again applying the Schur complement, but now for both, DoAs $\boldsymbol{\phi}^s$ and nuisance parameters $\boldsymbol{\alpha}^s$ and $\boldsymbol{\varphi}^s$, we obtain the EBIM for the sampling matrix elements

$$\boldsymbol{J}^s_{\boldsymbol{g}} = \boldsymbol{J}^{(s-1)}_{\boldsymbol{g}} + \tilde{\boldsymbol{I}}^s_{\boldsymbol{g}} - \begin{bmatrix}\tilde{\boldsymbol{I}}^s_{\boldsymbol{g}\boldsymbol{\phi}} & \tilde{\boldsymbol{I}}^s_{\boldsymbol{g}\mathrm{n}}\end{bmatrix} \begin{bmatrix}\tilde{\boldsymbol{I}}^s_{\boldsymbol{\phi}} & \tilde{\boldsymbol{I}}^s_{\boldsymbol{\phi}\mathrm{n}} \\ (\tilde{\boldsymbol{I}}^s_{\boldsymbol{\phi}\mathrm{n}})^T & \tilde{\boldsymbol{I}}^s_{\mathrm{n}}\end{bmatrix}^{-1} \begin{bmatrix}(\tilde{\boldsymbol{I}}^s_{\boldsymbol{g}\boldsymbol{\phi}})^T \\ (\tilde{\boldsymbol{I}}^s_{\boldsymbol{g}\mathrm{n}})^T\end{bmatrix}. \tag{4.38}$$

The rank of $\boldsymbol{J}^s_{\boldsymbol{g}}$ depends on whether a prior sampling matrix is considered or not, so these two cases are distinguished.

With Prior

Considering the prior pdf (4.4), we have $\boldsymbol{J}^0_{\boldsymbol{g}} = \frac{2}{\sigma^2_{\boldsymbol{g}^0}}\mathbb{I}_{2MU}$. Since $\boldsymbol{J}^0_{\boldsymbol{g}}$ is positive definite, and by (4.38) we recursively add the Schur complement of the expectation of the FIM, which is positive semidefinite, the sampling matrix EBIM $\boldsymbol{J}^s_{\boldsymbol{g}}$ is positive definite with full rank. Thus, we can obtain the BCRB of the sampling matrix elements by the inverse of the EBIM,

$$\mathrm{MSE}\left\{\hat{\boldsymbol{g}}^s\right\} \geq \mathrm{BCRB}(\boldsymbol{g}) \coloneqq \frac{1}{MU}\,\mathrm{tr}\left\{(\boldsymbol{J}^s_{\boldsymbol{g}})^{-1}\right\}. \tag{4.39}$$

The MSE matrix $\mathrm{MSE}\{\hat{\boldsymbol{g}}^s\}$ is again defined by (4.34). Since $\boldsymbol{J}_{\boldsymbol{g}}^s$ has full rank, we can apply the Schur complement to obtain the EBIM for the DoAs

$$\boldsymbol{J}_{\boldsymbol{\phi}}^s = \tilde{\boldsymbol{I}}_{\boldsymbol{\phi}}^s - \begin{bmatrix} (\tilde{\boldsymbol{I}}_{\boldsymbol{g}\boldsymbol{\phi}}^s)^T & \tilde{\boldsymbol{I}}_{\boldsymbol{\phi}\mathrm{n}}^s \end{bmatrix} \begin{bmatrix} \boldsymbol{J}_{\boldsymbol{g}}^{(s-1)} + \tilde{\boldsymbol{I}}_{\boldsymbol{g}}^s & \tilde{\boldsymbol{I}}_{\boldsymbol{g}\mathrm{n}}^s \\ (\tilde{\boldsymbol{I}}_{\boldsymbol{g}\mathrm{n}}^s)^T & \tilde{\boldsymbol{I}}_{\mathrm{n}}^s \end{bmatrix}^{-1} \begin{bmatrix} \tilde{\boldsymbol{I}}_{\boldsymbol{g}\boldsymbol{\phi}}^s \\ (\tilde{\boldsymbol{I}}_{\boldsymbol{\phi}\mathrm{n}}^s)^T \end{bmatrix}, \tag{4.40}$$

and the BCRB as a lower bound on the estimation MSE of the p-th DoA,

$$\mathrm{MSE}\left\{\hat{\phi}_p^s\right\} \geq \mathrm{BCRB}(\phi_p^s) := \left[(\boldsymbol{J}_{\boldsymbol{\phi}}^s)^{-1}\right]_{p,p}. \tag{4.41}$$

Without Prior

When no prior is considered, $\boldsymbol{J}_{\boldsymbol{g}}^0 = \mathbb{0}_{2MU}$. Calculating (4.38) recursively, one can observe that

$$\lim_{s\to\infty} \mathrm{rank}\left\{\boldsymbol{J}_{\boldsymbol{g}}^s\right\} = 2MU - 2, \tag{4.42}$$

which is also discussed at the beginning of Section 4.7. As the absolute amplitude and phase of the antenna are not observable, $\boldsymbol{J}_{\boldsymbol{g}}^s$ will be rank deficient by two in the limit. The absolute amplitude and phase do not contain DoA information, which is only contained in the relative amplitudes and phases of the antenna ports, see the proof in Appendix C.8. Thus, the non-observability of absolute amplitude and phase is not problematic for DoA estimation. However, a consequence is that by in-situ calibration, we do not estimate the true antenna response, but an antenna response which is equivalent for DoA estimation. This implies that the power pattern of the equivalent antenna response does not necessarily reflect the antenna gain. Still, the non-observability of the absolute amplitude and phase has implications on the theoretical analysis, as $\boldsymbol{J}_{\boldsymbol{g}}^s$ cannot be inverted. As a way forward, we can write explicit constraints on the sampling matrix in the form

$$\boldsymbol{f}(\boldsymbol{G}) = \boldsymbol{0}, \tag{4.43}$$

for an arbitrary function $\boldsymbol{f}(\boldsymbol{G})$. An example of such a function is

$$f_1(\boldsymbol{G}) = \frac{1}{2\pi M} \int_{-\pi}^{\pi} \sum_{m=1}^{M} |[\boldsymbol{G}\boldsymbol{b}(\phi)]_m| \mathrm{d}\phi - 1 = 0, \tag{4.44a}$$

$$f_2(\boldsymbol{G}) = \frac{1}{2\pi M} \int_{-\pi}^{\pi} \sum_{m=1}^{M} \arg\{[\boldsymbol{G}\boldsymbol{b}(\phi)]_m\} \mathrm{d}\phi = 0, \tag{4.44b}$$

Table 4.1. *MSE definitions, BCRBs and respective equations.*

Channel	Prior	Sampling matrix MSE	Sampling matrix BCRB	DoA BCRB
Known	yes	$\mathrm{MSE}\{\hat{\boldsymbol{g}}^s\}$ (4.34)	$\mathrm{BCRB}_{\mathrm{sync}}(\boldsymbol{g})$ (4.35)	$\mathrm{BCRB}_{\mathrm{sync}}(\phi_p^s)$ (4.37)
	no	$\mathrm{MSE}\{\hat{\boldsymbol{g}}^s\}$ (4.34)	$\mathrm{BCRB}_{\mathrm{sync}}(\boldsymbol{g})$ (4.35)	$\mathrm{BCRB}_{\mathrm{sync}}(\phi_p^s)$ (4.37)
Unknown	yes	$\mathrm{MSE}\{\hat{\boldsymbol{g}}^s\}$ (4.34)	$\mathrm{BCRB}(\boldsymbol{g})$ (4.39)	$\mathrm{BCRB}(\phi_p^s)$ (4.41)
	no	$\mathrm{MSE}'\{\hat{\boldsymbol{g}}^s\}$ (4.45)	$\mathrm{BCRB}'(\boldsymbol{g})$ (4.46)	$\mathrm{BCRB}'(\phi_p^s)$ (4.48)

which constrains absolute amplitude and phase. Being able to write down explicit constraints as (4.43), we can derive a meaningful BCRB on the constrained estimation problem by applying the Moore-Penrose pseudoinverse, see [174, 95, 96]. However, we also need to define a modified $\mathrm{MSE}'\{\hat{\boldsymbol{g}}^s\}$ for the sampling matrix elements $\hat{\boldsymbol{g}}^s$, as with the standard MSE definition, absolute amplitude and phase offsets would count as estimation errors. To this end, we apply an appropriate transformation [95] to the estimated sampling matrix elements $\hat{\boldsymbol{g}}^s$. Intuitively, the transformation adjusts the absolute amplitude and phase of $\hat{\boldsymbol{g}}^s$, such that they match the absolute amplitude and phase of $\boldsymbol{g}$. This can be achieved by multiplying $\hat{\boldsymbol{g}}^s$ by the complex coefficient $(\hat{\boldsymbol{g}}^s)^\dagger \boldsymbol{g}$. We thus define the modified MSE on the sampling matrix elements

$$\mathrm{MSE}'\{\hat{\boldsymbol{g}}^s\} = \frac{1}{MU}\,\mathrm{tr}\left\{\mathrm{E}_{\boldsymbol{z},\tilde{\boldsymbol{x}}}\left\{\left(\hat{\boldsymbol{g}}^s(\hat{\boldsymbol{g}}^s)^\dagger \boldsymbol{g} - \boldsymbol{g}\right)\left(\hat{\boldsymbol{g}}^s(\hat{\boldsymbol{g}}^s)^\dagger \boldsymbol{g} - \boldsymbol{g}\right)^H\right\}\right\}. \tag{4.45}$$

The BCRB as a lower bound on the modified MSE is then defined with the pseudoinverse as

$$\mathrm{MSE}'\{\hat{\boldsymbol{g}}^s\} \geq \mathrm{BCRB}'(\boldsymbol{g}) \coloneqq \frac{1}{MU}\,\mathrm{tr}\left\{(\boldsymbol{J}_{\boldsymbol{g}}^s)^\dagger\right\}. \tag{4.46}$$

Again applying the pseudoinverse, we can calculate the EBIM for the DoAs,

$$\boldsymbol{J}_{\boldsymbol{\phi}}^s = \tilde{\boldsymbol{I}}_{\boldsymbol{\phi}}^s - \begin{bmatrix}(\tilde{\boldsymbol{I}}_{\boldsymbol{g}\boldsymbol{\phi}}^s)^T & \tilde{\boldsymbol{I}}_{\boldsymbol{\phi}\mathrm{n}}^s\end{bmatrix}\begin{bmatrix}\boldsymbol{J}_{\boldsymbol{g}}^{(s-1)} + \tilde{\boldsymbol{I}}_{\boldsymbol{g}}^s & \tilde{\boldsymbol{I}}_{\boldsymbol{g}\mathrm{n}}^s \\ (\tilde{\boldsymbol{I}}_{\boldsymbol{g}\mathrm{n}}^s)^T & \tilde{\boldsymbol{I}}_{\mathrm{n}}^s\end{bmatrix}^\dagger \begin{bmatrix}\tilde{\boldsymbol{I}}_{\boldsymbol{g}\boldsymbol{\phi}}^s \\ (\tilde{\boldsymbol{I}}_{\boldsymbol{\phi}\mathrm{n}}^s)^T\end{bmatrix}, \tag{4.47}$$

and the BCRB as a lower bound on the estimation MSE of the p-th DoA,

$$\mathrm{MSE}'\left\{\hat{\phi}_p^s\right\} \geq \mathrm{BCRB}'(\phi_p^s) \coloneqq \left[(\boldsymbol{J}_{\boldsymbol{\phi}}^s)^{-1}\right]_{p,p}. \tag{4.48}$$

The MSE definitions and BCRBs derived for the different cases are summarized in Table 4.1.

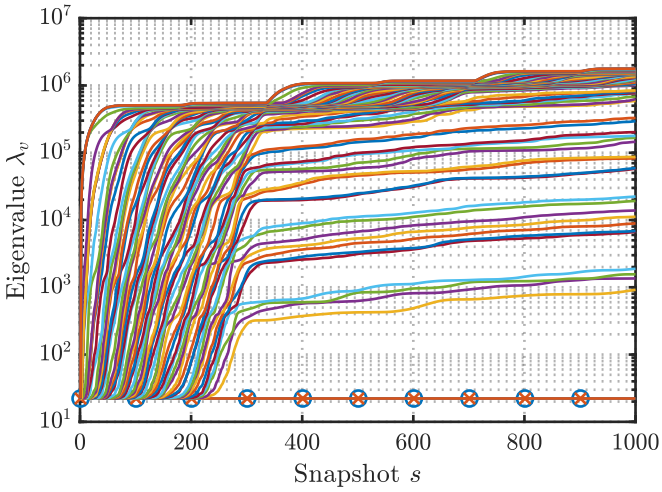

Figure 4.2. *Eigenvalues of $\boldsymbol{J}_{\boldsymbol{g}}^{s}$ for unknown propagation channel with prior. The two smallest eigenvalues are marked with circles and crosses © 2022 IEEE [175].*

4.7 Qualitative Behavior of the BCRB

We now discuss the behavior of the different BCRBs derived in Section 4.6, in order to gain an intuitive understanding of in-situ calibration. The parameters used to generate the results in this section are the same as for the simulation results, see Section 4.8.1, but are not relevant for a qualitative assessment. The expectation in (4.27) is evaluated numerically. First we analyze the behavior of the sampling matrix EBIM $\boldsymbol{J}_{\boldsymbol{g}}^{s}$ for the unknown channel case with prior, see (4.38). The eigenvalue decomposition of the real-valued symmetric matrix $\boldsymbol{J}_{\boldsymbol{g}}^{s}$ is

$$\boldsymbol{J}_{\boldsymbol{g}}^{s} = \boldsymbol{Q}\boldsymbol{\Lambda}\boldsymbol{Q}^{T}, \tag{4.49}$$

where $\boldsymbol{Q}$ is an orthonormal basis and $\boldsymbol{\Lambda}$ is a diagonal matrix containing the eigenvalues $\lambda_1, ..., \lambda_v, ...\lambda_{2MU}$. The evolution of the eigenvalues, when taking more snapshots into account, is shown in Fig. 4.2, assuming the unknown channel case with prior. For $s = 0$, due to the prior (4.4), all eigenvalues have a value of ${}^{2}/\sigma_{\boldsymbol{g}_0}^{2} = 22.\overline{22}$. Since $\mathrm{E}\left\{\phi_{\mathrm{obs}}^{s} - \phi_{\mathrm{obs}}^{(s-1)}\right\} = 1°$, see Section 4.8.1, one 360° turn corresponds to approximately 360 snapshots. During the first turn, the eigenvalues increase monotonically with increasing snapshot index, except for two eigenvalues, which remain at their initial value. The steep increase corresponds to a large information gain. After $s = 360$, the eigenvalues increase slowly, which means the information gain is small. The two eigenvalues remaining at the initial value of ${}^{2}/\sigma_{\boldsymbol{g}_0}^{2} = 22.\overline{22}$ correspond to the non-observable absolute amplitude and phase, which is previously discussed in Section 4.6.2.

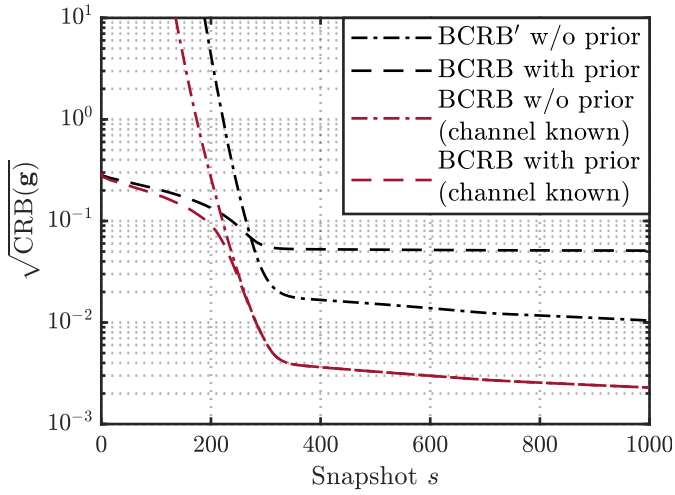

Figure 4.3. *BCRB for estimating the elements of the sampling matrix* $\boldsymbol{G}$ *without and with prior information on* $\boldsymbol{G}$ *and without and with known propagation channel © 2022 IEEE [175].*

Without prior, the two eigenvalues would be zero, which means we must apply the pseudoinverse in (4.46) and (4.47) to invert the EBIMs.

Next, we discuss the BCRB behavior qualitatively, where we start with the BCRBs of the sampling matrix elements $\boldsymbol{g}$ shown in Fig. 4.3. A single impinging signal ($P = 1$) is assumed. The BCRBs for the known propagation channel case (4.35) are plotted in red. The known channel BCRB without prior decreases steeply during the first 360 snapshots, i.e. the first 360° turn, then it flattens. With prior, the BCRB first decreases slowly, before decreasing steeply between $s = 180$ and $s = 360$. In this region, the known channel BCRBs with and without prior converge. Apparently, more than half of the manifold must have been observed in order to considerably improve the sampling matrix prior. When the entire manifold has been observed once, both known channel BCRBs decrease only slowly with increasing number of snapshots. The sampling matrix estimate is then only refined by averaging over noisy observations. For in-situ calibration, it is thus vital that the entire manifold is observed at least once. Now we focus on the unknown propagation channel BCRBs plotted in black. The unknown channel BCRB without prior (4.46) behaves similar as the known channel BCRB without prior. A steep decrease in the beginning is followed by a slow decrease after approximately 360 snapshots. However, for the unknown channel case, the BCRB in the slowly decreasing region is almost one order of magnitude higher. The unknown channel BCRB with prior (4.39) starts at the same value as the known channel BCRB with prior, but decreases only slightly and then reaches a floor. As discussed in the context of Fig. 4.2, two eigenvalues of $\boldsymbol{J}_{\boldsymbol{g}}^{s}$ will remain $2/\sigma_{\boldsymbol{g}^0}^2$ when $s \to \infty$. These two eigenvalues correspond to the non-observable absolute amplitude and phase. The two

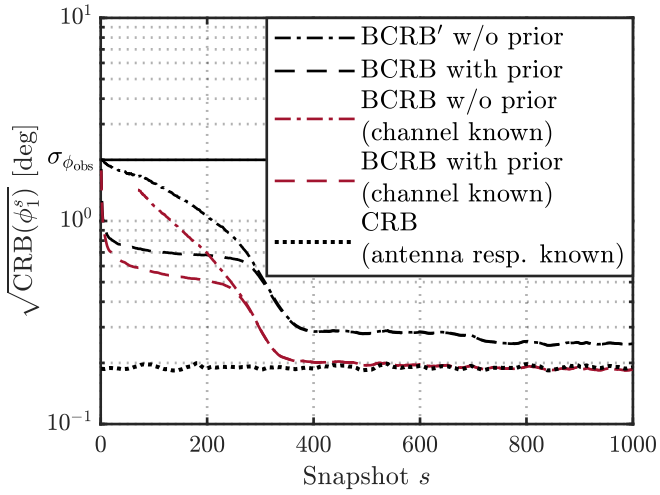

Figure 4.4. *BCRB for the estimation of ϕ_1^s without and with prior information on $\boldsymbol{G}$ and without and with known propagation channel. CRB for known antenna response, i.e. known $\boldsymbol{G}$, is plotted for comparison © 2022 IEEE [175].*

dominant eigenvalues of $(\boldsymbol{J}_{\boldsymbol{g}}^s)^{-1}$ will thus be $\sigma_{\boldsymbol{g}^0}^2/2$, which means

$$\lim_{s\to\infty} \text{BCRB}(\boldsymbol{g}) = \lim_{s\to\infty} \frac{\text{tr}\left\{(\boldsymbol{J}_{\boldsymbol{g}}^s)^{-1}\right\}}{MU} = \frac{\sigma_{\boldsymbol{g}^0}^2}{MU}. \tag{4.50}$$

For the chosen parameters detailed in Section 4.8.2, we have $\sqrt{\sigma_{\boldsymbol{g}^0}^2/MU} = 0.05$, which is precisely the floor value to which the unknown channel BCRB with prior converges in Fig. 4.3. In Section 4.6.2, we discuss that absolute amplitude and phase offsets defined by the prior count as errors for the regular MSE matrix (4.34). The floor of the unknown channel BCRB with prior (4.39) relates to the regular MSE matrix and is thus not a meaningful bound to asses the estimation error of the sampling matrix elements. For the case without prior, we find that

$$\lim_{s\to\infty} \text{BCRB}'(\boldsymbol{g}) = \lim_{s\to\infty} \frac{\text{tr}\left\{(\boldsymbol{J}_{\boldsymbol{g}}^s)^{\dagger}\right\}}{MU} = 0. \tag{4.51}$$

Since the true antenna response described by the sampling matrix elements is constant, it can be estimated perfectly when an infinite number of observations is available.

Analyzing the sampling matrix BCRB behavior helps to gain an intuitive understanding of in-situ calibration. However, it is not straightforward to determine what a certain error of the estimated sampling matrix elements $\hat{\boldsymbol{g}}^s$ means for the achievable DoA estimation accuracy. In Fig. 4.4, we thus plot the BCRBs of the DoA ϕ_1^s. Initially, the observed DoA by the external sensor is more accurate than the estimated DoAs from the received signal based on the prior sampling matrix $\hat{\boldsymbol{G}}^0$, causing all BCRBs to start at $\sigma_{\phi_{\text{obs}}}$ for $s = 0$. First, we focus on the BCRBs without prior for the known

channel case (4.37) and unknown channel case (4.48), which are plotted as dashed-dotted lines. The unknown channel BCRB without prior decreases, until it flattens after the first turn or approximately 360 snapshots. After the second turn or approx. 720 snapshots, another small decrease is evident. The behavior of the known channel BCRB without prior is similar, but it can be calculated only for $s \geq 70$, when the EBIM (4.36) has full rank. Next, we have a look at the BCRBs with prior for the known channel case (4.37) and unknown channel case (4.41) plotted as dashed lines, which both decrease quickly within the first few snapshots. We attribute the quick decrease in the beginning to the estimation of the parameters observable by a single snapshot like amplitude and phase offsets of the antenna ports. These parameters are not modeled explicitly, instead they are covered by the sampling matrix $\boldsymbol{G}$. Similar as for the sampling matrix elements, the DoA BCRBs with and without prior start to converge towards the end of the first full turn. The snapshot DoA estimation CRB (2.42), assuming the antenna response is perfectly known, is shown with a dotted line for comparison. Slight variations are visible due to the direction dependency of the CRB. The BCRB for known propagation channel almost reaches the known antenna response CRB after one full turn. Since the manifold is sampled dense enough and the SNR of the received signal is high, this is expected. However, it should be noted that the CRB with known antenna response is not a lower bound for the BCRB, as ϕ_{obs} is neglected by the CRB. Nevertheless, the CRB can serve as an indicator of close to optimum performance. For the chosen settings, the BCRB for unknown channel does not fully approach the known antenna response CRB, but comes fairly close.

4.8 Simulation Results

4.8.1 Simulation Setup and Random Antenna Response

To demonstrate that the proposed in-situ calibration algorithm can handle arbitrary antenna responses, we perform a Monte Carlo simulation with a randomly generated antenna response for each run. The random antenna response is generated based on a UCA with $M = 4$ antenna elements and radius $R = 0.9/(4\sin(\pi/M))$, which can be described by

$$a_{m,\text{UCA}}(\phi) = e^{j2\pi R\cos\left(\phi - 2\pi\frac{m}{M}\right)}, \tag{4.52}$$

$$\boldsymbol{a}_{\text{UCA}}(\phi) = \begin{bmatrix} a_{1,\text{UCA}}(\phi) & \dots & a_{M,\text{UCA}}(\phi) \end{bmatrix}^T, \tag{4.53}$$

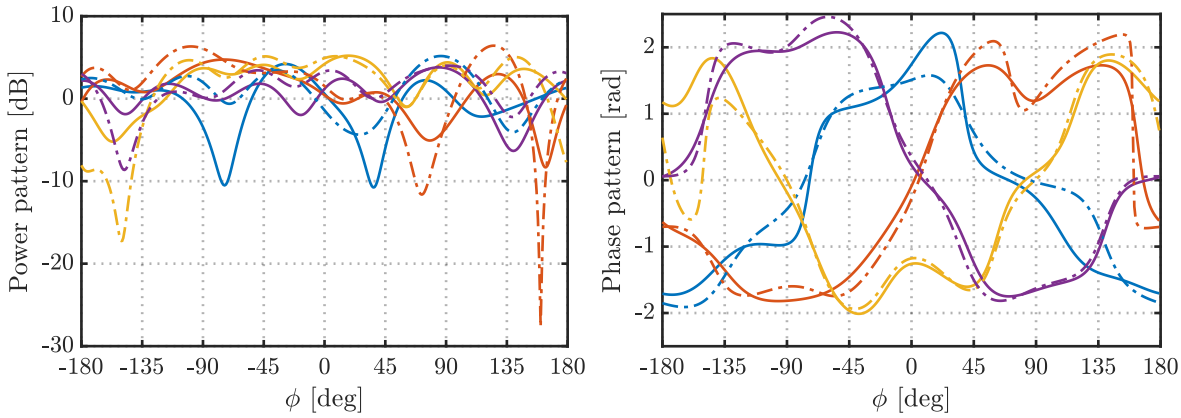

(a) *Power pattern.* **(b)** *Phase pattern.*

Figure 4.5. *Example realization of a random antenna response* $\boldsymbol{a}(\phi) = \boldsymbol{G}\boldsymbol{b}(\phi)$ *with* $M = 4$ *plotted with solid and prior antenna response* $\hat{\boldsymbol{a}}^0(\phi) = \hat{\boldsymbol{G}}^0\boldsymbol{b}(\phi)$ *plotted with dashed-dotted lines.*

see e.g. [28]. The UCA sampling matrix $\boldsymbol{G}_{\text{UCA}}$ with $U = 9$ basis functions is then obtained by (2.19) and (2.20) with (4.53) evaluated at a fixed angular grid

$$\boldsymbol{E} = \begin{bmatrix} \boldsymbol{a}_{\text{UCA}}(\phi_1) & \dots & \boldsymbol{a}_{\text{UCA}}(\phi_Q) \end{bmatrix}, \tag{4.54}$$

with ϕ_1, ..., ϕ_Q and $Q = 360$. For each run, a random sampling matrix is obtained by distorting the UCA sampling matrix

$$\boldsymbol{G} = \boldsymbol{G}_{\text{UCA}} + \boldsymbol{W}_{\boldsymbol{G}} \tag{4.55}$$

with circular symmetric Gaussian noise

$$\boldsymbol{W}_{\boldsymbol{G}} = \begin{bmatrix} \boldsymbol{w}_{\boldsymbol{g}}^1 & \dots & \boldsymbol{w}_{\boldsymbol{g}}^U \end{bmatrix}, \tag{4.56a}$$

$$\boldsymbol{w}_{\boldsymbol{g}}^u \sim \mathcal{CN}(0, \sigma_{\boldsymbol{g}}^2 \mathbb{I}_M), \tag{4.56b}$$

with $\sigma_{\boldsymbol{g}} = 0.3$. We choose this procedure to model deviations of the installed antenna response of a real-world UCA compared to the ideal model (4.53). Deviations can occur due to manufacturing tolerances, influence of the surrounding structure, mutual coupling and other nonidealities.

The prior sampling matrix $\hat{\boldsymbol{G}}^0$ is obtained by sampling the prior pdf (4.4). A realization of the random antenna response $\boldsymbol{a}(\phi) = \boldsymbol{G}\boldsymbol{b}(\phi)$ based on the random sampling matrix (4.55) and a realization of the prior antenna response $\hat{\boldsymbol{a}}^0(\phi) = \hat{\boldsymbol{G}}^0\boldsymbol{b}(\phi)$ are shown in Fig. 4.5 in terms of their power and phase patterns.

Furthermore, for this simulation we assume that the first DoA ϕ_1^s can be observed

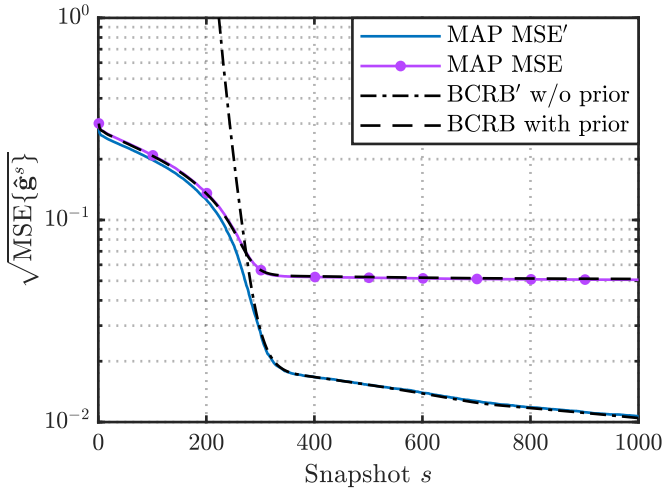

Figure 4.6. *Simulated RMSE for estimating the elements of the sampling matrix* $\boldsymbol{G}$ *calculated using the transformed* MSE′ (4.45) *and the regular* MSE (4.34)*. BCRB without and with prior are plotted for comparison © 2022 IEEE [175].*

with $\sigma_{\phi_{\text{obs}}} = 2°$. For each of the 500 Monte Carlo runs, we consider $S = 1000$ snapshots. The DoAs evolve according to $\phi_p^s = \phi_p^{(s-1)} + u^s$, where $u^s \sim \mathcal{U}(0°, 2°)$ is uniformly distributed. The SNR, see (2.11), is chosen as 10 dB and the signal is defined in Section 2.5.2.

4.8.2 Single Impinging Signal

We first investigate the case of a single impinging signal ($P = 1$). The RMSE of the estimated sampling matrix elements is shown in Fig. 4.6. Comparing the untransformed MSE (4.34) to the BCRB with prior (4.39), we see that the two curves overlap entirely. Both curves decrease during the first full turn and then reach a floor. Since the absolute amplitude and phase offsets defined by the prior count as errors, they limit the untransformed MSE. In contrast, the transformed MSE′ (4.45) proves to be useful to assess the estimation error of the sampling matrix errors. At first, MSE′ behaves similar to MSE, but then the transformed MSE′ reaches much lower values and gets close to the BCRB without prior (4.46). After one full turn, the MSE of the estimator with prior and the BCRB without prior are very close. Our interpretation is that after a full turn, the observations brought so much information that the prior can virtually be neglected.

Fig. 4.7 shows the DoA estimation RMSE of $\hat{\phi}_1^s$ and the corresponding BCRB (4.41). As the prior sampling matrix $\hat{\boldsymbol{G}}^0$ deviates from the real sampling matrix, the initial estimation error is determined by $\sigma_{\phi_{\text{obs}}}$. The RMSE drops quickly when the first snapshots are received. As discussed in the context of Fig. 4.4, the parameters

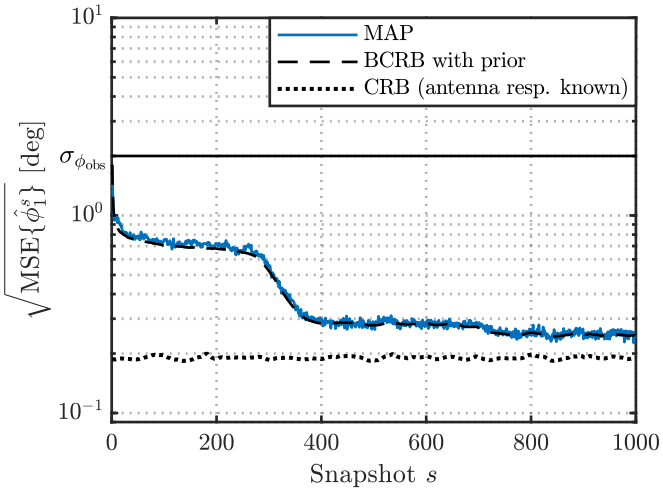

Figure 4.7. *Simulated RMSE for the estimation of ϕ_1^s. BCRB and snapshot CRB with known antenna response are plotted for comparison © 2022 IEEE [175].*

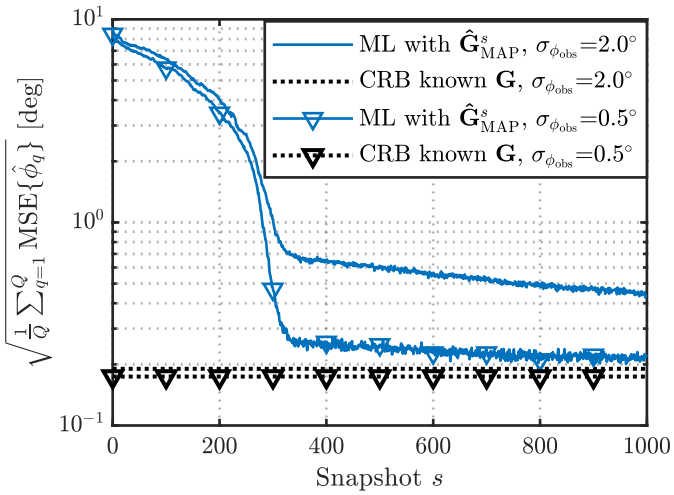

Figure 4.8. *Simulated DoA estimation RMSE. The mean is taken over the manifold, i.e. over $q = 1, ..., Q$ DoAs ϕ_q lying on a regular grid. CRB for known antenna response is plotted for comparison © 2022 IEEE [175].*

which are observable by a single snapshot, like absolute amplitude and phase offset of the antenna ports, are estimated during the first snapshots. These parameters are implicitly contained in the sampling matrix $\boldsymbol{G}$. Then the error decreases slowly until the end of the first turn, where it drops quickly. Most information is gathered during the first full turn. With increasing number of snapshots s, it slowly approaches the snapshot CRB for known antenna response (2.42). The snapshot CRB is not a lower bound for the BCRB, but can nevertheless serve as an indicator of good performance.

The external sensor providing the observable DoA ϕ_{obs} is only present during in-situ calibration. During operation, the external sensor is not present anymore. Thus for a practical application, the DoA estimation error after the in-situ calibration phase,

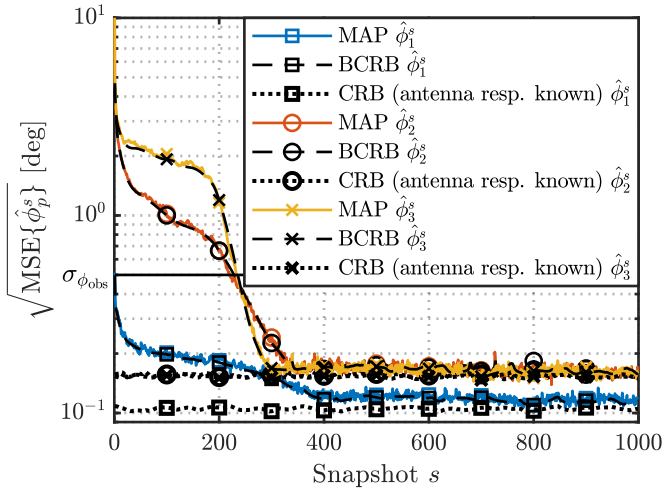

Figure 4.9. *Simulated RMSE for the estimation of ϕ_1^s, ϕ_2^s and ϕ_3^s. BCRBs and snapshot CRBs with known antenna response are plotted for comparison © 2022 IEEE [175].*

i.e. with the estimated sampling matrix $\hat{\boldsymbol{G}}^s$, is of major interest. Fig. 4.8 shows how the DoA estimation RMSE without observable DoA evolves with increasing number of snapshots. The RMSE is calculated over a discrete set of DoAs ϕ_q with $q \in \{1, ..., Q\}$ and $Q = 72$, which span a regular grid over the manifold. A lower bound is given by the snapshot CRB for the known sampling matrix. With $\sigma_{\phi_{\mathrm{obs}}} = 2°$, sub-degree accuracy DoA estimation is possible after one full turn. After the first turn, the DoA RMSE decreases slowly. To show the influence of the observable DoA on in-situ calibration, the simulation is also performed with $\sigma_{\phi_{\mathrm{obs}}} = 0.5°$. In this case, the DoA estimation RMSE comes close to the snapshot CRB after the first turn.

4.8.3 Multiple Impinging Signals

In contrast to calibration in a dedicated measurement chamber, in-situ calibration is not performed in a controlled environment and thus propagation conditions may be non-optimum. To evaluate the performance of the proposed in-situ calibration algorithm under multipath conditions, we perform a simulation for $P = 3$ impinging signals. For the first signal, the SNR is equal to 15 dB. We assume that the second and third signals arrive from reflections at fixed locations with $\phi_2^s = \phi_1^s + 45°$ and $\phi_3^s = \phi_1^s + 90°$ with ToAs $\tau_2 = \tau_1 + 48\,\mathrm{ns}$ and $\tau_3 = \tau_1 + 96\,\mathrm{ns}$ with an SNR 3 dB lower than the first signal. We further assume $\sigma_{\phi_{\mathrm{obs}}} = 0.5°$ for the observable DoA of the first signal. The RMSE for the estimated DoAs $\hat{\phi}_1^s$, $\hat{\phi}_2^s$ and $\hat{\phi}_3^s$ together with the BCRBs (4.41), and the known antenna response snapshot CRBs (2.42), is shown in Fig. 4.9. The RMSE of the first DoA $\hat{\phi}_1^s$ behaves similar as in Fig. 4.7, i.e. the case without multipath propagation. In contrast to $\hat{\phi}_1^s$, which is observable by ϕ_{obs}^s, the estimation

of $\hat{\phi}_2^s$ and $\hat{\phi}_3^s$ relies completely on an accurately known antenna response described by the sampling matrix $\hat{\boldsymbol{G}}^s$. In the beginning, $\hat{\phi}_2^s$ and $\hat{\phi}_3^s$ are estimated with an RMSE $> 10°$, which quickly decreases to $1° - 2°$. As discussed also for Figs. 4.4 and 4.7, the quick decrease in the beginning is attributed to antenna response parameters, which are observable by a single snapshot. When the first 360° turn is completed, the RMSEs of $\hat{\phi}_2^s$ and $\hat{\phi}_3^s$ approach the respective snapshot DoA estimation CRBs, which are higher compared to $\hat{\phi}_1^s$ due to 3 dB lower SNR. Based on the simulation result for the artificial multipath scenario, we conclude that in-situ calibration with the proposed algorithm can also be performed in multipath environments. However, it must be noted that the impinging signals should be separable in at least either DoA or ToA domain.

Chapter 5

Cooperative Simultaneous Localization and Calibration

In addition to in-situ calibration from Chapter 4, in this chapter we address calibration during operation. For this purpose, we develop an algorithm for cooperative simultaneous localization and calibration (SLAC), where the antenna responses and the ranging biases of the agents are estimated and tracked simultaneously with their positions and orientations. To this end, we define the state space, again parameterizing the antenna response by the sampling matrix $\boldsymbol{G}$, as well as motion and observation models. Then we derive a Bayesian filtering algorithm for cooperative SLAC. For nodes with a multi-port antenna, for example an MMA, a prior antenna response is considered. The prior antenna response could e.g. come from an EM simulation or from a measurement of the antenna in a near-field measurement chamber before installation on a robot. The antenna response is then gradually refined over time, taking into account the observed signals. Furthermore, ranging biases of all nodes in the network are estimated. We show by simulation that cooperative SLAC is able to estimate calibration states without external sensors. Thereby, cooperative SLAC considerably improves position and orientation accuracy compared to localization-only.

5.1 Concept

SLAC considers a moving multi-agent system. The agents form a cooperative network of radio nodes, which includes also static anchors. We thus extend the definition of a static cooperative network in Section 3.1 to the dynamic case by including the snapshot index s, which corresponds to discrete time. Fig. 5.1 shows two static anchors k and l and two moving agents i and j at two time instances, the previous snapshot $s-1$ and the

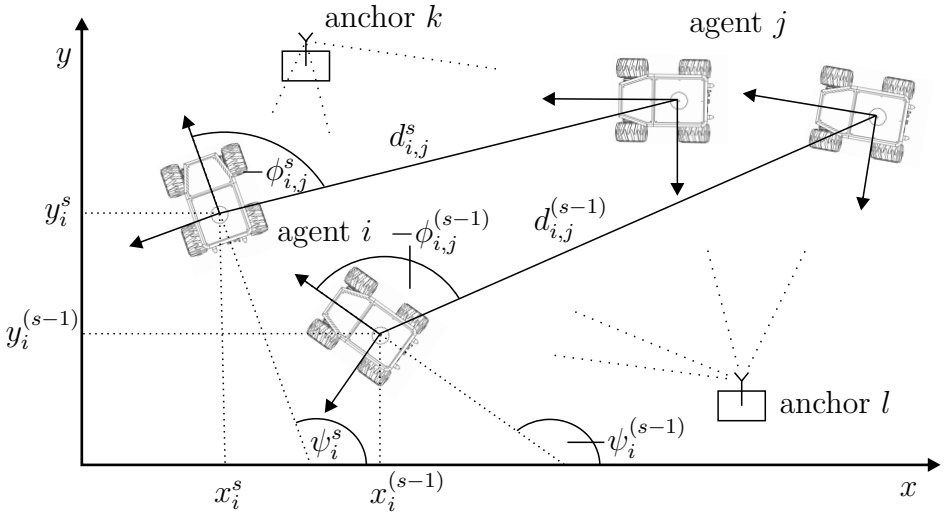

Figure 5.1. *Two anchors k and l and two moving agents i and j at previous snapshot $s-1$ and current snapshot s, the respective positions $\boldsymbol{p}_i^{(s-1)} = \left[x_i^{(s-1)}, y_i^{(s-1)}\right]^T$ and $\boldsymbol{p}_i^s = [x_i^s, y_i^s]^T$ of agent i, the respective orientations $\psi_i^{(s-1)}$ and ψ_i^s of agent i, the respective distances $d_{i,j}^{(s-1)}$ and $d_{i,j}^s$ as well as DoAs $\phi_{i,j}^{(s-1)}$ and $\phi_{i,j}^s$ between agents i and j.*

current snapshot s. The respective positions $\boldsymbol{p}_i^{(s-1)} = \left[x_i^{(s-1)}, y_i^{(s-1)}\right]^T$, $\boldsymbol{p}_i^s = [x_i^s, y_i^s]^T$ and orientations $\psi_i^{(s-1)}$, ψ_i^s of agent i and the respective distances $d_{i,j}^{(s-1)}$, $d_{i,j}^s$ between agents i and j and the respective DoAs $\phi_{i,j}^{(s-1)}$, $\phi_{i,j}^s$ for the signal received by agent i from agent j are shown as well.

By cooperative radio localization, positions and orientations of the agents and their evolution over time are estimated based on radio signals exchanged among the agents. By exchanging signals, state estimates, observations and payload data, e.g. telecommand and sensor data, can be communicated. For a centralized estimation approach, observations from all nodes are communicated to a central processing unit, which estimates the states. The estimated states and covariances are then communicated back to the nodes. By decentralized or distributed estimation, neighboring nodes exchange their estimated states and/or their observations. Thereby, their individual estimations converge to a common result.

Position and orientation estimation requires direction and distance information. Direction information is obtained by the DoA of radio signals, which requires accurate knowledge of the multiport antenna response. However, the antenna response can change during operation, for instance by changing surroundings of the antenna. As an example, consider a robot with a manipulator arm and the ability to carry payloads, e.g. [120]. For compact robots, both the manipulator arm and possibly present payloads are in close vicinity to the antenna. Thus, they influence the antenna response. Deviations of the true antenna response from the antenna response assumed for estimation lead to

a model mismatch and impaired DoA estimation performance. Distance information is obtained by the ToA of the delayed baseband signal, considering also the transmit time. In unsynchronized networks, the TWR protocol is applied to eliminate transmitter and receiver clock offsets. Hence, only the propagation time of the signal in free-space is related to the distance. Thus, other impacts on the signal delay like group delays in transmit and receive chains of the node transceivers must be calibrated and eliminated. However, transceiver group delays vary over time, e.g. due to changing temperature, which leads to ranging biases and thus impaired localization performance.

To cope with these challenges, we propose cooperative SLAC to calibrate antenna responses and ranging biases during operation. Thereby, we leverage the large number of observations available in cooperative networks. Considering for instance a fully connected network of $|\mathbb{N}|$ nodes, there are $|\mathbb{N}|(|\mathbb{N}|-1)$ observed signals. By simultaneous calibration, cooperative SLAC mitigates model mismatch and thereby improves localization performance. To demonstrate the feasibility of the SLAC concept, we restrict ourselves to radio signal observations. Thus, we do not use any external sensors like accelerometers or gyroscopes. Nonetheless, the Bayesian filtering approach would allow to integrate sensors and control inputs available on robotic platforms.

5.2 State Space

5.2.1 State Definition

As introduced in Section 3.1, the network is defined by the node set $\mathbb{N} = \mathbb{R} \cup \mathbb{A}$ consisting of mobile agents $\mathbb{R}$ and static anchors with known position and orientation $\mathbb{A}$. The node state vector

$$\boldsymbol{x}_i^s = \begin{cases} \begin{bmatrix} (\boldsymbol{x}_{i,\text{loc}}^s)^T & (\boldsymbol{x}_{i,\text{cal}}^s)^T \end{bmatrix}^T & \text{if } i \in \mathbb{R} \\ \boldsymbol{x}_{i,\text{cal}}^s & \text{if } i \in \mathbb{A} \end{cases} \tag{5.1}$$

of node i is defined differently for agents and anchors. For agents, the node state vector $\boldsymbol{x}_i^s$ consists of the agent kinematic states $\boldsymbol{x}_{i,\text{loc}}^s$ and the node calibration states $\boldsymbol{x}_{i,\text{cal}}^s$. For anchors, the node state vector only contains the node calibration states $\boldsymbol{x}_{i,\text{cal}}^s$. The agent kinematic states are given by

$$\boldsymbol{x}_{i,\text{loc}}^s = \begin{bmatrix} (\boldsymbol{p}_i^s)^T & v_i^s & \psi_i^s & \omega_i^s \end{bmatrix}^T, \tag{5.2}$$

with position $\boldsymbol{p}_i^s$, linear velocity v_i^s, orientation ψ_i^s, and angular velocity ω_i^s.

As mentioned in Section 2.2, we consider a TWR protocol [134, 153] to eliminate the

transmitter and receiver clock offsets. Furthermore, we assume that the processing time $T_{j,\text{proc}}$ between forward and backward transmission is very short, such that the influence of the relative frequency offset can be neglected [166]. Otherwise, the oscillator behavior must be considered by an appropriate clock model [154]. As discussed in Section 5.1, varying group delays in the transceiver RF components lead to a ranging bias of the respective node. Considering the ranging biases δ_i^s and δ_j^s of nodes i and j defined in distance domain and the transmit time of the forward signal $\bar{\tau}_{i,j}^s$ at node i, the ToA of the backward signal received by node i is defined as

$$\tau_{i,j}^s = \bar{\tau}_{i,j}^s + \frac{2(d_{i,j}^s - \delta_i^s - \delta_j^s)}{c} + T_{j,\text{proc}}. \tag{5.3}$$

The processing time $T_{j,\text{proc}}$ at node j is known. Thus, we assume $T_{j,\text{proc}} = 0\,\text{s}$ without loss of generality. To calibrate the antenna response

$$\boldsymbol{a}_i^s(\phi) = \boldsymbol{G}_i^s\, \boldsymbol{b}(\phi) \tag{5.4}$$

of the multiport antenna installed on node i, we represent the sampling matrix $\boldsymbol{G}_i^s$, see (2.12), in vectorized form of real and imaginary parts,

$$\boldsymbol{g}_{\text{RI},i}^s = \begin{bmatrix} \text{Re}\left\{\text{vec}\left\{\boldsymbol{G}_i^s\right\}\right\} \\ \text{Im}\left\{\text{vec}\left\{\boldsymbol{G}_i^s\right\}\right\} \end{bmatrix}. \tag{5.5}$$

The node calibration states are then defined as

$$\boldsymbol{x}_{i,\text{cal}}^s = \begin{cases} \delta_i^s & \text{if } M_i = 1 \\ \begin{bmatrix} \delta_i^s & (\boldsymbol{g}_{\text{RI},i}^s)^T \end{bmatrix}^T & \text{if } M_i > 1, \end{cases} \tag{5.6}$$

depending on the antenna type of the respective node. For agents with singleport antenna ($M_i = 1$), only the ranging bias δ_i^s is estimated. For agents with multiport antenna ($M_i > 1$), ranging bias δ_i^s and sampling matrix elements $\boldsymbol{g}_{\text{RI},i}^s$ are estimated. The state vector for the whole network

$$\boldsymbol{x}^s = \begin{bmatrix} (\boldsymbol{x}_1^s)^T & \dots & (\boldsymbol{x}_i^s)^T & \dots & (\boldsymbol{x}_{|\mathbb{N}|}^s)^T \end{bmatrix}^T \tag{5.7}$$

is created by stacking the node states. We also define the vectors $\boldsymbol{\iota}_i$, $\boldsymbol{\iota}_{i,\text{loc}}$, $\boldsymbol{\iota}_{i,\text{cal}}$ containing the indices of the elements of $\boldsymbol{x}_i^s$, $\boldsymbol{x}_{i,\text{loc}}^s$, $\boldsymbol{x}_{i,\text{cal}}^s$ in the state vector $\boldsymbol{x}^s$, such that $[\boldsymbol{x}^s]_{\boldsymbol{\iota}_i} = \boldsymbol{x}_i^s$, $[\boldsymbol{x}^s]_{\boldsymbol{\iota}_{i,\text{loc}}} = \boldsymbol{x}_{i,\text{loc}}^s$ and $[\boldsymbol{x}^s]_{\boldsymbol{\iota}_{i,\text{cal}}} = \boldsymbol{x}_{i,\text{cal}}^s$.

5.2.2 State Transition

The state transition of the agent kinematic states (5.2) from the previous snapshot $s-1$ to the current snapshot s is defined by the motion model

$$\boldsymbol{x}_{i,\mathrm{loc}}^{s} = \boldsymbol{f}\left(\boldsymbol{x}_{i,\mathrm{loc}}^{(s-1)}\right) + \boldsymbol{w}_{\boldsymbol{x}_{i,\mathrm{loc}}}^{s} \,\forall\, i \in \mathbb{R}. \tag{5.8}$$

We use the constant velocity constant turn model from [176, 177]. By trigonometric identities, it can be shown that the transition equations for position and orientation are a special case of the motion model proposed in [178] for robotic rovers. For time interval T between two consecutive snapshots, the motion model is defined as

$$\boldsymbol{f}\left(\boldsymbol{x}_{i,\mathrm{loc}}^{(s-1)}\right) = \begin{bmatrix} x_i^{(s-1)} - \frac{v_i^{(s-1)}}{\omega_i^{(s-1)}} \sin\left(\psi_i^{(s-1)}\right) + \frac{v_i^{(s-1)}}{\omega_i^{(s-1)}} \sin\left(\psi_i^{(s-1)} + \omega_i^{(s-1)} T\right) \\ y_i^{(s-1)} + \frac{v_i^{(s-1)}}{\omega_i^{(s-1)}} \cos\left(\psi_i^{(s-1)}\right) - \frac{v_i^{(s-1)}}{\omega_i^{(s-1)}} \cos\left(\psi_i^{(s-1)} + \omega_i^{(s-1)} T\right) \\ v_i^{(s-1)} \\ \psi_i^{(s-1)} + T\omega_i^{(s-1)} \\ \omega_i^{(s-1)} \end{bmatrix}. \tag{5.9}$$

The process noise in (5.8) is Gaussian,

$$\boldsymbol{w}_{\boldsymbol{x}_{i,\mathrm{loc}}}^{s} \sim \mathcal{N}(\mathbf{0}_5, \boldsymbol{\Sigma}_{\boldsymbol{x}_{i,\mathrm{loc}}}^{s}), \tag{5.10}$$

$$\boldsymbol{\Sigma}_{\boldsymbol{x}_{i,\mathrm{loc}}}^{s} = \begin{bmatrix} 0 & 0 & 0 & 0 & 0 \\ 0 & 0 & 0 & 0 & 0 \\ 0 & 0 & T\sigma_v^2 & 0 & 0 \\ 0 & 0 & 0 & \frac{1}{3}T^3\sigma_w^2 & \frac{1}{2}T^2\sigma_w^2 \\ 0 & 0 & 0 & \frac{1}{2}T^2\sigma_w^2 & T\sigma_w^2 \end{bmatrix}, \tag{5.11}$$

where $\boldsymbol{\Sigma}_{\boldsymbol{x}_{i,\mathrm{loc}}}^{s}$ is the process noise covariance matrix. Changes in linear and angular velocity between two snapshots are reflected by the process noise parameters σ_v^2 and σ_w^2. Consequently, in some literature also the term nearly constant velocity model is used. The calibration states are assumed to be constant over time, $\boldsymbol{x}_{i,\mathrm{cal}}^{s} = \boldsymbol{x}_{i,\mathrm{cal}}^{(s-1)} \,\forall\, i \in \mathbb{N}$, with zero process noise.

5.2.3 Observation Model

Based on (2.8), a signal transmitted by node j and received by node i at snapshot s expressed in discrete frequency domain with subcarrier index n is

$$\boldsymbol{r}_{i,j}^{s}(n) = \boldsymbol{a}_i(\phi_{i,j}^{s}) s(n, \tau_{i,j}^{s}) \alpha_{i,j}^{s}\, e^{\mathrm{j}\varphi_{i,j}^{s}} + \boldsymbol{w}_{i,j}^{s}(n). \tag{5.12}$$

Vectorizing (5.12), we obtain

$$\boldsymbol{r}_{i,j}^{s} = \begin{bmatrix} ... & (\boldsymbol{r}_{i,j}^{s}(n))^T & ... \end{bmatrix}^T, \; n \in \mathbb{N}_{\text{sc}}. \tag{5.13}$$

We consider a centralized estimation approach, where all observations are available at a central computing unit. Thus, the signals received by all nodes in the network are collected in the observation vector

$$\boldsymbol{z}^{s} = \begin{bmatrix} ... & (\boldsymbol{r}_{i,j}^{s})^T & ... & (\boldsymbol{r}_{j,i}^{s})^T & ... \end{bmatrix}^T. \tag{5.14}$$

We consider a TWR protocol with forward signal $\boldsymbol{r}_{i,j}^{s}$ and backward signal $\boldsymbol{r}_{j,i}^{s}$.

Many cooperative localization algorithms follow the two-step approach [24, 19, 179]. In a two-step approach, first the distances and/or directions are extracted from the signals and then positions and/or orientations are estimated by a subsequent algorithm. Since the antenna response must be observable by the algorithm, the two-step approach is not feasible for SLAC. Thus, to enable antenna response calibration, we directly evaluate the log-likelihood functions for the received signals (5.17) and (5.20), which are introduced separately for singleport and multiport antennas in the following. Position and/or orientation estimation directly based on the received signals is called direct localization, see e.g. [180]. Direct localization is known to be more robust w.r.t. multipath propagation than the two-step approach, especially in two cases: First, when the number of antennas is large and massive arrays are employed [181, 182, 183], and second, when the number of links is large and the cooperative network is dense [184].

Singleport Antenna

If nodes with singleport antenna ($M_i = 1$) are equipped with an omnidirectional antenna, they are not capable of DoA estimation. As an example, we consider a dipole oriented along the z-axis with the antenna response

$$a_i(\phi) = \sqrt{10^{\frac{2.15\,\text{dBi}}{10}}} = 1.28 \tag{5.15}$$

independent of the DoA ϕ. Analogous to (2.57), the log-likelihood function for the received signal (5.12) is given by

$$L_{\boldsymbol{r}_{i,j}^{s}}(\tau_{i,j}^{s}, \alpha_{i,j}^{s}, \varphi_{i,j}^{s}) = -N \ln(\pi \sigma_{\boldsymbol{r}_{i,j}^{s}}^{2}) - \frac{1}{\sigma_{\boldsymbol{r}_{i,j}^{s}}^{2}} \sum_{n \in \mathbb{N}_{\text{sc}}} \left| r_{i,j}^{s}(n) - s(n, \tau_{i,j}^{s}) \alpha_{i,j}^{s} e^{\mathrm{j}\varphi_{i,j}^{s}} \right|^2. \tag{5.16}$$

Analogous to (2.60), the log-likelihood function concentrated to the ToA $\tau_{i,j}^s$ is given by

$$\tilde{L}_{\boldsymbol{r}_{i,j}^s}(\tau_{i,j}^s) = \frac{1}{\sigma_{\boldsymbol{r}_{i,j}^s}^2} \frac{\left|\boldsymbol{s}^H(\tau_{i,j}^s)\boldsymbol{r}_{i,j}^s\right|^2}{\left\|\boldsymbol{s}(\tau_{i,j}^s)\right\|^2} \tag{5.17}$$

with

$$\boldsymbol{s}(\tau_{i,j}^s) = \begin{bmatrix} \dots & s(n, \tau_{i,j}^s) & \dots \end{bmatrix}^T, \; n \in \mathbb{N}_{\text{sc}}. \tag{5.18}$$

The noise variance $\sigma_{\boldsymbol{r}_{i,j}^s}^2$ is considered known. In practice, it can be estimated from the receiver noise floor. For a receiver with calibrated power level, the average received signal power is $\check{r}_{i,j}^s = \frac{1}{N}\sum_{n\in\mathbb{N}_{\text{sc}}}|r_{i,j}^s(n)|^2$ and $\text{SNR}(\boldsymbol{r}_{i,j}^s) = \frac{\check{r}_{i,j}^s - \sigma_{\boldsymbol{r}_{i,j}^s}^2}{\sigma_{\boldsymbol{r}_{i,j}^s}^2}$ represents the SNR. Alternatively, the noise variance $\sigma_{\boldsymbol{r}_{i,j}^s}^2$ can be eliminated from the concentrated log-likelihood function (5.17) by plugging the maximum of (5.16) w.r.t. $\sigma_{\boldsymbol{r}_{i,j}^s}^2$ into (5.17), which corresponds to ML SNR estimation based on the known transmitted signal [185].

Multiport Antenna

Nodes with $M_i > 1$ are equipped with a multiport antenna, e.g. an MMA. Analogous to (2.62), the log-likelihood function for the received signals (5.12) is given by

$$\begin{aligned} L_{\boldsymbol{r}_{i,j}^s}(\phi_{i,j}^s, \tau_{i,j}^s, \alpha_{i,j}^s, \varphi_{i,j}^s, \boldsymbol{g}_{\text{RI},i}^s) = \\ - N\ln(\pi\sigma_{\boldsymbol{r}_{i,j}^s}^2) - \frac{1}{\sigma_{\boldsymbol{r}_{i,j}^s}^2}\sum_{n\in\mathbb{N}_{\text{sc}}}\left\|\boldsymbol{r}_{i,j}^s(n) - \boldsymbol{a}_i^s(\phi_{i,j}^s)s(n,\tau_{i,j}^s)\alpha_{i,j}^s e^{\mathrm{j}\varphi_{i,j}^s}\right\|^2, \end{aligned} \tag{5.19}$$

where the sampling matrix elements $\boldsymbol{g}_{\text{RI},i}^s$ are part of the parameters and are contained in $\boldsymbol{a}_i^s(\phi_{i,j}^s)$, see (5.4) and (5.5). Analogous to (2.64), the log-likelihood function concentrated to the DoA $\phi_{i,j}^s$, ToA $\tau_{i,j}^s$ and sampling matrix elements $\boldsymbol{g}_{\text{RI},i}^s$ is given by

$$\tilde{L}_{\boldsymbol{r}_{i,j}^s}(\phi_{i,j}^s, \tau_{i,j}^s, \boldsymbol{g}_{\text{RI},i}^s) = \frac{1}{\sigma_{\boldsymbol{r}_{i,j}^s}^2}\left\|\frac{\boldsymbol{v}_{i,j}^s(\boldsymbol{v}_{i,j}^s)^H}{(\boldsymbol{v}_{i,j}^s)^H\boldsymbol{v}_{i,j}^s}\boldsymbol{r}_{i,j}^s\right\|^2, \tag{5.20}$$

with $\boldsymbol{v}_{i,j}^s = \text{vec}\left\{\boldsymbol{a}(\phi_{i,j}^s)\boldsymbol{s}^T(\tau_{i,j}^s)\right\}$. The noise variance is treated analogously to the singleport antenna case.

5.3 Cooperative SLAC Algorithm

As outlined in Section 5.1, we derive a Bayesian filtering algorithm for SLAC. Thus, we calculate the posterior pdf $p\left(\boldsymbol{x}^s|\boldsymbol{z}^{1:s}\right)$ recursively with the help of Bayes rule by prediction and update steps [178, 93]. Bayesian filtering for cooperative SLAC is challenging

for two reasons. First, the observation models (2.60) and (2.64) are highly nonlinear, which is challenging for instance for the extended Kalman filter (EKF). Second, the state vector (5.7) has high dimensionality due to the sampling matrix elements describing the antenna response. For example, the state vector dimension is 99 and 131 for the simulation scenario in Section 5.4 and the measurement scenario in Section 6.2.3, respectively. Sampling based approaches, like particle filters, experience difficulties with high state dimension. Thus, we use an algorithm similar to an iterated extended Kalman filter (IEKF) [93]. The algorithm can cope with high observation model nonlinearities and can also handle high state dimensionality, albeit at the price of higher computational complexity compared to an EKF.

5.3.1 Prediction

For the prediction step of the Bayesian filter, the pdf of the station transition $p\left(\boldsymbol{x}^s|\boldsymbol{x}^{(s-1)}\right)$ is incorporated into the posterior pdf of the previous snapshot, $p\left(\boldsymbol{x}^{(s-1)}|\boldsymbol{z}^{1:(s-1)}\right)$, which yields

$$p\left(\boldsymbol{x}^s|\boldsymbol{z}^{1:(s-1)}\right) = \int p\left(\boldsymbol{x}^s|\boldsymbol{x}^{(s-1)}\right) p\left(\boldsymbol{x}^{(s-1)}|\boldsymbol{z}^{1:(s-1)}\right) \mathrm{d}\boldsymbol{x}^{(s-1)}. \tag{5.21}$$

We assume that the pdf in (5.21) is approximately Gaussian distributed,

$$p\left(\boldsymbol{x}^s|\boldsymbol{z}^{1:(s-1)}\right) \approx \mathcal{N}(\bar{\boldsymbol{x}}^s, \bar{\boldsymbol{\Sigma}}^s), \tag{5.22}$$

with the predicted mean $\bar{\boldsymbol{x}}^s$ and covariance matrix $\bar{\boldsymbol{\Sigma}}^s$. For the kinematic states of the agents $\mathbb{R}$, prediction is defined by

$$\bar{\boldsymbol{x}}^s_{i,\mathrm{loc}} = \boldsymbol{f}\left(\hat{\boldsymbol{x}}^{(s-1)}_{i,\mathrm{loc}}\right) \quad \forall\, i \in \mathbb{R}, \tag{5.23}$$

where the motion model (5.9) is applied to the estimated agent kinematic states at the previous snapshot $\hat{\boldsymbol{x}}^{(s-1)}_{i,\mathrm{loc}}$. The calibration states remain constant,

$$\bar{\boldsymbol{x}}^s_{i,\mathrm{cal}} = \hat{\boldsymbol{x}}^{(s-1)}_{i,\mathrm{cal}} \quad \forall\, i \in \mathbb{N}, \tag{5.24}$$

where $\hat{\boldsymbol{x}}^{(s-1)}_{i,\mathrm{cal}}$ are the estimated node calibration states at the previous snapshot. The predicted covariance matrix

$$\bar{\boldsymbol{\Sigma}}^s = \boldsymbol{F}^{(s-1)}\hat{\boldsymbol{\Sigma}}^{(s-1)}\left(\boldsymbol{F}^{(s-1)}\right)^T + \boldsymbol{\Sigma}^s_{\boldsymbol{x}} \tag{5.25}$$

is obtained by linearization as in the EKF, where $\hat{\boldsymbol{\Sigma}}^{(s-1)}$ is the estimated covariance matrix at the previous snapshot, $\boldsymbol{F}^{(s-1)}$ is the Jacobian matrix of the state transition and $\boldsymbol{\Sigma}_{\boldsymbol{x}}^{s}$ is the process noise covariance matrix. The nonzero elements of $\boldsymbol{F}^{(s-1)}$ are given by

$$\left[\boldsymbol{F}^{(s-1)}\right]_{\boldsymbol{\iota}_{i,\mathrm{loc}},\boldsymbol{\iota}_{i,\mathrm{loc}}} = \left.\frac{\partial \boldsymbol{f}\left(\boldsymbol{x}_{i,\mathrm{loc}}^{(s-1)}\right)}{\partial \boldsymbol{x}_{i,\mathrm{loc}}^{(s-1)}}\right|_{\boldsymbol{x}_{i,\mathrm{loc}}^{(s-1)}=\hat{\boldsymbol{x}}_{i,\mathrm{loc}}^{(s-1)}} \tag{5.26a}$$

$$\left[\boldsymbol{F}^{(s-1)}\right]_{\boldsymbol{\iota}_{i,\mathrm{cal}},\boldsymbol{\iota}_{i,\mathrm{cal}}} = \begin{cases} 1 & \text{if } M_i = 1 \\ \mathbb{I}_{2M_iU+1} & \text{if } M_i > 1, \end{cases} \tag{5.26b}$$

where the Jacobian matrix of the motion model $\frac{\partial \boldsymbol{f}\left(\boldsymbol{x}_{i,\mathrm{loc}}^{(s-1)}\right)}{\partial \boldsymbol{x}_{i,\mathrm{loc}}^{(s-1)}}$ is derived in Appendix C.11 and the nonzero elements of the process noise covariance matrix $\boldsymbol{\Sigma}_{\boldsymbol{x}}^{s}$ are given by

$$\left[\boldsymbol{\Sigma}_{\boldsymbol{x}}^{s}\right]_{\boldsymbol{\iota}_{i,\mathrm{loc}},\boldsymbol{\iota}_{i,\mathrm{loc}}} = \boldsymbol{\Sigma}_{\boldsymbol{x}_{i,\mathrm{loc}}}^{s}, \tag{5.27}$$

with $\boldsymbol{\Sigma}_{\boldsymbol{x}_{i,\mathrm{loc}}}^{s}$ defined in (5.11).

5.3.2 Update

By the update step of the Bayesian filter, the posterior pdf of the current snapshot s is obtained by taking the observation likelihood $p\left(\boldsymbol{z}^{s}|\boldsymbol{x}^{s}\right)$ into account using Bayes rule,

$$p\left(\boldsymbol{x}^{s}|\boldsymbol{z}^{1:s}\right) = \frac{p\left(\boldsymbol{z}^{s}|\boldsymbol{x}^{s}\right) p\left(\boldsymbol{x}^{s}|\boldsymbol{z}^{1:(s-1)}\right)}{p\left(\boldsymbol{z}^{s}|\boldsymbol{z}^{1:(s-1)}\right)}, \tag{5.28}$$

where $p\left(\boldsymbol{x}^{s}|\boldsymbol{z}^{1:(s-1)}\right)$ is the posterior pdf after prediction from (5.21). Again we assume

$$p\left(\boldsymbol{x}^{s}|\boldsymbol{z}^{1:s}\right) \approx \mathcal{N}(\hat{\boldsymbol{x}}^{s}, \hat{\boldsymbol{\Sigma}}^{s}), \tag{5.29}$$

i.e. the posterior pdf is approximately Gaussian distributed with mean $\hat{\boldsymbol{x}}^{s}$ and covariance matrix $\hat{\boldsymbol{\Sigma}}^{s}$. Using a MAP approach [93, 186], the update of the state estimate

$$\begin{aligned} \hat{\boldsymbol{x}}^{s} &= \arg\max_{\boldsymbol{x}^{s}} p\left(\boldsymbol{x}^{s}|\boldsymbol{z}^{1:s}\right) \\ &= \arg\max_{\boldsymbol{x}^{s}} p\left(\boldsymbol{z}^{s}|\boldsymbol{x}^{s}\right) p\left(\boldsymbol{x}^{s}|\boldsymbol{z}^{1:(s-1)}\right) \end{aligned} \tag{5.30}$$

becomes a maximization problem, for which the denominator of (5.28) is constant. Going to logarithm domain, assuming independent process noise for the nodes and independent observation noise for the signals received by the nodes and inserting the

logarithm of the Gaussian pdf from (5.22), we arrive at

$$\begin{aligned}\hat{\boldsymbol{x}}^s &= \arg\max_{\boldsymbol{x}^s} \sum_{i\in\mathbb{N}} \ln p\left(\boldsymbol{z}_i^s|\boldsymbol{x}^s\right) + \ln p\left(\boldsymbol{x}^s|\boldsymbol{z}^{1:(s-1)}\right) \\ &= \arg\max_{\boldsymbol{x}^s} \underbrace{\sum_{i\in\mathbb{N}}\sum_{j\in\mathbb{L}_i^s} L_{\boldsymbol{r}_{i,j}^s}\left(\boldsymbol{x}_i^s,\boldsymbol{x}_j^s\right) + \frac{1}{2}(\boldsymbol{x}^s-\bar{\boldsymbol{x}}^s)^T\left(\bar{\boldsymbol{\Sigma}}^s\right)^{-1}(\boldsymbol{x}^s-\bar{\boldsymbol{x}}^s)}_{=:-h(\boldsymbol{x}^s)}.\end{aligned} \tag{5.31}$$

According to Section 3.1, the neighbor set $\mathbb{L}_i^s \subseteq \mathbb{N}\setminus\{i\}$ contains the neighboring nodes, from which node i has received signals for snapshot s. If e.g. the link between nodes i and k is blocked for snapshot s, then $k \notin \mathbb{L}_i^s$ and $i \notin \mathbb{L}_k^s$. The double sum in (5.31) thus accumulates all observations by all nodes $\mathbb{N}$ in the network, which corresponds to a centralized approach. The formulation in (5.31) is similar to an IEKF [93]. The IEKF is based on the standard EKF, for which a linearization, i.e. a first order Taylor series expansion of state transition and observation equations, is applied. For the IEKF, the update step of the EKF is replaced by a MAP estimate, which is obtained by iteration. The iterations amount to relinearization of the observation equation. Thus, compared to the EKF, the IEKF is superior for highly nonlinear observation models at the cost of higher computational complexity. The log-likelihood function in (5.31) for a signal transmitted by node j and received by node i,

$$L_{\boldsymbol{r}_{i,j}^s}\left(\boldsymbol{x}_i^s,\boldsymbol{x}_j^s\right) = \begin{cases}\tilde{L}_{\boldsymbol{r}_{i,j}^s}\left(\tau_{i,j}^s\right) & \text{if } M_i = 1\\ \tilde{L}_{\boldsymbol{r}_{i,j}^s}\left(\phi_{i,j}^s,\tau_{i,j}^s,\boldsymbol{g}_{\mathrm{RI},i}^s\right) & \text{if } M_i > 1,\end{cases} \tag{5.32}$$

is defined separately for receiving nodes with singleport and with multiport antennas. For a singleport antenna, $\tilde{L}_{\boldsymbol{r}_{i,j}^s}\left(\tau_{i,j}^s\right)$ is defined by (5.17) and for a multiport antenna, $\tilde{L}_{\boldsymbol{r}_{i,j}^s}\left(\phi_{i,j}^s,\tau_{i,j}^s,\boldsymbol{g}_{\mathrm{RI},i}^s\right)$ is defined by (5.20). The minimization problem for the update step of the Bayesian filter,

$$\hat{\boldsymbol{x}}^s = \arg\min_{\boldsymbol{x}^s} h(\boldsymbol{x}^s), \tag{5.33}$$

is solved by the BFGS algorithm, which requires the gradient

$$\nabla h(\boldsymbol{x}^s) = -\sum_{i\in\mathbb{N}}\sum_{j\in\mathbb{L}_i^s}\frac{\partial L_{\boldsymbol{r}_{i,j}^s}\left(\boldsymbol{x}_i^s,\boldsymbol{x}_j^s\right)}{\partial \boldsymbol{x}^s} - \left(\bar{\boldsymbol{\Sigma}}^s\right)^{-1}(\boldsymbol{x}^s-\bar{\boldsymbol{x}}^s). \tag{5.34}$$

The partial derivative of the log-likelihood function w.r.t. the state vector $\frac{\partial L_{\boldsymbol{r}_{i,j}^s}\left(\boldsymbol{x}_i^s,\boldsymbol{x}_j^s\right)}{\partial \boldsymbol{x}^s}$ in (5.34) is derived in Appendix C.12. BFGS is a quasi-Newton method [173]. Since $h(\boldsymbol{x}^s)$ in (5.33) is in general non-convex, care must be taken to ensure convergence. First, an informative prior $p(\boldsymbol{x}^0)$ is required for the initialization of the SLAC algo-

rithm at $s = 0$, which is detailed in Section 5.3.3. Second, the filter update rate must be chosen according to the system dynamics. A sufficiently high update rate is required, such that the position and orientation changes between two consecutive snapshots are small. Thus, the estimated state after prediction $\bar{\boldsymbol{x}}^s$, which is the starting point for BFGS, is always close to the estimated state after the update $\hat{\boldsymbol{x}}^s$. The simulation results in Section 5.4 show that the SLAC algorithm converges despite uncertainty in antenna responses and initializations. Furthermore, measurement results in Section 6.2.3 demonstrate convergence of SLAC with vague antenna response prior. Whether initialized with a prior antenna response obtained by EM simulation or in a near-field measurement chamber, cooperative SLAC converges to approximately the same DoA estimation performance, despite the antenna response from EM simulation deviates considerably from the true antenna response.

When the updated states estimate $\hat{\boldsymbol{x}}^s$ is calculated, the Laplace approximation [187] is applied to obtain the updated covariance matrix

$$[\hat{\boldsymbol{\Sigma}}^s]_{v,w} = \left(\frac{\partial^2 h(\boldsymbol{x}^s)}{\partial [\boldsymbol{x}^s]_v \partial [\boldsymbol{x}^s]_w} \bigg|_{\boldsymbol{x}^s = \hat{\boldsymbol{x}}^s} \right)^{-1} \tag{5.35}$$

by numerically calculating the inverse of the Hessian matrix at the obtained minimum in (5.33).

5.3.3 Prior

For $s = 0$, the Bayesian filter must be initialized. For that, we need an informative prior pdf for every node $i \in \mathbb{N}$,

$$p(\boldsymbol{x}^0) = \prod_{i \in \mathbb{N}} p(\boldsymbol{x}_i^0). \tag{5.36}$$

We assume the node prior pdf is Gausssian

$$p(\boldsymbol{x}_i^0) = (2\pi)^{-\frac{5}{2}} \det(\hat{\boldsymbol{\Sigma}}_i^0)^{-\frac{1}{2}} e^{-\frac{1}{2}(\boldsymbol{x}_i^0 - \hat{\boldsymbol{x}}_i^0)^T \hat{\boldsymbol{\Sigma}}_i^0 (\boldsymbol{x}_i^0 - \hat{\boldsymbol{x}}_i^0)}, \tag{5.37}$$

with mean

$$\hat{\boldsymbol{x}}_i^0 = \left[(\hat{\boldsymbol{p}}_i^0)^T \quad \hat{v}_i^0 \quad \hat{\psi}_i^0 \quad \hat{\omega}_i^0 \quad \hat{\delta}_i^0 \quad \left(\hat{\boldsymbol{g}}_{\mathrm{RI},i}^0\right)^T \right]^T \tag{5.38}$$

and covariance matrix

$$\hat{\boldsymbol{\Sigma}}_i^0 = \mathrm{diag}\left\{ \left[\mathbf{1}_2 \sigma_{\boldsymbol{p}^0}^2 / 2 \quad \sigma_{v^0}^2 \quad \sigma_{\psi^0}^2 \quad \sigma_{\omega^0}^2 \quad \sigma_{\delta^0}^2 \quad \mathbf{1}_{2MU} \sigma_{\boldsymbol{g}^0}^2 \right] \right\}. \tag{5.39}$$

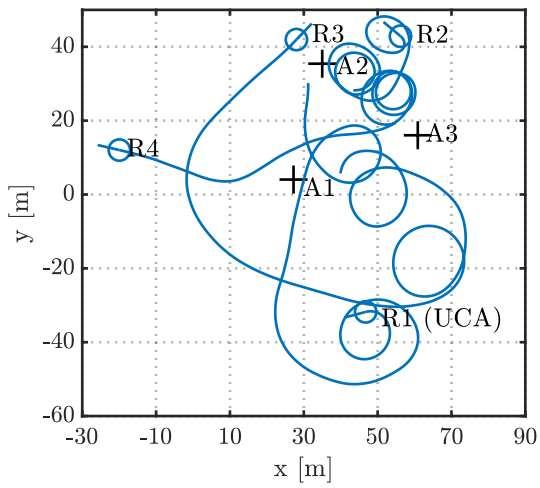

Figure 5.2. *Example simulation scenario with anchors A1, A2, A3 and randomly generated trajectories for agents R1 (UCA), R2, R3, R4 © 2022 IEEE [190].*

For nodes with singleport antenna, the sampling matrix elements $\hat{\boldsymbol{g}}^0_{\mathrm{RI},i}$ are omitted from the prior. The kinematic states of anchors are known exactly. For $s = 0$, the prior agent positions $\hat{\boldsymbol{p}}^0_i = [\hat{x}^0_i, \hat{y}^0_i]^T$ and orientations $\hat{\psi}^0_i$ with variances $\sigma^2_{\boldsymbol{p}^0}$ and $\sigma^2_{\psi^0}$ can be obtained by a snapshot-based cooperative localization algorithm, e.g. one of the algorithms [179, 188, 189], based on estimated distances and directions among the nodes. We assume that initially the agents are not moving, so we have $\hat{v}^0_i = 0\,\mathrm{m/s}$ and $\hat{\omega}^0_i = 0\,°/\mathrm{s}$. The ranging bias is expected to be small compared to the actual distance, so we initialize it as $\hat{\delta}^0_i = 0\,\mathrm{m}$. We further assume that a prior antenna response is available, e.g. from EM simulation or an antenna measurement in a near-field measurement chamber, see Section 2.3. Thus we have a matrix $\boldsymbol{E}_i$ available, which contains spatial samples of the antenna response at discrete directions, see (2.18) and (2.19). The prior sampling matrix

$$\hat{\boldsymbol{G}}^0_i = \boldsymbol{E}_i \boldsymbol{B}^H (\boldsymbol{B}\boldsymbol{B}^H)^{-1} \tag{5.40}$$

is then obtained as in (2.20), where we have added the subscript i to denote the respective agent.

5.4 Simulation Results

5.4.1 Simulation Setup

We evaluate the performance of the cooperative SLAC algorithm derived in Section 5.3 by simulation. For that, we compare SLAC to localization-only. To provide a fair

comparison, the same Bayesian filtering algorithm is applied to both, SLAC and localization-only. For localization-only, the node calibration states (5.6) are omitted from the node state vector (5.1). For the simulation, we assume a setup that is inspired by the experimental validation in Chapter 6. An example scenario is shown in Fig. 5.2. We have three anchors A1, A2, A3 and four moving agents R1, R2, R3, R4. The agent R1 is assumed to be equipped with a UCA with $M_i = 4$ antenna elements. The other agents and the anchors are equipped with singleport antennas. We perform a Monte Carlo simulation with 100 runs. For each run, we generate random trajectories for all agents based on the motion model (5.8) to (5.11). We assume an update interval of $T = 0.1\,\mathrm{s}$. The process noise parameters of the motion model (5.11) are $\sigma_{\dot{v}} = 0.015\,{}^{\mathrm{m}}/_{\mathrm{s}^{1.5}}$ for the linear and $\sigma_{\dot{\omega}} = 0.3\,{}^{\circ}/_{\mathrm{s}^{1.5}}$ for the angular velocity. One example realization of the random trajectories is shown in Fig. 5.2. By simulating random trajectories, we ensure that SLAC is not limited to specific motion patterns.

Furthermore, we randomly generate a sampling matrix $\boldsymbol{G}_i$ for the multiport antenna of agent R1 for each run. The random sampling matrix is generated by distorting the antenna response of a UCA, as outlined in Section 4.8.1, where we assume $\sigma_{\boldsymbol{g}} = 0.2$. Thus, we also demonstrate that SLAC is not limited to a specific antenna response. The ranging biases are also chosen randomly by $\delta_i \sim \mathcal{N}(0, \sigma_\delta^2)$ with $\sigma_\delta = 0.2\,\mathrm{m}$. The assumed standard deviations of the Gaussian prior (5.37) are $\sigma_{\boldsymbol{p}^0} = 2\,\mathrm{m}$, $\sigma_{v^0} = 0.01\,{}^{\mathrm{m}}/_{\mathrm{s}}$, $\sigma_{\psi^0} = 7.5^\circ$, $\sigma_{\omega^0} = 0.01\,{}^{\circ}/_{\mathrm{s}}$, $\sigma_{\delta^0} = 0.01\sigma_\delta$ and $\sigma_{\boldsymbol{g}^0} = 0.01\sigma_{\boldsymbol{g}}$. For the ranging biases and the sampling matrix elements, we have chosen a low prior covariance. Too fast adjustment of the ranging bias or the antenna response could cause the numerical optimization in (5.33) to get caught in a local minimum. At the beginning of each simulation run, position, orientation and the sampling matrix elements are initialized randomly by sampling from the Gaussian prior (5.37). Ranging bias and velocity states are initialized with zeros as described in Section 5.3.3.

The transmitted signals are Zadoff-Chu sequences [167] of length $N = 463$, which are mapped onto 925 subcarriers out of $N_{\mathrm{fft}} = 1024$ by occupying every second subcarrier. A unique sequence is assigned to each node. The sequences are chosen to have low cross correlation. The sampling rate is $B_{\mathrm{s}} = 31.25\,\mathrm{MHz}$ and the occupied bandwidth is $B \approx 28.2\,\mathrm{MHz}$. We further assume $P_{\mathrm{Tx}} = -15\,\mathrm{dBm}$ transmit power, $T_{\mathrm{n}} = 290\,\mathrm{K}$ receiver noise temperature, 8 dB noise figure, $f_{\mathrm{c}} = 1.68\,\mathrm{GHz}$ carrier frequency and free-space path loss. The system parameters are chosen to be in line with the experimental validation in Chapter 6, as summarized in Table 6.1.

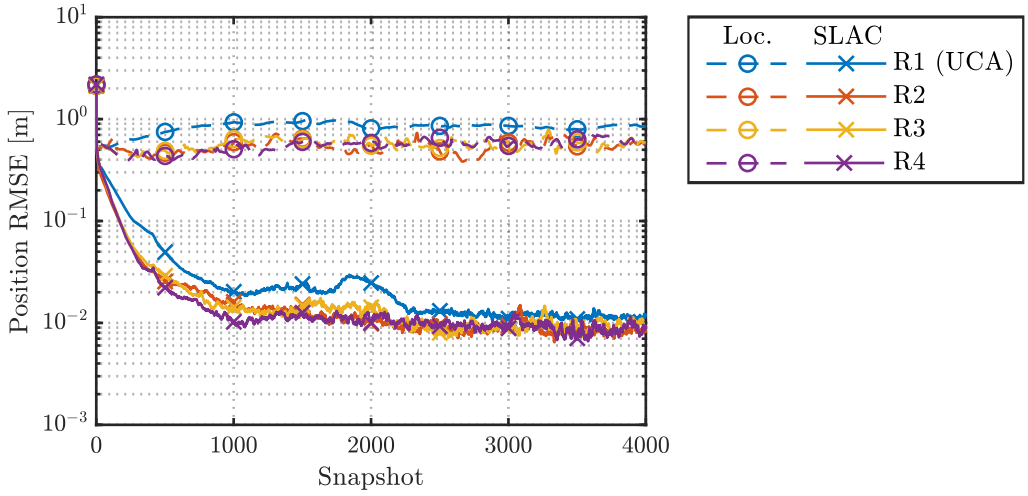

(a) *Position RMSE.*

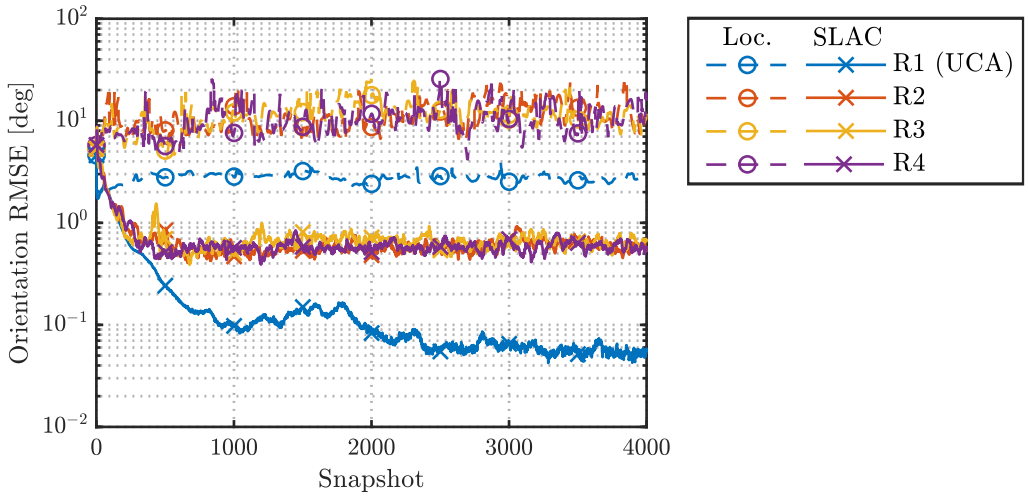

(b) *Orientation RMSE.*

Figure 5.3. *Position and orientation RMSEs of agents R1, R2, R3, R4 for simulation with* 100 *random trajectories. Localization-only is plotted with dashed, SLAC with solid lines.*

5.4.2 Position and Orientation Estimation

First, we compare the position RMSE of localization-only to SLAC on the basis of Fig. 5.3a. In the beginning, the position RMSEs are dominated by the prior. For localization-only, the position RMSEs drop quickly at the beginning. Then they stay relatively constant around 0.4 m to 1.0 m. With SLAC, due to the estimation of the calibration states, the position RMSEs decreases much more and reach cm level after approximately 1000 snapshots. Until $s = 2300$ the position RMSEs decrease further, as the estimations of the calibration states are refined. After $s = 2300$, the position RMSEs stay approximately constant. For localization-only and until $s = 2300$ also for SLAC, the position RMSE of R1 equipped with a multiport UCA is slightly worse

compared to the agents R2, R3 and R4, which are equipped with singleport antennas. The increased position RMSE is caused by a mismatch of assumed and true antenna response of R1. When the antenna response of R1 has been estimated by SLAC after $s = 2300$, its position RMSE is approximately the same as the position RMSE of the other agents. Nevertheless, the simulation for the chosen parameters, see Section 5.4.1, shows that SLAC is able to improve the position RMSEs by more than one order of magnitude compared to localization-only.

Second, we compare the orientation RMSE of localization-only to SLAC shown in Fig. 5.3b. With localization-only, the orientation RMSEs of agents R2, R3 and R4 with singleport antennas are around 5° to 25°. Agents R2, R3 and R4 are equipped with singleport antennas and by that are not able to observe their orientation directly. Instead, they can only infer their orientation over time through the motion model (5.9) when moving. Thus, the estimated orientations appear noisy. Agent R1 can observe its orientation not only indirectly through the motion model, but also directly by the UCA with four elements. Thus its orientation RMSE is around 3°, which is lower compared to the other agents. With SLAC, the orientation RMSEs of agents R2, R3 and R4 decrease to sub-degree level until $s = 500$. The ranging biases are estimated, which leads to more accurate distance information. The positions are estimated with higher accuracy, see Fig. 5.3a, and thus the position differences become more accurate, which leads to improved orientation accuracy. Furthermore, the UCA of agent R1 is being calibrated, which allows higher orientation accuracy for R1. After $s = 2000$, the orientation RMSE of R1 (UCA) is below 0.1°. The figure shows that for the chosen simulation parameters, see Section 5.4.1, SLAC improves also the orientation RMSE by more than one order of magnitude.

The analysis of position and orientation RMSEs shows the overall performance of SLAC. However, position and orientation RMSEs are subject to different aspects such as the geometry of the formation, the SNR and the motion model. In the following, we thus investigate antenna response calibration and ranging bias calibration separately.

5.4.3 Antenna Calibration

To investigate the antenna response calibration by SLAC, we evaluate the achieved DoA estimation performance over time. We apply the *C-ML* estimator (2.39) to estimate DoAs ϕ_q with $q \in \{1, ..., Q\}$ and $Q = 360$ spanning a regular grid over the manifold with step size 1°. The DoA estimation RMSE is then calculated over both, this grid and 100 different trajectories and antenna responses, see Section 5.4.1. Fig. 5.4 shows the resulting DoA estimation RMSE using the antenna response estimated by SLAC $\hat{\boldsymbol{a}}_i^s(\phi) = \hat{\boldsymbol{G}}_i^s \boldsymbol{b}(\phi)$, and the prior antenna response $\hat{\boldsymbol{a}}_i^0(\phi) = \hat{\boldsymbol{G}}_i^0 \boldsymbol{b}(\phi)$ for comparison.

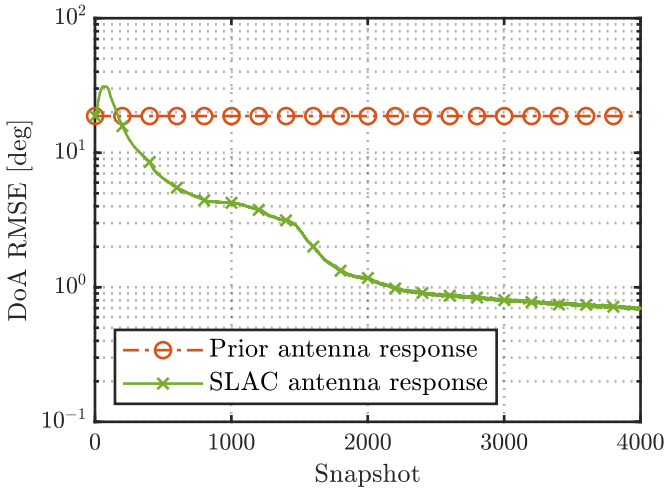

Figure 5.4. *ML DoA estimation RMSE calculated over manifold and* 100 *random trajectories and random antenna responses. The C-ML estimator* (2.39) *uses either the prior antenna response* $\hat{\boldsymbol{a}}_i^0(\phi) = \hat{\boldsymbol{G}}_i^0\boldsymbol{b}(\phi)$ *or the antenna response estimated by SLAC* $\hat{\boldsymbol{a}}_i^s(\phi) = \hat{\boldsymbol{G}}_i^s\boldsymbol{b}(\phi)$ *© 2022 IEEE [190].*

With the prior antenna response, the DoA estimation RMSE is approximately 11° due to the deviation of prior and true antenna response. When SLAC estimates the antenna response, initially the DoA estimation RMSE slightly increases. Then the DoA estimation RMSE using SLAC decreases, after $s = 2200$ to sub-degree accuracy. From the continuous improvement of the DoA estimation RMSE, we conclude that the estimated antenna response converges towards an antenna response which is equivalent to the true antenna response for DoA estimation, see Section 4.6.2. In summary, antenna response calibration by SLAC is feasible and improves DoA estimation performance.

5.4.4 Ranging Bias Calibration

Finally, we investigate ranging bias calibration by SLAC. Fig. 5.5 shows the ranging bias RMSEs for all nodes over time. The RMSE is also calculated over 100 Monte Carlo runs. The true ranging biases are of the order of several decimeters, see Section 5.4.1. Since the ranging bias prior is zero, this order of magnitude is directly reflected in the RMSEs of the estimated ranging biases. At the beginning, the ranging bias RMSEs of all nodes decrease quickly. After around $s = 1000$, the ranging bias RMSEs decrease more slowly and reach sub-centimeter levels after $s = 2100$. Interestingly, the ranging bias RMSE curves are visually separated into three distinct groups. The ranging bias RMSEs of the anchors A1, A2 and A3 reach the lowest values, which can be explained by their known positions. The agents R2, R3 and R4 with singleport antennas achieve lower ranging bias RMSEs than the agent R1 with four-element UCA. For R1, also the antenna response must be estimated simultaneously, which impacts ranging bias

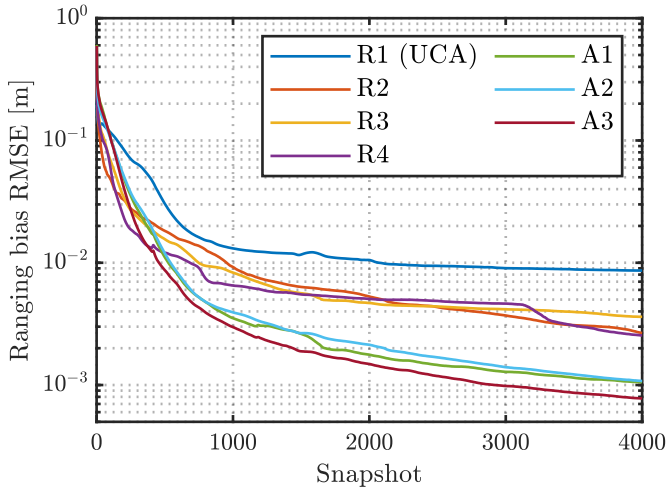

Figure 5.5. *Simulated ranging bias RMSEs over* 100 *random trajectories for agents R1, R2, R3, R4 and anchors A1, A2, A3 © 2022 IEEE [190].*

calibration. In conclusion, with SLAC the ranging biases of all nodes are estimated successfully for the simulated random trajectories. Ranging bias estimation by SLAC enhances the accuracy of distance information, which contributes to improved position and orientation estimation performance, see Fig. 5.3.

Chapter 6

Experimental Validation

In this chapter, we describe experiments, which we have conducted for validating the theoretical and simulation results obtained in the previous chapters. We introduce the cooperative localization testbed based on SDR and the hardware integration into robotic rovers for an outdoor experiment with multiple agents. Then we demonstrate DoA estimation with a single MMA. The in-situ antenna calibration algorithm proposed in Chapter 4 is evaluated with measurement data. Furthermore, we analyze the performance of antenna response and ranging bias calibration by cooperative SLAC.

6.1 Cooperative Localization Testbed

6.1.1 System Architecture

The experiments are based on a joint communication and localization system for robotic planetary exploration developed at the DLR [191]. The system is designed to enable joint communication with high update rates and high data rates and cooperative localization on the physical layer. Decentralized localization, exploration and control algorithms often require multiple iterations of information exchange over the network. Thus, high update rates are needed for a dynamic system [192], and the exchanged packets typically have low to medium size. High data rates are required e.g. to transfer data from scientific payloads or to allow remote operation of robots for special tasks. Channel access is provided by a self-organized TDMA scheme, in order to prevent a single point-of-failure. The system uses OFDM, as it is spectrally efficient and used in state-of-the-art communications systems, e.g. IEEE 802.11 Wi-Fi and 4G and 5G cellular networks. The self-organized TDMA scheme and the OFDM frame structure are visualized in Fig. 6.1. An OFDM frame consists of a guard time (GT), a preamble symbol with cyclic prefix (CP), and one or more data symbols with CP.

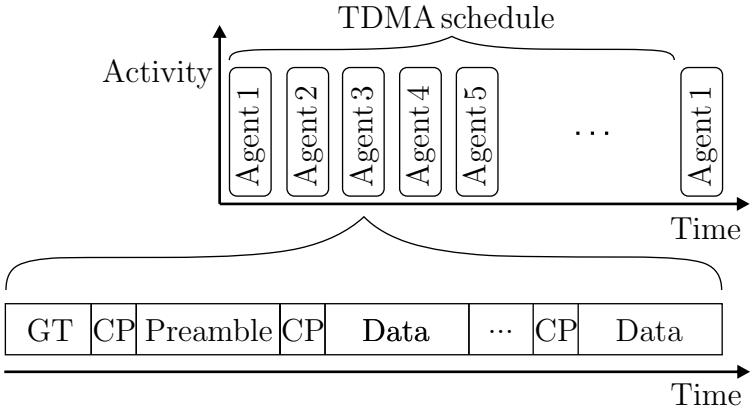

Figure 6.1. *TDMA scheme and OFDM frame structure with guard time (GT), cyclic prefix (CP), preamble and data symbols.*

Table 6.1. *Joint communication and localization system parameters.*

Parameter	**Variable**	**Value**
Carrier frequency	f_c	1.68 GHz
Sampling rate	B_s	31.25 MHz
Occupied bandwidth	B	$\approx$ 28.2 MHz
FFT length	N_{fft}	1024
Occupied subcarriers (preamble)	N	463
Occupied subcarriers (data)		924
Subcarrier spacing	f_{fsc}	$\approx$ 30.5 kHz
CP length		50 samples
TDMA schedule		100 ms
Transmit power	P_{Tx}	-15 dBm

The joint communication and localization system is designed as a flexible framework that can be tailored to specific mission requirements. The system parameters such as carrier frequency, bandwidth, number of subcarriers, number of OFDM symbols per frame etc. can be adapted. For the conducted experiments, the system parameters were chosen according to Table 6.1. The preamble is a Zadoff-Chu sequence [167] of length $N = 463$, which is mapped on 925 subcarriers by occupying every second subcarrier. The allocation of every second subcarrier enables efficient OFDM frame synchronization by differential correlation [193]. Every node in the network is assigned a unique Zadoff-Chu sequence, where the sequences are chosen to have low cross-correlation. The preamble is thus used for OFDM frame synchronization, node identification, ToA and channel estimation. For the experiments we used $N_{fft} = 1024$ FFT length and $B_s = 31.25$ MHz sampling rate, resulting in $B \approx 28.2$ MHz occupied bandwidth. The transmit power was $P_{Tx} = -15$ dBm.

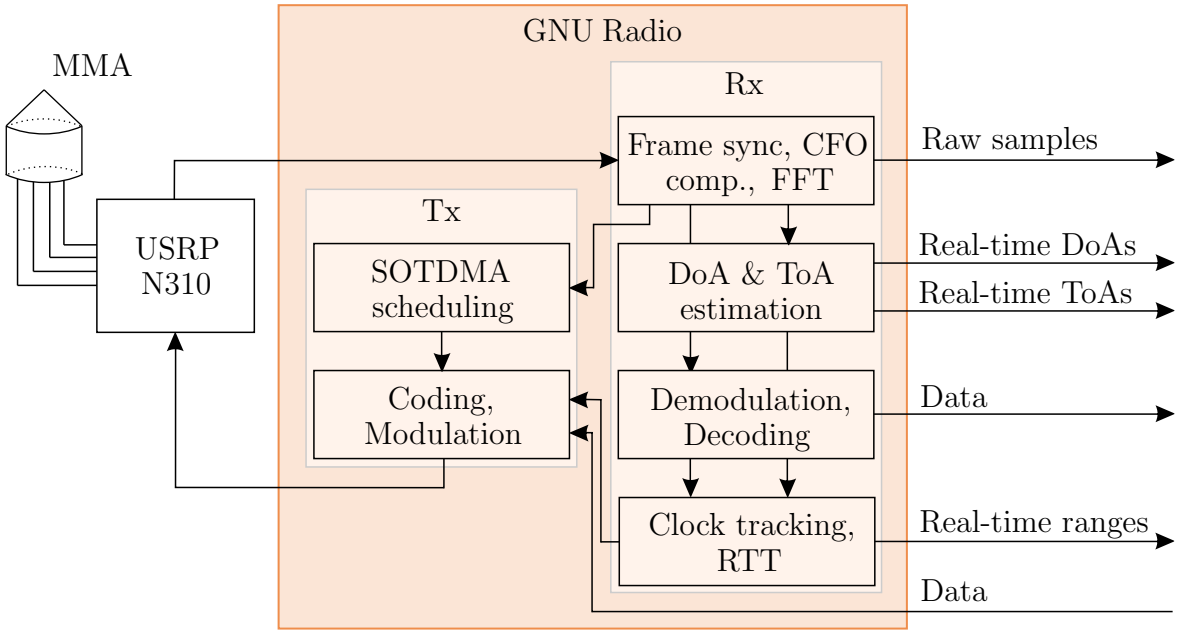

Figure 6.2. *Schematic of the SDR implementation in GNU Radio.*

6.1.2 Software-Defined Radio Implementation

A demonstrator of the joint communication and localization system has been implemented as SDR. For the four-port *MMA-2* introduced in Section 2.1, an Ettus Research Universal Software Radio Peripheral (USRP) N310 was used as coherent multichannel radio transceiver. The real-time signal processing was performed on a computer with signal processing blocks implemented within the GNU Radio software. The structure is shown in Fig. 6.2. The sampled signals are first passed to a block for OFDM frame detection and coarse frame synchronization [193]. The CFO is compensated and the signals are transformed to discrete frequency domain by an FFT. At this point, the signal samples in discrete frequency domain are also stored for post-processing together with meta data like timestamp etc. For the evaluations in Section 6.2 we use the stored preamble symbols, which we call snapshots. The transmitting node is identified from the preamble, then DoA and ToA of the signal are estimated, see Chapter 2. Then the received data symbols are demodulated and decoded. Based on the decoded transmit time stamp and the ToA, the signal RTT is calculated. Due to the delay between forward and backward transmission, see the TDMA schedule in Table 6.1, the relative frequency offset of transmitter and receiver oscillators is compensated, see [154] for more details. Data to be transmitted is encoded and modulated and the transmission is scheduled according to the self-organized TDMA scheme. For the nodes with single-port antenna, the Ettus Research USRP B200mini SDR is used. The signal processing in GNU Radio is analogous to Fig. 6.2, except without DoA estimation.

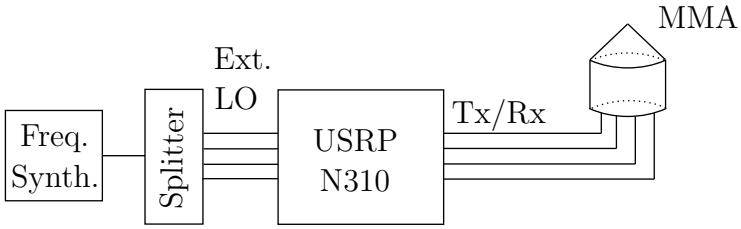

Figure 6.3. *USRP N310 setup with external LO.*

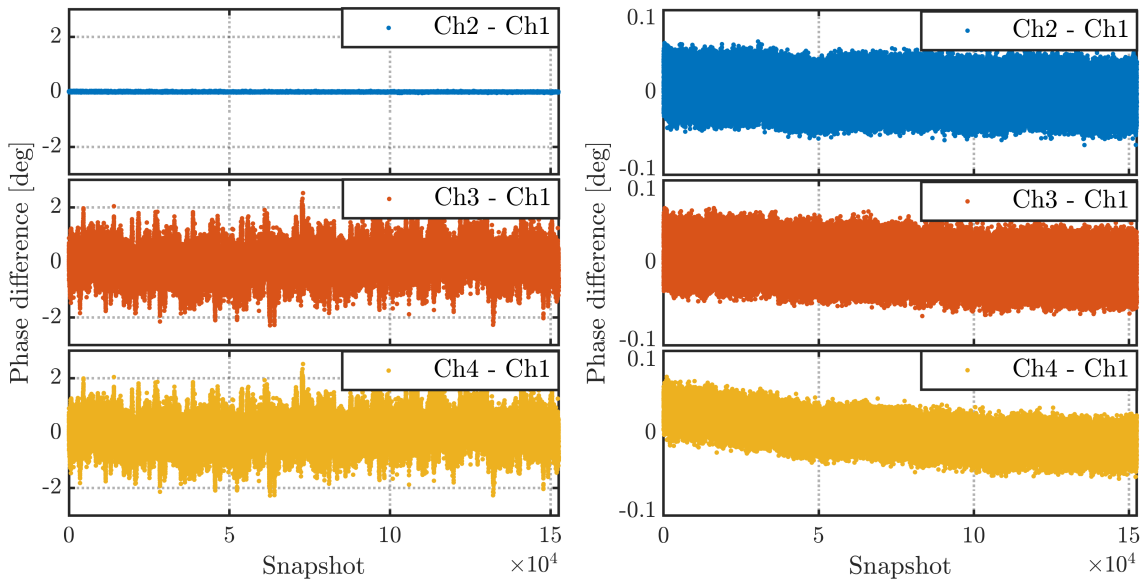

(a) *Internal LO.* **(b)** *External LO.*

Figure 6.4. *Phase difference between USRP N310 channels, averaged over snapshot length of* $N_{\text{fft}} = 1024$ *samples. Left and right figures have different y-axis scale.*

In Chapter 2 it is shown that for an MMA, DoA information is contained in both, amplitude and phase of the received signals at the different antenna ports. To fully exploit the DoA information, the receiver channels connected to the antenna ports must be phase-coherent. For the applied USRP N310, phase-coherency is achieved when the local oscillator (LO) is supplied externally. The setup is shown in Fig. 6.3. An external frequency synthesizer followed by a four-way splitter is used to generate four LO signals for Tx LO and Rx LO of each of the two radio-frequency integrated circuits (RFICs) inside the USRP N310. To verify phase coherency of the receiver channels, a CW signal is supplied to all four channels via an RF splitter. Phase differences between the channels are calculated and averaged over a snapshot length of $N_{\text{fft}} = 1024$ samples, which corresponds to one OFDM symbol. The resulting phase differences between the channels with internal LO are shown in Fig. 6.4a and with external LO in Fig. 6.4b. With internal LO, phase differences between channel two and channel one are small, as they share the same RFIC. However, for channels three and four, quickly varying phase

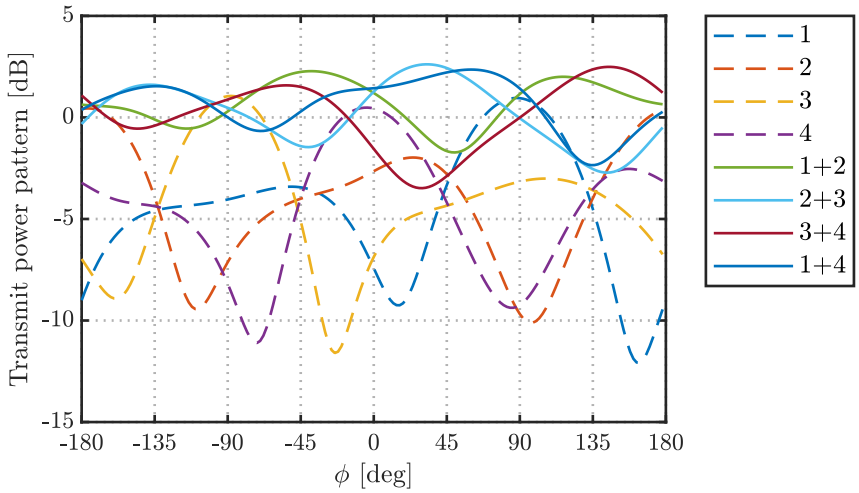

Figure 6.5. *Transmit power patterns of MMA-2 for linear vertical polarization, when a single antenna port or a combination of two antenna ports are used for transmission.*

differences w.r.t. channel one in the order of $1° - 3°$ are apparent. With external LO, the phase differences among all channels are below 0.1°, making this setup suitable for coherent DoA estimation. Constant amplitude imbalances and phase offsets between the channels are compensated by a calibration procedure.

The concept of the communication and localization system is based on broadcast transmission. However, the power pattern of *MMA-2*, which was used for the experiments, is highly direction-dependent, see Fig. 2.6a. For a broadcast system, omnidirectional coverage is desirable. A more omnidirectional power pattern of *MMA-2* is obtained when using multiple modes, i.e. multiple antenna ports, simultaneously for transmission. Fig. 6.5 shows the resulting transmit power pattern of *MMA-2* transmitting either on a single port or on two ports simultaneously. For the two port case, the same signal is fed to both antenna ports in-phase. For the experiments, a combination of ports 1 and 2 was used, resulting in a transmit power pattern varying from -1.7 dB to 2.3 dB.

6.1.3 Hardware Integration

Fig. 6.6a shows the multichannel SDR setup from Section 6.1.2 integrated into a custom assembly on top of a Robotnik SUMMIT-XL rover. On the top plate, the *MMA-2*, and two GNSS antennas for a commercial two-antenna GNSS RTK system are mounted [194]. The GNSS RTK system also uses inertial sensors internally and provides position and orientation ground truth for the experiments. The MMA is connected to the Ettus Research USRP N310 SDR. The LO for the USRP N310 is provided by an external frequency synthesizer via a splitter, see Fig. 6.3. The USRP N310

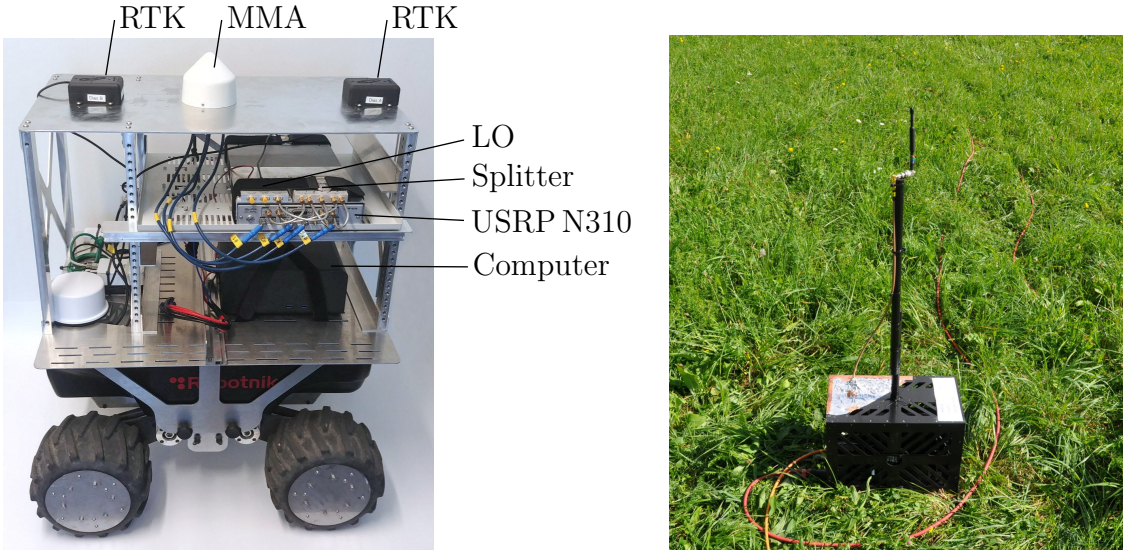

(a) *Rover Dias with USRP N310 and MMA.* **(b)** *Anchor node.*

Figure 6.6. *Multichannel SDR Ettus Research USRP N310 with external LO and MMA-2 integrated on robotic rover Dias and an anchor node.*

is connected to a computer, where the real-time signal processing is performed in GNU Radio according to the schematic in Fig. 6.2. Three anchors are each equipped with a dipole antenna, the singlechannel SDR Ettus Research USRP B200mini and a computer for real-time signal processing. One of the anchors is shown in Fig. 6.6b. Fig. 6.7 shows three Robotnik SUMMIT-XL rovers Drake, Magellan and Vespucci with custom assembly next to the experimental site. The three rovers are equipped with a singleport dipole antenna. Equal to the anchors, they are each equipped with the singlechannel SDR Ettus Research USRP B200mini and a computer for real-time signal processing. Furthermore, they are also equipped with a commercial two-antenna GNSS RTK system for ground truth.

6.2 Measurement Results

We use two different sets of measurement data, the *single-agent scenario* and the *multi-agent scenario*, for the experimental validation. Recorded data from the *single-agent scenario* is used to demonstrate DoA estimation with a single MMA in Section 6.2.1 and to evaluate the in-situ antenna calibration algorithm in Section 6.2.2. To analyze the performance of cooperative SLAC in Section 6.2.3, we use data from the *multi-agent scenario*.

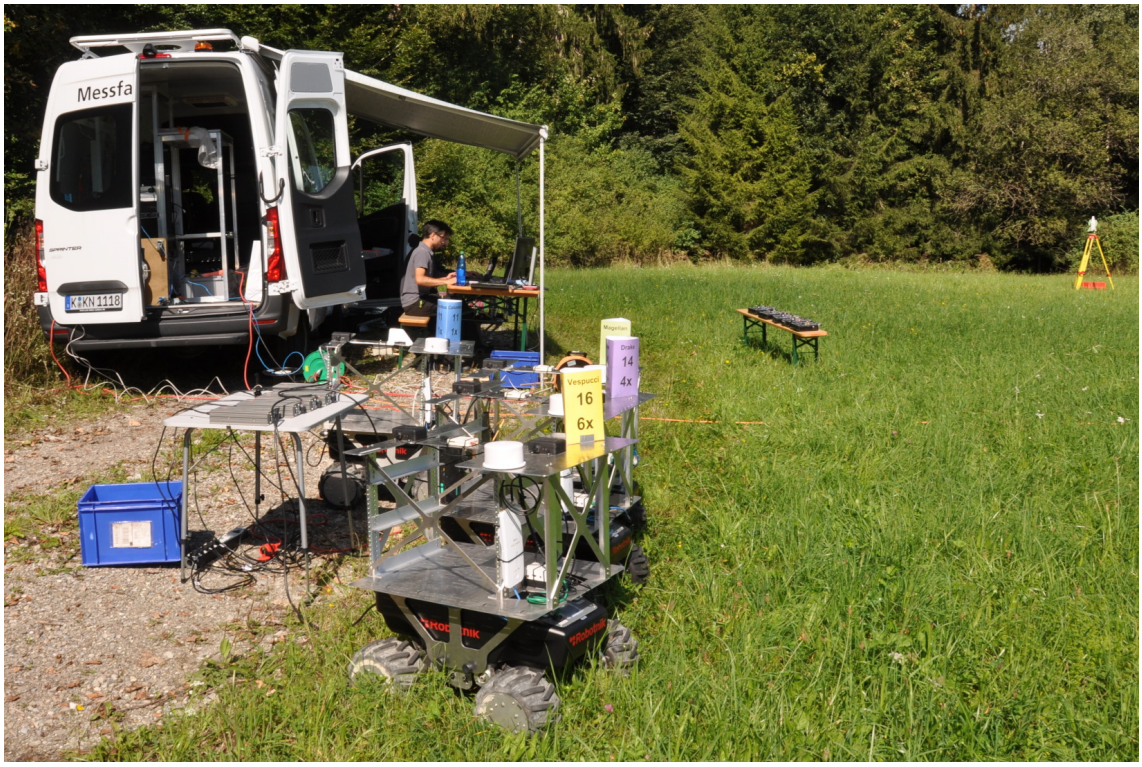

Figure 6.7. *Robotic rovers Vespucci, Drake and Magellan and the outdoor control center next to the experimental site.*

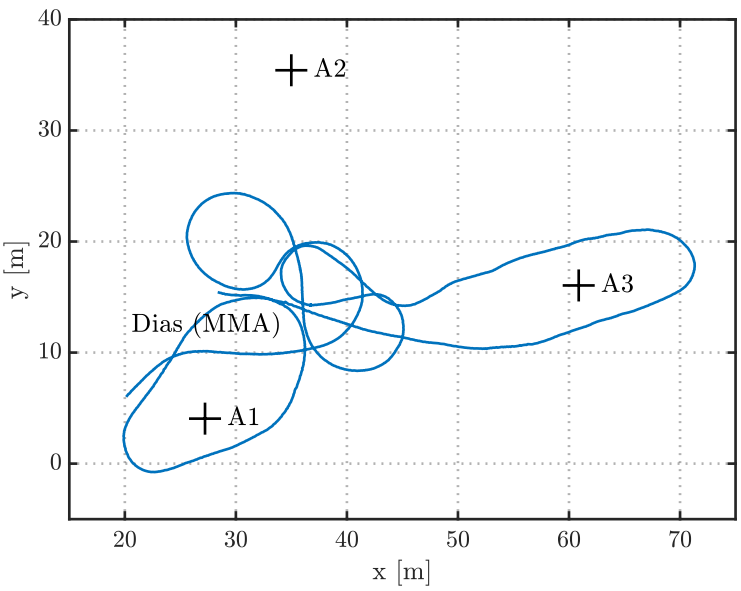

Figure 6.8. *Map of the single-agent scenario with the trajectory of the robotic rover Dias with MMA and three anchors A1, A2 and A3.*

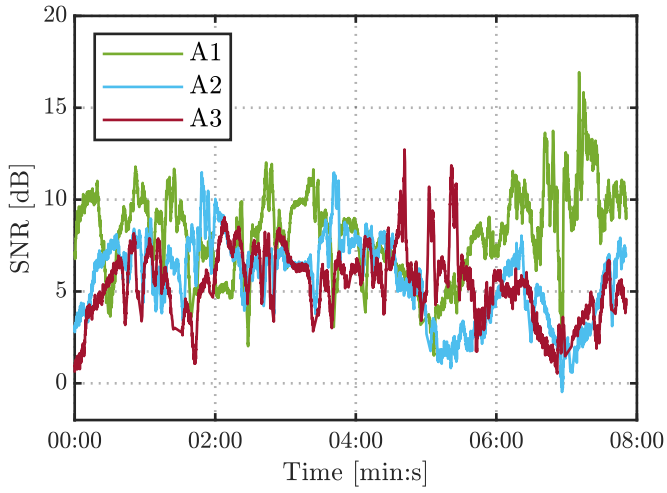

Figure 6.9. *SNR of the signals received by the MMA on Dias from the anchors nodes A1, A2 and A3 for the single-agent scenario.*

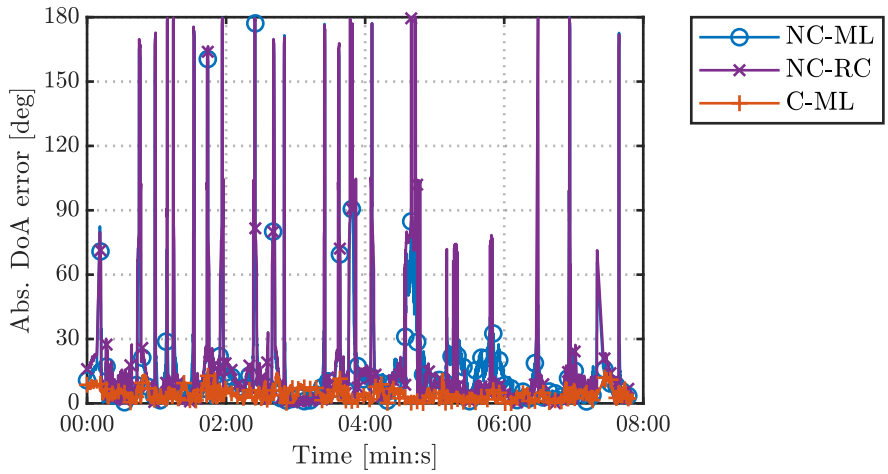

Figure 6.10. *Absolute DoA estimation error* $|\hat{\phi}^s_{i,j} - \phi^s_{i,j}|$ *for signals received from anchor A2 using non-coherent ML estimator (NC-ML)* (2.28)*, non-coherent RC estimator (NC-RC)* (2.34) *or coherent ML estimator (C-ML)* (2.39) *for the single-agent scenario.*

6.2.1 DoA Estimation with a Multi-Mode Antenna

Fig. 6.8 shows a map of the *single-agent scenario* with three anchor positions and the ground truth trajectory of the robotic rover Dias with installed MMA. The anchor positions were measured with a tachymeter. The rover was driving with a speed in the range of 0.3 m/s to 0.6 m/s.

The estimated SNR of the signals received by the MMA installed on Dias from the three anchors is shown in Fig. 6.9, where an ML SNR estimator based on the known preambles was used [185]. The SNRs vary due to changing distances, but also due to fading caused by the ground reflection.

First, we experimentally validate the simulation results presented in Chapter 2,

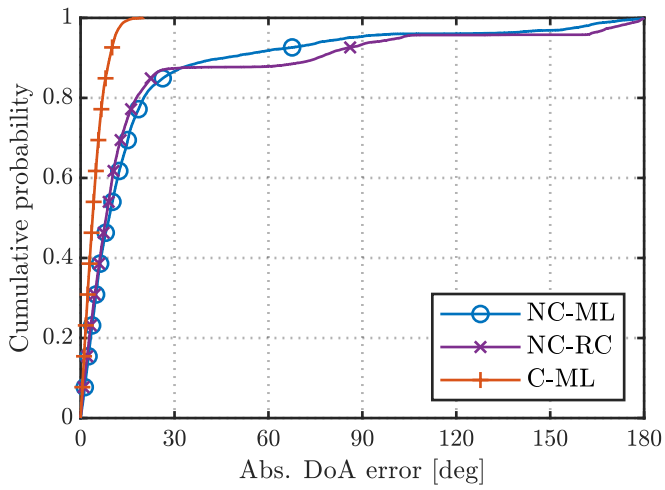

Figure 6.11. *Empirical CDF of the absolute DoA estimation error* $|\hat{\phi}^s_{i,j} - \phi^s_{i,j}|$ *for all signals received from the anchors A1, A2 and A3 using non-coherent ML estimator (NC-ML)* (2.28)*, non-coherent RC estimator (NC-RC)* (2.34) *or coherent ML estimator (C-ML)* (2.39) *for the single-agent scenario.*

where we compare different DoA estimators for an MMA. We consider the non-coherent ML estimator (*NC-ML*) (2.28) and the non-coherent reduced-complexity estimator (*NC-RC*) (2.34). The non-coherent estimators are based solely on RSS estimates of the different antenna ports and aim at simpler receiver architectures. For the *NC-RC* estimator, the noise variance is estimated separately from the receiver noise floor. We also analyze the coherent ML estimator (*C-ML*) (2.39), which requires a coherent multichannel receiver to account for the MMA phase response. For the estimators, we use the antenna response of *MMA-2* measured in a near-field measurement chamber, see Figs. 2.6 and 6.13. Fig. 6.10 shows the absolute DoA estimation error $|\hat{\phi}^s_{i,j} - \phi^s_{i,j}|$ over time using the three different estimators for the signals received from anchor A2. Both non-coherent estimators show large outliers up to 180°. The outliers are caused by estimation ambiguities, see Section 2.4.4. For the coherent DoA estimator, the absolute estimation error always remains $< 15°$ without outliers. The outliers of the non-coherent estimators are sparse, but also in between outliers the error is larger compared to the coherent estimator.

To further investigate the performance of the different DoA estimators, we analyze the empirical cumulative distribution function (CDF) of the absolute DoA estimation error $|\hat{\phi}^s_{i,j} - \phi^s_{i,j}|$ for the signals received from A1, A2 and A3, shown in Fig. 6.11. The CDF reveals that for both non-coherent estimators, less than 15% of the observations are outliers. If they can be filtered out, non-coherent DoA estimation with an MMA is a feasible option for low-cost receivers with less strict requirements on DoA accuracy. For $|\hat{\phi}^s_{i,j} - \phi^s_{i,j}| < 30°$, the performance of *NC-ML* and *NC-RC* is comparable. However, *NC-*

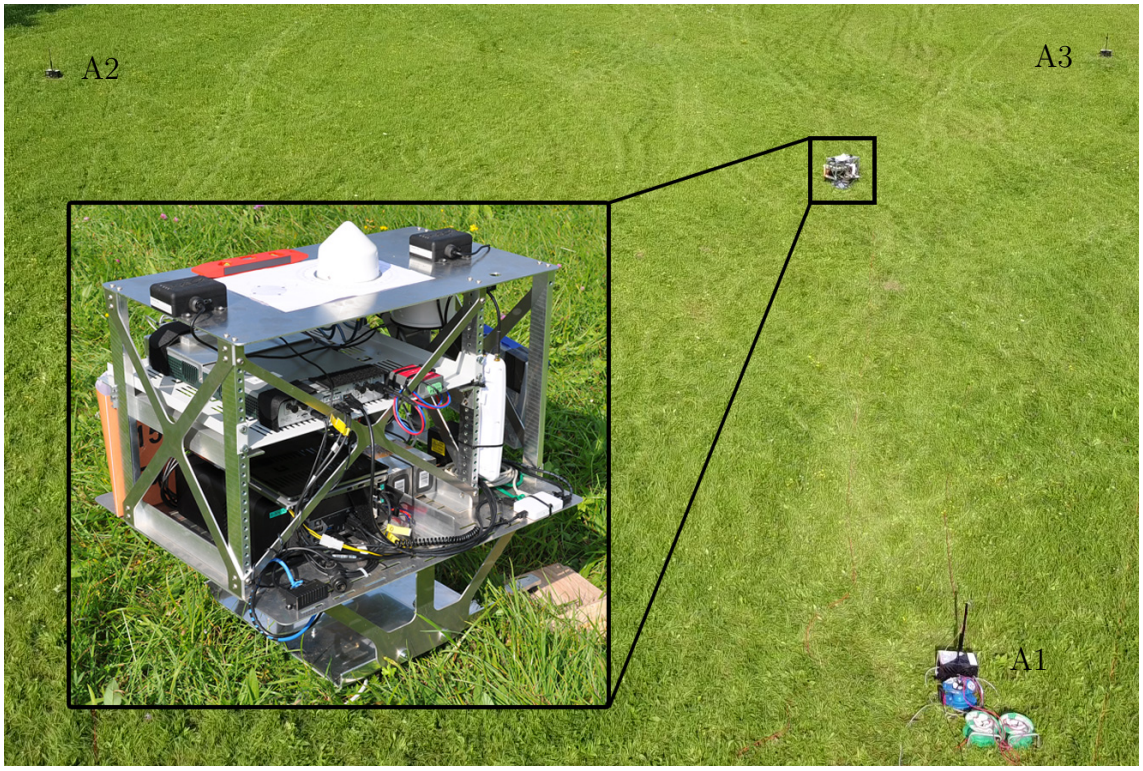

Figure 6.12. *Aerial view of the in-situ calibration with MMA assembly on turntable and anchors A1, A2, A3.*

RC has also slightly more outliers. From the empirical CDF, but also from Fig. 6.10, we see that there are two groups of outliers, one in the range of $60° < |\hat{\phi}^s_{i,j} - \phi^s_{i,j}| < 110°$ and one in the range of $160° < |\hat{\phi}^s_{i,j} - \phi^s_{i,j}| \leq 180°$. The outliers indicate 90° and 180° estimation ambiguities for the non-coherent DoA estimation. The coherent DoA estimator outperforms both non-coherent estimators and shows a 90th percentile DoA estimation error of 9.3°. In conclusion, the experiment has shown that DoA estimation with a single MMA is feasible. The simulation results from Section 2.4.4 have been confirmed regarding the difference between non-coherent and coherent DoA estimation. However, the accuracy level predicted by theory and simulation could not be achieved in practice. The reason are biased estimates due to a mismatch of the antenna response used by the estimator and the true antenna response of the MMA. To reduce the model mismatch and improve DoA estimation performance, we perform in-situ antenna calibration.

6.2.2 In-Situ Antenna Calibration

For the validation of the in-situ antenna calibration introduced in Chapter 4 we recorded measurement data, where the assembly with installed MMA was mounted on a turntable, see Fig. 6.12. The MMA assembly on the turntable was placed in

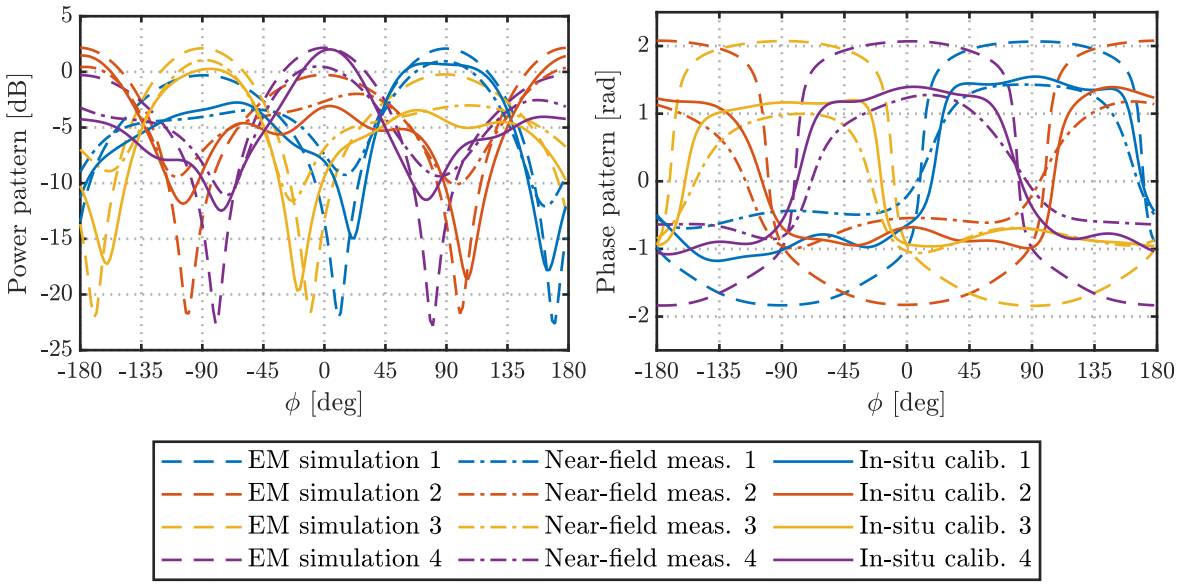

Figure 6.13. *Power pattern and phase pattern of ports 1-4 of the MMA obtained by EM simulation, in a near-field measurement chamber and by in-situ calibration.*

between the three anchors. Two full turns of the turntable were performed, during which a total of $S = 2264$ snapshots were received, 757 from A1, 750 from A2 and 747 from A3. The average estimated SNR of the received signals was 12 dB for A1, and 9 dB for A2 and A3.

The in-situ calibration algorithm introduced in Section 4.4 was applied to the recorded data. The antenna responses of the *MMA-2* from EM simulation, obtained in a near-field measurement chamber and by the in-situ calibration algorithm are shown as power and phase patterns in Fig. 6.13. The antenna response from the near-field measurement chamber was used to initialize the in-situ calibration algorithm. The antenna response of the MMA from EM simulation deviates considerably from the measured antenna response, as the antenna was simulated in free-space and the simulation does not account for imperfect manufacturing etc. The antenna response from in-situ calibration is closer to the measured antenna response, nevertheless deviations in power and phase are visible.

Fig. 6.14 shows the absolute DoA estimation error of the coherent *C-ML* estimator (2.39) using the three different antenna responses for the signals received from anchor A2 over time. Again, we use the recorded measurement data from the *single-agent scenario*. Using the antenna response from EM simulation clearly shows the highest DoA estimation errors up to 29.5°. With the antenna response from the near-field measurement chamber, the DoA estimation errors are reduced to a maximum error of 14.3°. This error curve is identical to *C-ML* from Fig. 6.10. With the antenna

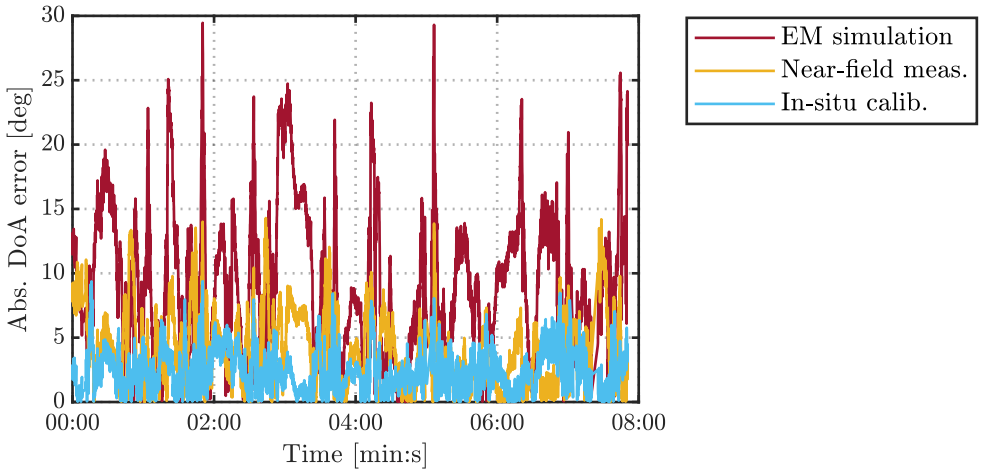

Figure 6.14. *Absolute DoA estimation error* $|\hat{\phi}^s_{i,j} - \phi^s_{i,j}|$ *with the C-ML estimator* (2.39) *for the signals received from anchor A2 using the antenna response from EM simulation, from the near-field measurement chamber and from in-situ calibration for the single-agent scenario.*

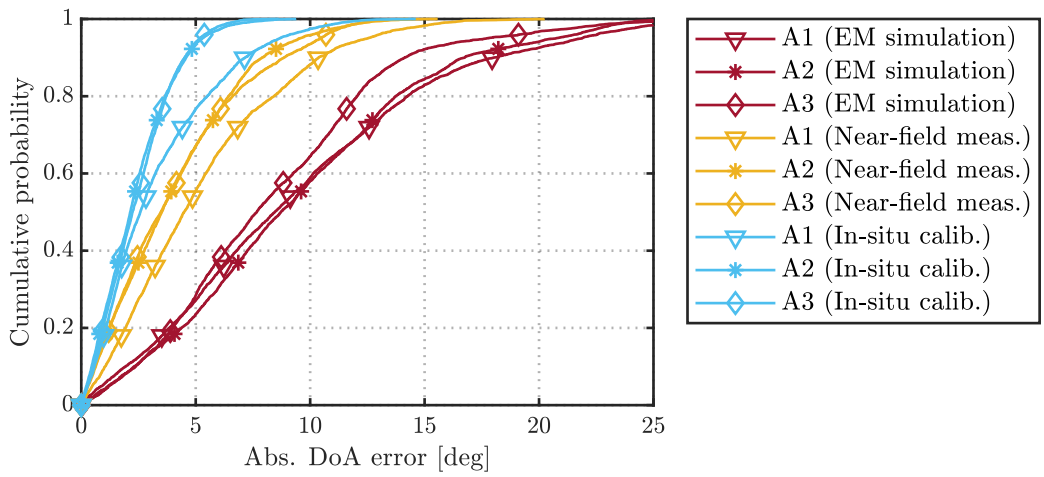

Figure 6.15. *Empirical CDF of the absolute DoA estimation error* $|\hat{\phi}^s_{i,j} - \phi^s_{i,j}|$ *with the C-ML estimator* (2.39) *for the signals received from the anchors A1, A2, A3 using the antenna response from EM simulation, from the near-field measurement chamber and from in-situ calibration for the single-agent scenario.*

response from in-situ calibration, the lowest DoA estimation errors are achieved and the maximum error is reduced to 9.4°.

To further evaluate in-situ antenna calibration, we have a look at the empirical CDF of the absolute DoA estimation error $|\hat{\phi}^s_{i,j} - \phi^s_{i,j}|$ shown in Fig. 6.15. The figure shows the individual curves for the signals received from anchors A1, A2 and A3, respectively. For all three anchors, DoA estimation performance using the antenna response from in-situ calibration is superior to the antenna response from the near-field measurement. DoA estimation with the antenna response from the near-field measurement performs

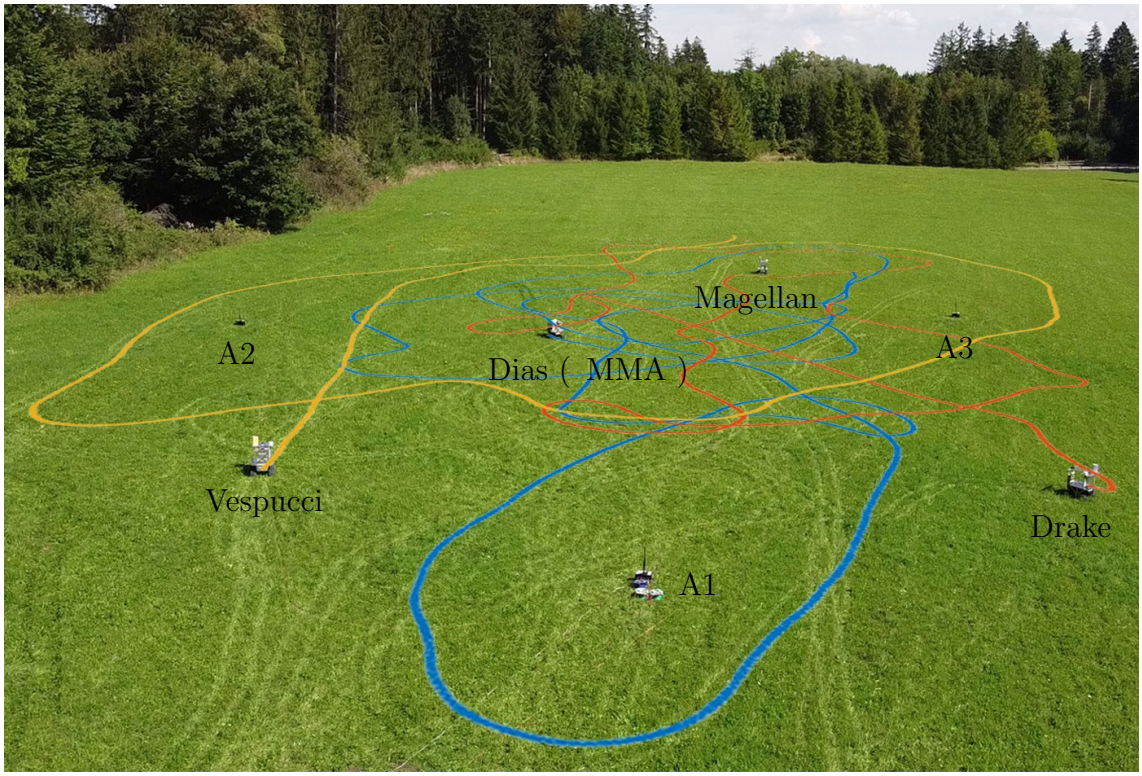

Figure 6.16. *Aerial view of the multi-agent scenario with the trajectories of agents Dias (MMA) in blue, Drake in orange, Vespucci in yellow and the positions of agent Magellan and anchors A1, A2, A3.*

better than with the antenna response from EM simulation. A1 shows higher DoA errors than A2 and A3 with antenna responses from near-field measurement and in-situ calibration, despite higher SNR values. A potential cause could be that the dipole antenna of A1 is not perfectly vertical, which also leads to a model mismatch. With in-situ calibration, the 90th percentile DoA estimation error for the signals received from all three anchors has improved from 9.5° to 6.7° compared to antenna calibration in a near-field measurement chamber, see also Fig. 6.20.

6.2.3 Cooperative Simultaneous Localization and Calibration

Position and Orientation Estimation

To experimentally validate SLAC introduced in Chapter 5, we conducted the *multi-agent scenario* experiment shown in Fig. 6.16 with the robotic rovers Dias with MMA, Drake, Vespucci and Magellan. The total duration of the experiment was 12 min 30 s. For the first part of the experiment, only Dias was moving. For the second part starting around 6 min, Drake and Vespucci were moving as well. Magellan remained static during the whole experiment. Dias traveled a total distance of 326 m, Drake

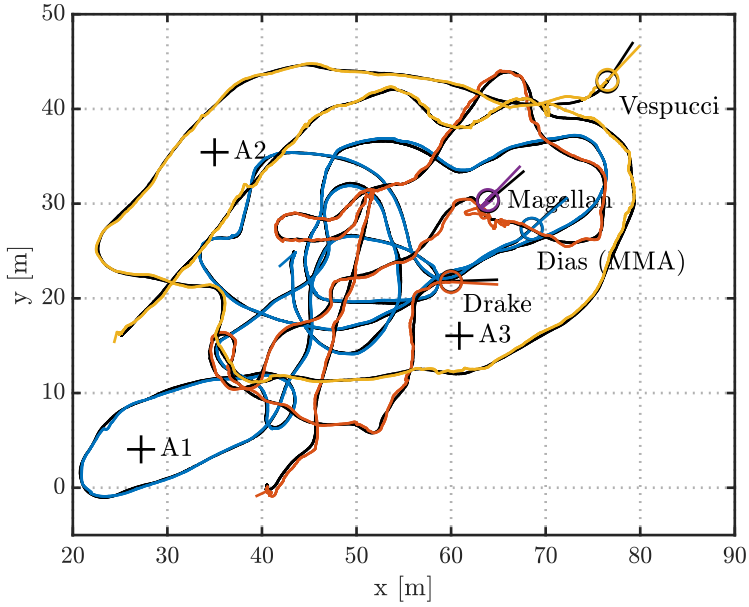

Figure 6.17. *Map of the multi-agent scenario with the positions of anchors A1, A2, A3 and the trajectories estimated by SLAC of agents Dias (MMA) in blue, Drake in orange, Vespucci in yellow, Magellan in purple and underlaid ground truth agent trajectories in black. The markers at the end of the respective trajectories show the estimated agent orientation and ground truth.*

201 m and Vespucci 211 m. Again, all received signals were recorded and evaluated in post-processing.

The parameters for the SLAC algorithm were chosen identical to the simulation from Section 5.4.1. To account for experimental effects like shaking of the rovers due to rough terrain, the noise standard deviation of the received signals $\sigma_{\boldsymbol{r}_{i,j}^s}$ was multiplied by two to increase the assumed observation variance. Fig. 6.17 shows the estimated trajectories of the robotic rovers Dias with MMA, Drake, Vespucci and Magellan by SLAC. The estimated trajectory of each agent is underlaid with the corresponding ground truth in black. All trajectories are very close to the ground truth, which indicates accurate position estimation by SLAC.

Analogous to the simulation results shown in Section 5.4, we compare SLAC to localization-only for a detailed performance analysis. For a fair comparison, the Bayesian filtering algorithm derived in Section 5.3 is applied to both SLAC and localization-only. For localization-only, the calibration states (5.6) are not part of the state vector. Fig. 6.18 shows the absolute position error of the agents for the second part of the measurements, from 6 min to 12 min 30 s, when all agents except Magellan are moving. For the agents Dias with MMA, Drake and Vespucci, cooperative SLAC considerably improves the position estimation compared to localization-only. For Dias, the 90th percentile position error was reduced by a factor of two, from 0.6 m

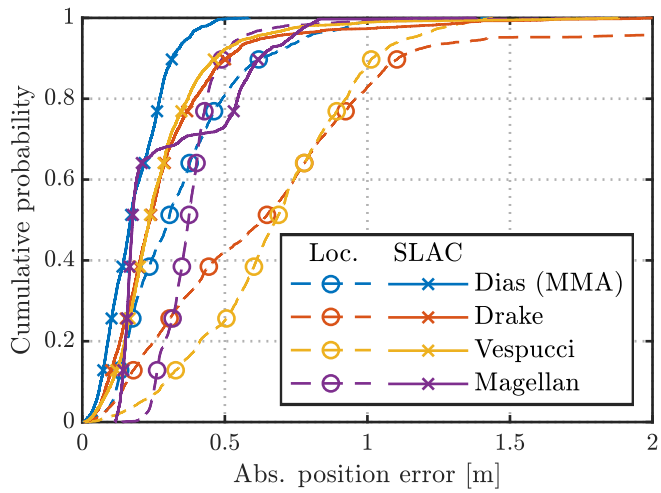

Figure 6.18. *Empirical CDFs of the absolute position error* $\|\hat{\boldsymbol{p}}_i^s - \boldsymbol{p}_i^s\|$ *of the agents for localization-only and SLAC.*

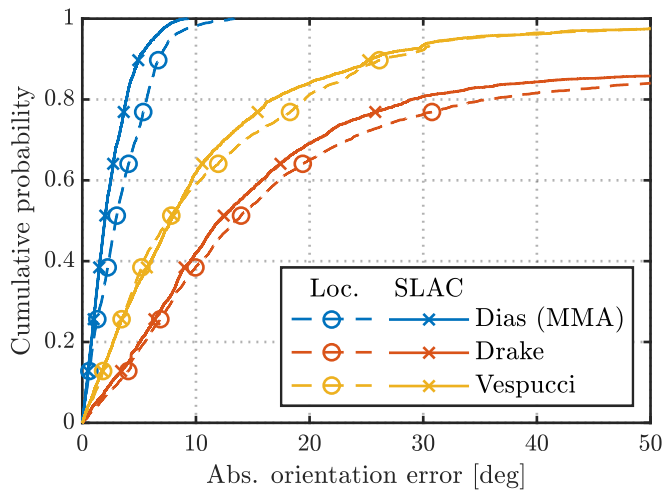

Figure 6.19. *Empirical CDFs of the absolute orientation error* $|\hat{\psi}_i^s - \psi_i^s|$ *of the agents for localization-only and SLAC.*

to 0.3 m. Magellan remained static during the experiment, which causes impaired observability of the calibration states and incorrectly estimated ranging bias for the first part, see Fig. 6.22. Thus the CDF curve of Magellan in Fig. 6.18 shows an amount of position estimates with larger position errors, which we attribute to the beginning of the second part, before the estimated ranging bias is corrected. We also see that the positioning performance of Dias with MMA is slightly better compared to Drake and Vespucci, which are equipped with singleport antennas. In conclusion, cooperative SLAC considerably improves the positioning performance compared to localization-only, which confirms the simulation results.

We now have a look at the empirical CDF of the absolute orientation error in Fig. 6.19. It stands out that the orientation estimation of Drake and Vespucci with

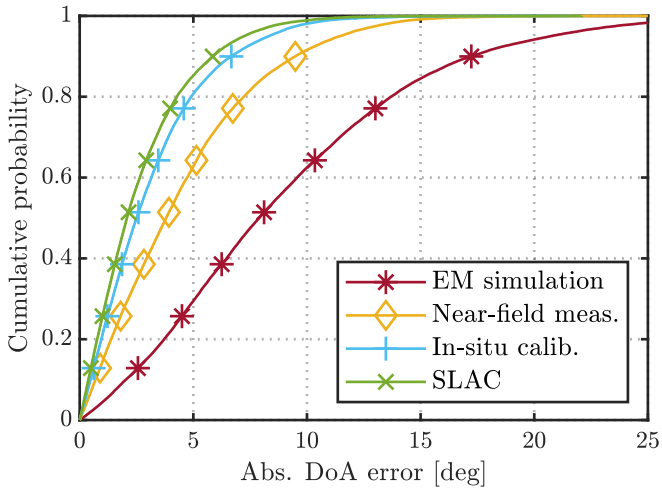

Figure 6.20. *Empirical CDF of the absolute DoA estimation error over all signals received by Dias (MMA), using the antenna response from EM simulation, from the near-field measurement chamber, from in-situ calibration and by SLAC.*

singleport antenna is considerably worse than the orientation estimation of Dias with the MMA. As we do not use additional sensors like gyroscopes, the agents with singleport antenna can observe their orientation only indirectly through position changes over time and the motion model (5.9). As Magellan is not moving, it cannot estimate its orientation and is not shown in Fig. 6.19. In the simulation results, orientation estimation of the agents with singleport antenna is also considerably worse compared to the agent with multiport antenna, see Fig. 5.3b. Fig. 6.19 shows that SLAC improves the orientation estimation compared to localization-only, the 90th percentile orientation error of Dias with MMA was reduced from 6.7° to 5.0°. The improvement is not as pronounced as in the position domain. A possible explanation could be found in the motion model (5.9). The model assumes constant linear velocity and constant angular velocity, which leads to overshoots or undershoots of the estimation when the velocities are changing. This could be solved by including other sensors, e.g. a gyroscope or wheel odometry, which could be considered by the Bayesian filter. However, our goal was to analyze the pure radio localization performance, without the influence of other sensors.

Position and orientation performance is influenced by different aspects like the geometry of the formation, propagation conditions, SNR, and the chosen motion model. To analyze the impact of calibration in a more isolated fashion, we treat antenna and ranging bias calibration separately.

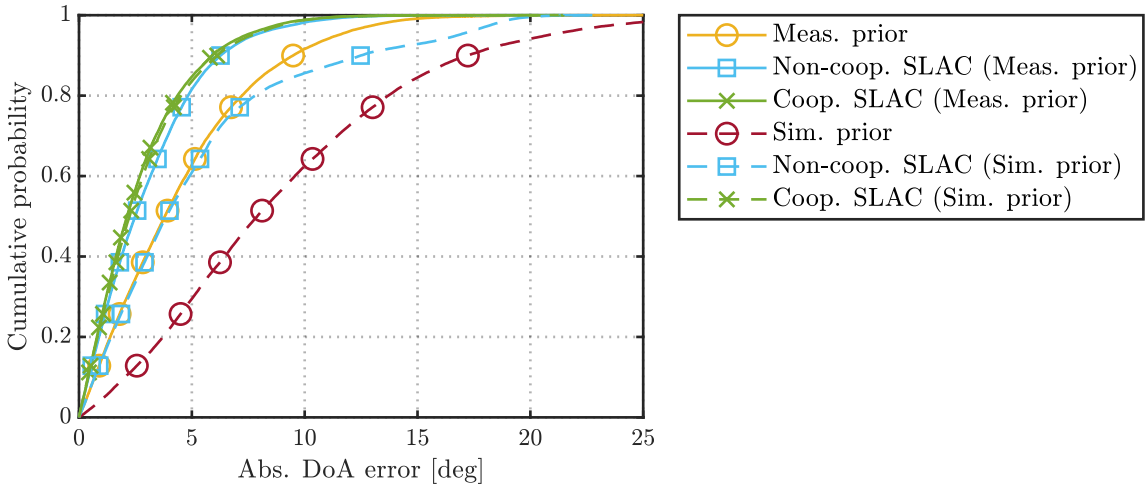

Figure 6.21. *Empirical CDF of the absolute DoA estimation error over all signals received by Dias (MMA), using the prior antenna response from a near-field measurement chamber (Meas. prior) and the antenna response estimated by non-cooperative and cooperative SLAC. A second case with the prior antenna response from EM simulation (Sim. prior) is shown with dashed lines.*

Antenna Calibration

To analyze antenna calibration by SLAC, Fig. 6.20 shows the empirical CDF of the absolute DoA estimation error $|\hat{\phi}^s_{i,j} - \phi^s_{i,j}|$. Similar to Fig. 6.15, in Fig. 6.20 we compare coherent DoA estimation with the *C-ML* estimator (2.39) using different antenna responses, but now for the *multi-agent scenario*. We consider the signals received by the MMA on Dias from all neighbors. DoA estimation is performed using the antenna response from EM simulation, near-field measurement chamber, in-situ calibration and the final estimation by SLAC, respectively. Fig. 6.20 shows that both, SLAC and in-situ calibration perform considerably better than antenna calibration in the near-field measurement chamber. Interestingly, SLAC slightly outperforms in-situ calibration.

Next, we want to investigate two aspects of antenna response calibration by SLAC in more detail. First, we want to analyze the benefit of cooperation. Thus, we compare non-cooperative SLAC, where no agent to agent links are present, to cooperative SLAC. Second, we are interested in the impact of the prior and the robustness of SLAC regarding a vague prior. Fig. 6.21 shows the empirical CDF of the absolute DoA estimation error using the prior antenna response and the final estimated antenna response by SLAC. We compare two cases with different prior antenna response, from near-field measurement chamber and EM simulation, respectively. For each case we analyze both, cooperative and non-cooperative SLAC. The DoA estimation error curves using directly the prior antenna responses from the near-field measurement and the EM simulation are identical to Fig. 6.20, but are shown again for comparison. With the

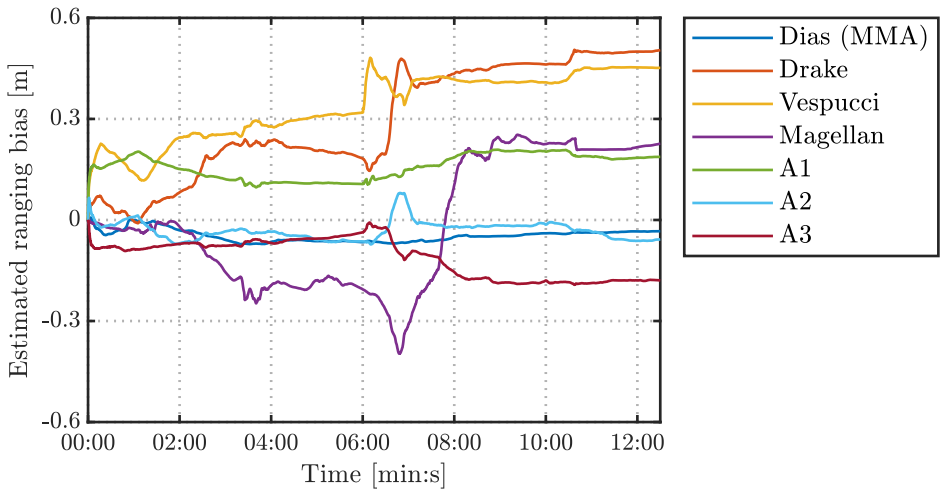

Figure 6.22. *Estimated ranging biases $\hat{\delta}_i^s$ for all nodes.*

prior antenna response from the near-field measurement chamber, cooperative SLAC is slightly better than non-cooperative SLAC. From Fig. 6.13, we see that the antenna response from the EM simulation deviates considerably and is thus considered as vague prior, where we assume $\sigma_{\boldsymbol{g}^0} = 0.3$ for the standard deviation of the Gaussian prior pdf of the sampling matrix elements. With the vague prior from EM simulation, the DoA estimation performance is improved by non-cooperative SLAC, but it remains slightly worse than using directly the antenna response from the near-field measurement. Cooperative SLAC, in contrast, achieves almost the same performance as with the more accurate prior antenna response from the near-field measurement. This result demonstrates the robustness of the SLAC algorithm w.r.t. a vague antenna response prior. From literature, it is known that cooperation improves position and orientation accuracy [20, 83, 22, 21, 23]. Applied to SLAC, cooperation leads to faster convergence of the antenna response calibration due to improved localization accuracy and higher number of observations.

Ranging Bias Calibration

Finally, we analyze ranging bias calibration by SLAC. The estimated ranging biases δ_i^s of all nodes over time are shown Fig. 6.22. Starting from the initial value 0 m, the ranging biases converge to preliminary estimates, which stay approximately constant from 3 min to 6 min. When Drake and Vespucci start moving at 6 min, the estimated ranging biases change again. After 8 min they stay approximately constant until the end. We conclude that motion is very important for the observability of the ranging biases. During the first part, where only Dias is moving, not all ranging biases are observable.

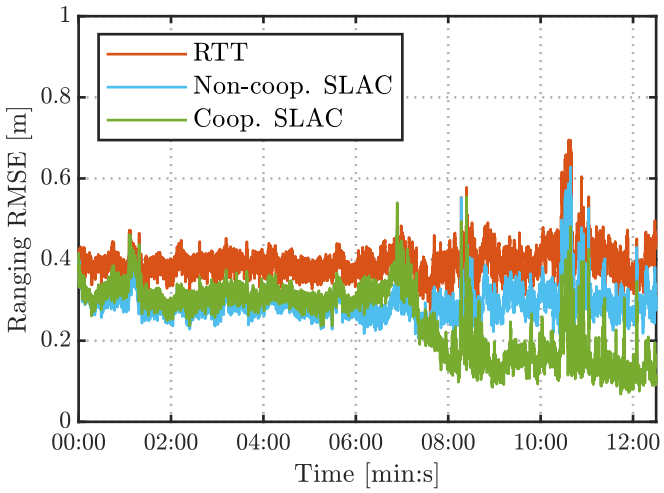

Figure 6.23. *Ranging RMSE over all links in the network without ranging bias correction (RTT) and with non-cooperative and cooperative SLAC.*

To evaluate the ranging accuracy with estimated ranging biases, we calculate the ranging RMSE over all links in the network $\sqrt{\sum_{i\in\mathbb{N}}(\sum_{j\in\mathbb{L}_i^s}|\hat{d}_{i,j}^s - d_{i,j}^s|^2/|\mathbb{L}_i^s|)/|\mathbb{N}|}$. From (5.3), the estimated distance with ranging bias correction by SLAC is $\hat{d}_{i,j}^s = c(\hat{\tau}_{i,j}^s - \bar{\tau}_{i,j}^s)/2 + \hat{\delta}_i^s + \hat{\delta}_j^s$. Without ranging bias correction (RTT), the estimated distance is obtained by the signal RTT, $\hat{d}_{i,j}^s = c(\hat{\tau}_{i,j}^s - \bar{\tau}_{i,j}^s)/2$. Fig. 6.23 shows the ranging RMSE without ranging bias correction and with ranging bias correction by non-cooperative and cooperative SLAC. For the first part until 6 min, non-cooperative and cooperative SLAC perform similar and both outperform RTT without ranging bias correction. For the second part from 6 min to the end, the ranging RMSE with non-cooperative SLAC remains the same. By cooperative SLAC, the ranging RMSE can be further improved, which is explained by the corrected ranging bias estimates of Drake, Magellan and A3, see Fig. 6.22. When the estimated ranging biases have converged, the ranging RMSE by cooperative SLAC is less than half of the RTT ranging RMSE. The spikes of the ranging RMSE affect all methods and are attributed to propagation conditions. In conclusion, cooperation is vital for the observability of the ranging biases.

Chapter 7

Conclusion and Outlook

7.1 Conclusion

In this thesis, we have investigated cooperative position and orientation estimation in radio networks. The estimation of positions and orientations requires distance and direction information. In the context of radio localization, distance and direction information is obtained by the ToA and DoA of radio signals.

To this end, we have started the analysis with a single MMA. An MMA is a single antenna element with multiple ports. Based on the excitation of orthogonal characteristic modes, it is especially promising in applications with tight size or shape constraints. The orthogonality property of the characteristic modes leads to orthogonal far-field characteristics of the antenna. Thus, the antenna response of an MMA strongly depends on the DoA, which enables DoA estimation, given the antenna response is known. While the potential of MMAs for MIMO communications had been realized earlier, we have provided a first study on their use for localization, specifically DoA estimation. As a first step, we have shown how a continuous representation of the MMA antenna response is obtained by wavefield modeling and manifold separation. Then different types of estimators have been studied. Their performance has been validated by simulations and experiments, for which a four-port MMA and an SDR have been integrated into a robotic rover. For low-complexity receivers, non-coherent DoA estimation solely based on RSS estimates of the different antenna ports is a suitable approach. Especially for the 3D case, i.e. azimuth and inclination estimation, the non-coherent approach suffers from ambiguities, which lead to estimation outliers. Better performance can be achieved including the phase response with coherent DoA estimation, which requires a receiver with multiple coherent channels. We have further shown how the polarization of incoming EM waves can be estimated jointly with the

DoAs using the investigated MMA. In conclusion, DoA estimation with a single MMA has been shown to be feasible and accurate by simulations and experiments.

We have then extended the perspective to a cooperative multi-agent system, where each agent is equipped with an MMA. We have performed a theoretical analysis by investigating the Fisher information for ToA and DoA. The Fisher information for ToA and DoA reveals the asymptotic independence of ToA and DoA estimation for high SNR, assuming a narrowband signal with symmetric spectrum. Intuitively, for separate estimation, ToA is estimated from the observation of a delayed baseband signal, while DoA is estimated from the relative amplitudes and phases of the antenna ports. Nevertheless, joint estimation of ToA and DoA is beneficial in the low SNR regime. We have then derived the CRB as a lower bound on the achievable position and orientation error for absolute and relative localization with MMAs. It allows to determine the impact of the agent formation on the localization accuracy and serves as a benchmark. However, the CRB is a variance bound. From both, literature and our own experiments, we have seen that the major contribution to the estimation MSE stems from the bias instead of the variance. Thus, there is a considerable gap between the performance achieved in practice and theoretical lower bounds. The biased estimates are caused by model mismatches. Specifically, we have identified two causes of estimation bias for radio localization. First, group delay variations in RF components of the transceiver hardware lead to ranging biases. Second, deviations of the antenna response assumed by the estimation algorithm from the true antenna response lead to biased DoA estimation.

To mitigate model mismatch and improve DoA estimation, we have investigated in-situ calibration of arbitrary multiport antennas, including MMAs. For in-situ calibration, we do not require a measurement chamber and synchronization between transmitter and receiver. The propagation channel is considered unknown for in-situ calibration, with possible multipath propagation. An external, noisy sensor is available to observe the LoS DoA. We have first performed a theoretical study of in-situ antenna calibration. Specifically, we have derived the Bayesian information for in-situ calibration to analyze the observability and to obtain the BCRB as benchmark. When the propagation channel is unknown, the absolute amplitude and phase of the antenna response cannot be observed. As DoA estimation is invariant to the absolute amplitude and phase, we propose to estimate an equivalent antenna response. In that case, the regular MSE is not a meaningful error metric, as absolute amplitude and phase offsets count as errors. Instead, we have introduced a transformed MSE as a figure of merit. The derived Bayesian information matrix for in-situ calibration is rank deficient when the propagation channel is unknown and no prior information is available.

Still, a meaningful BCRB can be obtained, which is a lower bound for the transformed MSE. We have then proposed an in-situ calibration algorithm based on a MAP estimator. The algorithm takes arbitrary nonidealities of real-world antennas like gain-phase offsets and mutual coupling into account. We have shown by simulation that the algorithm operates close to the BCRB. DoA estimation performance using in-situ calibration asymptotically approaches the case where the antenna response is perfectly known. We have also validated our in-situ calibration algorithm by an experiment. For that, we have mounted a rover assembly with integrated MMA onto a turntable. With in-situ calibration, the 90th percentile DoA estimation error for a measurement data set has improved from 9.5° to 6.7° compared to antenna calibration in a near-field measurement chamber. We conclude that in-situ antenna calibration for DoA estimation in unknown propagation conditions is feasible, provided an external direction sensor is available.

In addition to in-situ calibration, we have also addressed calibration during operation. We have introduced cooperative SLAC, which leverages the large amount of observations available in a cooperative network. Cooperative SLAC estimates and tracks antenna responses and ranging biases of the agents simultaneously with their positions and orientations, without external sensors. Implementing cooperative SLAC as a Bayesian filter poses two challenges. First, considering antenna response calibration causes a high state dimensionality. Second, evaluating the received signals directly, which is required for the observability of the antenna response, results in a highly nonlinear observation model. We have consequentially derived a Bayesian filter for cooperative SLAC similar to an IEKF with Laplace approximation for the covariance update. Analogous to in-situ calibration, our algorithm can handle arbitrary antenna types and nonidealities. By simulations, we have shown that cooperative SLAC is able to accurately estimate ranging biases and antenna response deviations. Thus, ranging and DoA estimation are enhanced, which leads to a considerable improvement in position and orientation accuracy. We have demonstrated cooperative SLAC also experimentally for a multi-agent system with four robotic rovers and three anchors. With cooperative SLAC, the 90th percentile position error was reduced from 0.6 m to 0.3 m and the 90th percentile orientation error was reduced from 6.7° to 5.0° for the robotic rover with MMA compared to localization-only. We have found that cooperation and movement of the agents is crucial for the estimation of the ranging biases. The cooperative SLAC algorithm is robust regarding a vague antenna response prior, in which case we have shown a considerable cooperation gain. In conclusion, cooperative SLAC is a promising approach to perform or improve calibration during operation without

external sensors. Cooperative SLAC mitigates model mismatches and thus improves localization performance.

With this thesis, we have improved cooperative radio localization regarding multiple aspects. We have shown that MMAs can be employed for position and orientation estimation. Bridging theory and practice, we have proposed novel approaches to mitigate model mismatch and reduce the gap between theoretical lower bounds and real-world performance. Specifically, we have introduced in-situ calibration for arbitrary antennas and cooperative SLAC.

7.2 Outlook

In this thesis, we have shown the feasibility of DoA and ToA estimation with a single MMA by simulations and experiments. The two investigated MMAs were not specifically designed for that purpose. In order to further explore the potential of MMAs for localization, an interdisciplinary approach is required, as the requirements for radio localization should already be considered in the design phase of the MMA. Specific localization requirements include the polarization and the radiation characteristic, e.g. omnidirectional for ground-based robots or hemispherical if also aerial vehicles are considered. Regarding propagation time based approaches, the group delay and especially the direction dependency of the group delay of the antenna should be considered. Ultimately, the MMA response could be optimized for DoA estimation. We consider it promising to apply estimation theory already at the design phase of the antenna, to minimize DoA estimation lower bounds and improve ambiguity resolution.

By simulation, we have shown 3D DoA estimation of both azimuth and inclination with a single MMA in this thesis. Experimentally, we have demonstrated azimuth estimation with an MMA, as we were constrained to robotic rovers moving on a 2D plane. To demonstrate the full potential of MMAs for localization, an experimental validation of 3D DoA estimation would be worthwhile. For the 3D case, accurate knowledge of the antenna response might even be more critical, thus an extension of the in-situ antenna calibration algorithm to 3D would be of interest. Furthermore, also the extension of cooperative SLAC to 3D position and 3D orientation estimation would be a promising direction of future research, for instance to include also aerial vehicles into the multi-agent system.

We have introduced the concept of cooperative SLAC and shown an implementation of SLAC as a centralized Bayesian filtering algorithm. In practice, a centralized approach implies that all observations in the network must be transmitted to a central computing unit, where the states of all nodes are estimated. The estimated states must

then be transmitted back to the nodes. In case not all nodes have a direct connection to the central computing unit, multi hop transmissions are required, leading to increased latency. In case of communication outages e.g. due to deep fading, nodes do not receive state updates. For centralized approaches, communication load grows quickly with the network size, posing a problem for larger networks. Furthermore, the central computing unit is a single point of failure, which is unfavorable especially for space missions. Thus, further research should investigate a decentralized implementation of cooperative SLAC, which avoids a single point of failure. We consider decentralized cooperative SLAC a promising approach to improve scalability by distributing the computational load among nodes and reducing the communication requirement for larger networks.

Bibliography

[1] Y. Gao and S. Chien, "Review on space robotics: Toward top-level science through space exploration," *Science Robotics*, vol. 2, no. 7, Jun. 2017.

[2] J. P. Grotzinger, J. Crisp, A. R. Vasavada, R. C. Anderson, C. J. Baker, R. Barry, D. F. Blake, P. Conrad, K. S. Edgett, B. Ferdowski, R. Gellert, J. B. Gilbert, M. Golombek, J. Gómez-Elvira, D. M. Hassler, L. Jandura, M. Litvak, P. Mahaffy, J. Maki, M. Meyer, M. C. Malin, I. Mitrofanov, J. J. Simmonds, D. Vaniman, R. V. Welch, and R. C. Wiens, "Mars science laboratory mission and science investigation," *Space Science Reviews*, vol. 170, no. 1, pp. 5–56, Sep. 2012.

[3] NASA, "Where is Curiosity?" https://mars.nasa.gov/msl/mission/where-is-the-rover.

[4] A. S. McEwen, C. M. Dundas, S. S. Mattson, A. D. Toigo, L. Ojha, J. J. Wray, M. Chojnacki, S. Byrne, S. L. Murchie, and N. Thomas, "Recurring slope lineae in equatorial regions of Mars," *Nature Geoscience*, vol. 7, no. 1, pp. 53–58, Jan. 2014.

[5] D. E. Stillman, T. I. Michaels, and R. E. Grimm, "Characteristics of the numerous and widespread recurring slope lineae (RSL) in Valles Marineris, Mars," *Icarus*, vol. 285, pp. 195–210, Mar. 2017.

[6] International Space Exploration Coordination Group, "The global exploration roadmap," Jan. 2018. [Online]. Available: https://www.globalspaceexploration.org

[7] M. Bajracharya, M. W. Maimone, and D. Helmick, "Autonomy for mars rovers: Past, present, and future," *Computer*, vol. 41, no. 12, pp. 44–50, Dec. 2008.

[8] A. Wedler, M. Wilde, A. Dömel, M. G. Müller, J. Reill, M. Schuster, W. Stürzl, R. Triebel, H. Gmeiner, B. Vodermayer, K. Bussmann, M. Vayugundla, S. Brunner, H. Lehner, P. Lehner, A. Börner, R. Krenn, A. Dammann, U.-C. Fiebig, E. Staudinger, F. Wenzhöfer, S. Flögel, S. Sommer, T. Asfour, M. Flad, S. Hohmann, M. Brandauer, and A. O. Albu-Schäffer, "From single autonomous robots toward cooperative robotic interactions for future planetary exploration missions," in *Proc. Int. Astronautical Congr., IAC*, Bremen, Germany, Oct. 2018.

[9] M. J. Schuster, M. G. Müller, S. G. Brunner, H. Lehner, P. Lehner, R. Sakagami, A. Dömel, L. Meyer, B. Vodermayer, R. Giubilato, M. Vayugundla, J. Reill, F. Steidle, I. von Bargen, K. Bussmann, R. Belder, P. Lutz, W. Stürzl, M. Smisek, M. Maier, S. Stoneman, A. Fonseca Prince, B. Rebele, M. Durner, E. Staudinger, S. Zhang, R. Pöhlmann, E. Bischoff, C. Braun, S. Schröder, E. Dietz, S. Frohmann, A. Börner, H.-W. Hübers, B. Foing, R. Triebel, A. Albu-Schäffer, A. Wedler, J. Roberts, and G. Ishigami, "The ARCHES space-analogue demonstration mission: Towards heterogeneous teams of autonomous robots for collaborative scientific sampling in planetary exploration," *IEEE Robotics and Automation Letters*, vol. 5, no. 4, pp. 5315–5322, Oct. 2020.

[10] K. A. Farley, K. H. Williford, K. M. Stack, R. Bhartia, A. Chen, M. de la Torre, K. Hand, Y. Goreva, C. D. K. Herd, R. Hueso, Y. Liu, J. N. Maki, G. Martinez, R. C. Moeller, A. Nelessen, C. E. Newman, D. Nunes, A. Ponce, N. Spanovich, P. A. Willis, L. W. Beegle, J. F. Bell, A. J. Brown, S.-E. Hamran, J. A. Hurowitz, S. Maurice, D. A. Paige, J. A. Rodriguez-Manfredi, M. Schulte, and R. C. Wiens, "Mars 2020 mission overview," *Space Science Reviews*, vol. 216, no. 8, p. 142, Dec. 2020.

[11] M. Bernard, K. Kondak, I. Maza, and A. Ollero, "Autonomous transportation and deployment with aerial robots for search and rescue missions," *Journal of Field Robotics*, vol. 28, no. 6, pp. 914–931, 2011.

[12] M. Dunbabin and L. Marques, "Robots for environmental monitoring: Significant advancements and applications," *IEEE Robotics Automation Magazine*, vol. 19, no. 1, pp. 24–39, Mar. 2012.

[13] T. Wiedemann, C. Manss, and D. Shutin, "Multi-agent exploration of spatial dynamical processes under sparsity constraints," *Autonomous Agents and Multi-Agent Systems*, vol. 32, no. 1, pp. 134–162, Jan. 2018.

[14] S. Zhang, R. Pöhlmann, T. Wiedemann, A. Dammann, H. Wymeersch, and P. A. Hoeher, "Self-aware swarm navigation in autonomous exploration missions," *Proceedings of the IEEE*, vol. 108, no. 7, pp. 1168–1195, Jul. 2020.

[15] E. Şahin and A. Winfield, "Special issue on swarm robotics," *Swarm Intelligence*, vol. 2, no. 2-4, pp. 69–72, Dec. 2008.

[16] M. Brambilla, E. Ferrante, M. Birattari, and M. Dorigo, "Swarm robotics: A review from the swarm engineering perspective," *Swarm Intelligence*, vol. 7, no. 1, pp. 1–41, Mar. 2013.

[17] S.-J. Chung, A. A. Paranjape, P. Dames, S. Shen, and V. Kumar, "A survey on aerial swarm robotics," *IEEE Transactions on Robotics*, vol. 34, no. 4, pp. 837–855, Aug. 2018.

[18] M. Dorigo, G. Theraulaz, and V. Trianni, "Swarm robotics: Past, present, and future," *Proceedings of the IEEE*, vol. 109, no. 7, pp. 1152–1165, Jul. 2021.

[19] H. Wymeersch, J. Lien, and M. Z. Win, "Cooperative localization in wireless networks," *Proceedings of the IEEE*, vol. 97, no. 2, pp. 427–450, Feb. 2009.

[20] Y. Shen, H. Wymeersch, and M. Z. Win, "Fundamental limits of wideband localization—Part II: Cooperative networks," *IEEE Transactions on Information Theory*, vol. 56, no. 10, pp. 4981–5000, Oct. 2010.

[21] J. Schloemann and R. M. Buehrer, "On the value of collaboration in location estimation," *IEEE Transactions on Vehicular Technology*, vol. 65, no. 5, pp. 3585–3596, May 2016.

[22] M. Z. Win, Y. Shen, and W. Dai, "A theoretical foundation of network localization and navigation," *Proceedings of the IEEE*, vol. 106, no. 7, pp. 1136–1165, Jul. 2018.

[23] A. Conti, M. Guerra, D. Dardari, N. Decarli, and M. Z. Win, "Network experimentation for cooperative localization," *IEEE Journal on Selected Areas in Communications*, vol. 30, no. 2, pp. 467–475, Feb. 2012.

[24] N. Patwari, J. N. Ash, S. Kyperountas, A. O. Hero, R. L. Moses, and N. S. Correal, "Locating the nodes: Cooperative localization in wireless sensor networks," *IEEE Signal Processing Magazine*, vol. 22, no. 4, pp. 54–69, Jul. 2005.

[25] J. A. del Peral-Rosado, R. Raulefs, J. A. López-Salcedo, and G. Seco-Granados, "Survey of cellular mobile radio localization methods: From 1G to 5G," *IEEE Communications Surveys & Tutorials*, vol. 20, no. 2, pp. 1124–1148, Secondquarter 2018.

[26] E. D. Kaplan and C. J. Hegarty, Eds., *Understanding GPS: Principles and Applications*, 2nd ed., ser. Artech House Mobile Communications. Boston, Mass.: Artech House, 2006.

[27] Z. Sahinoglu, S. Gezici, and I. Güvenc, *Ultra-Wideband Positioning Systems: Theoretical Limits, Ranging Algorithms, and Protocols.* Cambridge University Press, Jun. 2011.

[28] M. Viberg, "Introduction to array processing," in *Array and Statistical Signal Processing*, ser. Academic Press Library in Signal Processing, A. M. Zoubir, M. Viberg, R. Chellappa, and S. Theodoridis, Eds. Boston: Elsevier, 2014, vol. 3, ch. 11, pp. 463–502.

[29] B. Friedlander, "Wireless direction-finding fundamentals," in *Classical and Modern Direction-of-Arrival Estimation*, T. E. Tuncer and B. Friedlander, Eds. Boston: Academic Press, Jan. 2009, pp. 1–51.

[30] R. M. Buehrer, H. Wymeersch, and R. M. Vaghefi, "Collaborative sensor network localization: Algorithms and practical issues," *Proceedings of the IEEE*, vol. 106, no. 6, pp. 1089–1114, Jun. 2018.

[31] M. Steinbauer, A. F. Molisch, and E. Bonek, "The double-directional radio channel," *IEEE Antennas and Propagation Magazine*, vol. 43, no. 4, pp. 51–63, Aug. 2001.

[32] S. Maranò, W. M. Gifford, H. Wymeersch, and M. Z. Win, "NLOS identification and mitigation for localization based on UWB experimental data," *IEEE Journal on Selected Areas in Communications*, vol. 28, no. 7, pp. 1026–1035, Sep. 2010.

[33] S. Aditya, A. F. Molisch, and H. M. Behairy, "A survey on the impact of multipath on wideband time-of-arrival-based localization," *Proceedings of the IEEE*, vol. 106, no. 7, pp. 1183–1203, Jul. 2018.

[34] B. H. Fleury, M. Tschudin, R. Heddergott, D. Dahlhaus, and K. I. Pedersen, "Channel parameter estimation in mobile radio environments using the SAGE algorithm," *IEEE Journal on Selected Areas in Communications*, vol. 17, no. 3, pp. 434–450, Mar. 1999.

[35] A. Richter, "Estimation of radio channel parameters: Models and algorithms," Ph.D. dissertation, Fakultät für Elektrotechnik und Informationstechnik, Technische Universität Ilmenau, 2005.

[36] M. Haardt, "Efficient one-, two-, and multidimensional high resolution array signal processing," Ph.D. dissertation, Fakultät für Elektrotechnik und Informationstechnik, Technische Universität München, 1997.

[37] C. Gentner, T. Jost, W. Wang, S. Zhang, A. Dammann, and U. C. Fiebig, "Multipath assisted positioning with simultaneous localization and mapping," *IEEE Transactions on Wireless Communications*, vol. 15, no. 9, pp. 6104–6117, Sep. 2016.

[38] K. Witrisal, P. Meissner, E. Leitinger, Y. Shen, C. Gustafson, F. Tufvesson, K. Haneda, D. Dardari, A. F. Molisch, A. Conti, and M. Z. Win, "High-accuracy localization for assisted Lliving: 5G systems will turn multipath channels from foe to friend," *IEEE Signal Processing Magazine*, vol. 33, no. 2, pp. 59–70, Mar. 2016.

[39] R. Mendrzik, H. Wymeersch, G. Bauch, and Z. Abu-Shaban, "Harnessing NLOS components for position and orientation estimation in 5G millimeter wave MIMO," *IEEE Transactions on Wireless Communications*, vol. 18, no. 1, pp. 93–107, Jan. 2019.

[40] J. Ash and L. Potter, "Sensor network localization via received signal strength measurements with directional antennas," in *Proc. Allerton Conf. Communication, Control, and Computing*, 2004, pp. 1861–1870.

[41] B. N. Hood and P. Barooah, "Estimating DoA from radio-frequency RSSI measurements using an actuated reflector," *IEEE Sensors Journal*, vol. 11, no. 2, pp. 413–417, Feb. 2011.

[42] M. Malajner, P. Planinsic, and D. Gleich, "Angle of arrival estimation using RSSI and omnidirectional rotatable antennas," *IEEE Sensors Journal*, vol. 12, no. 6, pp. 1950–1957, Jun. 2012.

[43] J. T. Isaacs, F. Quitin, L. R. G. Carrillo, U. Madhow, and J. P. Hespanha, "Quadrotor control for RF source localization and tracking," in *Proc. Int. Conf. Unmanned Aircraft Systems (ICUAS)*, May 2014, pp. 244–252.

[44] A. Cidronali, S. Maddio, G. Giorgetti, and G. Manes, "Analysis and performance of a smart antenna for 2.45-GHz single-anchor indoor positioning," *IEEE Transactions on Microwave Theory and Techniques*, vol. 58, no. 1, pp. 21–31, Jan. 2010.

[45] L. Kulas, "Simple 2-D direction-of-arrival estimation using an ESPAR antenna," *IEEE Antennas and Wireless Propagation Letters*, vol. 16, pp. 2513–2516, 2017.

[46] J. P. Lie, T. Blu, and C. M. S. See, "Single antenna power measurements based direction finding," *IEEE Transactions on Signal Processing*, vol. 58, no. 11, pp. 5682–5692, Nov. 2010.

[47] M. Passafiume, S. Maddio, A. Cidronali, and G. Manes, "MUSIC algorithm for RSSI-based DoA estimation on standard IEEE 802.11/802.15.x systems," *WSEAS Trans. Signal Process.*, vol. 11, pp. 58–68, 2015.

[48] R. Hoctor and S. Kassam, "The unifying role of the coarray in aperture synthesis for coherent and incoherent imaging," *Proceedings of the IEEE*, vol. 78, no. 4, pp. 735–752, Apr. 1990.

[49] A. Moffet, "Minimum-redundancy linear arrays," *IEEE Transactions on Antennas and Propagation*, vol. 16, no. 2, pp. 172–175, Mar. 1968.

[50] M. Costa, V. Koivunen, and M. Viberg, "Array processing in the face of nonidealities," in *Academic Press Library in Signal Processing*, ser. Academic Press Library in Signal Processing, A. M. Zoubir, M. Viberg, R. Chellappa, and S. Theodoridis, Eds. Boston: Elsevier, Jan. 2014, vol. 3, pp. 819–857.

[51] M. Zatman, "How narrow is narrowband?" *IEE Proceedings - Radar, Sonar and Navigation*, vol. 145, no. 2, pp. 85–91, Apr. 1998.

[52] J. Sorelius, R. Moses, T. Söderström, and A. Swindlehurst, "Effects of nonzero bandwidth on direction of arrival estimators in array signal processing," *IEE Proceedings - Radar, Sonar and Navigation*, vol. 145, no. 6, p. 317, Dec. 1998.

[53] J.-P. Delmas and Y. Meurisse, "Robustness of narrowband DOA algorithms with respect to signal bandwidth," *Signal Processing*, vol. 83, no. 3, pp. 493–510, Mar. 2003.

[54] P.-J. Chung, M. Viberg, and J. Yu, "DOA estimation methods and algorithms," in *Array and Statistical Signal Processing*, ser. Academic Press Library in Signal Processing, A. M. Zoubir, M. Viberg, R. Chellappa, and S. Theodoridis, Eds. Boston: Elsevier, 2014, vol. 3, ch. 14, pp. 599–650.

[55] H. Krim and M. Viberg, "Two decades of array signal processing research: The parametric approach," *IEEE Signal Processing Magazine*, vol. 13, no. 4, pp. 67–94, Jul. 1996.

[56] R. Schmidt, "Multiple emitter location and signal parameter estimation," *IEEE Transactions on Antennas and Propagation*, vol. 34, no. 3, pp. 276–280, Mar. 1986.

[57] M. Trinh-Hoang, M. Viberg, and M. Pesavento, "Partial relaxation approach: An eigenvalue-based DOA estimator framework," *IEEE Transactions on Signal Processing*, vol. 66, no. 23, pp. 6190–6203, Dec. 2018.

[58] V. Koivunen and E. Ollila, "Model order selection," in *Academic Press Library in Signal Processing*, ser. Academic Press Library in Signal Processing: Volume 3, A. M. Zoubir, M. Viberg, R. Chellappa, and S. Theodoridis, Eds. Boston: Elsevier, Jan. 2014, vol. 3, pp. 9–25.

[59] R. C. Adam and P. A. Hoeher, "Simultaneous model and parameter estimation for joint communication and positioning," *IEEE Access*, vol. 9, pp. 2934–2949, Dec. 2020.

[60] R. C. Adam, "Joint communication and positioning based on channel estimation," Ph.D. dissertation, Technische Fakultät, Christian-Albrechts-Universität zu Kiel, 2020.

[61] P. Stoica and A. Nehorai, "Performance study of conditional and unconditional direction-of-arrival estimation," *IEEE Transactions on Acoustics, Speech, and Signal Processing*, vol. 38, no. 10, pp. 1783–1795, Oct. 1990.

[62] J. A. Fessler and A. O. Hero, "Space-alternating generalized expectation-maximization algorithm," *IEEE Transactions on Signal Processing*, vol. 42, no. 10, pp. 2664–2677, Oct. 1994.

[63] S. Sand, A. Dammann, and C. Mensing, *Positioning in Wireless Communications Systems*. John Wiley & Sons, 2014.

[64] M. Vanderveen, C. Papadias, and A. Paulraj, "Joint angle and delay estimation (JADE) for multipath signals arriving at an antenna array," *IEEE Communications Letters*, vol. 1, no. 1, pp. 12–14, Jan. 1997.

[65] M. Wax and A. Leshem, "Joint estimation of time delays and directions of arrival of multiple reflections of a known signal," *IEEE Transactions on Signal Processing*, vol. 45, no. 10, pp. 2477–2484, Oct. 1997.

[66] R. Garbacz and R. Turpin, "A generalized expansion for radiated and scattered fields," *IEEE Transactions on Antennas and Propagation*, vol. 19, no. 3, pp. 348–358, May 1971.

[67] R. Harrington and J. Mautz, "Theory of characteristic modes for conducting bodies," *IEEE Transactions on Antennas and Propagation*, vol. 19, no. 5, pp. 622–628, Sep. 1971.

[68] R. Martens, E. Safin, and D. Manteuffel, "Inductive and capacitive excitation of the characteristic modes of small terminals," in *Proc. Loughborough Antennas and Propagation Conf. (LAPC)*, Loughborough, UK, Nov. 2011.

[69] X. Zhao, S. P. Yeo, and L. C. Ong, "Planar UWB MIMO antenna with pattern diversity and isolation improvement for mobile platform based on the theory of characteristic modes," *IEEE Transactions on Antennas and Propagation*, vol. 66, no. 1, pp. 420–425, Jan. 2018.

[70] D. Manteuffel and R. Martens, "Compact multimode multielement antenna for indoor UWB massive MIMO," *IEEE Transactions on Antennas and Propagation*, vol. 64, no. 7, pp. 2689–2697, Jul. 2016.

[71] S. K. Chaudhury, H. J. Chaloupka, and A. Ziroff, "Multiport antenna systems for MIMO and diversity," in *Proc. 4th European Conf. Antennas and Propagation (EuCAP)*, Barcelona, Spain, Apr. 2010.

[72] H. Li, Z. T. Miers, and B. K. Lau, "Design of orthogonal MIMO handset antennas based on characteristic mode manipulation at frequency bands below 1 GHz," *IEEE Transactions on Antennas and Propagation*, vol. 62, no. 5, pp. 2756–2766, May 2014.

[73] M. Bouezzeddine and W. L. Schroeder, "Design of a wideband, tunable four-port MIMO antenna system with high isolation based on the theory of characteristic modes," *IEEE Transactions on Antennas and Propagation*, vol. 64, no. 7, pp. 2679–2688, Jul. 2016.

[74] D.-W. Kim and S. Nam, "Systematic design of a multiport MIMO antenna with bilateral symmetry based on characteristic mode analysis," *IEEE Transactions on Antennas and Propagation*, vol. 66, no. 3, pp. 1076–1085, Mar. 2018.

[75] T. Svantesson, "Multimode based direction finding," in *Proc. 34th Asilomar Conf. Signals, Systems, and Computers*, Pacific Grove, USA, Oct. 2000, pp. 595–599.

[76] R. Ma and N. Behdad, "Design of platform-based HF direction-finding antennas using the characteristic mode theory," *IEEE Transactions on Antennas and Propagation*, vol. 67, no. 3, pp. 1417–1427, 2018.

[77] R. Ma and N. Behdad, "A spatially-confined, platform-based HF direction finding array," *IEEE Transactions on Antennas and Propagation*, 2021.

[78] K. Ren, R. Ma, and N. Behdad, "Performance-enhancement of platform-based, HF direction-finding systems using dynamic mode selection," *IEEE Open Journal of Antennas and Propagation*, vol. 2, pp. 793–806, 2021.

[79] L. Grundmann, N. Peitzmeier, and D. Manteuffel, "Investigation of direction of arrival estimation using characteristic modes," in *Proc. 15th European Conf. Antennas and Propagation (EuCAP)*, Mar. 2021.

[80] S. M. Kay, *Fundamentals of Statistical Signal Processing, Volume I: Estimation Theory*, 1st ed. Englewood Cliffs, N.J: Prentice Hall, 1993.

[81] H. L. Van Trees and K. L. Bell, Eds., *Bayesian Bounds for Parameter Estimation and Nonlinear Filtering/Tracking.* Hoboken, NJ: IEEE Press, 2007.

[82] Y. Shen and M. Z. Win, "Fundamental limits of wideband localization—Part I: A general framework," *IEEE Transactions on Information Theory*, vol. 56, no. 10, pp. 4956–4980, Oct. 2010.

[83] Y. Shen and M. Win, "On the accuracy of localization systems using wideband antenna arrays," *IEEE Transactions on Communications*, vol. 58, no. 1, pp. 270–280, Jan. 2010.

[84] Y. Han, Y. Shen, X.-P. Zhang, M. Z. Win, and H. Meng, "Performance limits and geometric properties of array localization," *IEEE Transactions on Information Theory*, vol. 62, no. 2, pp. 1054–1075, Feb. 2016.

[85] A. Shahmansoori, G. E. Garcia, G. Destino, G. Seco-Granados, and H. Wymeersch, "Position and orientation estimation through millimeter-wave MIMO in 5G systems," *IEEE Transactions on Wireless Communications*, vol. 17, no. 3, pp. 1822–1835, Mar. 2018.

[86] A. Guerra, F. Guidi, and D. Dardari, "Single-anchor localization and orientation performance limits using massive arrays: MIMO vs. beamforming," *IEEE Transactions on Wireless Communications*, vol. 17, no. 8, pp. 5241–5255, Aug. 2018.

[87] A. Kakkavas, M. H. C. Garcia, R. A. Stirling-Gallacher, and J. A. Nossek, "Performance limits of single-anchor mm-wave positioning," *IEEE Transactions on Wireless Communications*, vol. 18, no. 11, pp. 5196–5210, 2019.

[88] Z. Abu-Shaban, X. Zhou, T. Abhayapala, G. Seco-Granados, and H. Wymeersch, "Error bounds for uplink and downlink 3D localization in 5G millimeter wave systems," *IEEE Transactions on Wireless Communications*, vol. 17, no. 8, pp. 4939–4954, Aug. 2018.

[89] A. Shahmansoori, G. E. Garcia, G. Destino, G. Seco-Granados, and H. Wymeersch, "5G position and orientation estimation through millimeter wave MIMO," in *Proc. IEEE Globecom Workshops (GC Wkshps)*, San Diego, CA, USA, Dec. 2015.

[90] M. Z. Win, A. Conti, S. Mazuelas, Y. Shen, W. M. Gifford, D. Dardari, and M. Chiani, "Network localization and navigation via cooperation," *IEEE Communications Magazine*, vol. 49, no. 5, pp. 56–62, May 2011.

[91] Y. Shen, S. Mazuelas, and M. Z. Win, "Network navigation: Theory and interpretation," *IEEE Journal on Selected Areas in Communications*, vol. 30, no. 9, pp. 1823–1834, Oct. 2012.

[92] S. Mazuelas, Y. Shen, and M. Z. Win, "Spatio-temporal information coupling in network navigation," *IEEE Transactions on Information Theory*, vol. 64, no. 12, pp. 7759–7779, 2018.

[93] Y. Bar-Shalom, X. R. Li, and T. Kirubarajan, *Estimation with Applications to Tracking and Navigation: Theory Algorithms and Software.* John Wiley & Sons, 2004.

[94] C. Chang and A. Sahai, "Cramér-Rao-type bounds for localization," *EURASIP Journal on Advances in Signal Processing*, vol. 2006, no. 1, Dec. 2006.

[95] J. N. Ash and R. L. Moses, "On the relative and absolute positioning errors in self-localization systems," *IEEE Transactions on Signal Processing*, vol. 56, no. 11, pp. 5668–5679, Nov. 2008.

[96] D. C. Popescu, M. Hedley, and T. Sathyan, "Posterior Cramér-Rao bound for anchorless tracking," *IEEE Signal Processing Letters*, vol. 20, no. 12, pp. 1183–1186, Dec. 2013.

[97] A. S. Konanur, K. Gosalia, S. H. Krishnamurthy, B. Hughes, and G. Lazzi, "Increasing wireless channel capacity through MIMO systems employing co-located antennas," *IEEE Transactions on Microwave Theory and Techniques*, vol. 53, no. 6, pp. 1837–1844, Jun. 2005.

[98] C. Chiu, J. Yan, and R. D. Murch, "Compact three-port orthogonally polarized MIMO antennas," *IEEE Antennas and Wireless Propagation Letters*, vol. 6, pp. 619–622, Dec. 2007.

[99] B. Elnour and D. Erricolo, "A novel colocated cross-polarized two-loop PCB antenna in the ISM 2.4-GHz band," *IEEE Antennas and Wireless Propagation Letters*, vol. 9, pp. 1237–1240, 2010.

[100] M. A. Doron and E. Doron, "Wavefield modeling and array processing. I. Spatial sampling," *IEEE Transactions on Signal Processing*, vol. 42, no. 10, pp. 2549–2559, Oct. 1994.

[101] M. Costa, A. Richter, and V. Koivunen, "Unified array manifold decomposition based on spherical harmonics and 2-D fourier basis," *IEEE Transactions on Signal Processing*, vol. 58, no. 9, pp. 4634–4645, Sep. 2010.

[102] J. E. Hansen, *Spherical Near-field Antenna Measurements*. London: Peter Peregrinus Ltd, 1988.

[103] M. Viberg, M. Lanne, and A. Lundgren, "Calibration in array processing," in *Classical and Modern Direction-of-Arrival Estimation*, T. E. Tuncer and B. Friedlander, Eds. Boston: Academic Press, Jan. 2009, pp. 93–124.

[104] D. Astely, A. L. Swindlehurst, and B. Ottersten, "Spatial signature estimation for uniform linear arrays with unknown receiver gains and phases," *IEEE Transactions on Signal Processing*, vol. 47, no. 8, pp. 2128–2138, Aug. 1999.

[105] Y. Rockah and P. Schultheiss, "Array shape calibration using sources in unknown locations–Part I: Far-field sources," *IEEE Transactions on Acoustics, Speech, and Signal Processing*, vol. 35, no. 3, pp. 286–299, Mar. 1987.

[106] A. Liu, G. Liao, C. Zeng, Z. Yang, and Q. Xu, "An eigenstructure method for estimating DOA and sensor gain-phase errors," *IEEE Transactions on Signal Processing*, vol. 59, no. 12, pp. 5944–5956, Dec. 2011.

[107] J. Liu, X. Wu, W. J. Emery, L. Zhang, C. Li, and K. Ma, "Direction-of-arrival estimation and sensor array error calibration based on blind signal separation," *IEEE Signal Processing Letters*, vol. 24, no. 1, pp. 7–11, Jan. 2017.

[108] Z. Ye, J. Dai, X. Xu, and X. Wu, "DOA estimation for uniform linear array with mutual coupling," *IEEE Transactions on Aerospace and Electronic Systems*, vol. 45, no. 1, pp. 280–288, Jan. 2009.

[109] M. Lin and L. Yang, "Blind calibration and DOA estimation with uniform circular arrays in the presence of mutual coupling," *IEEE Antennas and Wireless Propagation Letters*, vol. 5, pp. 315–318, 2006.

[110] M. Viberg and A. L. Swindlehurst, "A Bayesian approach to auto-calibration for parametric array signal processing," *IEEE Transactions on Signal Processing*, vol. 42, no. 12, pp. 3495–3507, Dec. 1994.

[111] M. Jansson, A. L. Swindlehurst, and B. Ottersten, "Weighted subspace fitting for general array error models," *IEEE Transactions on Signal Processing*, vol. 46, no. 9, pp. 2484–2498, Sep. 1998.

[112] B. P. Flanagan and K. L. Bell, "Array self-calibration with large sensor position errors," *Signal Processing*, vol. 81, no. 10, pp. 2201–2214, Oct. 2001.

[113] Z.-M. Liu and Y.-Y. Zhou, "A unified framework and sparse Bayesian perspective for direction-of-arrival estimation in the presence of array imperfections," *IEEE Transactions on Signal Processing*, vol. 61, no. 15, pp. 3786–3798, Aug. 2013.

[114] H. Liu, L. Zhao, Y. Li, X. Jing, and T.-K. Truong, "A sparse-based approach for DOA estimation and array calibration in uniform linear array," *IEEE Sensors Journal*, vol. 16, no. 15, pp. 6018–6027, Aug. 2016.

[115] B. C. Ng and C. M. S. See, "Sensor-array calibration using a maximum-likelihood approach," *IEEE Transactions on Antennas and Propagation*, vol. 44, no. 6, pp. 827–835, Jun. 1996.

[116] M. Mowlér, B. Lindmark, E. G. Larsson, and B. Ottersten, "Joint estimation of mutual coupling, element factor, and phase center in antenna arrays," *EURASIP Journal on Wireless Communications and Networking*, vol. 2007, no. 1, p. 030684, Dec. 2007.

[117] E. Sippel, M. Lipka, J. Geiß, M. Hehn, and M. Vossiek, "In-situ calibration of antenna arrays within wireless locating systems," *IEEE Transactions on Antennas and Propagation*, vol. 68, no. 4, pp. 2832–2841, Apr. 2020.

[118] T. Sathyan, D. Humphrey, and M. Hedley, "WASP: A system and algorithms for accurate radio localization using low-cost hardware," *IEEE Transactions on*

Systems, Man, and Cybernetics, Part C (Applications and Reviews), vol. 41, no. 2, pp. 211–222, Mar. 2011.

[119] E. Staudinger, "Round-trip delay ranging with orthogonal frequency division multiplex signals," Ph.D. dissertation, Fachbereich für Physik und Elektrotechnik, Universität Bremen, 2015.

[120] M. J. Schuster, S. G. Brunner, K. Bussmann, S. Büttner, A. Dömel, M. Hellerer, H. Lehner, P. Lehner, O. Porges, J. Reill, S. Riedel, M. Vayugundla, B. Vodermayer, T. Bodenmüller, C. Brand, W. Friedl, I. Grixa, H. Hirschmüller, M. Kaßecker, Z.-C. Márton, C. Nissler, F. Ruess, M. Suppa, and A. Wedler, "Towards autonomous planetary exploration: The Lightweight Rover Unit (LRU), its success in the SpaceBotCamp challenge, and beyond," *Journal of Intelligent & Robotic Systems*, vol. 93, no. 3-4, pp. 461–494, Mar. 2019.

[121] C. Cadena, L. Carlone, H. Carrillo, Y. Latif, D. Scaramuzza, J. Neira, I. Reid, and J. J. Leonard, "Past, present, and future of simultaneous localization and mapping: Toward the robust-perception age," *IEEE Transactions on Robotics*, vol. 32, no. 6, pp. 1309–1332, Dec. 2016.

[122] E. Foxlin, "Generalized architecture for simultaneous localization, autocalibration, and map-building," in *Proc. IEEE/RSJ Int. Conf. Intelligent Robots and System (IROS)*, vol. 1, Lausanne, Switzerland, 2002, pp. 527–533.

[123] H. Miura, T. Yoshida, K. Nakamura, and K. Nakadai, "SLAM-based online calibration for asynchronous microphone array," *Advanced Robotics*, vol. 26, no. 17, pp. 1941–1965, Dec. 2012.

[124] A. Martinelli, N. Tomatis, and R. Siegwart, "Simultaneous localization and odometry self calibration for mobile robot," *Autonomous Robots*, vol. 22, no. 1, pp. 75–85, Jan. 2007.

[125] H. Sadjadi, K. Hashtrudi-Zaad, and G. Fichtinger, "Simultaneous localization and calibration for electromagnetic tracking systems," *The International Journal of Medical Robotics and Computer Assisted Surgery*, vol. 12, no. 2, pp. 189–198, Jun. 2016.

[126] H. Kim, K. Granström, L. Gao, G. Battistelli, S. Kim, and H. Wymeersch, "5G mmWave cooperative positioning and mapping using multi-model PHD filter and map fusion," *IEEE Transactions on Wireless Communications*, vol. 19, no. 6, pp. 3782–3795, Jun. 2020.

[127] A. Fascista, A. Coluccia, H. Wymeersch, and G. Seco-Granados, "Downlink single-snapshot localization and mapping with a single-antenna receiver," *IEEE Transactions on Wireless Communications*, vol. 20, no. 7, pp. 4672–4684, Jul. 2021.

[128] R. Mendrzik, H. Wymeersch, and G. Bauch, "Joint localization and mapping through millimeter wave MIMO in 5G systems," in *Proc. IEEE Global Communications Conf. (GLOBECOM)*, Abu Dhabi, Dec. 2018.

[129] N. Petrov, O. Krasnov, and A. G. Yarovoy, "Auto-calibration of automotive radars in operational mode using simultaneous localisation and mapping," *IEEE Transactions on Vehicular Technology*, vol. 70, no. 3, pp. 2062–2075, Mar. 2021.

[130] V. N. Ekambaram and K. Ramchandran, "SLAC-RF: Simultaneous 3D localization of mobile readers and calibration of RFID supertags," EECS Department, University of California, Berkeley, Tech. Rep. UCB/EECS-2012-188, Aug. 2012.

[131] S. He, S.-H. G. Chan, L. Yu, and N. Liu, "SLAC: Calibration-free pedometer-fingerprint fusion for indoor localization," *IEEE Transactions on Mobile Computing*, vol. 17, no. 5, pp. 1176–1189, May 2018.

[132] C. Taylor, A. Rahimi, J. Bachrach, H. Shrobe, and A. Grue, "Simultaneous localization, calibration, and tracking in an ad hoc sensor network," in *Proc. 5th Int. Conf. Information Processing in Sensor Networks*, Nashville, Tennessee, Apr. 2006, pp. 27–33.

[133] F. Demmel, "Practical aspects of design and application of direction-finding systems," in *Classical and Modern Direction-of-Arrival Estimation*, T. E. Tuncer and B. Friedlander, Eds. Boston: Academic Press, Jan. 2009, pp. 53–92.

[134] J.-Y. Lee and R. Scholtz, "Ranging in a dense multipath environment using an UWB radio link," *IEEE Journal on Selected Areas in Communications*, vol. 20, no. 9, pp. 1677–1683, Dec. 2002.

[135] Y. Luo and C. L. Law, "Indoor positioning using UWB-IR signals in the presence of dense multipath with path overlapping," *IEEE Transactions on Wireless Communications*, vol. 11, no. 10, pp. 3734–3743, Oct. 2012.

[136] B. Teague, Z. Liu, F. Meyer, A. Conti, and M. Win, "Network localization and navigation with scalable inference and efficient operation," *IEEE Transactions on Mobile Computing*, pp. 1–1, 2020.

[137] R. Harrington and J. Mautz, "Computation of characteristic modes for conducting bodies," *IEEE Transactions on Antennas and Propagation*, vol. 19, no. 5, pp. 629–639, 1971.

[138] B. K. Lau, D. Manteuffel, H. Arai, and S. V. Hum, "Guest editorial: Theory and applications of characteristic modes," *IEEE Transactions on Antennas and Propagation*, vol. 64, no. 7, pp. 2590–2594, Jul. 2016.

[139] J. Villanen, J. Ollikainen, O. Kivekas, and P. Vainikainen, "Coupling element based mobile terminal antenna structures," *IEEE Transactions on Antennas and Propagation*, vol. 54, no. 7, pp. 2142–2153, Jul. 2006.

[140] Y. Chen and C.-F. Wang, *Characteristics Modes: Theory and Applications in Antenna Engineering.* Hoboken, New Jersey: John Wiley & Sons, Inc., 2015.

[141] M. Cabedo-Fabres, E. Antonino-Daviu, A. Valero-Nogueira, and M. F. Bataller, "The theory of characteristic modes revisited: A contribution to the design of antennas for modern applications," *IEEE Antennas and Propagation Magazine*, vol. 49, no. 5, pp. 52–68, Oct. 2007.

[142] T. Svantesson, "Correlation and channel capacity of MIMO systems employing multimode antennas," *IEEE Transactions on Vehicular Technology*, vol. 51, no. 6, pp. 1304–1312, Nov. 2002.

[143] P. A. Hoeher and N. Doose, "A massive MIMO terminal concept based on small-size multi-mode antennas," *Transactions on Emerging Telecommunications Technologies*, vol. 28, no. 2, p. e2934, Mar. 2015.

[144] N. Doose and P. A. Hoeher, "Joint precoding and power control for EIRP-limited MIMO systems," *IEEE Transactions on Wireless Communications*, vol. 17, no. 3, pp. 1727–1737, Mar. 2018.

[145] N. L. Johannsen, N. Peitzmeier, P. A. Hoeher, and D. Manteuffel, "On the feasibility of multi-mode antennas in UWB and IoT applications below 10 GHz," *IEEE Communications Magazine*, vol. 58, no. 3, pp. 69–75, Mar. 2020.

[146] D. Manteuffel and R. Martens, "Systematic design method of a mobile multiple antenna system using the theory of characteristic modes," *IET Microwaves, Antennas & Propagation*, vol. 8, no. 12, pp. 887–893, Sep. 2014.

[147] R. Pöhlmann, S. A. Almasri, S. Zhang, T. Jost, A. Dammann, and P. A. Hoeher, "On the potential of multi-mode antennas for direction-of-arrival estimation,"

IEEE Transactions on Antennas and Propagation, vol. 67, no. 5, pp. 3374–3386, May 2019.

[148] S. Caizzone, M. S. Circiu, W. Elmarissi, and C. Enneking, "All-GNSS-band DRA antenna for high-precision applications," in *Proc. 12th European Conf. Antennas and Propagation (EuCAP)*, Apr. 2018, pp. 543–547.

[149] "IEEE Standard Test Procedures for Antennas," *ANSI/IEEE Std 149-1979*, 1979.

[150] C. A. Balanis, *Antenna Theory: Analysis and Design.* John Wiley & Sons, 2015.

[151] D. Tse and P. Viswanath, *Fundamentals of Wireless Communication.* Cambridge University Press, May 2005.

[152] C. A. Balanis and P. I. Ioannides, *Introduction to Smart Antennas.* San Rafael: Morgan & Claypool Publishers, 2007.

[153] E. Larsson, "Cramér–Rao bound analysis of distributed positioning in sensor networks," *IEEE Signal Processing Letters*, vol. 11, no. 3, pp. 334–337, Mar. 2004.

[154] E. Staudinger, S. Zhang, R. Pöhlmann, and A. Dammann, "The role of time in a robotic swarm: A joint view on communications, localization, and sensing," *IEEE Communications Magazine*, vol. 59, no. 2, pp. 98–104, Feb. 2021.

[155] F. W. J. Olver, D. W. Lozier, R. F. Boisvert, and C. W. Clark, Eds., *NIST Handbook of Mathematical Functions.* Cambridge, New York: Cambridge University Press, 2010.

[156] F. Belloni, A. Richter, and V. Koivunen, "DoA estimation via manifold separation for arbitrary array structures," *IEEE Transactions on Signal Processing*, vol. 55, no. 10, pp. 4800–4810, Oct. 2007.

[157] S. A. Almasri, R. Pöhlmann, N. Doose, P. A. Hoeher, and A. Dammann, "Modeling aspects of planar multi-mode antennas for direction-of-arrival estimation," *IEEE Sensors Journal*, vol. 19, no. 12, pp. 4585–4597, Jun. 2019.

[158] G. H. Golub and V. Pereyra, "The differentiation of pseudo-inverses and nonlinear least squares problems whose variables separate," *SIAM Journal on Numerical Analysis*, vol. 10, no. 2, pp. 413–432, 1973.

[159] T. E. Tuncer and B. Friedlander, *Classical and Modern Direction-of-Arrival Estimation.* Boston: Academic Press, 2009.

[160] J. P. Delmas, "Performance bounds and statistical analysis of DOA estimation," in *Array and Statistical Signal Processing*, ser. Academic Press Library in Signal Processing, A. M. Zoubir, M. Viberg, R. Chellappa, and S. Theodoridis, Eds. Boston: Elsevier, 2014, vol. 3, ch. 16, pp. 719–764.

[161] W. L. Stutzman, *Polarization in Electromagnetic Systems*, 2nd ed. Artech House, Feb. 2018.

[162] K. T. Wong, L. Li, and M. D. Zoltowski, "Root-MUSIC-based direction-finding and polarization estimation using diversely polarized possibly collocated antennas," *IEEE Antennas and Wireless Propagation Letters*, vol. 3, no. 8, pp. 129–132, Dec. 2004.

[163] M. Costa, A. Richter, and V. Koivunen, "DoA and polarization estimation for arbitrary array configurations," *IEEE Transactions on Signal Processing*, vol. 60, no. 5, pp. 2330–2343, May 2012.

[164] A. Swindlehurst and M. Viberg, "Subspace fitting with diversely polarized antenna arrays," *IEEE Transactions on Antennas and Propagation*, vol. 41, no. 12, pp. 1687–1694, Dec. 1993.

[165] A. Goldsmith, *Wireless Communications.* Cambridge, UK: Cambridge University Press, Aug. 2005.

[166] D. Dardari, A. Conti, U. Ferner, A. Giorgetti, and M. Z. Win, "Ranging with ultrawide bandwidth signals in multipath environments," *Proceedings of the IEEE*, vol. 97, no. 2, pp. 404–426, Feb. 2009.

[167] D. Chu, "Polyphase codes with good periodic correlation properties," *IEEE Transactions on Information Theory*, vol. 18, no. 4, pp. 531–532, Jul. 1972.

[168] R. A. Horn and C. R. Johnson, *Matrix Analysis*, 2nd ed. New York, USA: Cambridge University Press, Oct. 2012.

[169] A. Dammann, T. Jost, R. Raulefs, M. Walter, and S. Zhang, "Optimizing waveforms for positioning in 5G," in *Proc. IEEE 17th Int. Workshop Signal Processing Advances in Wireless Communications (SPAWC)*, Edinburgh, UK, Jul. 2016.

[170] S. Zhang, "Autonomous swarm navigation," Ph.D. dissertation, Technische Fakultät, Christian-Albrechts-Universität zu Kiel, 2020.

[171] P. Stoica and B. C. Ng, "On the Cramer-Rao bound under parametric constraints," *IEEE Signal Processing Letters*, vol. 5, no. 7, pp. 177–179, Jul. 1998.

[172] K. V. Mardia and P. E. Jupp, *Directional Statistics.* Hoboken, NJ, USA: John Wiley & Sons, Sep. 2009.

[173] R. Fletcher, *Practical Methods of Optimization.* Chichester, UK: Wiley, 1987.

[174] P. Stoica and T. L. Marzetta, "Parameter estimation problems with singular information matrices," *IEEE Transactions on Signal Processing*, vol. 49, no. 1, pp. 87–90, Jan. 2001.

[175] R. Pöhlmann, S. Zhang, E. Staudinger, S. Caizzone, A. Dammann, and P. A. Hoeher, "Bayesian in-situ calibration of multiport antennas for DoA estimation: Theory and measurements," *IEEE Access*, vol. 10, pp. 37 967–37 983, Apr. 2022.

[176] X. Rong Li and V. Jilkov, "Survey of maneuvering target tracking. Part I: Dynamic models," *IEEE Transactions on Aerospace and Electronic Systems*, vol. 39, no. 4, pp. 1333–1364, Oct. 2003.

[177] M. T. Busch and S. S. Blackman, "Evaluation of IMM filtering for an air defense system application," in *Proc. SPIE's Int. Symp. Optical Science, Engineering, and Instrumentation*, San Diego, CA, Sep. 1995, pp. 435–447.

[178] S. Thrun, W. Burgard, and D. Fox, *Probabilistic Robotics.* MIT Press, Aug. 2005.

[179] H. Naseri and V. Koivunen, "A Bayesian algorithm for distributed cooperative localization using distance and direction estimates," *IEEE Transactions on Signal and Information Processing over Networks*, pp. 290–304, Nov. 2018.

[180] P. Closas and A. Gusi-Amigo, "Direct position estimation of GNSS receivers: Analyzing main results, architectures, enhancements, and challenges," *IEEE Signal Processing Magazine*, vol. 34, no. 5, pp. 72–84, Sep. 2017.

[181] H. Zhao, N. Zhang, and Y. Shen, "Beamspace direct localization for large-scale antenna array systems," *IEEE Transactions on Signal Processing*, pp. 3529–3544, May 2020.

[182] A. Fascista, A. Coluccia, and G. Ricci, "A pseudo maximum likelihood approach to position estimation in dynamic multipath environments," *Signal Processing*, vol. 181, p. 107907, Apr. 2021.

[183] N. Garcia, H. Wymeersch, E. G. Larsson, A. M. Haimovich, and M. Coulon, "Direct localization for massive MIMO," *IEEE Transactions on Signal Processing*, vol. 65, no. 10, pp. 2475–2487, May 2017.

[184] S. Zhang, E. Staudinger, T. Jost, W. Wang, C. Gentner, A. Dammann, H. Wymeersch, and P. A. Hoeher, "Distributed direct localization suitable for dense networks," *IEEE Transactions on Aerospace and Electronic Systems*, pp. 1209–1227, Apr. 2020.

[185] D. Pauluzzi and N. Beaulieu, "A comparison of SNR estimation techniques for the AWGN channel," *IEEE Transactions on Communications*, vol. 48, no. 10, pp. 1681–1691, Oct. 2000.

[186] M. Fatemi, L. Svensson, L. Hammarstrand, and M. Morelande, "A study of MAP estimation techniques for nonlinear filtering," in *Proc. 15th Int. Conf. Information Fusion*, Singapore, Jul. 2012, pp. 1058–1065.

[187] L. Tierney and J. B. Kadane, "Accurate approximations for posterior moments and marginal densities," *Journal of the American Statistical Association*, vol. 81, no. 393, pp. 82–86, Mar. 1986.

[188] B. Q. Ferreira, J. Gomes, C. Soares, and J. P. Costeira, "FLORIS and CLORIS: Hybrid source and network localization based on ranges and video," *Signal Processing*, vol. 153, pp. 355–367, Dec. 2018.

[189] S. Tomic, M. Beko, and R. Dinis, "3-D target localization in wireless sensor networks using RSS and AoA measurements," *IEEE Transactions on Vehicular Technology*, vol. 66, no. 4, pp. 3197–3210, Apr. 2017.

[190] R. Pöhlmann, S. Zhang, E. Staudinger, A. Dammann, and P. A. Hoeher, "Simultaneous localization and calibration for cooperative radio navigation," *IEEE Transactions on Wireless Communications*, vol. 21, no. 8, pp. 6195–6210, Aug. 2022.

[191] S. Zhang, R. Pöhlmann, E. Staudinger, and A. Dammann, "Assembling a swarm navigation system: Communication, localization, sensing and control," in *Proc. 1st IEEE Int. Workshop Communication and Networking for Swarms Robotics (RoboCom)*, Jan. 2021.

[192] E. Staudinger, D. Shutin, C. Manss, A. Viseras, and S. Zhang, "Swarm technologies for future space exploration missions," in *Proc. I-SAIRAS '18: Int. Symp.*

Artificial Intelligence, Robotics and Automation in Space, Madrid, Spain, Jun. 2018.

[193] T. Schmidl and D. Cox, "Robust frequency and timing synchronization for OFDM," *IEEE Transactions on Communications*, vol. 45, no. 12, pp. 1613–1621, Dec. 1997.

[194] ANavS GmbH, "ANavS Multi-Sensor RTK Module," https://www.anavs.de.

[195] J. G. Proakis and M. Salehi, *Digital Communications*, 5th ed. Boston, Mass.: McGraw-Hill, 2008.

[196] G. E. P. Box, J. S. Hunter, and W. G. Hunter, *Statistics for Experimenters: Design, Innovation, and Discovery*, 2nd ed. Hoboken, New Jersey: John Wiley & Sons, 2005.

Appendix A

List of Acronyms and Abbreviations

AIC	Akaike information criterion
AIT	Array interpolation technique
BCRB	Bayesian Cramér-Rao bound
BFGS	Broyden–Fletcher–Goldfarb–Shanno
BIC	Bayesian information criterion
BIM	Bayesian information matrix
CDF	Cumulative distribution function
CFO	Carrier frequency offset
COTS	Commercial off-the-shelf
CP	Cyclic prefix
CRB	Cramér-Rao bound
CW	Continuous wave
DLR	German Aerospace Center
DoA	Direction-of-arrival
DoD	Direction-of-departure
EADF	Effective aperture distribution function
EBIM	Equivalent Bayesian information matrix
EFIM	Equivalent Fisher information matrix
EKF	Extended Kalman filter
EM	Electromagnetic
FFT	Fast Fourier transform
FIM	Fisher information matrix
FoV	Field of view
FSPL	Free-space path loss
GLRT	Generalized likelihood ratio test
GNSS	Global navigation satellite system

GT	Guard time
i.i.d.	Independent and identically distributed
ICOMP	Information complexity criterion
IEEE	Institute of Electrical and Electronics Engineers
IEKF	Iterated extended Kalman filter
LO	Local oscillator
LoS	Line-of-sight
MAP	Maximum a posteriori
MIMO	Multiple-input multiple-output
ML	Maximum likelihood
MMA	Multi-mode antenna
mmWave	Millimeter wave
MSE	Mean squared error
MUSIC	Multiple signal characterization
MVDR	Minimum variance distortionless response
NLoS	Non-line-of-sight
OFDM	Orthogonal frequency-division multiplexing
pdf	Probability density function
PSK	Phase-shift keying
RC	Reduced complexity
RF	Radio frequency
RFIC	Radio-frequency integrated circuit
RFID	Radio-frequency identification
RHCP	Right-hand circular polarization
RMSE	Root-mean-square error
RSS	Received signal strength
RTK	Real-time kinematic
RTT	Round-trip time
SAGE	Space-alternating generalized expectation maximization
SDR	Software-defined radio
SLAC	Simultaneous localization and calibration
SLAM	Simultaneous localization and mapping
SNR	Signal-to-noise ratio
TCM	Theory of characteristic modes
TDMA	Time-division multiple access
ToA	Time-of-arrival
ToF	Time-of-flight

TWR	Two-way ranging
UAV	Unmanned aerial vehicle
UCA	Uniform circular array
ULA	Uniform linear array
URA	Uniform rectangular array
USRP	Universal Software Radio Peripheral
UWB	Ultra-wideband
w.r.t.	With respect to
WWB	Weiss-Weinstein bound
ZZB	Ziv-Zakai bound

Appendix B

List of Mathematical Notations

Subscripts and superscripts written in gray are optional. Optional sub-/superscripts occur frequently for indices referring to the receiving (Rx) node i, the transmitting (Tx) node j, the impinging signal p and the snapshot s.

General and Constants

$:=$	Equal by definition
c	Speed of light
k_{B}	Boltzmann constant

Scalars

a^*	Complex conjugate
$\lvert a \rvert$	Absolute value
$\lvert \mathbb{A} \rvert$	Cardinality of set $\mathbb{A}$
$\lfloor a \rfloor$	Floor function
j	Imaginary unit
$\mathbb{R}$	Set of real numbers
$\mathbb{C}$	Set of complex numbers
$\mathrm{Re}\{\cdot\}$, $\mathrm{Im}\{.\}$	Real and imaginary part
$\arg\{\cdot\}$	Complex argument

Vectors

$\boldsymbol{a}$	Column vector
$[\boldsymbol{a}]_v$	Element v
$\lvert\lvert \boldsymbol{a} \rvert\rvert$	Euclidean norm
$\mathbf{1}_N$	Column vector of ones of length N

$\mathbf{0}_N$	Column vector of zeros of length N
$\nabla f(\boldsymbol{a})$	Gradient

Matrices

$\boldsymbol{A}$	Matrix
$[\boldsymbol{A}]_{v,w}$	Element in row v and column w
$[\boldsymbol{A}]_{v,:}$	Row vector of v-th row
$[\boldsymbol{A}]_{:,w}$	Column vector of w-th column
$[\boldsymbol{A}]_{\boldsymbol{\iota},\boldsymbol{\iota}}$	Submatrix of element indices $\boldsymbol{\iota}$
$\boldsymbol{A}^T$	Transpose
$\boldsymbol{A}^H$	Conjugate transpose
$\boldsymbol{A}^{-1}$	Inverse
$\boldsymbol{A}^\dagger$	Moore-Penrose pseudoinverse
$\|\|\boldsymbol{A}\|\|_{\mathrm{F}}$	Frobenius norm
$\boldsymbol{A} \odot \boldsymbol{B}$	Hadamard-Schur product
$\boldsymbol{A} \otimes \boldsymbol{B}$	Kronecker product
$\mathbb{I}_N$	Identity matrix of size $N \times N$
$\mathbb{0}_N$	Zero matrix of size $N \times N$
$\mathrm{tr}\{\boldsymbol{A}\}$	Trace
$\det\{\boldsymbol{A}\}$	Determinant
$\mathrm{rank}\{\boldsymbol{A}\}$	Rank
$\mathrm{diag}\{\boldsymbol{a}\}$	Diagonal matrix
$\mathrm{diag}\{\boldsymbol{A}\}$	Vector of diagonal elements of matrix $\boldsymbol{A}$
$\mathrm{vec}\{\boldsymbol{A}\}$	Vectorization by stacking columns
$\boldsymbol{A} = \boldsymbol{Q}\boldsymbol{\Lambda}\boldsymbol{Q}^T$	Eigendecomp. of symmetric matrix
$\lambda_1,\ldots,\lambda_N$	Eigenvalues
$\boldsymbol{A} \succcurlyeq \boldsymbol{B}$	$\boldsymbol{A} - \boldsymbol{B}$ is positive semidefinite
$\frac{\partial \boldsymbol{f}(\boldsymbol{a})}{\partial \boldsymbol{a}}$	Jacobian matrix
$[\boldsymbol{H}]_{v,w} = \frac{\partial^2 f(\boldsymbol{a})}{\partial [\boldsymbol{a}]_v \partial [\boldsymbol{a}]_w}$	Hessian matrix

Estimation Theory

$\hat{a}$	Estimate
$\mathcal{N}$	Gaussian distribution
$\mathcal{CN}$	Complex circular symmetric Gaussian distribution
$\mathcal{U}$	Uniform distribution
χ^2	Chi-square distribution
$\mathrm{E}\{\cdot\}$	Expectation

$\mathrm{var}\{\cdot\}$	Variance
$\mathrm{cov}\{\cdot\}$	Covariance matrix
$\mathrm{MSE}\{\cdot\}$	Mean squared error
$p(a)$	Probability density function (pdf)
$p(a\|b)$	Conditional pdf
$L_a(b) = \ln p(a\|b)$	Log-likelihood function
$\tilde{L}_a(b)$	Concentrated log-likelihood function
$\boldsymbol{I}$	Fisher information matrix (FIM)
$\boldsymbol{I}^{\mathrm{e}}$	Equivalent Fisher information matrix (EFIM)
$\boldsymbol{J}$	Bayesian information matrix (BIM)
$\boldsymbol{J}^{\mathrm{e}}$	Equivalent Bayesian information matrix (EBIM)
$\mathrm{CRB}(a)$	Cramér-Rao bound (CRB)
$\mathrm{BCRB}(a)$	Bayesian Cramér-Rao bound (BCRB)

Signal Model

t	Continuous time
$y(t)$	Time domain RF signal
$x(t)$	Time domain baseband signal
k	Discrete time domain sample index
λ_{c}	Carrier wavelength
$f_{\mathrm{c}} = \frac{c}{\lambda_{\mathrm{c}}}$	Carrier frequency
$\kappa_{\mathrm{c}} = \frac{2\pi}{\lambda_{\mathrm{c}}}$	Carrier wavenumber
ω	Angular frequency
$\omega_{\mathrm{c}} = 2\pi f_{\mathrm{c}}$	Carrier angular frequency
n	Subcarrier index
ω_n	Angular frequency of n-th subcarrier
$\mathbb{N}_{\mathrm{sc}}$	Set of occupied subcarriers
$N = \|\mathbb{N}_{\mathrm{sc}}\|$	Number of occupied subcarriers
N_{fft}	FFT length
B_{s}	Sampling rate
B	Occupied bandwidth
f_{sc}	Subcarrier spacing
$s(n)$	OFDM symbol
$s(n, \tau)$	Delayed OFDM symbol
$\boldsymbol{s}(\tau) \quad \in \mathbb{C}^{N\times 1}$	Delayed OFDM symbol vector
p	Signal index
P	Number of impinging signals

s		Snapshot index
S		Number of snapshots
T		Snapshot interval
τ_p^s		ToA (of p-th signal at snapshot s)
$\tau_{i,j}^s$		ToA (Rx node i, Tx node j, snapshot s)
$\boldsymbol{\tau}^s$		ToA vector (at snapshot s)
α_p^s		Absolute amplitude (of p-th signal at snapshot s)
$\alpha_{i,j}^s$		Absolute amplitude (Rx node i, Tx node j, snapshot s)
$\boldsymbol{\alpha}^s$	$\in \mathbb{R}^{P\times 1}$	Absolute amplitude vector (at snapshot s)
φ_p^s		Absolute phase (of p-th signal at snapshot s)
$\varphi_{i,j}^s$		Absolute phase (Rx node i, Tx node j, snapshot s)
$\boldsymbol{\varphi}^s$	$\in \mathbb{R}^{P\times 1}$	Absolute phase vector (at snapshot s)
$\boldsymbol{r}_{i,j}^s(n)$	$\in \mathbb{C}^{M\times 1}$	Received signal in discrete frequency domain (Rx node i, Tx node j, snapshot s)
$\boldsymbol{r}_{i,j}^s$	$\in \mathbb{C}^{MN\times 1}$	Received signal vector in discrete frequency domain (Rx node i, Tx node j, snapshot s)
$w_m(n)$		Noise at port m
$w_{i,j}^s(n)$		Noise (Rx node i, Tx node j, snapshot s)
$\boldsymbol{w}_{i,j}^s(n)$	$\in \mathbb{C}^{M\times 1}$	Noise vector (Rx node i, Tx node j, snapshot s)
$\sigma^2_{\boldsymbol{r}_{i,j}^s}$		Noise variance
T_{n}		Receiver noise temperature
P_{Tx}		Average transmit power
SNR		Average SNR

Antenna

m		Antenna port
M_i		Number of antenna ports (of node i)
θ_p^s		Inclination DoA (of p-th signal at snapshot s)
$\boldsymbol{\theta}$	$\in \mathbb{R}^{P\times 1}$	Inclination DoA vector
ϕ_p^s		Azimuth DoA (of p-th signal at snapshot s)
$\phi_{i,j}^s$		Azimuth DoA (Rx node i, Tx node j, snapshot s)
$\boldsymbol{\phi}^s$	$\in \mathbb{R}^{P\times 1}$	Azimuth DoA vector (at snapshot s)
$g(\omega,\theta,\phi)$		Antenna gain for angular frequency ω
$g_m(\theta,\phi)$		Antenna gain of port m
$g_{\mathrm{co},m}(\theta,\phi)$		Antenna gain of port m for co-polarization
$g_{\mathrm{cross},m}(\theta,\phi)$		Antenna gain of port m for cross-polarization
$\boldsymbol{g}(\theta,\phi)$	$\in \mathbb{R}^{M\times 1}$	Antenna gain vector

$\Phi(\omega, \theta, \phi)$		Antenna phase response for angular frequency ω
$\Phi_m(\theta, \phi)$		Antenna phase response of port m
$\Phi_{\mathrm{co},m}(\theta, \phi)$		Antenna phase response of port m for co-polarization
$\Phi_{\mathrm{cross},m}(\theta, \phi)$		Antenna phase response of port m for cross-polarization
$\tau_m(\theta, \phi)$		Antenna group delay of port m
$a(\omega, \theta, \phi)$		Antenna response for angular frequency ω
$a_m(\theta, \phi)$		Antenna response of port m
$\boldsymbol{a}(\theta)$	$\in \mathbb{C}^{M\times 1}$	Antenna response vector for inclination θ
$\boldsymbol{a}_i^s(\phi)$	$\in \mathbb{C}^{M\times 1}$	Antenna response vector for azimuth ϕ (of node i at snapshot s)
$\boldsymbol{a}(\theta, \phi)$	$\in \mathbb{C}^{M\times 1}$	Antenna response vector for inclination and azimuth
$\boldsymbol{A}(\theta)$	$\in \mathbb{C}^{M\times P}$	Antenna response matrix for inclination θ
$\boldsymbol{A}(\phi)$	$\in \mathbb{C}^{M\times P}$	Antenna response matrix for azimuth ϕ
$\boldsymbol{A}(\theta, \phi)$	$\in \mathbb{C}^{M\times P}$	Antenna response matrix for inclination and azimuth
θ_q		Sampled inclination
ϕ_q		Sampled azimuth
q		Spatial sample index
Q		Number of spatial samples
$e_{q,m}$		Sampled antenna response with index q of port m
$\boldsymbol{e}_q$	$\in \mathbb{C}^{M}$	Sampled antenna response vector with index q
$\boldsymbol{E}_i$	$\in \mathbb{C}^{M\times Q}$	Sampled antenna response matrix (of node i)
R		Radius of sphere enclosing antenna
γ_p		Auxiliary angle (of p-th signal)
$\boldsymbol{\gamma}$	$\in \mathbb{R}^{P\times 1}$	Auxiliary angle vector
β_p		Polarization phase (of p-th signal)
$\boldsymbol{\beta}$	$\in \mathbb{R}^{P\times 1}$	Polarization phase vector
$a_{\mathrm{co},m}(\theta, \phi)$		Partial antenna response of port m for co-polarization
$a_{\mathrm{cross},m}(\theta, \phi)$		Partial antenna response of port m for cross-polarization
$\boldsymbol{a}_{\mathrm{co}}(\theta, \phi)$	$\in \mathbb{C}^{M\times 1}$	Partial antenna response vector for co-polarization
$\boldsymbol{a}_{\mathrm{cross}}(\theta, \phi)$	$\in \mathbb{C}^{M\times 1}$	Partial antenna response vector for cross-polarization
$\boldsymbol{a}(\theta, \phi, \gamma, \beta)$	$\in \mathbb{C}^{M\times 1}$	Polarimetric antenna response vector
$\boldsymbol{A}(\boldsymbol{\theta}, \boldsymbol{\phi}, \boldsymbol{\gamma}, \boldsymbol{\beta})$	$\in \mathbb{C}^{M\times P}$	Polarimetric antenna response matrix

Wavefield Modeling

u		Coefficient index
U		Number of coefficients
$\boldsymbol{b}(\theta)$	$\in \mathbb{C}^{U\times 1}$	Basis vector for inclination θ

$\boldsymbol{b}(\phi)$	$\in \mathbb{C}^{U\times 1}$	Basis vector for azimuth ϕ
$\boldsymbol{b}(\theta,\phi)$	$\in \mathbb{C}^{U\times 1}$	Basis vector for inclination and azimuth
$\boldsymbol{B}$	$\in \mathbb{C}^{U\times Q}$	Basis matrix
$\boldsymbol{G}_i^s$	$\in \mathbb{C}^{M\times U}$	Sampling matrix (of node i at snapshot s)
$\hat{\boldsymbol{G}}_i^0$	$\in \mathbb{C}^{M\times U}$	Prior sampling matrix (of node i)
$\boldsymbol{g}$	$\in \mathbb{C}^{MU\times 1}$	Vectorized sampling matrix
$\boldsymbol{g}_{\mathrm{R}}$	$\in \mathbb{R}^{MU\times 1}$	Real part of vectorized sampling matrix
$\boldsymbol{g}_{\mathrm{I}}$	$\in \mathbb{R}^{MU\times 1}$	Imaginary part of vectorized sampling matrix
$\boldsymbol{g}_{\mathrm{RI},i}^s$	$\in \mathbb{R}^{2MU\times 1}$	Real and imaginary parts of vectorized sampling matrix (of node i at snapshot s)
$\hat{\boldsymbol{g}}_{\mathrm{RI},i}^0$	$\in \mathbb{R}^{2MU\times 1}$	Real and imaginary parts of vectorized prior sampling matrix (of node i)
Different use of l and m:		
$Y_l^m(\theta,\phi)$		Spherical harmonics of degree l and order m
N_l^m		Normalization factor of degree l and order m
$P_l^m(x)$		Associated Legendre polynomial of degree l and order m
$P_l(x)$		Legendre polynomial of degree l

DoA and ToA Estimation

$\check{s}$		Reference signal power
$\check{r}_m$		Estimated RSS on port m
$\check{\boldsymbol{r}}$	$\in \mathbb{R}^{M\times 1}$	Estimated RSS vector
$\check{r}_{i,j}^s$		Estimated RSS for Rx node i, Tx node j and snapshot s
$\check{\boldsymbol{\mu}}$	$\in \mathbb{R}^{M\times 1}$	Mean vector of RSS observations
$\check{\boldsymbol{\Sigma}}$	$\in \mathbb{R}^{M\times M}$	Covariance matrix of RSS observations
$\check{\sigma}_m^2$		Variance of RSS observations of port m
$\boldsymbol{\zeta}$		Parameter vector for non-coherent DoA estimation
$\boldsymbol{\zeta}'$		Reduced parameter vector for non-coherent DoA estimation
$\tilde{\boldsymbol{s}}(n)$	$\in \mathbb{C}^{P\times 1}$	Arbitrary deterministic signals
$\boldsymbol{R}_{\tilde{\boldsymbol{s}}}$	$\in \mathbb{C}^{P\times P}$	Signal covariance matrix
$\hat{\boldsymbol{R}}_{\boldsymbol{r}}$	$\in \mathbb{C}^{M\times M}$	Sample covariance matrix
$\boldsymbol{\Pi}_{\boldsymbol{A}}$	$\in \mathbb{C}^{M\times M}$	Projector onto signal subspace
$\boldsymbol{\Pi}_{\boldsymbol{A}}^{\perp}$	$\in \mathbb{C}^{M\times M}$	Projector onto noise subspace
$\boldsymbol{D}$	$\in \mathbb{C}^{M\times 2P}$	Matrix of derivatives
$\boldsymbol{Z}$	$\in \mathbb{C}^{P\times 2P}$	Selection matrix
$\boldsymbol{w}_{\mathrm{BF},p}$	$\in \mathbb{C}^{M\times 1}$	Conventional beamforming weight vector

$r_{\mathrm{BF},p}(n)$		Received signal after beamforming
$\boldsymbol{r}_{\mathrm{BF},p}$	$\in \mathbb{C}^{N\times 1}$	Received signal vector after beamforming
$\bar{\beta}^2$		Mean square bandwidth
$\bar{\gamma}^2(\phi_{i,j})$		DoA estimation capability of antenna
$\bar{\alpha}^2(\phi_{i,j})$		Unknown absolute amplitude impact on DoA estimation
$\bar{\varphi}^2(\phi_{i,j})$		Unknown absolute phase impact on DoA estimation

Cooperative Network

$\mathbb{R}$	Agent set
$\mathbb{A}$	Anchor set
$\mathbb{N}$	Node set
i	Rx node index
j	Tx node index
$\mathbb{L}_i^s$	Neighbor set of node i (at snapshot s)
$l(i,j)$	Link index
$\boldsymbol{l}_{l(i,j)}$	Link metrics for one link
$\boldsymbol{l}$	Link metrics for all links
$\boldsymbol{n}_{l(i,j)}$	Link unknowns for one link
$\boldsymbol{n}$	Link unknowns for all links
$\boldsymbol{p}_i^s = [x_i^s,\, y_i^s]^T$	Position of agent i (at snapshot s)
$d_{i,j}^s$	Distance between nodes i and j (at snapshot s)
ψ_i^s	Orientation of node i (at snapshot s)
v_i^s	Linear velocity of node i at snapshot s
ω_i^s	Angular velocity of node i at snapshot s
δ_i^s	Ranging bias of node i at snapshot s
$\boldsymbol{x}^s$	State vector (at snapshot s)
$\tilde{\boldsymbol{x}}^s$	Augmented state vector (at snapshot s)
$\boldsymbol{x}_i^s$	Node state vector (at snapshot s)
$\boldsymbol{x}_{i,\mathrm{loc}}^s$	Node kinematic states at snapshot s
$\boldsymbol{x}_{i,\mathrm{cal}}^s$	Node calibration states at snapshot s
$\boldsymbol{x}^s$	Network state vector (at snapshot s)
$\boldsymbol{z}^s$	Observation vector (at snapshot s)
$\boldsymbol{x}^{1:S}$	States from snapshots 1 to S
$\boldsymbol{z}^{1:S}$	Observations from snapshots 1 to S
$\boldsymbol{f}\left(\boldsymbol{x}_{i,\mathrm{loc}}^{(s-1)}\right)$	Motion model for agent i
$\boldsymbol{w}_{\boldsymbol{x}_{i,\mathrm{loc}}}^s$	Kinematic process noise for agent i
$\boldsymbol{\Sigma}_{\boldsymbol{x}_{i,\mathrm{loc}}}^s$	Kinematic process noise covariance matrix for agent i

$\boldsymbol{F}^{(s-1)}$	State transition Jacobian matrix
$\boldsymbol{\Sigma}_{\boldsymbol{x}}^{s}$	Process noise covariance matrix

In-Situ Antenna Calibration

ϕ_{obs}^{s}	Observable DoA from external sensor at snapshot s
$w_{\phi_{\text{obs}}}^{s}$	Observable DoA noise at snapshot s
$\sigma_{\phi_{\text{obs}}}^{2}$	Observable DoA noise variance
$\boldsymbol{J}_{\boldsymbol{g},\text{sync}}^{s}$	EBIM for the sampling matrix elements with known propagation channel at snapshot s
$\boldsymbol{J}_{\boldsymbol{\phi},\text{sync}}^{s}$	EBIM for the DoAs with known propagation channel at snapshot s
$\boldsymbol{J}_{\boldsymbol{g}}^{s}$	EBIM for the sampling matrix elements at snapshot s
$\boldsymbol{J}_{\boldsymbol{\phi}}^{s}$	EBIM for the DoAs at snapshot s
$q(\boldsymbol{x}^{s})$	In-situ calibration MAP estimator cost function
$a_{m,\text{UCA}}(\phi)$	UCA antenna response of port m
$\boldsymbol{a}_{\text{UCA}}(\phi)$	UCA antenna response vector / steering vector
$\boldsymbol{G}_{\text{UCA}}$	UCA sampling matrix
$\boldsymbol{W}_{\boldsymbol{G}}$	Sampling matrix noise matrix
$\boldsymbol{w}_{\boldsymbol{g}}^{u}$	Sampling matrix noise vector
$\sigma_{\boldsymbol{g}}^{2}$	Sampling matrix noise variance

Cooperative SLAC

$p(\boldsymbol{x}^{0})$	Prior pdf
$p\left(\boldsymbol{x}^{0:S}\middle\vert\boldsymbol{z}^{1:S}\right)$	Posterior pdf
$p\left(\boldsymbol{x}^{s}\middle\vert\boldsymbol{x}^{(s-1)}\right)$	State transition pdf
$p\left(\boldsymbol{z}^{s}\middle\vert\boldsymbol{x}^{s}\right)$	Observation likelihood
$\bar{\boldsymbol{x}}^{s}$	Estimated mean after prediction
$\bar{\boldsymbol{\Sigma}}^{s}$	Estimated covariance after prediction
$\hat{\boldsymbol{x}}^{s}$	Estimated mean after update
$\hat{\boldsymbol{\Sigma}}^{s}$	Estimated covariance after update
$\hat{\boldsymbol{x}}_{i}^{0}$	Mean of Gaussian prior
$\hat{\boldsymbol{\Sigma}}_{i}^{0}$	Covariance of Gaussian prior
$\boldsymbol{\iota}_{i}$	Vector containing the indices of the elements of $\boldsymbol{x}_{i}^{s}$ in $\boldsymbol{x}^{s}$
$\boldsymbol{\iota}_{i,\text{loc}}$	Vector containing the indices of the elements of $\boldsymbol{x}_{i,\text{loc}}^{s}$ in $\boldsymbol{x}^{s}$
$\boldsymbol{\iota}_{i,\text{cal}}$	Vector containing the indices of the elements of $\boldsymbol{x}_{i,\text{cal}}^{s}$ in $\boldsymbol{x}^{s}$
$h(\boldsymbol{x}^{s})$	SLAC update step cost function

Appendix C

Definitions, Proofs and Derivations

C.1 Legendre Polynomials and Derivatives of Complex Spherical Harmonics

The spherical harmonics (2.14) with degree l and order m can be calculated with the associated Legendre polynomial [155]

$$P_l^m(x) = (-1)^m (1-x^2)^{m/2} \frac{\mathrm{d}^m}{\mathrm{d}x^m} P_l(x) \tag{C.1}$$

and the Legendre polynomial

$$P_l(x) = \frac{1}{2^l\, l!} \frac{\mathrm{d}^l}{\mathrm{d}x^l} (x^2-1)^l. \tag{C.2}$$

The partial derivatives of the spherical harmonics (2.14) with respect to θ and ϕ are

$$\frac{\partial}{\partial\theta} Y_l^m(\theta,\phi) = m\cot(\theta) Y_l^m(\theta,\phi) + \sqrt{(l-m)(l+m+1)}\, e^{-\mathrm{j}\phi} Y_l^{m+1}(\theta,\phi), \tag{C.3a}$$

$$\frac{\partial}{\partial\phi} Y_l^m(\theta,\phi) = \mathrm{j}m Y_l^m(\theta,\phi). \tag{C.3b}$$

C.2 Real Spherical Harmonics and their Derivatives

The real version of the spherical harmonic functions, which can be applied in (2.15) for the non-coherent DoA estimator described in Section 2.4.1, are given by

$$Y_l^m(\theta,\phi) = \begin{cases} \sqrt{2} N_l^m \cos(m\phi) P_l^m(\cos(\theta)) & \text{if } m > 0 \\ N_l^0 P_l^m(\cos(\theta)) & \text{if } m = 1 \\ \sqrt{2} N_l^{|m|} \sin(|m|\phi) P_l^{|m|}(\cos(\theta)) & \text{if } m < 0, \end{cases} \tag{C.4}$$

with degree $l = 0, ..., L$, order $m = -l, ..., l$ and $P_l^m(.)$ given by (C.1). The normalization factor N_l^m is defined as

$$N_l^m = \sqrt{\frac{2l+1}{4\pi}\frac{(l-m)!}{(l+m)!}}. \tag{C.5}$$

The derivative of the real spherical harmonics with respect to θ is given by

$$\frac{\partial}{\partial\theta}Y_l^m(\theta,\phi) = \begin{cases} \sqrt{2}N_l^m\cos(m\phi)\frac{\partial P_l^m(\cos(\theta))}{\partial\theta} & \text{if } m > 0 \\ N_l^0\frac{\partial P_l^m(\cos(\theta))}{\partial\theta} & \text{if } m = 1 \\ \sqrt{2}N_l^{|m|}\sin(|m|\phi)\frac{\partial P_l^{|m|}(\cos(\theta))}{\partial\theta} & \text{if } m < 0. \end{cases} \tag{C.6}$$

It contains the derivative of the associated Legendre polynomial [155]

$$\frac{\partial P_l^m(\cos(\theta))}{\partial\theta} = 1 + l - m\ \sin(\theta)P_{l+1}^m(cos(\theta)) - \frac{l+1}{\tan(\theta)}P_l^m(\cos(\theta)). \tag{C.7}$$

The derivative of the real spherical harmonics with respect to ϕ is given by

$$\frac{\partial}{\partial\phi}Y_l^m(\theta,\phi) = \begin{cases} \sqrt{2}N_l^m(-m)\sin(m\phi)P_l^m(\cos(\theta)) & \text{if } m > 0 \\ 0 & \text{if } m = 1 \\ \sqrt{2}N_l^{|m|}(-m)\cos(m\phi)P_l^{|m|}(\cos(\theta)) & \text{if } m < 0. \end{cases} \tag{C.8}$$

C.3 Proof that RSS Observations are Approximately Gaussian Distributed

Defining $r_{m,\mathrm{R}}(n) = \mathrm{Re}\{r_m(n)\}$ and $r_{m,\mathrm{I}}(n) = \mathrm{Im}\{r_m(n)\}$, the sum of the squared magnitude of the received signal

$$\begin{aligned} \tilde{r}_m &= \sum_{n\in\mathbb{N}_{\mathrm{sc}}} |r_m(n)|^2 \\ &= \sum_{n\in\mathbb{N}_{\mathrm{sc}}} r_{m,\mathrm{R}}^2(n) + r_{m,\mathrm{I}}^2(n) \\ &\sim \chi^2(2N, \Lambda_m, \sigma_{\boldsymbol{r}}^2/2) \end{aligned} \tag{C.9}$$

follows a noncentral χ^2 distribution [195] with $2N$ degrees of freedom. The noncentrality parameter can be derived as

$$\begin{aligned}\Lambda_m &= \sum_{n\in\mathbb{N}_{\mathrm{sc}}} \left(\mathrm{E}\{r_{m,\mathrm{R}}(n)\}^2 + \mathrm{E}\{r_{m,\mathrm{I}}(n)\}^2\right) \\ &= \sum_{n\in\mathbb{N}_{\mathrm{sc}}} \left(\mathrm{Re}\{a_m(\theta,\phi)s(n)\}^2 + \mathrm{Im}\{a_m(\theta,\phi)s(n)\}^2\right) \\ &= \sum_{n\in\mathbb{N}_{\mathrm{sc}}} |a_m(\theta,\phi)|^2|s(n)|^2 \\ &= \sum_{n\in\mathbb{N}_{\mathrm{sc}}} g_m(\theta,\phi)|s(n)|^2 \\ &= N g_m(\theta,\phi)\check{s}.\end{aligned} \tag{C.10}$$

The pdf of the noncentral χ^2 distribution is given by

$$p_{\tilde{r}_m}(x) = \frac{1}{\sigma_{\boldsymbol{r}}^2}\left(\frac{x}{\Lambda_m}\right)^{\frac{N}{2}} e^{-\frac{\Lambda_m+x}{\sigma_{\boldsymbol{r}}^2}} I_N\left(\frac{2\sqrt{\Lambda_m x}}{\sigma_{\boldsymbol{r}}^2}\right), \tag{C.11}$$

where $I_\nu(.)$ is the modified Bessel function of the first kind, see [155]. Since $\check{r}_m$ is just a scaled version of that, its distribution can be obtained by transformation $p_{\check{r}_m}(x) = N p_{\tilde{r}_m}(Nx)$. By inserting (C.10), we obtain the pdf

$$p_{\check{r}_m}(x) = \frac{N}{\sigma_{\boldsymbol{r}}^2}\left(\frac{x}{g_m(\theta,\phi)\check{s}}\right)^{\frac{N}{2}} e^{-\frac{N(g_m(\theta,\phi)\check{s}+x)}{\sigma^2}} I_N\left(\frac{2N\sqrt{g_m(\theta,\phi)\check{s}x}}{\sigma_{\boldsymbol{r}}^2}\right). \tag{C.12}$$

The mean and variance are derived as

$$\begin{aligned}\check{\mu}_m &= \mathrm{E}\{\check{r}_m\} \\ &= N^{-1}\ \mathrm{E}\{\tilde{r}_m\} \\ &= N^{-1}(N\sigma_{\boldsymbol{r}}^2 + \Lambda_m) \\ &= g_m(\theta,\phi)\check{s} + \sigma_{\boldsymbol{r}}^2,\end{aligned} \tag{C.13}$$

$$\begin{aligned}\check{\sigma}_m^2 &= \mathrm{var}\{\check{r}_m\} \\ &= N^{-2}\ \mathrm{var}\{\tilde{r}_m\} \\ &= N^{-2}(N\sigma_{\boldsymbol{r}}^4 + 2\sigma_{\boldsymbol{r}}^2\Lambda_m) \\ &= N^{-1}(\sigma_{\boldsymbol{r}}^4 + 2g_m(\theta,\phi)\check{s}\sigma_{\boldsymbol{r}}^2).\end{aligned} \tag{C.14}$$

For a growing number of occupied subcarriers N, (C.12) approaches a Gaussian distribution $\check{r}_m \sim \mathcal{N}(\check{\mu}_m, \check{\sigma}_m^2)$ due to the central limit theorem. The approximation is reasonable for $N > 25$ [196].

C.4 Derivation of Fisher Information in ToA and DoA Domain

First, we calculate the entities (C.15), (C.17) and (C.18). We have

$$\sum_{n\in\mathbb{N}_{\mathrm{sc}}} |s(n,\tau_{i,j})|^2 = \sum_{n\in\mathbb{N}_{\mathrm{sc}}} |s(n)|^2 = NP_{\mathrm{Tx}}, \tag{C.15}$$

see (2.10). With the derivative of (2.4),

$$\frac{\partial}{\partial\tau_{i,j}} s(n,\tau_{i,j}) = -\mathrm{j}2\pi n f_{\mathrm{sc}} s(n) e^{-\mathrm{j}2\pi n f_{\mathrm{sc}}\tau_{i,j}}, \tag{C.16}$$

and assuming that the number of occupied subcarriers N is odd and the signal spectrum is symmetric, $|s(-n)| = |s(n)|\,\forall\, n \in \mathbb{N}_{\mathrm{sc}}$, we have

$$\sum_{n\in\mathbb{N}_{\mathrm{sc}}} s^*(n,\tau_{i,j}) \frac{\partial s(n,\tau_{i,j})}{\partial\tau_{i,j}} = -\mathrm{j}2\pi f_{\mathrm{sc}} \sum_{n\in\mathbb{N}_{\mathrm{sc}}} n|s(n)|^2 = 0, \tag{C.17}$$

see also [84]. Again with (C.16), we find that

$$\sum_{n\in\mathbb{N}_{\mathrm{sc}}} \left|\frac{\partial s(n,\tau_{i,j})}{\partial\tau_{i,j}}\right|^2 = 4\pi^2 f_{\mathrm{sc}}^2 \sum_{n\in\mathbb{N}_{\mathrm{sc}}} n^2|s(n)|^2. \tag{C.18}$$

With (3.10), the sub-matrices of (3.11) are defined by (C.19) to (C.21).

$$[\boldsymbol{I_l}]_{l(i,j),l(i,j)} = \frac{2}{\sigma_{\boldsymbol{r}}^2} \sum_{n\in\mathbb{N}_{\mathrm{sc}}} \begin{bmatrix} \left\|\frac{\partial\,\mathrm{E}\{\boldsymbol{r}_{i,j}(n)\}}{\partial\tau_{i,j}}\right\|^2 & \mathrm{Re}\left\{\frac{\partial\,\mathrm{E}\{\boldsymbol{r}_{i,j}(n)\}^H}{\partial\tau_{i,j}} \frac{\partial\,\mathrm{E}\{\boldsymbol{r}_{i,j}(n)\}}{\partial\phi_{i,j}}\right\} \\ \mathrm{Re}\left\{\frac{\partial\,\mathrm{E}\{\boldsymbol{r}_{i,j}(n)\}^H}{\partial\tau_{i,j}} \frac{\partial\,\mathrm{E}\{\boldsymbol{r}_{i,j}(n)\}}{\partial\phi_{i,j}}\right\} & \left\|\frac{\partial\,\mathrm{E}\{\boldsymbol{r}_{i,j}(n)\}}{\partial\phi_{i,j}}\right\|^2 \end{bmatrix} \tag{C.19}$$

$$[\boldsymbol{I_{ln}}]_{l(i,j),l(i,j)} = \frac{2}{\sigma_{\boldsymbol{r}}^2} \sum_{n\in\mathbb{N}_{\mathrm{sc}}} \begin{bmatrix} \mathrm{Re}\left\{\frac{\partial\,\mathrm{E}\{\boldsymbol{r}_{i,j}(n)\}^H}{\partial\tau_{i,j}} \frac{\partial\,\mathrm{E}\{\boldsymbol{r}_{i,j}(n)\}}{\partial\alpha_{i,j}}\right\} & \mathrm{Re}\left\{\frac{\partial\,\mathrm{E}\{\boldsymbol{r}_{i,j}(n)\}^H}{\partial\tau_{i,j}} \frac{\partial\,\mathrm{E}\{\boldsymbol{r}_{i,j}(n)\}}{\partial\varphi_{i,j}}\right\} \\ \mathrm{Re}\left\{\frac{\partial\,\mathrm{E}\{\boldsymbol{r}_{i,j}(n)\}^H}{\partial\phi_{i,j}} \frac{\partial\,\mathrm{E}\{\boldsymbol{r}_{i,j}(n)\}}{\partial\alpha_{i,j}}\right\} & \mathrm{Re}\left\{\frac{\partial\,\mathrm{E}\{\boldsymbol{r}_{i,j}(n)\}^H}{\partial\phi_{i,j}} \frac{\partial\,\mathrm{E}\{\boldsymbol{r}_{i,j}(n)\}}{\partial\varphi_{i,j}}\right\} \end{bmatrix} \tag{C.20}$$

$$[\boldsymbol{I_n}]_{l(i,j),l(i,j)} = \frac{2}{\sigma_{\boldsymbol{r}}^2} \sum_{n\in\mathbb{N}_{\mathrm{sc}}} \begin{bmatrix} \left\|\frac{\partial\,\mathrm{E}\{\boldsymbol{r}_{i,j}(n)\}}{\partial\alpha_{i,j}}\right\|^2 & \mathrm{Re}\left\{\frac{\partial\,\mathrm{E}\{\boldsymbol{r}_{i,j}(n)\}^H}{\partial\alpha_{i,j}} \frac{\partial\,\mathrm{E}\{\boldsymbol{r}_{i,j}(n)\}}{\partial\varphi_{i,j}}\right\} \\ \mathrm{Re}\left\{\frac{\partial\,\mathrm{E}\{\boldsymbol{r}_{i,j}(n)\}^H}{\partial\alpha_{i,j}} \frac{\partial\,\mathrm{E}\{\boldsymbol{r}_{i,j}(n)\}}{\partial\varphi_{i,j}}\right\} & \left\|\frac{\partial\,\mathrm{E}\{\boldsymbol{r}_{i,j}(n)\}}{\partial\varphi_{i,j}}\right\|^2 \end{bmatrix} \tag{C.21}$$

Using the definitions (3.14) and (3.16) and (C.15), (C.17) and (C.18), the elements of $\boldsymbol{I_l}$ evaluate to (C.22) to (C.24).

$$\begin{aligned}\sum_{n\in\mathbb{N}_{\mathrm{sc}}}\left\|\frac{\partial\,\mathrm{E}\left\{\boldsymbol{r}_{i,j}(n)\right\}}{\partial\tau_{i,j}}\right\|^2 &= \alpha_{i,j}^2 4\pi^2 f_{\mathrm{sc}}^2\|\boldsymbol{a}(\phi_{i,j})\|^2\sum_{n\in\mathbb{N}_{\mathrm{sc}}} n^2|s(n)|^2\\ &= \alpha_{i,j}^2 N P_{\mathrm{Tx}}\bar{\beta}^2\|\boldsymbol{a}(\phi_{i,j})\|^2\end{aligned} \tag{C.22}$$

$$\begin{aligned}\sum_{n\in\mathbb{N}_{\mathrm{sc}}}\mathrm{Re}\left\{\frac{\partial\,\mathrm{E}\left\{\boldsymbol{r}_{i,j}(n)\right\}^H}{\partial\tau_{i,j}}\frac{\partial\,\mathrm{E}\left\{\boldsymbol{r}_{i,j}(n)\right\}}{\partial\phi_{i,j}}\right\} =&\alpha_{i,j}^2 2\pi f_{\mathrm{sc}}\,\mathrm{Re}\left\{\mathrm{j}\boldsymbol{a}^H(\phi_{i,j})\frac{\partial\boldsymbol{a}(\phi_{i,j})}{\partial\phi_{i,j}}\sum_{n\in\mathbb{N}_{\mathrm{sc}}} n|s(n)|^2\right\}\\ =&0\end{aligned} \tag{C.23}$$

$$\begin{aligned}\sum_{n\in\mathbb{N}_{\mathrm{sc}}}\left\|\frac{\partial\,\mathrm{E}\left\{\boldsymbol{r}_{i,j}(n)\right\}}{\partial\phi_{i,j}}\right\|^2 &= \alpha_{i,j}^2 N P_{\mathrm{Tx}}\left\|\frac{\partial\boldsymbol{a}(\phi_{i,j})}{\partial\phi_{i,j}}\right\|^2\\ &= \alpha_{i,j}^2 N P_{\mathrm{Tx}}\bar{\gamma}^2\|\boldsymbol{a}(\phi_{i,j})\|^2\end{aligned} \tag{C.24}$$

Again using (C.15), (C.17) and (C.18), the elements of $\boldsymbol{I_{ln}}$ evaluate to (C.25) to (C.28).

$$\begin{aligned}\sum_{n\in\mathbb{N}_{\mathrm{sc}}}\mathrm{Re}\left\{\frac{\partial\,\mathrm{E}\left\{\boldsymbol{r}_{i,j}(n)\right\}^H}{\partial\tau_{i,j}}\frac{\partial\,\mathrm{E}\left\{\boldsymbol{r}_{i,j}(n)\right\}}{\partial\alpha_{i,j}}\right\} &= \alpha_{i,j}2\pi\|\boldsymbol{a}(\phi_{i,j})\|^2\sum_{n\in\mathbb{N}_{\mathrm{sc}}}\mathrm{Re}\left\{\mathrm{j}n|s(n)|^2\right\}\\ &= 0\end{aligned} \tag{C.25}$$

$$\begin{aligned}\sum_{n\in\mathbb{N}_{\mathrm{sc}}}\mathrm{Re}\left\{\frac{\partial\,\mathrm{E}\left\{\boldsymbol{r}_{i,j}(n)\right\}^H}{\partial\tau_{i,j}}\frac{\partial\,\mathrm{E}\left\{\boldsymbol{r}_{i,j}(n)\right\}}{\partial\varphi_{i,j}}\right\} &= -\alpha_{i,j}^2 2\pi\|\boldsymbol{a}(\phi_{i,j})\|^2\sum_{n\in\mathbb{N}_{\mathrm{sc}}} n|s(n)|^2\\ &= 0\end{aligned} \tag{C.26}$$

$$\begin{aligned}\sum_{n\in\mathbb{N}_{\mathrm{sc}}}\mathrm{Re}\left\{\frac{\partial\,\mathrm{E}\left\{\boldsymbol{r}_{i,j}(n)\right\}^H}{\partial\phi_{i,j}}\frac{\partial\,\mathrm{E}\left\{\boldsymbol{r}_{i,j}(n)\right\}}{\partial\alpha_{i,j}}\right\} &= \alpha_{i,j}\,\mathrm{Re}\left\{\frac{\partial\boldsymbol{a}^H(\phi_{i,j})}{\partial\phi_{i,j}}\boldsymbol{a}(\phi_{i,j})\right\}\sum_{n\in\mathbb{N}_{\mathrm{sc}}}|s(n)|^2\\ &= \alpha_{i,j}N P_{\mathrm{Tx}}\,\mathrm{Re}\left\{\frac{\partial\boldsymbol{a}^H(\phi_{i,j})}{\partial\phi_{i,j}}\boldsymbol{a}(\phi_{i,j})\right\}\end{aligned} \tag{C.27}$$

$$\begin{aligned}\sum_{n\in\mathbb{N}_{\mathrm{sc}}}\mathrm{Re}\left\{\frac{\partial\,\mathrm{E}\left\{\boldsymbol{r}_{i,j}(n)\right\}^H}{\partial\phi_{i,j}}\frac{\partial\,\mathrm{E}\left\{\boldsymbol{r}_{i,j}(n)\right\}}{\partial\varphi_{i,j}}\right\} &= \alpha_{i,j}^2\,\mathrm{Re}\left\{\mathrm{j}\frac{\partial\boldsymbol{a}^H(\phi_{i,j})}{\partial\phi_{i,j}}\boldsymbol{a}(\phi_{i,j})\right\}\sum_{n\in\mathbb{N}_{\mathrm{sc}}}|s(n)|^2\\ &= -\alpha_{i,j}^2 N P_{\mathrm{Tx}}\,\mathrm{Im}\left\{\frac{\partial\boldsymbol{a}^H(\phi_{i,j})}{\partial\phi_{i,j}}\boldsymbol{a}(\phi_{i,j})\right\}\end{aligned} \tag{C.28}$$

Finally, the elements of $\boldsymbol{I_n}$ evaluate to (C.29) to (C.31).

$$\begin{aligned}\sum_{n\in\mathbb{N}_{\mathrm{sc}}}\left\|\frac{\partial\,\mathrm{E}\left\{\boldsymbol{r}_{i,j}(n)\right\}}{\partial\alpha_{i,j}}\right\|^2 &= \|\boldsymbol{a}(\phi_{i,j})\|^2\sum_{n\in\mathbb{N}_{\mathrm{sc}}}|s(n)|^2\\ &= NP_{\mathrm{Tx}}\|\boldsymbol{a}(\phi_{i,j})\|^2\end{aligned}\tag{C.29}$$

$$\begin{aligned}\sum_{n\in\mathbb{N}_{\mathrm{sc}}}\mathrm{Re}\left\{\frac{\partial\,\mathrm{E}\left\{\boldsymbol{r}_{i,j}(n)\right\}^H}{\partial\alpha_{i,j}}\frac{\partial\,\mathrm{E}\left\{\boldsymbol{r}_{i,j}(n)\right\}}{\partial\varphi_{i,j}}\right\} &= \alpha_{i,j}\|\boldsymbol{a}(\phi_{i,j})\|^2\sum_{n\in\mathbb{N}_{\mathrm{sc}}}\mathrm{Re}\left\{\mathrm{j}|s(n)|^2\right\}\\ &= 0\end{aligned}\tag{C.30}$$

$$\begin{aligned}\sum_{n\in\mathbb{N}_{\mathrm{sc}}}\left\|\frac{\partial\,\mathrm{E}\left\{\boldsymbol{r}_{i,j}(n)\right\}}{\partial\varphi_{i,j}}\right\| &= \alpha_{i,j}^2\|\boldsymbol{a}(\phi_{i,j})\|^2\sum_{n\in\mathbb{N}_{\mathrm{sc}}}|s(n)|^2\\ &= \alpha_{i,j}^2NP_{\mathrm{Tx}}\|\boldsymbol{a}(\phi_{i,j})\|^2\end{aligned}\tag{C.31}$$

Inserting the above equations into (C.19) to (C.21) and using definitions (3.17) and (3.18), we obtain

$$[\boldsymbol{I_l}]_{l(i,j),l(i,j)} = \frac{2}{\sigma_{\boldsymbol{r}}^2}\begin{bmatrix}\alpha_{i,j}^2NP_{\mathrm{Tx}}\|\boldsymbol{a}(\phi_{i,j})\|^2\bar{\beta}^2 & 0\\ 0 & \alpha_{i,j}^2NP_{\mathrm{Tx}}\|\boldsymbol{a}(\phi_{i,j})\|^2\bar{\gamma}^2\end{bmatrix}\tag{C.32}$$

and

$$\begin{aligned}&[\boldsymbol{I_{ln}}\boldsymbol{I_n}^{-1}\boldsymbol{I_{ln}}^T]_{l(i,j),l(i,j)}\\ &= \frac{2}{\sigma_{\boldsymbol{r}}^2}\begin{bmatrix}0 & 0\\ \alpha_{i,j}NP_{\mathrm{Tx}}\,\mathrm{Re}\left\{\frac{\partial\boldsymbol{a}^H(\phi_{i,j})}{\partial\phi_{i,j}}\boldsymbol{a}(\phi_{i,j})\right\} & -\alpha_{i,j}^2NP_{\mathrm{Tx}}\,\mathrm{Im}\left\{\frac{\partial\boldsymbol{a}^H(\phi_{i,j})}{\partial\phi_{i,j}}\boldsymbol{a}(\phi_{i,j})\right\}\end{bmatrix}\\ &\quad\begin{bmatrix}NP_{\mathrm{Tx}}\|\boldsymbol{a}(\phi_{i,j})\|^2 & 0\\ 0 & \alpha_{i,j}^2NP_{\mathrm{Tx}}\|\boldsymbol{a}(\phi_{i,j})\|^2\end{bmatrix}^{-1}\\ &\quad\begin{bmatrix}0 & 0\\ \alpha_{i,j}NP_{\mathrm{Tx}}\,\mathrm{Re}\left\{\frac{\partial\boldsymbol{a}^H(\phi_{i,j})}{\partial\phi_{i,j}}\boldsymbol{a}(\phi_{i,j})\right\} & -\alpha_{i,j}^2NP_{\mathrm{Tx}}\,\mathrm{Im}\left\{\frac{\partial\boldsymbol{a}^H(\phi_{i,j})}{\partial\phi_{i,j}}\boldsymbol{a}(\phi_{i,j})\right\}\end{bmatrix}^T\\ &= \frac{2}{\sigma_{\boldsymbol{r}}^2}\begin{bmatrix}0 & 0\\ 0 & \frac{\alpha_{i,j}^2NP_{\mathrm{Tx}}\,\mathrm{Re}\left\{\frac{\partial\boldsymbol{a}^H(\phi_{i,j})}{\partial\phi_{i,j}}\boldsymbol{a}(\phi_{i,j})\right\}^2}{\|\boldsymbol{a}(\phi_{i,j})\|^2}+\frac{\alpha_{i,j}^2NP_{\mathrm{Tx}}\,\mathrm{Im}\left\{\frac{\partial\boldsymbol{a}^H(\phi_{i,j})}{\partial\phi_{i,j}}\boldsymbol{a}(\phi_{i,j})\right\}^2}{\|\boldsymbol{a}(\phi_{i,j})\|^2}\end{bmatrix}\\ &= \frac{2}{\sigma_{\boldsymbol{r}}^2}\begin{bmatrix}0 & 0\\ 0 & \alpha_{i,j}^2NP_{\mathrm{Tx}}\|\boldsymbol{a}(\phi_{i,j})\|^2\left(\bar{\alpha}^2+\bar{\varphi}^2\right)\end{bmatrix}.\end{aligned}\tag{C.33}$$

With (3.12), we finally arrive at

$$[\boldsymbol{I}_{\boldsymbol{l}}^{\mathrm{e}}]_{l(i,j),l(i,j)} = \frac{2\alpha_{i,j}^2 N P_{\mathrm{Tx}} \|\boldsymbol{a}(\phi_{i,j})\|^2}{\sigma_{\boldsymbol{r}}^2} \begin{bmatrix} \bar{\beta}^2 & 0 \\ 0 & \bar{\gamma}^2(\phi_{i,j}) - \bar{\alpha}^2(\phi_{i,j}) - \bar{\varphi}^2(\phi_{i,j}) \end{bmatrix}. \tag{C.34}$$

C.5 Proof that $\bar{\alpha}^2(\phi_{i,j}) = 0$ for an Ideal Antenna Array

An arbitrary ideal antenna array located in the x-y-plane with the antenna element positions $\boldsymbol{p}_m = [x_m, y_m]^T$ for $m \in \{1, ..., M\}$, is described by the steering vector or antenna response

$$a_m(\phi_{i,j}) = e^{-\mathrm{j}2\pi(x_m \cos(\phi_{i,j}) + y_m \sin(\phi_{i,j}))/\lambda_{\mathrm{c}}}, \tag{C.35}$$

see e.g. [28]. Realizing that

$$\mathrm{Re}\left\{\frac{\partial a_m^*(\phi_{i,j})}{\partial \phi_{i,j}} a_m(\phi_{i,j})\right\} = \mathrm{Re}\left\{\frac{-\mathrm{j}2\pi}{\lambda_{\mathrm{c}}}(-x_m \sin(\phi_{i,j}) + y_m \cos(\phi_{i,j}))\right\} = 0 \tag{C.36}$$

for all m, thus

$$\mathrm{Re}\left\{\frac{\partial \boldsymbol{a}^H(\phi_{i,j})}{\partial \phi_{i,j}} \boldsymbol{a}(\phi_{i,j})\right\} = 0 \tag{C.37}$$

and with (3.17)

$$\bar{\alpha}^2(\phi_{i,j}) = 0. \tag{C.38}$$

C.6 Proof that $\bar{\varphi}^2(\phi_{i,j}) = 0$ for an Ideal UCA

For a UCA with radius R measured in wavelengths, the steering vector or antenna response is given by

$$a_m(\phi_{i,j}) = e^{\mathrm{j}2\pi R \cos\left(\phi_{i,j} - 2\pi \frac{m-1}{M}\right)}, \tag{C.39}$$

see e.g. [28]. The derivative of (C.39) w.r.t. $\phi_{i,j}$ is

$$\frac{\partial a_m^*(\phi_{i,j})}{\partial \phi_{i,j}} a_m(\phi_{i,j}) = -\mathrm{j}2\pi R \sin\left(\phi_{i,j} - 2\pi \frac{m-1}{M}\right). \tag{C.40}$$

Realizing that

$$\begin{aligned} \mathrm{Im}\left\{\frac{\partial \boldsymbol{a}^H(\phi_{i,j})}{\partial \phi_{i,j}} \boldsymbol{a}(\phi_{i,j})\right\} &= \mathrm{Im}\left\{\sum_{m=1}^{M} \frac{\partial a_m^*(\phi_{i,j})}{\partial \phi_{i,j}} a_m(\phi_{i,j})\right\} \\ &= -2\pi R \sum_{m=1}^{M} \sin\left(\phi_{i,j} - 2\pi \frac{m-1}{M}\right) \\ &= 0 \end{aligned} \tag{C.41}$$

and with (3.18)

$$\bar{\varphi}^2(\phi_{i,j}) = 0. \tag{C.42}$$

C.7 Proof that DoA CRB from (3.13) is Equal to *C-CRB* (2.42)

According to the assumptions from Section 3.1, we estimate only the azimuth ϕ of a single impinging signal ($P = 1$). With (2.36) and (3.5), we have $\tilde{\boldsymbol{s}}(n) = s(n,\tau)\alpha e^{\mathrm{j}\varphi}$ and the signal covariance matrix becomes

$$\boldsymbol{R}_{\tilde{\boldsymbol{s}}} = \frac{1}{N}\sum_{n\in\mathbb{N}_{\mathrm{sc}}} \tilde{\boldsymbol{s}}(n)\tilde{\boldsymbol{s}}^H(n) = \alpha^2 P_{\mathrm{Tx}}. \tag{C.43}$$

Thus (2.42) simplifies to

$$\begin{aligned}
\mathrm{CRB}(\phi) &= \frac{\sigma_{\boldsymbol{r}}^2}{2\alpha^2 P_{\mathrm{Tx}} N}\,\mathrm{Re}\{\boldsymbol{D}^H \boldsymbol{\Pi}_{\boldsymbol{A}}^{\perp}\boldsymbol{D}\}^{-1} \\
&= \frac{\sigma_{\boldsymbol{r}}^2}{2\alpha^2 P_{\mathrm{Tx}} N}\,\mathrm{Re}\left\{\frac{\partial \boldsymbol{a}^H(\phi)}{\partial\phi}\left(\mathbb{I}_M - \frac{\boldsymbol{a}(\phi)\boldsymbol{a}^H(\phi)}{\boldsymbol{a}^H(\phi)\boldsymbol{a}(\phi)}\right)\frac{\partial \boldsymbol{a}(\phi)}{\partial\phi}\right\}^{-1} \\
&= \frac{\sigma_{\boldsymbol{r}}^2}{2\alpha^2 P_{\mathrm{Tx}} N}\left(\left\|\frac{\partial \boldsymbol{a}(\phi)}{\partial\phi}\right\|^2 - \frac{\left|\frac{\partial \boldsymbol{a}^H(\phi)}{\partial\phi}\boldsymbol{a}(\phi)\right|^2}{\|\boldsymbol{a}(\phi)\|^2}\right)^{-1}.
\end{aligned} \tag{C.44}$$

Omitting the agent indices and taking the inverse of the DoA related EFIM element from (3.13) yields

$$\begin{aligned}
\mathrm{CRB}(\phi) &= \frac{\sigma_{\boldsymbol{r}}^2}{2\alpha^2 P_{\mathrm{Tx}} N\|\boldsymbol{a}(\phi)\|^2}\left(\bar{\gamma}^2(\phi) - \bar{\alpha}^2(\phi) - \bar{\varphi}^2(\phi)\right)^{-1} \\
&= \frac{\sigma_{\boldsymbol{r}}^2}{2\alpha^2 P_{\mathrm{Tx}} N\|\boldsymbol{a}(\phi)\|^2}\left(\frac{\left\|\frac{\partial \boldsymbol{a}(\phi)}{\partial\phi}\right\|^2}{\|\boldsymbol{a}(\phi)\|^2} - \frac{\mathrm{Re}\left\{\frac{\partial \boldsymbol{a}^H(\phi)}{\partial\phi}\boldsymbol{a}(\phi)\right\}^2}{\|\boldsymbol{a}(\phi)\|^4} - \frac{\mathrm{Im}\left\{\frac{\partial \boldsymbol{a}^H(\phi)}{\partial\phi}\boldsymbol{a}(\phi)\right\}^2}{\|\boldsymbol{a}(\phi)\|^4}\right)^{-1} \\
&= \frac{\sigma_{\boldsymbol{r}}^2}{2\alpha^2 P_{\mathrm{Tx}} N}\left(\left\|\frac{\partial \boldsymbol{a}(\phi)}{\partial\phi}\right\|^2 - \frac{\left|\frac{\partial \boldsymbol{a}^H(\phi)}{\partial\phi}\boldsymbol{a}(\phi)\right|^2}{\|\boldsymbol{a}(\phi)\|^2}\right)^{-1},
\end{aligned} \tag{C.45}$$

which is equivalent to (C.44).

C.8 Proof that DoA Estimation is Invariant to Absolute Amplitude and Phase of the Antenna Response

The coherent DoA estimator C-ML (2.39) evaluates the projector onto the signal subspace (2.41), which requires any subset of P antenna response vectors $\boldsymbol{a}(\theta_p, \phi_p)$ to be linearly independent. This is equivalent to $\text{rank}\{\boldsymbol{A}(\boldsymbol{\theta}, \boldsymbol{\phi})\} = P$. Assume that instead of the antenna response matrix $\boldsymbol{A}(\boldsymbol{\theta}, \boldsymbol{\phi})$, we have an antenna response matrix

$$\tilde{\boldsymbol{A}}(\boldsymbol{\theta}, \boldsymbol{\phi}) = \left[\boldsymbol{a}(\theta_1, \phi_1)\alpha(\theta_1, \phi_1)e^{\mathrm{j}\varphi(\theta_1,\phi_1)} \quad ... \quad \boldsymbol{a}(\theta_P, \phi_P)\alpha(\theta_P, \phi_P)e^{\mathrm{j}\varphi(\theta_P,\phi_P)},\right] \tag{C.46}$$

which is corrupted by arbitrary direction-dependent absolute amplitudes $\alpha(\theta_p, \phi_p)$ and absolute phases $e^{\mathrm{j}\varphi(\theta_p,\phi_p)}$. Rewriting in matrix form yields

$$\tilde{\boldsymbol{A}}(\boldsymbol{\theta}, \boldsymbol{\phi}) = \boldsymbol{A}(\boldsymbol{\theta}, \boldsymbol{\phi})\boldsymbol{C}(\boldsymbol{\theta}, \boldsymbol{\phi}) \tag{C.47}$$

with

$$\boldsymbol{C}(\boldsymbol{\theta}, \boldsymbol{\phi}) = \text{diag}\left\{\left[\alpha(\theta_1, \phi_1)e^{\mathrm{j}\varphi(\theta_1,\phi_1)} \quad ... \quad \alpha(\theta_P, \phi_P)e^{\mathrm{j}\varphi(\theta_P,\phi_P)}\right]^T\right\}. \tag{C.48}$$

The projector onto the signal subspace (2.41) assuming $\tilde{\boldsymbol{A}}(\boldsymbol{\theta}, \boldsymbol{\phi})$ is then

$$\begin{aligned}
\boldsymbol{\Pi}_{\tilde{\boldsymbol{A}}} &= \tilde{\boldsymbol{A}}(\boldsymbol{\theta}, \boldsymbol{\phi})\left(\tilde{\boldsymbol{A}}^H(\boldsymbol{\theta}, \boldsymbol{\phi})\tilde{\boldsymbol{A}}(\boldsymbol{\theta}, \boldsymbol{\phi})\right)^{-1}\tilde{\boldsymbol{A}}^H(\boldsymbol{\theta}, \boldsymbol{\phi}) \\
&= \boldsymbol{A}(\boldsymbol{\theta}, \boldsymbol{\phi})\boldsymbol{C}(\boldsymbol{\theta}, \boldsymbol{\phi})\left(\boldsymbol{C}^H(\boldsymbol{\theta}, \boldsymbol{\phi})\boldsymbol{A}^H(\boldsymbol{\theta}, \boldsymbol{\phi})\boldsymbol{A}(\boldsymbol{\theta}, \boldsymbol{\phi})\boldsymbol{C}(\boldsymbol{\theta}, \boldsymbol{\phi})\right)^{-1}\boldsymbol{C}^H(\boldsymbol{\theta}, \boldsymbol{\phi})\boldsymbol{A}^H(\boldsymbol{\theta}, \boldsymbol{\phi}) \\
&= \boldsymbol{A}(\boldsymbol{\theta}, \boldsymbol{\phi})\boldsymbol{C}(\boldsymbol{\theta}, \boldsymbol{\phi})\boldsymbol{C}^{-1}(\boldsymbol{\theta}, \boldsymbol{\phi})\left(\boldsymbol{A}^H(\boldsymbol{\theta}, \boldsymbol{\phi})\boldsymbol{A}(\boldsymbol{\theta}, \boldsymbol{\phi})\right)^{-1} \\
&\qquad \left(\boldsymbol{C}^H(\boldsymbol{\theta}, \boldsymbol{\phi})\right)^{-1}\boldsymbol{C}^H(\boldsymbol{\theta}, \boldsymbol{\phi})\,\boldsymbol{A}^H(\boldsymbol{\theta}, \boldsymbol{\phi}) \\
&= \boldsymbol{A}(\boldsymbol{\theta}, \boldsymbol{\phi})\left(\boldsymbol{A}^H(\boldsymbol{\theta}, \boldsymbol{\phi})\boldsymbol{A}(\boldsymbol{\theta}, \boldsymbol{\phi})\right)^{-1}\boldsymbol{A}^H(\boldsymbol{\theta}, \boldsymbol{\phi}),
\end{aligned} \tag{C.49}$$

which is identical to (2.41). The coherent DoA estimator C-ML (2.39) is thus invariant to absolute amplitude and phase variations of the antenna response.

C.9 Gradient of In-Situ Calibration MAP Estimator Cost Function

The parts of the gradient $\nabla q(\boldsymbol{x}^{0:S})$ (4.20) are given by the partial derivatives (C.50) to (C.52).

$$\frac{\partial q(\boldsymbol{x}^{0:S})}{\partial \boldsymbol{g}_{\mathrm{R}}} = \frac{-1}{\sigma_{\boldsymbol{r}}^2}\sum_{s=1}^{S}\frac{\partial \tilde{L}_{\boldsymbol{r}^s}(\boldsymbol{\phi}^s, \boldsymbol{g})}{\partial \boldsymbol{g}_{\mathrm{R}}} + \frac{\boldsymbol{g}_{\mathrm{R}} - \boldsymbol{g}_{\mathrm{R}}^0}{\sigma_{\boldsymbol{g}^0}^2} \tag{C.50}$$

$$\frac{\partial q(\boldsymbol{x}^{0:S})}{\partial \boldsymbol{g}_{\mathrm{I}}} = \frac{-1}{\sigma_{\boldsymbol{r}}^2} \sum_{s=1}^{S} \frac{\partial \tilde{L}_{\boldsymbol{r}^s}(\boldsymbol{\phi}^s, \boldsymbol{g})}{\partial \boldsymbol{g}_{\mathrm{I}}} + \frac{\boldsymbol{g}_{\mathrm{I}} - \boldsymbol{g}_{\mathrm{I}}^0}{\sigma_{\boldsymbol{g}^0}^2} \tag{C.51}$$

$$\frac{\partial q(\boldsymbol{x}^{0:S})}{\partial \boldsymbol{\phi}^s} = -\begin{bmatrix} \frac{\partial \tilde{L}_{\boldsymbol{r}^s}(\boldsymbol{\phi}^s, \boldsymbol{g})}{\partial \phi_1^s} \\ \vdots \\ \frac{\partial \tilde{L}_{\boldsymbol{r}^s}(\boldsymbol{\phi}^s, \boldsymbol{g})}{\partial \phi_P^s} \end{bmatrix} + \begin{bmatrix} \frac{1}{\sigma_{\phi_{\mathrm{obs}}}^2}(\phi_1^s - \phi_{\mathrm{obs}}^s) \\ \boldsymbol{0} \end{bmatrix} \tag{C.52}$$

With the partial derivative of (4.12) w.r.t. the complex matrix $\boldsymbol{V}$,

$$\frac{\partial \tilde{L}_{\boldsymbol{r}^s}(\boldsymbol{\phi}^s, \boldsymbol{g})}{\partial \boldsymbol{V}} = -2\left(\boldsymbol{V}^{\perp}\boldsymbol{r} - \boldsymbol{r}\right)\left(\boldsymbol{r}^H \boldsymbol{V}(\boldsymbol{V}^H\boldsymbol{V})^{-1}\right), \tag{C.53}$$

from which we extract the p-th column $\partial \boldsymbol{V}_p = \left[\frac{\partial \tilde{L}_{\boldsymbol{r}^s}(\boldsymbol{\phi}^s, \boldsymbol{g})}{\partial \boldsymbol{V}}\right]_{:,p}$, we apply the chain rule to obtain (C.54) to (C.56).

$$\frac{\partial \tilde{L}_{\boldsymbol{r}^s}(\boldsymbol{\phi}^s, \boldsymbol{g})}{\partial \boldsymbol{g}_{\mathrm{R}}} = \sum_{p=1}^{P} \mathrm{Re}\left\{\left(\boldsymbol{b}^*(\phi_p)\boldsymbol{s}^H(\tau_p) \otimes \mathbb{I}_M\right)\partial \boldsymbol{V}_p\right\} \tag{C.54}$$

$$\frac{\partial \tilde{L}_{\boldsymbol{r}^s}(\boldsymbol{\phi}^s, \boldsymbol{g})}{\partial \boldsymbol{g}_{\mathrm{I}}} = \sum_{p=1}^{P} \mathrm{Im}\left\{\left(\boldsymbol{b}^*(\phi_p)\boldsymbol{s}^H(\tau_p) \otimes \mathbb{I}_M\right)\partial \boldsymbol{V}_p\right\} \tag{C.55}$$

$$\frac{\partial \tilde{L}_{\boldsymbol{r}^s}(\boldsymbol{\phi}^s, \boldsymbol{g})}{\partial \phi_p} = \mathrm{Re}\left\{\partial \boldsymbol{V}_p^H \,\mathrm{vec}\left\{\boldsymbol{G}\frac{\partial \boldsymbol{b}(\phi_p)}{\partial \phi_p}\boldsymbol{s}^T(\tau_p)\right\}\right\} \tag{C.56}$$

C.10 Derivation of In-Situ Calibration FIM Elements

For the derivation of the elements of the FIMs (4.28) to (4.32), we write the expectation of (4.9) in different forms using matrix and vector notations,

$$\begin{aligned}
\mathrm{E}_{\boldsymbol{r}^s(n)|\tilde{\boldsymbol{x}}^s}\left\{\boldsymbol{r}^s(n)\right\} &= \sum_{p=1}^{P} \boldsymbol{a}(\phi_p^s) s(n, \tau_p^s) \alpha_p^s e^{\mathrm{j}\varphi_p^s} \\
&= \boldsymbol{A}(\boldsymbol{\phi}^s)\boldsymbol{C}(\boldsymbol{\alpha}^s, \boldsymbol{\varphi}^s)\boldsymbol{s}(n, \boldsymbol{\tau}^s) \\
&= \left((\boldsymbol{B}(\boldsymbol{\phi}^s)\boldsymbol{C}(\boldsymbol{\alpha}^s, \boldsymbol{\varphi}^s)\boldsymbol{s}(n, \boldsymbol{\tau}^s))^T \otimes \mathbb{I}_M\right)(\boldsymbol{g}_{\mathrm{R}} + \mathrm{j}\boldsymbol{g}_{\mathrm{I}}) \\
&= \left((\boldsymbol{C}(\boldsymbol{\alpha}^s, \boldsymbol{\varphi}^s)\boldsymbol{s}(n, \boldsymbol{\tau}^s))^T \otimes \boldsymbol{G}\right)\mathrm{vec}\left\{\boldsymbol{B}(\boldsymbol{\phi}^s)\right\} \\
&= \left(\boldsymbol{s}^T(n, \boldsymbol{\tau}^s) \otimes \boldsymbol{A}(\boldsymbol{\phi}^s)\right)\mathrm{vec}\left\{\boldsymbol{C}(\boldsymbol{\alpha}^s, \boldsymbol{\varphi}^s)\right\},
\end{aligned} \tag{C.57}$$

with

$$\boldsymbol{A}(\boldsymbol{\phi}^s) = \boldsymbol{G}\boldsymbol{B}(\boldsymbol{\phi}^s) \in \mathbb{C}^{M\times P}, \tag{C.58}$$

$$\boldsymbol{B}(\boldsymbol{\phi}^s) = \begin{bmatrix} \boldsymbol{b}(\phi_1^s) & \dots & \boldsymbol{b}(\phi_P^s) \end{bmatrix} \in \mathbb{C}^{U\times P}, \tag{C.59}$$

$$\boldsymbol{C}(\boldsymbol{\alpha}^s, \boldsymbol{\varphi}^s) = \begin{bmatrix} \alpha_1^s e^{\mathrm{j}\varphi_1^s} & & \\ & \ddots & \\ & & \alpha_P^s e^{\mathrm{j}\varphi_P^s} \end{bmatrix} \in \mathbb{C}^{P\times P}, \tag{C.60}$$

$$\boldsymbol{s}(n, \boldsymbol{\tau}^s) = \begin{bmatrix} s(n, \tau_1^s) \\ \vdots \\ s(n, \tau_P^s) \end{bmatrix} \in \mathbb{C}^{P\times 1}. \tag{C.61}$$

We define the signal covariance matrix

$$\boldsymbol{R}_{\boldsymbol{s}} = \frac{1}{N} \sum_{n\in\mathbb{N}_{\mathrm{sc}}} \boldsymbol{s}(n, \tau^s)\boldsymbol{s}^H(n, \tau^s) \tag{C.62}$$

and the Jacobian matrices (C.63) to (C.65).

$$\boldsymbol{B}_{\boldsymbol{\phi}^s} := \frac{\partial \operatorname{vec}\{\boldsymbol{B}(\boldsymbol{\phi}^s)\}}{\partial \boldsymbol{\phi}^s} \in \mathbb{C}^{P\times P} \tag{C.63a}$$

$$[\boldsymbol{B}_{\boldsymbol{\phi}^s}]_{p,p} = \frac{\partial \boldsymbol{b}(\phi_p^s)}{\partial \phi_p^s},\ p \in \{1, ..., P\} \tag{C.63b}$$

$$\boldsymbol{C}_{\boldsymbol{\alpha}^s} := \frac{\partial \operatorname{vec}\{\boldsymbol{C}(\boldsymbol{\alpha}^s, \boldsymbol{\varphi}^s)\}}{\partial \boldsymbol{\alpha}^s} \in \mathbb{C}^{P^2\times P} \tag{C.64a}$$

$$[\boldsymbol{C}_{\boldsymbol{\alpha}^s}]_{P(p-1)+p,p} = e^{\mathrm{j}\varphi_p},\ p \in \{1, ..., P\} \tag{C.64b}$$

$$\boldsymbol{C}_{\boldsymbol{\varphi}^s}\mathrm{j} := \frac{\partial \operatorname{vec}\{\boldsymbol{C}(\boldsymbol{\alpha}^s, \boldsymbol{\varphi}^s)\}}{\partial \boldsymbol{\varphi}^s} \in \mathbb{C}^{P^2\times P} \tag{C.65a}$$

$$[\boldsymbol{C}_{\boldsymbol{\varphi}^s}\mathrm{j}]_{P(p-1)+p,p} = \alpha_p e^{\mathrm{j}\varphi_p},\ p \in \{1, ..., P\} \tag{C.65b}$$

Using the appropriate forms of (C.57) and the Kronecker product property

$$(\boldsymbol{A} \otimes \boldsymbol{B})^H(\boldsymbol{C} \otimes \boldsymbol{D}) = \boldsymbol{A}^H\boldsymbol{C} \otimes \boldsymbol{B}^H\boldsymbol{D}, \tag{C.66}$$

the elements of (4.28) to (4.32) are given by (C.67) to (C.81).

$$\begin{aligned}
\boldsymbol{I}^s_{\boldsymbol{g}_\mathrm{R}} &= \frac{2}{\sigma^2_{\boldsymbol{r}}} \operatorname{Re}\left\{ \sum_{n\in\mathbb{N}_\mathrm{sc}} \frac{\partial \operatorname{E}_{\boldsymbol{r}^s(n)|\tilde{\boldsymbol{x}}^s}\left\{\boldsymbol{r}^s(n)\right\}^H}{\partial \boldsymbol{g}_\mathrm{R}} \frac{\partial \operatorname{E}_{\boldsymbol{r}^s(n)|\tilde{\boldsymbol{x}}^s}\left\{\boldsymbol{r}^s(n)\right\}}{\partial \boldsymbol{g}_\mathrm{R}} \right\} \\
&= \frac{2}{\sigma^2_{\boldsymbol{r}}} \operatorname{Re}\left\{ \sum_{n\in\mathbb{N}_\mathrm{sc}} \left(\left(\boldsymbol{B}(\boldsymbol{\phi}^s)\boldsymbol{C}(\boldsymbol{\alpha}^s,\boldsymbol{\varphi}^s)\boldsymbol{s}(n,\boldsymbol{\tau}^s)\right)^T \otimes \mathbb{I}_M\right)^H \right. \\
&\qquad\qquad \left. \left(\left(\boldsymbol{B}(\boldsymbol{\phi}^s)\boldsymbol{C}(\boldsymbol{\alpha}^s,\boldsymbol{\varphi}^s)\boldsymbol{s}(n,\boldsymbol{\tau}^s)\right)^T \otimes \mathbb{I}_M\right) \right\} \\
&= \frac{2N}{\sigma^2_{\boldsymbol{r}}} \operatorname{Re}\left\{\boldsymbol{B}(\boldsymbol{\phi}^s)\boldsymbol{C}(\boldsymbol{\alpha}^s,\boldsymbol{\varphi}^s)\boldsymbol{R}_{\boldsymbol{s}}\boldsymbol{C}^H(\boldsymbol{\alpha}^s,\boldsymbol{\varphi}^s)\boldsymbol{B}^H(\boldsymbol{\phi}^s) \otimes \mathbb{I}_M\right\}
\end{aligned} \tag{C.67}$$

$$\begin{aligned}
\boldsymbol{I}^s_{\boldsymbol{g}_\mathrm{I}} &= \frac{2}{\sigma^2_{\boldsymbol{r}}} \operatorname{Re}\left\{ \sum_{n\in\mathbb{N}_\mathrm{sc}} \frac{\partial \operatorname{E}_{\boldsymbol{r}^s(n)|\tilde{\boldsymbol{x}}^s}\left\{\boldsymbol{r}^s(n)\right\}^H}{\partial \boldsymbol{g}_\mathrm{I}} \frac{\partial \operatorname{E}_{\boldsymbol{r}^s(n)|\tilde{\boldsymbol{x}}^s}\left\{\boldsymbol{r}^s(n)\right\}}{\partial \boldsymbol{g}_\mathrm{I}} \right\} \\
&= \frac{2}{\sigma^2_{\boldsymbol{r}}} \operatorname{Re}\left\{ \sum_{n\in\mathbb{N}_\mathrm{sc}} \left(\left(\boldsymbol{B}(\boldsymbol{\phi}^s)\boldsymbol{C}(\boldsymbol{\alpha}^s,\boldsymbol{\varphi}^s)\boldsymbol{s}(n,\boldsymbol{\tau}^s)\right)^T \otimes \mathbb{I}_M\right)^H \right. \\
&\qquad\qquad \left. \left(\left(\boldsymbol{B}(\boldsymbol{\phi}^s)\boldsymbol{C}(\boldsymbol{\alpha}^s,\boldsymbol{\varphi}^s)\boldsymbol{s}(n,\boldsymbol{\tau}^s)\right)^T \otimes \mathbb{I}_M\right) \right\} \\
&= \boldsymbol{I}^s_{\boldsymbol{g}_\mathrm{R}}
\end{aligned} \tag{C.68}$$

$$\begin{aligned}
\boldsymbol{I}^s_{\boldsymbol{g}_\mathrm{R}\boldsymbol{g}_\mathrm{I}} &= \frac{2}{\sigma^2_{\boldsymbol{r}}} \operatorname{Re}\left\{ \sum_{n\in\mathbb{N}_\mathrm{sc}} \frac{\partial \operatorname{E}_{\boldsymbol{r}^s(n)|\tilde{\boldsymbol{x}}^s}\left\{\boldsymbol{r}^s(n)\right\}^H}{\partial \boldsymbol{g}_\mathrm{R}} \frac{\partial \operatorname{E}_{\boldsymbol{r}^s(n)|\tilde{\boldsymbol{x}}^s}\left\{\boldsymbol{r}^s(n)\right\}}{\partial \boldsymbol{g}_\mathrm{I}} \right\} \\
&= \frac{2}{\sigma^2_{\boldsymbol{r}}} \operatorname{Re}\left\{ \sum_{n\in\mathbb{N}_\mathrm{sc}} \left(\left(\boldsymbol{B}(\boldsymbol{\phi}^s)\boldsymbol{C}(\boldsymbol{\alpha}^s,\boldsymbol{\varphi}^s)\boldsymbol{s}(n,\boldsymbol{\tau}^s)\right)^T \otimes \mathbb{I}_M\right)^H \right. \\
&\qquad\qquad \left. \left(\left(\boldsymbol{B}(\boldsymbol{\phi}^s)\boldsymbol{C}(\boldsymbol{\alpha}^s,\boldsymbol{\varphi}^s)\boldsymbol{s}(n,\boldsymbol{\tau}^s)\right)^T \otimes \mathbb{I}_M\right) \mathrm{j} \right\} \\
&= \frac{2N}{\sigma^2_{\boldsymbol{r}}} \operatorname{Im}\left\{\boldsymbol{B}(\boldsymbol{\phi}^s)\boldsymbol{C}(\boldsymbol{\alpha}^s,\boldsymbol{\varphi}^s)\boldsymbol{R}_{\boldsymbol{s}}\boldsymbol{C}^H(\boldsymbol{\alpha}^s,\boldsymbol{\varphi}^s)\boldsymbol{B}^H(\boldsymbol{\phi}^s) \otimes \mathbb{I}_M\right\}
\end{aligned} \tag{C.69}$$

$$\begin{aligned}
\boldsymbol{I}^s_{\boldsymbol{g}_\mathrm{R}\boldsymbol{\phi}} &= \frac{2}{\sigma^2_{\boldsymbol{r}}} \operatorname{Re}\left\{ \sum_{n\in\mathbb{N}_\mathrm{sc}} \frac{\partial \operatorname{E}_{\boldsymbol{r}^s(n)|\tilde{\boldsymbol{x}}^s}\left\{\boldsymbol{r}^s(n)\right\}^H}{\partial \boldsymbol{g}_\mathrm{R}} \frac{\partial \operatorname{E}_{\boldsymbol{r}^s(n)|\tilde{\boldsymbol{x}}^s}\left\{\boldsymbol{r}^s(n)\right\}}{\partial \boldsymbol{\phi}^s} \right\} \\
&= \frac{2}{\sigma^2_{\boldsymbol{r}}} \operatorname{Re}\left\{ \sum_{n\in\mathbb{N}_\mathrm{sc}} \left(\left(\boldsymbol{B}(\boldsymbol{\phi}^s)\boldsymbol{C}(\boldsymbol{\alpha}^s,\boldsymbol{\varphi}^s)\boldsymbol{s}(n,\boldsymbol{\tau}^s)\right)^T \otimes \mathbb{I}_M\right)^H \right. \\
&\qquad\qquad \left. \left(\left(\boldsymbol{C}(\boldsymbol{\alpha}^s,\boldsymbol{\varphi}^s)\boldsymbol{s}(n,\boldsymbol{\tau}^s)\right)^T \otimes \boldsymbol{G}\right) \boldsymbol{B}_{\boldsymbol{\phi}^s} \right\}
\end{aligned}$$

$$= \frac{2N}{\sigma_{\boldsymbol{r}}^2} \operatorname{Re}\left\{\left(\boldsymbol{B}^*(\boldsymbol{\phi}^s)\boldsymbol{C}^*(\boldsymbol{\alpha}^s,\boldsymbol{\varphi}^s)\boldsymbol{R}_{\boldsymbol{s}}^*\boldsymbol{C}(\boldsymbol{\alpha}^s,\boldsymbol{\varphi}^s)\otimes\boldsymbol{G}\right)\boldsymbol{B}_{\boldsymbol{\phi}^s}\right\} \tag{C.70}$$

$$\begin{aligned}
\boldsymbol{I}_{\boldsymbol{g}_{\mathrm{R}}\boldsymbol{\alpha}}^s &= \frac{2}{\sigma_{\boldsymbol{r}}^2} \operatorname{Re}\left\{\sum_{n\in\mathbb{N}_{\mathrm{sc}}} \frac{\partial \operatorname{E}_{\boldsymbol{r}^s(n)|\tilde{\boldsymbol{x}}^s}\left\{\boldsymbol{r}^s(n)\right\}^H}{\partial \boldsymbol{g}_{\mathrm{R}}} \frac{\partial \operatorname{E}_{\boldsymbol{r}^s(n)|\tilde{\boldsymbol{x}}^s}\left\{\boldsymbol{r}^s(n)\right\}}{\partial \boldsymbol{\alpha}^s}\right\} \\
&= \frac{2}{\sigma_{\boldsymbol{r}}^2} \operatorname{Re}\left\{\sum_{n\in\mathbb{N}_{\mathrm{sc}}} \left(\left(\boldsymbol{B}(\boldsymbol{\phi}^s)\boldsymbol{C}(\boldsymbol{\alpha}^s,\boldsymbol{\varphi}^s)\boldsymbol{s}(n,\boldsymbol{\tau}^s)\right)^T\otimes\mathbb{I}_M\right)^H \left(\boldsymbol{s}^T(n,\boldsymbol{\tau}^s)\otimes\boldsymbol{A}(\boldsymbol{\phi}^s)\right)\boldsymbol{C}_{\boldsymbol{\alpha}^s}\right\} \\
&= \frac{2N}{\sigma_{\boldsymbol{r}}^2} \operatorname{Re}\left\{\left(\boldsymbol{B}^*(\boldsymbol{\phi}^s)\boldsymbol{C}^*(\boldsymbol{\alpha}^s,\boldsymbol{\varphi}^s)\boldsymbol{R}_{\boldsymbol{s}}^*\otimes\boldsymbol{A}(\boldsymbol{\phi}^s)\right)\boldsymbol{C}_{\boldsymbol{\alpha}^s}\right\}
\end{aligned} \tag{C.71}$$

$$\begin{aligned}
\boldsymbol{I}_{\boldsymbol{g}_{\mathrm{R}}\boldsymbol{\varphi}}^s &= \frac{2}{\sigma_{\boldsymbol{r}}^2} \operatorname{Re}\left\{\sum_{n\in\mathbb{N}_{\mathrm{sc}}} \frac{\partial \operatorname{E}_{\boldsymbol{r}^s(n)|\tilde{\boldsymbol{x}}^s}\left\{\boldsymbol{r}^s(n)\right\}^H}{\partial \boldsymbol{g}_{\mathrm{R}}} \frac{\partial \operatorname{E}_{\boldsymbol{r}^s(n)|\tilde{\boldsymbol{x}}^s}\left\{\boldsymbol{r}^s(n)\right\}}{\partial \boldsymbol{\varphi}^s}\right\} \\
&= \frac{2}{\sigma_{\boldsymbol{r}}^2} \operatorname{Re}\left\{\sum_{n\in\mathbb{N}_{\mathrm{sc}}} \left(\left(\boldsymbol{B}(\boldsymbol{\phi}^s)\boldsymbol{C}(\boldsymbol{\alpha}^s,\boldsymbol{\varphi}^s)\boldsymbol{s}(n,\boldsymbol{\tau}^s)\right)^T\otimes\mathbb{I}_M\right)^H \left(\boldsymbol{s}^T(n,\boldsymbol{\tau}^s)\otimes\boldsymbol{A}(\boldsymbol{\phi}^s)\right)\boldsymbol{C}_{\boldsymbol{\varphi}^s}\mathrm{j}\right\} \\
&= \frac{-2N}{\sigma_{\boldsymbol{r}}^2} \operatorname{Im}\left\{\left(\boldsymbol{B}^*(\boldsymbol{\phi}^s)\boldsymbol{C}^*(\boldsymbol{\alpha}^s,\boldsymbol{\varphi}^s)\boldsymbol{R}_{\boldsymbol{s}}^*\otimes\boldsymbol{A}(\boldsymbol{\phi}^s)\right)\boldsymbol{C}_{\boldsymbol{\varphi}^s}\right\}
\end{aligned} \tag{C.72}$$

$$\begin{aligned}
\boldsymbol{I}_{\boldsymbol{g}_{\mathrm{I}}\boldsymbol{\phi}}^s &= \frac{2}{\sigma_{\boldsymbol{r}}^2} \operatorname{Re}\left\{\sum_{n\in\mathbb{N}_{\mathrm{sc}}} \frac{\partial \operatorname{E}_{\boldsymbol{r}^s(n)|\tilde{\boldsymbol{x}}^s}\left\{\boldsymbol{r}^s(n)\right\}^H}{\partial \boldsymbol{g}_{\mathrm{I}}} \frac{\partial \operatorname{E}_{\boldsymbol{r}^s(n)|\tilde{\boldsymbol{x}}^s}\left\{\boldsymbol{r}^s(n)\right\}}{\partial \boldsymbol{\phi}^s}\right\} \\
&= \frac{2}{\sigma_{\boldsymbol{r}}^2} \operatorname{Re}\left\{\sum_{n\in\mathbb{N}_{\mathrm{sc}}} \left(\left(\left(\boldsymbol{B}(\boldsymbol{\phi}^s)\boldsymbol{C}(\boldsymbol{\alpha}^s,\boldsymbol{\varphi}^s)\boldsymbol{s}(n,\boldsymbol{\tau}^s)\right)^T\otimes\mathbb{I}_M\right)\mathrm{j}\right)^H \right. \\
&\qquad\qquad \left. \left(\left(\boldsymbol{C}(\boldsymbol{\alpha}^s,\boldsymbol{\varphi}^s)\boldsymbol{s}(n,\boldsymbol{\tau}^s)\right)^T\otimes\boldsymbol{G}\right)\boldsymbol{B}_{\boldsymbol{\phi}^s}\right\} \\
&= \frac{2N}{\sigma_{\boldsymbol{r}}^2} \operatorname{Im}\left\{\left(\boldsymbol{B}^*(\boldsymbol{\phi}^s)\boldsymbol{C}^*(\boldsymbol{\alpha}^s,\boldsymbol{\varphi}^s)\boldsymbol{R}_{\boldsymbol{s}}^*\boldsymbol{C}^T(\boldsymbol{\alpha}^s,\boldsymbol{\varphi}^s)\otimes\boldsymbol{G}\right)\boldsymbol{B}_{\boldsymbol{\phi}^s}\right\}
\end{aligned} \tag{C.73}$$

$$\begin{aligned}
\boldsymbol{I}_{\boldsymbol{g}_{\mathrm{I}}\boldsymbol{\alpha}}^s &= \frac{2}{\sigma_{\boldsymbol{r}}^2} \operatorname{Re}\left\{\sum_{n\in\mathbb{N}_{\mathrm{sc}}} \frac{\partial \operatorname{E}_{\boldsymbol{r}^s(n)|\tilde{\boldsymbol{x}}^s}\left\{\boldsymbol{r}^s(n)\right\}^H}{\partial \boldsymbol{g}_{\mathrm{I}}} \frac{\partial \operatorname{E}_{\boldsymbol{r}^s(n)|\tilde{\boldsymbol{x}}^s}\left\{\boldsymbol{r}^s(n)\right\}}{\partial \boldsymbol{\alpha}^s}\right\} \\
&= \frac{2}{\sigma_{\boldsymbol{r}}^2} \operatorname{Re}\left\{\sum_{n\in\mathbb{N}_{\mathrm{sc}}} \left(\left(\left(\boldsymbol{B}(\boldsymbol{\phi}^s)\boldsymbol{C}(\boldsymbol{\alpha}^s,\boldsymbol{\varphi}^s)\boldsymbol{s}(n,\boldsymbol{\tau}^s)\right)^T\otimes\mathbb{I}_M\right)\mathrm{j}\right)^H \right. \\
&\qquad\qquad \left. \left(\boldsymbol{s}^T(n,\boldsymbol{\tau}^s)\otimes\boldsymbol{A}(\boldsymbol{\phi}^s)\right)\boldsymbol{C}_{\boldsymbol{\alpha}^s}\right\} \\
&= \frac{2N}{\sigma_{\boldsymbol{r}}^2} \operatorname{Im}\left\{\left(\boldsymbol{B}^*(\boldsymbol{\phi}^s)\boldsymbol{C}^*(\boldsymbol{\alpha}^s,\boldsymbol{\varphi}^s)\boldsymbol{R}_{\boldsymbol{s}}^*\otimes\boldsymbol{A}(\boldsymbol{\phi}^s)\right)\boldsymbol{C}_{\boldsymbol{\alpha}^s}\right\}
\end{aligned} \tag{C.74}$$

$$
\begin{aligned}
\boldsymbol{I}^s_{\boldsymbol{g}_\mathrm{I}\boldsymbol{\varphi}} &= \frac{2}{\sigma^2_{\boldsymbol{r}}} \operatorname{Re}\left\{ \sum_{n\in\mathbb{N}_\mathrm{sc}} \frac{\partial \operatorname{E}_{\boldsymbol{r}^s(n)|\tilde{\boldsymbol{x}}^s}\left\{\boldsymbol{r}^s(n)\right\}^H}{\partial \boldsymbol{g}_\mathrm{I}} \frac{\partial \operatorname{E}_{\boldsymbol{r}^s(n)|\tilde{\boldsymbol{x}}^s}\left\{\boldsymbol{r}^s(n)\right\}}{\partial \boldsymbol{\varphi}^s} \right\} \\
&= \frac{2}{\sigma^2_{\boldsymbol{r}}} \operatorname{Re}\left\{ \sum_{n\in\mathbb{N}_\mathrm{sc}} \left(\left(\left(\boldsymbol{B}(\boldsymbol{\phi}^s)\boldsymbol{C}(\boldsymbol{\alpha}^s,\boldsymbol{\varphi}^s)\boldsymbol{s}(n,\boldsymbol{\tau}^s)\right)^T \otimes \mathbb{I}_M\right)\mathrm{j}\right)^H \right. \\
&\qquad\qquad \left. \left(\boldsymbol{s}^T(n,\boldsymbol{\tau}^s)\otimes \boldsymbol{A}(\boldsymbol{\phi}^s)\right)\boldsymbol{C}_{\boldsymbol{\varphi}^s}\mathrm{j} \right\} \\
&= \frac{2N}{\sigma^2_{\boldsymbol{r}}} \operatorname{Re}\left\{\left(\boldsymbol{B}^*(\boldsymbol{\phi}^s)\boldsymbol{C}^*(\boldsymbol{\alpha}^s,\boldsymbol{\varphi}^s)\boldsymbol{R}^*_{\boldsymbol{s}} \otimes \boldsymbol{A}(\boldsymbol{\phi}^s)\right)\boldsymbol{C}_{\boldsymbol{\varphi}^s}\right\}
\end{aligned}
\tag{C.75}
$$

$$
\begin{aligned}
\boldsymbol{I}^s_{\boldsymbol{\phi}} &= \frac{2}{\sigma^2_{\boldsymbol{r}}} \operatorname{Re}\left\{ \sum_{n\in\mathbb{N}_\mathrm{sc}} \frac{\partial \operatorname{E}_{\boldsymbol{r}^s(n)|\tilde{\boldsymbol{x}}^s}\left\{\boldsymbol{r}^s(n)\right\}^H}{\partial \boldsymbol{\phi}^s} \frac{\partial \operatorname{E}_{\boldsymbol{r}^s(n)|\tilde{\boldsymbol{x}}^s}\left\{\boldsymbol{r}^s(n)\right\}}{\partial \boldsymbol{\phi}^s} \right\} \\
&\quad + \frac{1}{\sigma^2_{\phi_\mathrm{obs}}} \operatorname{Re}\left\{ \frac{\partial \operatorname{E}_{\phi^s_\mathrm{obs}|\tilde{\boldsymbol{x}}^s}\left\{\phi^s_\mathrm{obs}\right\}^H}{\partial [\tilde{\boldsymbol{x}}^s]_i} \frac{\partial \operatorname{E}_{\phi^s_\mathrm{obs}|\tilde{\boldsymbol{x}}^s}\left\{\phi^s_\mathrm{obs}\right\}}{\partial [\tilde{\boldsymbol{x}}^s]_j} \right\} \\
&= \frac{2}{\sigma^2_{\boldsymbol{r}}} \operatorname{Re}\left\{ \sum_{n\in\mathbb{N}_\mathrm{sc}} \left(\left(\left(\boldsymbol{C}(\boldsymbol{\alpha}^s,\boldsymbol{\varphi}^s)\boldsymbol{s}(n,\boldsymbol{\tau}^s)\right)^T \otimes \boldsymbol{G}\right)\boldsymbol{B}_{\boldsymbol{\phi}^s}\right)^H \right. \\
&\qquad\qquad \left. \left(\left(\boldsymbol{C}(\boldsymbol{\alpha}^s,\boldsymbol{\varphi}^s)\boldsymbol{s}(n,\boldsymbol{\tau}^s)\right)^T \otimes \boldsymbol{G}\right)\boldsymbol{B}_{\boldsymbol{\phi}^s} \right\} + \begin{bmatrix} 1/\sigma^2_{\phi_\mathrm{obs}} & \boldsymbol{0}^T_{P-1} \\ \boldsymbol{0}_{P-1} & \mathbb{0}_{P-1} \end{bmatrix} \\
&= \frac{2N}{\sigma^2_{\boldsymbol{r}}} \operatorname{Re}\left\{\boldsymbol{B}^H_{\boldsymbol{\phi}^s}\left(\boldsymbol{C}^*(\boldsymbol{\alpha}^s,\boldsymbol{\varphi}^s)\boldsymbol{R}^*_{\boldsymbol{s}}\boldsymbol{C}(\boldsymbol{\alpha}^s,\boldsymbol{\varphi}^s)\otimes \boldsymbol{G}^H\boldsymbol{G}\right)\boldsymbol{B}_{\boldsymbol{\phi}^s}\right\} + \begin{bmatrix} 1/\sigma^2_{\phi_\mathrm{obs}} & \boldsymbol{0}^T_{P-1} \\ \boldsymbol{0}_{P-1} & \mathbb{0}_{P-1} \end{bmatrix}
\end{aligned}
\tag{C.76}
$$

$$
\begin{aligned}
\boldsymbol{I}^s_{\boldsymbol{\phi}\boldsymbol{\alpha}} &= \frac{2}{\sigma^2_{\boldsymbol{r}}} \operatorname{Re}\left\{ \sum_{n\in\mathbb{N}_\mathrm{sc}} \frac{\partial \operatorname{E}_{\boldsymbol{r}^s(n)|\tilde{\boldsymbol{x}}^s}\left\{\boldsymbol{r}^s(n)\right\}^H}{\partial \boldsymbol{\phi}^s} \frac{\partial \operatorname{E}_{\boldsymbol{r}^s(n)|\tilde{\boldsymbol{x}}^s}\left\{\boldsymbol{r}^s(n)\right\}}{\partial \boldsymbol{\alpha}^s} \right\} \\
&= \frac{2}{\sigma^2_{\boldsymbol{r}}} \operatorname{Re}\left\{ \sum_{n\in\mathbb{N}_\mathrm{sc}} \left(\left(\left(\boldsymbol{C}(\boldsymbol{\alpha}^s,\boldsymbol{\varphi}^s)\boldsymbol{s}(n,\boldsymbol{\tau}^s)\right)^T \otimes \boldsymbol{G}\right)\boldsymbol{B}_{\boldsymbol{\phi}^s}\right)^H \left(\boldsymbol{s}^T(n,\boldsymbol{\tau}^s)\otimes \boldsymbol{A}(\boldsymbol{\phi}^s)\right)\boldsymbol{C}_{\boldsymbol{\alpha}^s} \right\} \\
&= \frac{2N}{\sigma^2_{\boldsymbol{r}}} \operatorname{Re}\left\{\boldsymbol{B}^H_{\boldsymbol{\phi}^s}\left(\boldsymbol{C}^*(\boldsymbol{\alpha}^s,\boldsymbol{\varphi}^s)\boldsymbol{R}^*_{\boldsymbol{s}}\otimes \boldsymbol{G}^H\boldsymbol{A}(\boldsymbol{\phi}^s)\right)\boldsymbol{C}_{\boldsymbol{\alpha}^s}\right\}
\end{aligned}
\tag{C.77}
$$

$$
\begin{aligned}
\boldsymbol{I}^s_{\boldsymbol{\phi}\boldsymbol{\varphi}} &= \frac{2}{\sigma^2_{\boldsymbol{r}}} \operatorname{Re}\left\{ \sum_{n\in\mathbb{N}_\mathrm{sc}} \frac{\partial \operatorname{E}_{\boldsymbol{r}^s(n)|\tilde{\boldsymbol{x}}^s}\left\{\boldsymbol{r}^s(n)\right\}^H}{\partial \boldsymbol{\phi}^s} \frac{\partial \operatorname{E}_{\boldsymbol{r}^s(n)|\tilde{\boldsymbol{x}}^s}\left\{\boldsymbol{r}^s(n)\right\}}{\partial \boldsymbol{\varphi}^s} \right\} \\
&= \frac{2}{\sigma^2_{\boldsymbol{r}}} \operatorname{Re}\left\{ \sum_{n\in\mathbb{N}_\mathrm{sc}} \left(\left(\left(\boldsymbol{C}(\boldsymbol{\alpha}^s,\boldsymbol{\varphi}^s)\boldsymbol{s}(n,\boldsymbol{\tau}^s)\right)^T \otimes \boldsymbol{G}\right)\boldsymbol{B}_{\boldsymbol{\phi}^s}\right)^H \left(\boldsymbol{s}^T(n,\boldsymbol{\tau}^s)\otimes \boldsymbol{A}(\boldsymbol{\phi}^s)\right)\boldsymbol{C}_{\boldsymbol{\varphi}^s}\mathrm{j} \right\} \\
&= \frac{-2N}{\sigma^2_{\boldsymbol{r}}} \operatorname{Im}\left\{\boldsymbol{B}^H_{\boldsymbol{\phi}^s}\left(\boldsymbol{C}^*(\boldsymbol{\alpha}^s,\boldsymbol{\varphi}^s)\boldsymbol{R}^*_{\boldsymbol{s}}\otimes \boldsymbol{G}^H\boldsymbol{A}(\boldsymbol{\phi}^s)\right)\boldsymbol{C}_{\boldsymbol{\varphi}^s}\right\}
\end{aligned}
\tag{C.78}
$$

$$
\begin{aligned}
\boldsymbol{I}_{\boldsymbol{\alpha}}^{s} &= \frac{2}{\sigma_{\boldsymbol{r}}^{2}} \operatorname{Re}\left\{ \sum_{n \in \mathbb{N}_{\mathrm{sc}}} \frac{\partial \operatorname{E}_{\boldsymbol{r}^{s}(n)|\tilde{\boldsymbol{x}}^{s}} \left\{ \boldsymbol{r}^{s}(n) \right\}^{H}}{\partial \boldsymbol{\alpha}^{s}} \frac{\partial \operatorname{E}_{\boldsymbol{r}^{s}(n)|\tilde{\boldsymbol{x}}^{s}} \left\{ \boldsymbol{r}^{s}(n) \right\}}{\partial \boldsymbol{\alpha}^{s}} \right\} \\
&= \frac{2}{\sigma_{\boldsymbol{r}}^{2}} \operatorname{Re}\left\{ \sum_{n \in \mathbb{N}_{\mathrm{sc}}} \left(\left(\boldsymbol{s}^{T}(n, \boldsymbol{\tau}^{s}) \otimes \boldsymbol{A}(\boldsymbol{\phi}^{s}) \right) \boldsymbol{C}_{\boldsymbol{\alpha}^{s}} \right)^{H} \left(\boldsymbol{s}^{T}(n, \boldsymbol{\tau}^{s}) \otimes \boldsymbol{A}(\boldsymbol{\phi}^{s}) \right) \boldsymbol{C}_{\boldsymbol{\alpha}^{s}} \right\} \\
&= \frac{2N}{\sigma_{\boldsymbol{r}}^{2}} \operatorname{Re}\left\{ \boldsymbol{C}_{\boldsymbol{\alpha}^{s}}^{H} \left(\boldsymbol{R}_{\boldsymbol{s}}^{*} \otimes \boldsymbol{A}^{H}(\boldsymbol{\phi}^{s}) \boldsymbol{A}(\boldsymbol{\phi}^{s}) \right) \boldsymbol{C}_{\boldsymbol{\alpha}^{s}} \right\}
\end{aligned} \tag{C.79}
$$

$$
\begin{aligned}
\boldsymbol{I}_{\boldsymbol{\alpha\varphi}}^{s} &= \frac{2}{\sigma_{\boldsymbol{r}}^{2}} \operatorname{Re}\left\{ \sum_{n \in \mathbb{N}_{\mathrm{sc}}} \frac{\partial \operatorname{E}_{\boldsymbol{r}^{s}(n)|\tilde{\boldsymbol{x}}^{s}} \left\{ \boldsymbol{r}^{s}(n) \right\}^{H}}{\partial \boldsymbol{\alpha}^{s}} \frac{\partial \operatorname{E}_{\boldsymbol{r}^{s}(n)|\tilde{\boldsymbol{x}}^{s}} \left\{ \boldsymbol{r}^{s}(n) \right\}}{\partial \boldsymbol{\varphi}^{s}} \right\} \\
&= \frac{2}{\sigma_{\boldsymbol{r}}^{2}} \operatorname{Re}\left\{ \sum_{n \in \mathbb{N}_{\mathrm{sc}}} \left(\left(\boldsymbol{s}^{T}(n, \boldsymbol{\tau}^{s}) \otimes \boldsymbol{A}(\boldsymbol{\phi}^{s}) \right) \boldsymbol{C}_{\boldsymbol{\alpha}^{s}} \right)^{H} \left(\boldsymbol{s}^{T}(n, \boldsymbol{\tau}^{s}) \otimes \boldsymbol{A}(\boldsymbol{\phi}^{s}) \right) \boldsymbol{C}_{\boldsymbol{\varphi}^{s}} \mathrm{j} \right\} \\
&= \frac{-2N}{\sigma_{\boldsymbol{r}}^{2}} \operatorname{Im}\left\{ \boldsymbol{C}_{\boldsymbol{\alpha}^{s}}^{H} \left(\boldsymbol{R}_{\boldsymbol{s}}^{*} \otimes \boldsymbol{A}^{H}(\boldsymbol{\phi}^{s}) \boldsymbol{A}(\boldsymbol{\phi}^{s}) \right) \boldsymbol{C}_{\boldsymbol{\varphi}^{s}} \right\}
\end{aligned} \tag{C.80}
$$

$$
\begin{aligned}
\boldsymbol{I}_{\boldsymbol{\varphi}}^{s} &= \frac{2}{\sigma_{\boldsymbol{r}}^{2}} \operatorname{Re}\left\{ \sum_{n \in \mathbb{N}_{\mathrm{sc}}} \frac{\partial \operatorname{E}_{\boldsymbol{r}^{s}(n)|\tilde{\boldsymbol{x}}^{s}} \left\{ \boldsymbol{r}^{s}(n) \right\}^{H}}{\partial \boldsymbol{\varphi}^{s}} \frac{\partial \operatorname{E}_{\boldsymbol{r}^{s}(n)|\tilde{\boldsymbol{x}}^{s}} \left\{ \boldsymbol{r}^{s}(n) \right\}}{\partial \boldsymbol{\varphi}^{s}} \right\} \\
&= \frac{2}{\sigma_{\boldsymbol{r}}^{2}} \operatorname{Re}\left\{ \sum_{n \in \mathbb{N}_{\mathrm{sc}}} \left(\left(\boldsymbol{s}^{T}(n, \boldsymbol{\tau}^{s}) \otimes \boldsymbol{A}(\boldsymbol{\phi}^{s}) \right) \boldsymbol{C}_{\boldsymbol{\varphi}^{s}} \mathrm{j} \right)^{H} \left(\boldsymbol{s}^{T}(n, \boldsymbol{\tau}^{s}) \otimes \boldsymbol{A}(\boldsymbol{\phi}^{s}) \right) \boldsymbol{C}_{\boldsymbol{\varphi}^{s}} \mathrm{j} \right\} \\
&= \frac{2N}{\sigma_{\boldsymbol{r}}^{2}} \operatorname{Re}\left\{ \boldsymbol{C}_{\boldsymbol{\varphi}^{s}}^{H} \left(\boldsymbol{R}_{\boldsymbol{s}}^{*} \otimes \boldsymbol{A}^{H}(\boldsymbol{\phi}^{s}) \boldsymbol{A}(\boldsymbol{\phi}^{s}) \right) \boldsymbol{C}_{\boldsymbol{\varphi}^{s}} \right\}
\end{aligned} \tag{C.81}
$$

C.11 Jacobian Matrix of the Motion Model

The Jacobian matrix of the motion model $\boldsymbol{f}\left(\boldsymbol{x}_{i,\mathrm{loc}}^{(s-1)}\right)$ defined in (5.9) is

$$
\frac{\partial \boldsymbol{f}\left(\boldsymbol{x}_{i,\mathrm{loc}}^{s(s-1)}\right)}{\partial \boldsymbol{x}_{i,\mathrm{loc}}^{s^{-}}} = \begin{bmatrix} 1 & 0 & \frac{\partial x_i^s}{\partial v_i^{s^-}} & \frac{\partial x_i^s}{\partial \psi_i^{s^-}} & \frac{\partial x_i^s}{\partial \omega_i^{s^-}} \\ 0 & 1 & \frac{\partial y_i^s}{\partial v_i^{s^-}} & \frac{\partial y_i^s}{\partial \psi_i^{s^-}} & \frac{\partial y_i^s}{\partial \omega_i^{s^-}} \\ 0 & 0 & 1 & 0 & 0 \\ 0 & 0 & 0 & 1 & T \\ 0 & 0 & 0 & 0 & 1 \end{bmatrix}, \tag{C.82}
$$

with (C.83a) to (C.83f), where for notational brevity we use $s^{-} := s - 1$ to denote the previous snapshot index.

$$\frac{\partial x_i^s}{\partial v_i^{s^-}} = -\frac{1}{\omega_i^{s^-}} \sin\left(\psi_i^{s^-}\right) + \frac{1}{\omega_i^{s^-}} \sin\left(\psi_i^{s^-} + \omega_i^{s^-} T\right) \tag{C.83a}$$

$$\frac{\partial x_i^s}{\partial \psi_i^{s^-}} = -\frac{v_i^{s^-}}{\omega_i^{s^-}} \cos\left(\psi_i^{s^-}\right) + \frac{v_i^{s^-}}{\omega_i^{s^-}} \cos\left(\psi_i^{s^-} + \omega_i^{s^-} T\right) \tag{C.83b}$$

$$\frac{\partial x_i^s}{\partial \omega_i^{s^-}} = \frac{v_i^{s^-}}{(\omega_i^{s^-})^2} \sin\left(\psi_i^{s^-}\right) - \frac{v_i^{s^-}}{(\omega_i^{s^-})^2} \sin\left(\psi_i^{s^-} + \omega_i^{s^-} T\right) + T\frac{v_i^{s^-}}{\omega_i^{s^-}} \cos\left(\psi_i^{s^-} + \omega_i^{s^-} T\right) \tag{C.83c}$$

$$\frac{\partial y_i^s}{\partial v_i^{s^-}} = \frac{1}{\omega_i^{s^-}} \cos\left(\psi_i^{s^-}\right) - \frac{1}{\omega_i^{s^-}} \cos\left(\psi_i^{s^-} + \omega_i^{s^-} T\right) \tag{C.83d}$$

$$\frac{\partial y_i^s}{\partial \psi_i^{s^-}} = -\frac{v_i^{s^-}}{\omega_i^{s^-}} \sin\left(\psi_i^{s^-}\right) + \frac{v_i^{s^-}}{\omega_i^{s^-}} \sin\left(\psi_i^{s^-} + \omega_i^{s^-} T\right) \tag{C.83e}$$

$$\frac{\partial y_i^s}{\partial \omega_i^{s^-}} = -\frac{v_i^{s^-}}{(\omega_i^{s^-})^2} \cos\left(\psi_i^{s^-}\right) + \frac{v_i^{s^-}}{(\omega_i^{s^-})^2} \cos\left(\psi_i^{s^-} + \omega_i^{s^-} T\right) + T\frac{v_i^{s^-}}{\omega_i^{s^-}} \sin\left(\psi_i^{s^-} + \omega_i^{s^-} T\right) \tag{C.83f}$$

C.12 Partial Derivative of Log-Likelihood Function w.r.t. State Vector for Gradient of SLAC Update Step

By the definition of the state vector (5.7) we have

$$\frac{\partial L_{\boldsymbol{r}_{i,j}^s}\left(\boldsymbol{x}_i^s, \boldsymbol{x}_j^s\right)}{\partial \boldsymbol{x}^s} = \begin{bmatrix} \frac{\partial L_{\boldsymbol{r}_{i,j}^s}\left(\boldsymbol{x}_i^s, \boldsymbol{x}_j^s\right)}{\partial \boldsymbol{x}_1^s} \\ \vdots \\ \frac{\partial L_{\boldsymbol{r}_{i,j}^s}\left(\boldsymbol{x}_i^s, \boldsymbol{x}_j^s\right)}{\partial \boldsymbol{x}_i^s} \\ \vdots \\ \frac{\partial L_{\boldsymbol{r}_{i,j}^s}\left(\boldsymbol{x}_i^s, \boldsymbol{x}_j^s\right)}{\partial \boldsymbol{x}_{|\mathbb{N}|}^s} \end{bmatrix} \tag{C.84}$$

with different definition for agents $\mathbb{R}$ and anchors $\mathbb{A}$ according to (5.1), such that

$$\frac{\partial L_{\boldsymbol{r}_{i,j}^s}\left(\boldsymbol{x}_i^s, \boldsymbol{x}_j^s\right)}{\partial \boldsymbol{x}_i^s} = \begin{cases} \left[\left(\frac{\partial L_{\boldsymbol{r}_{i,j}^s}\left(\boldsymbol{x}_i^s, \boldsymbol{x}_j^s\right)}{\partial \boldsymbol{x}_{i,\mathrm{loc}}^s}\right)^T \quad \left(\frac{\partial L_{\boldsymbol{r}_{i,j}^s}\left(\boldsymbol{x}_i^s, \boldsymbol{x}_j^s\right)}{\partial \boldsymbol{x}_{i,\mathrm{cal}}^s}\right)^T\right]^T & \text{if } i \in \mathbb{R} \\ \frac{\partial L_{\boldsymbol{r}_{i,j}^s}\left(\boldsymbol{x}_i^s, \boldsymbol{x}_j^s\right)}{\partial \boldsymbol{x}_{i,\mathrm{cal}}^s} & \text{if } i \in \mathbb{A}. \end{cases} \tag{C.85}$$

The partial derivatives w.r.t. the node kinematic states (5.2) evaluate to

$$\frac{\partial L_{\boldsymbol{r}^s_{i,j}}\left(\boldsymbol{x}^s_i,\boldsymbol{x}^s_j\right)}{\partial \boldsymbol{x}^s_{i,\mathrm{loc}}} = \begin{bmatrix} \left(\frac{\partial L_{\boldsymbol{r}^s_{i,j}}\left(\boldsymbol{x}^s_i,\boldsymbol{x}^s_j\right)}{\partial \boldsymbol{p}^s_i}\right)^T \\ \frac{\partial L_{\boldsymbol{r}^s_{i,j}}\left(\boldsymbol{x}^s_i,\boldsymbol{x}^s_j\right)}{\partial v^s_i} \\ \frac{\partial L_{\boldsymbol{r}^s_{i,j}}\left(\boldsymbol{x}^s_i,\boldsymbol{x}^s_j\right)}{\partial \psi^s_i} \\ \frac{\partial L_{\boldsymbol{r}^s_{i,j}}\left(\boldsymbol{x}^s_i,\boldsymbol{x}^s_j\right)}{\partial \omega^s_i} \end{bmatrix} = \begin{bmatrix} \left(\frac{\partial L_{\boldsymbol{r}^s_{i,j}}\left(\boldsymbol{x}^s_i,\boldsymbol{x}^s_j\right)}{\partial \boldsymbol{p}^s_i}\right)^T \\ 0 \\ \frac{\partial L_{\boldsymbol{r}^s_{i,j}}\left(\boldsymbol{x}^s_i,\boldsymbol{x}^s_j\right)}{\partial \psi^s_i} \\ 0 \end{bmatrix} \tag{C.86}$$

with

$$\frac{\partial L_{\boldsymbol{r}^s_{i,j}}\left(\boldsymbol{x}^s_i,\boldsymbol{x}^s_j\right)}{\partial \boldsymbol{p}^s_i} = \frac{L_{\boldsymbol{r}^s_{i,j}}\left(\boldsymbol{x}^s_i,\boldsymbol{x}^s_j\right)}{\partial \tau^s_{i,j}}\frac{\partial \tau^s_{i,j}}{\partial \boldsymbol{p}^s_i} + \frac{L_{\boldsymbol{r}^s_{i,j}}\left(\boldsymbol{x}^s_i,\boldsymbol{x}^s_j\right)}{\partial \phi^s_{i,j}}\frac{\partial \phi^s_{i,j}}{\partial \boldsymbol{p}^s_i}, \tag{C.87}$$

$$\frac{\partial L_{\boldsymbol{r}^s_{i,j}}\left(\boldsymbol{x}^s_i,\boldsymbol{x}^s_j\right)}{\partial \boldsymbol{p}^s_j} = -\frac{\partial L_{\boldsymbol{r}^s_{i,j}}\left(\boldsymbol{x}^s_i,\boldsymbol{x}^s_j\right)}{\partial \boldsymbol{p}^s_i}, \tag{C.88}$$

$$\frac{\partial L_{\boldsymbol{r}^s_{i,j}}\left(\boldsymbol{x}^s_i,\boldsymbol{x}^s_j\right)}{\partial \psi^s_i} = \frac{L_{\boldsymbol{r}^s_{i,j}}(\boldsymbol{x}^s_i,\boldsymbol{x}^s_j)}{\partial \phi^s_{i,j}}\frac{\partial \phi^s_{i,j}}{\partial \psi^s_i}. \tag{C.89}$$

where $\frac{L_{\boldsymbol{r}^s_{i,j}}\left(\boldsymbol{x}^s_i,\boldsymbol{x}^s_j\right)}{\partial \tau^s_{i,j}}$ is given by (C.92), $\frac{L_{\boldsymbol{r}^s_{i,j}}\left(\boldsymbol{x}^s_i,\boldsymbol{x}^s_j\right)}{\partial \phi^s_{i,j}}$ by (C.93), $\frac{\partial \phi^s_{i,j}}{\partial \boldsymbol{p}^s_i}$ and $\frac{\partial \phi^s_{i,j}}{\partial \boldsymbol{p}^s_j}$ by (3.25), $\frac{\partial \phi^s_{i,j}}{\partial \psi^s_i}$ by (3.26), $\frac{\partial \tau^s_{i,j}}{\partial \boldsymbol{p}^s_i} = \frac{-2(\boldsymbol{p}_j-\boldsymbol{p}_i)}{c||\boldsymbol{p}_j-\boldsymbol{p}_i||}$ and $\frac{\partial \tau^s_{i,j}}{\partial \boldsymbol{p}^s_j} = \frac{2(\boldsymbol{p}_j-\boldsymbol{p}_i)}{c||\boldsymbol{p}_j-\boldsymbol{p}_i||}$. The partial derivatives w.r.t. the node calibration states (5.6) evaluate to

$$\frac{\partial L_{\boldsymbol{r}^s_{i,j}}\left(\boldsymbol{x}^s_i,\boldsymbol{x}^s_j\right)}{\partial \boldsymbol{x}^s_{i,\mathrm{cal}}} = \begin{cases} \frac{\partial L_{\boldsymbol{r}^s_{i,j}}\left(\boldsymbol{x}^s_i,\boldsymbol{x}^s_j\right)}{\partial \delta^s_i} & \text{if } M_i = 1 \\ \begin{bmatrix} \frac{\partial L_{\boldsymbol{r}^s_{i,j}}\left(\boldsymbol{x}^s_i,\boldsymbol{x}^s_j\right)}{\partial \delta^s_i} & \left(\frac{\tilde{L}_{\boldsymbol{r}^s_{i,j}}\left(\phi^s_{i,j},\tau^s_{i,j},\boldsymbol{g}^s_{\mathrm{RI},i}\right)}{\partial \boldsymbol{g}^s_{\mathrm{RI},i}}\right)^T \end{bmatrix}^T & \text{if } M_i > 1, \end{cases} \tag{C.90}$$

where

$$\frac{\partial L_{\boldsymbol{r}^s_{i,j}}\left(\boldsymbol{x}^s_i,\boldsymbol{x}^s_j\right)}{\partial \delta^s_i} = \frac{-2}{c}\frac{\partial L_{\boldsymbol{r}^s_{i,j}}\left(\boldsymbol{x}^s_i,\boldsymbol{x}^s_j\right)}{\partial \tau^s_{i,j}}, \tag{C.91}$$

with $\frac{L_{\boldsymbol{r}^s_{i,j}}\left(\boldsymbol{x}^s_i,\boldsymbol{x}^s_j\right)}{\partial \tau^s_{i,j}}$ given by (C.92) and $\frac{\tilde{L}_{\boldsymbol{r}^s_{i,j}}\left(\phi^s_{i,j},\tau^s_{i,j},\boldsymbol{g}^s_{\mathrm{RI},i}\right)}{\partial \boldsymbol{g}^s_{\mathrm{RI},i}}$ given by (C.97). According to (5.32), the log-likelihood function is defined separately for nodes with singleport and multiport antenna, thus

$$\frac{\partial L_{\boldsymbol{r}^s_{i,j}}\left(\boldsymbol{x}^s_i,\boldsymbol{x}^s_j\right)}{\partial \tau^s_{i,j}} = \begin{cases} \frac{\partial \tilde{L}_{\boldsymbol{r}^s_{i,j}}\left(\tau^s_{i,j}\right)}{\partial \tau^s_{i,j}} & \text{if } M_i = 1 \\ \frac{\partial \tilde{L}_{\boldsymbol{r}^s_{i,j}}\left(\phi^s_{i,j},\tau^s_{i,j},\boldsymbol{g}^s_{\mathrm{RI},i}\right)}{\partial \tau^s_{i,j}} & \text{if } M_i > 1, \end{cases} \tag{C.92}$$

and

$$\frac{\partial L_{\boldsymbol{r}_{i,j}^s}\left(\boldsymbol{x}_i^s, \boldsymbol{x}_j^s\right)}{\partial \phi_{i,j}^s} = \begin{cases} 0 & \text{if } M_i = 1 \\ \frac{\partial \tilde{L}_{\boldsymbol{r}_{i,j}^s}\left(\phi_{i,j}^s, \tau_{i,j}^s, \boldsymbol{g}_{\mathrm{RI},i}^s\right)}{\partial \phi_{i,j}^s} & \text{if } M_i > 1, \end{cases} \tag{C.93}$$

Finally, the partial derivative of the log-likelihood function for nodes with singleport antenna (5.17) evaluates to

$$\frac{\partial \tilde{L}_{\boldsymbol{r}_{i,j}^s}\left(\tau_{i,j}^s\right)}{\partial \tau_{i,j}^s} = \frac{1}{\sigma_{\boldsymbol{r}_{i,j}^s}^2} \operatorname{Re}\left\{ \frac{2(\boldsymbol{r}_{i,j}^s)^H \left(\boldsymbol{s}^H(\tau_{i,j}^s)\boldsymbol{r}_{i,j}^s\right)}{\|\boldsymbol{s}(\tau_{i,j}^s)\|^2} \frac{\partial \boldsymbol{s}(\tau_{i,j}^s)}{\partial \tau_{i,j}^s} \right\}, \tag{C.94}$$

and the partial derivative of the log-likelihood functions for nodes with multiport antenna (5.20) evaluate to

$$\frac{\tilde{L}_{\boldsymbol{r}_{i,j}^s}\left(\phi_{i,j}^s, \tau_{i,j}^s, \boldsymbol{g}_{\mathrm{RI},i}^s\right)}{\partial \phi_{i,j}^s} = \frac{1}{\sigma_{\boldsymbol{r}_{i,j}^s}^2} \operatorname{Re}\left\{ \left(\frac{\partial \tilde{L}_{\boldsymbol{r}_{i,j}^s}(\phi_{i,j}^s, \tau_{i,j}^s, \boldsymbol{g}_{\mathrm{RI},i}^s)}{\partial \boldsymbol{v}_{i,j}^s} \right)^H \operatorname{vec}\left\{ \boldsymbol{G}_{i,j}^s \frac{\partial \boldsymbol{b}(\phi_{i,j}^s)}{\partial \phi_{i,j}^s} \boldsymbol{s}^T(\tau_{i,j}^s) \right\} \right\}, \tag{C.95}$$

$$\frac{\tilde{L}_{\boldsymbol{r}_{i,j}^s}\left(\phi_{i,j}^s, \tau_{i,j}^s, \boldsymbol{g}_{\mathrm{RI},i}^s\right)}{\partial \tau_{i,j}^s} = \frac{1}{\sigma_{\boldsymbol{r}_{i,j}^s}^2} \operatorname{Re}\left\{ \left(\frac{\partial \tilde{L}_{\boldsymbol{r}_{i,j}^s}(\phi_{i,j}^s, \tau_{i,j}^s, \boldsymbol{g}_{\mathrm{RI},i}^s)}{\partial \boldsymbol{v}_{i,j}^s} \right)^H \left(\frac{\partial \boldsymbol{s}(\tau_{i,j}^s)}{\partial \tau_{i,j}^s} \otimes \left(\boldsymbol{G}_{i,j}^s \boldsymbol{b}(\phi_{i,j}^s) \right) \right) \right\}, \tag{C.96}$$

$$\frac{\tilde{L}_{\boldsymbol{r}_{i,j}^s}\left(\phi_{i,j}^s, \tau_{i,j}^s, \boldsymbol{g}_{\mathrm{RI},i}^s\right)}{\partial \boldsymbol{g}_{\mathrm{RI},i}^s} = \begin{bmatrix} \operatorname{Re}\left\{ \left(\boldsymbol{b}^*(\phi_{i,j}^s)\boldsymbol{s}^H(\tau_{i,j}^s) \otimes \mathbb{I}_{M_i}\right) \frac{\partial \tilde{L}_{\boldsymbol{r}_{i,j}^s}(\phi_{i,j}^s, \tau_{i,j}^s, \boldsymbol{g}_{\mathrm{RI},i}^s)}{\partial \boldsymbol{v}_{i,j}^s} \right\} \\ \operatorname{Im}\left\{ \left(\boldsymbol{b}^*(\phi_{i,j}^s)\boldsymbol{s}^H(\tau_{i,j}^s) \otimes \mathbb{I}_{M_i}\right) \frac{\partial \tilde{L}_{\boldsymbol{r}_{i,j}^s}(\phi_{i,j}^s, \tau_{i,j}^s, \boldsymbol{g}_{\mathrm{RI},i}^s)}{\partial \boldsymbol{v}_{i,j}^s} \right\} \end{bmatrix}, \tag{C.97}$$

with

$$\frac{\tilde{L}_{\boldsymbol{r}_{i,j}^s}\left(\phi_{i,j}^s, \tau_{i,j}^s, \boldsymbol{g}_{\mathrm{RI},i}^s\right)}{\partial \boldsymbol{v}_{i,j}^s} = \frac{-2}{\sigma_{\boldsymbol{r}_{i,j}^s}^2} \left(\frac{\boldsymbol{v}_{i,j}^s (\boldsymbol{v}_{i,j}^s)^H}{(\boldsymbol{v}_{i,j}^s)^H \boldsymbol{v}_{i,j}^s} \boldsymbol{r}_{i,j}^s - \boldsymbol{r}_{i,j}^s \right) \left((\boldsymbol{r}_{i,j}^s)^H \frac{\boldsymbol{v}_{i,j}^s}{(\boldsymbol{v}_{i,j}^s)^H \boldsymbol{v}_{i,j}^s} \right). \tag{C.98}$$

Appendix D

List of Author's Publications

Journal Publications

[J1] R. Pöhlmann, S. A. Almasri, S. Zhang, T. Jost, A. Dammann, and P. A. Hoeher, "On the potential of multi-mode antennas for direction-of-arrival estimation," *IEEE Transactions on Antennas and Propagation*, vol. 67, no. 5, pp. 3374–3386, May 2019.

[J2] R. Pöhlmann, S. Zhang, E. Staudinger, A. Dammann, and P. A. Hoeher, "Simultaneous localization and calibration for cooperative radio navigation," *IEEE Transactions on Wireless Communications*, vol. 21, no. 8, pp. 6195–6210, Aug. 2022.

[J3] R. Pöhlmann, S. Zhang, E. Staudinger, S. Caizzone, A. Dammann, and P. A. Hoeher, "Bayesian in-situ calibration of multiport antennas for DoA estimation: Theory and measurements," *IEEE Access*, vol. 10, pp. 37 967–37 983, Apr. 2022.

[J4] S. Zhang, T. Jost, R. Pöhlmann, A. Dammann, D. Shutin, and P. A. Hoeher, "Spherical wave positioning based on curvature of arrival by an antenna array," *IEEE Wireless Communications Letters*, vol. 8, no. 2, pp. 504–507, Apr. 2019.

[J5] S. A. Almasri, R. Pöhlmann, N. Doose, P. A. Hoeher, and A. Dammann, "Modeling aspects of planar multi-mode antennas for direction-of-arrival estimation," *IEEE Sensors Journal*, vol. 19, no. 12, pp. 4585–4597, Jun. 2019.

[J6] S. Zhang, R. Pöhlmann, T. Wiedemann, A. Dammann, H. Wymeersch, and P. A. Hoeher, "Self-aware swarm navigation in autonomous exploration missions," *Proceedings of the IEEE*, vol. 108, no. 7, pp. 1168–1195, Jul. 2020.

[J7] M. J. Schuster, M. G. Müller, S. G. Brunner, H. Lehner, P. Lehner, R. Sakagami, A. Dömel, L. Meyer, B. Vodermayer, R. Giubilato, M. Vayugundla, J. Reill, F. Steidle, I. von Bargen, K. Bussmann, R. Belder, P. Lutz, W. Stürzl, M. Smisek, M. Maier, S. Stoneman, A. Fonseca Prince, B. Rebele, M. Durner, E. Staudinger, S. Zhang, R. Pöhlmann, E. Bischoff, C. Braun, S. Schröder, E. Dietz, S. Frohmann, A. Börner, H.-W. Hübers, B. Foing, R. Triebel, A. Albu-Schäffer, A. Wedler, J. Roberts, and G. Ishigami, "The ARCHES space-analogue demonstration mission: Towards heterogeneous teams of autonomous robots for collaborative scientific sampling in planetary exploration," *IEEE Robotics and Automation Letters*, vol. 5, no. 4, pp. 5315–5322, Oct. 2020.

[J8] E. Staudinger, S. Zhang, R. Pöhlmann, and A. Dammann, "The role of time in a robotic swarm: A joint view on communications, localization, and sensing," *IEEE Communications Magazine*, vol. 59, no. 2, pp. 98–104, Feb. 2021.

Conference Publications

[C1] R. Pöhlmann, S. Zhang, T. Jost, and A. Dammann, "Power-based direction-of-arrival estimation using a single multi-mode antenna," in *Proc. 14th Workshop Positioning, Navigation and Communications (WPNC)*, Bremen, Germany, Oct. 2017.

[C2] R. Pöhlmann, S. Zhang, Yinusa, Kazeem A., and A. Dammann, "Multi-mode antenna specific direction-of-arrival estimation schemes," in *Proc. IEEE 7th Int. Workshop Computational Advances in Multi-Sensor Adaptive Processing (CAMSAP)*, Curacao, Dec. 2017, pp. 462–466.

[C3] R. Pöhlmann, S. Zhang, A. Dammann, and P. A. Hoeher, "Fundamental limits for joint relative position and orientation estimation," in *Proc. IEEE Int. Conf. Communications Workshops (ICC Workshops)*, Kansas City, MO, USA, May 2018.

[C4] R. Pöhlmann, S. Zhang, A. Dammann, and P. A. Hoeher, "Fundamental limits for joint relative position and orientation estimation with generic antennas," in *Proc. 26th European Signal Processing Conf. (EUSIPCO)*, Rome, Italy, 2018, pp. 697–701.

[C5] R. Pöhlmann, G. Pedregosa, S. Caizzone, E. Staudinger, and P. A. Hoeher, "Multi-mode antenna enabled direction-of-arrival estimation for swarm navi-

gation," in *Proc. 16th Workshop Positioning, Navigation and Communications (WPNC)*, Bremen, Germany, Oct. 2019.

[C6] R. Pöhlmann, S. Zhang, and A. Dammann, "In-field calibration of antennas or antenna arrays using wavefield modeling," in *Proc. 53rd Asilomar Conf. Signals, Systems, and Computers*, Pacific Grove, USA, Nov. 2019.

[C7] R. Pöhlmann, S. Zhang, A. Dammann, and P. A. Hoeher, "Manifold optimization based beamforming for DoA and DoD estimation with a single multi-mode antenna," in *Proc. 28th European Signal Processing Conf. (EUSIPCO)*, 2020, pp. 1841–1845.

[C8] R. Pöhlmann, E. Staudinger, S. Zhang, S. Caizzone, A. Dammann, and P. A. Hoeher, "In-field calibration of a multi-mode antenna for DoA estimation," in *Proc. 15th European Conf. Antennas and Propagation (EuCAP)*, Mar. 2021.

[C9] R. Pöhlmann, S. Zhang, E. Staudinger, A. Dammann, and P. A. Hoeher, "Simultaneous localization and antenna calibration," in *Proc. 16th European Conf. Antennas and Propagation (EuCAP)*, Mar. 2022.

[C10] E. Staudinger, R. Pöhlmann, T. Wiedemann, S. Zhang, A. Dammann, and D. Shutin, "Swarm navigation and exploration for planetary surface missions: Experimental results," in *Proc. 16th Int. Planetary Probe Workshop*, Oxford, UK, Jul. 2019.

[C11] S. Zhang, R. Pöhlmann, and A. Dammann, "Heterogeneous network localization with a distributed phased array composed of cooperative vehicles," in *Proc. 27th European Signal Processing Conf. (EUSIPCO)*, A Coruna, Spain, Sep. 2019.

[C12] M. J. Schuster, B. Rebele, M. G. Müller, S. G. Brunner, A. Dömel, B. Vodermayer, R. Giubilato, M. Vayugundla, H. Lehner, P. Lehner, F. Steidle, L. Meyer, K. Bussmann, J. Reill, W. Stürzl, I. von Bargen, R. Sakagami, M. Smisek, M. Durner, E. Staudinger, R. Pöhlmann, S. Zhang, C. Braun, E. Dietz, S. Frohmann, S. Schröder, A. Börner, H.-W. Hübers, R. Triebel, B. Foing, A. O. Albu-Schäffer, and A. Wedler, "The ARCHES moon-analogue demonstration mission: Towards teams of autonomous robots for collaborative scientific sampling in lunar environments," in *Proc. European Lunar Symp. (ELS)*, May 2020.

[C13] S. Zhang, R. Pöhlmann, E. Staudinger, and A. Dammann, "Assembling a swarm navigation system: Communication, localization, sensing and control," in *Proc. 1st IEEE Int. Workshop Communication and Networking for Swarms Robotics (RoboCom)*, Jan. 2021.

[C14] S. Zhang, E. Staudinger, R. Pöhlmann, and A. Dammann, "Cooperative communication, localization, sensing and control for autonomous robotic networks," in *Proc. IEEE Int. Conf. Autonomous Systems (ICAS)*, Jun. 2021.

[C15] E. Staudinger, R. Giubilato, M. Schuster, R. Pöhlmann, S. Zhang, A. Dömel, A. Wedler, and A. Dammann, "Terrain-aware communication coverage prediction for cooperative networked robots in unstructured environments," in *Proc. 72nd Int. Astronautical Congr. (IAC)*, Dubai, United Arab Emirates, Oct. 2021.